

Distribution Agreement

In presenting this thesis or dissertation as a partial fulfillment of the requirements for an advanced degree from Emory University, I hereby grant to Emory University and its agents the non-exclusive license to archive, make accessible, and display my thesis or dissertation in whole or in part in all forms of media, now or hereafter known, including display on the world wide web. I understand that I may select some access restrictions as part of the online submission of this thesis or dissertation. I retain all ownership rights to the copyright of the thesis or dissertation. I also retain the right to use in future works (such as articles or books) all or part of this thesis or dissertation.

Signature:

George Andrew S. Inglis

Date

Roles of the *SCN1A* and *SCN8A* Voltage-Gated Sodium Channel Genes in Neurological Disease

By

George Andrew S. Inglis

Doctor of Philosophy

Graduate Division of Biological and Biomedical Science

Genetics and Molecular Biology

Andrew Escayg, Ph.D.
Advisor

Jeremy M. Boss, Ph.D.
Committee Member

Tamara Caspary, Ph.D.
Committee Member

Anita H. Corbett, Ph.D.
Committee Member

Peng Jin, Ph.D.
Committee Member

Accepted:

Lisa A. Tedesco, Ph.D.
Dean of the James T. Laney School of Graduate Studies

Date

Roles of the *SCN1A* and *SCN8A* Voltage-Gated Sodium Channel Genes in Neurological Disease

By

George Andrew S. Inglis
B.S., Pennsylvania State University, 2014

Advisor: Andrew Escayg, Ph.D.

An abstract of
a dissertation submitted to the Faculty of the
James T. Laney School of Graduate Studies of Emory University
in partial fulfillment of the requirements for the degree of
Doctor of Philosophy
in the Graduate Division of Biological and Biomedical Science
Genetics and Molecular Biology
2020

Abstract

Roles of the *SCN1A* and *SCN8A* Voltage-Gated Sodium Channel Genes in Neurological Disease

By George Andrew S. Inglis

The neuronal voltage-gated sodium channel genes, *SCN1A* and *SCN8A*, play a critical role in the control of normal neuronal excitability. Mutations in both genes have been linked to several neurological disorders, most prominently epilepsy. Though both channels are detectable in a variety of neuronal subtypes, loss-of-function mutations in *SCN1A* particularly impact the activity of GABAergic interneurons that drive neuronal inhibition. Therefore, modulating *SCN1A* transcription may have broad translational relevance to neurological disorders associated with impaired neuronal inhibition, such as epilepsy, schizophrenia, or Alzheimer's disease. In contrast, increased *SCN8A* activity in excitatory pyramidal neurons is sufficient to induce seizures in mice, suggesting that *SCN8A* mutations may drive neuronal hyperexcitability. However, patients with *SCN8A* mutations exhibit a diverse range of clinical phenotypes, thereby complicating efforts to develop efficacious treatments. Given the broad contributions of *SCN1A* and *SCN8A* to neurological disease, the aims of this dissertation were (1) to identify genetic elements or pathways contributing toward transcriptional regulation of *SCN1A* and (2) to characterize the phenotypic impacts of novel, overlapping *Scn8a* mutations. For the first aim, we analyzed publicly available neuronal open chromatin data to identify putative functional genomic elements in *SCN1A*, such as transcriptional enhancer sequences. Given that *SCN1A* is robustly expressed in GABAergic interneurons, we also performed ATAC-seq and mRNA-seq at three time points during interneuron development from human-derived iPSCs, to identify additional genetic elements associated with elevated *SCN1A* expression. At the same time, we developed a comprehensive profile of genome-wide epigenomic and transcriptomic changes concordant with GABAergic interneuron development. From this study, we identified several genes that may play an important role in interneuron function and the pathogenesis of schizophrenia. In line with our second aim, we generated three mouse lines with varying degrees reduced activity of the *Scn8a* channel protein, Na_v1.6: $\Delta 19$, $\Delta 3$, and $\Delta 35$. Our results suggest that hypomorphic *Scn8a* alleles may exert effects on Na_v1.6 function that are distinct from null alleles, potentially due to aberrant channel heterodimerization. Altogether, the results presented in this dissertation expand our existing knowledge of *SCN1A* regulation, the pathways contributing toward a GABAergic interneuron cell fate, and the phenotypic impact of hypomorphic and loss-of-function Na_v1.6 mutations.

Roles of the *SCN1A* and *SCN8A* Voltage-Gated Sodium Channel Genes in Neurological Disease

By

George Andrew S. Inglis
B.S., Pennsylvania State University, 2014

Advisor: Andrew Escayg, Ph.D.

A dissertation to the Faculty of the
James T. Laney School of Graduate Studies of Emory University
in partial fulfillment of the requirements for the degree of
Doctor of Philosophy
in the Graduate Division of Biological and Biomedical Science
Genetics and Molecular Biology
2020

Acknowledgments

First and foremost, I would like to thank my adviser, Dr. Andrew Escayg, for his invaluable guidance and mentorship over the past 5.5 years. Practically speaking, I came into Emory as a microbiologist, and it was unclear to everyone as to what I was doing in a human genetics program. Andrew nevertheless welcomed me into the lab and empowered me to pursue projects that matched my own professional interests, while also remaining engaged in the Emory community through student leadership and teaching. Dr. Jennifer Wong has also been, professional and personally, a critical staple of my graduate career, and I am thankful to have had her as a (unofficial) mentor and (official) friend. Thank you for your support in science (grants, experiments) and life (donuts, not running). To the past and present members of the Escayg lab: Dr. Stacey Dutton, Dr. Tyra Lamar, Dr. Kameryn Butler, Lindsey Shapiro, Kari Mattison, Jackie Thelin, Thomas Shiu, and Samantha Reed, thank you for providing an incredibly supportive work environment; I am grateful for the collaboration and beer. The *Scn8a* $\Delta 9$, $\Delta 3$, $\Delta 35$ mouse lines were initially generated by Dr. Kameryn Butler, and without her immense contribution, I would not have been able to generate the data presented in Chapter 4 of this dissertation. To my committee: Dr. Jerry Boss, Dr. Tamara Caspary, Dr. Anita Corbett, and Dr. Peng Jin, thank you all for keeping me on track and your invaluable feedback, particularly in shaping the experiments described in Chapters 2-3. All things considered, I would not have been able to pursue as many interesting research questions without the support of a collaborative research network at Emory University, and I am grateful to have been able to work with the Boss, English, Lin, and Wen labs throughout my graduate career. While most people will not read beyond this page, except to possibly skim some pretty figures, it has altogether been satisfying (and oddly therapeutic) to formalize the entirety of my graduate work in this document.

Table of Contents

CHAPTER 1: Introduction	1
1.1 The voltage-gated sodium channel gene family.....	1
1.2 Voltage-gated sodium channels in the central nervous system.....	3
1.2.1 Overview of the neuronal voltage-gated sodium channels	3
1.2.2 <i>SCN1A</i> , <i>SCN8A</i> , and the excitatory-inhibitory balance	5
1.3 <i>SCN1A</i> and <i>SCN8A</i> dysfunction in neurological disease.....	5
1.3.1 Familial hemiplegic migraine.....	5
1.3.2 <i>SCN1A</i> -derived epilepsy.....	6
1.3.3 <i>SCN8A</i> -derived epilepsy.....	6
1.3.4 Neuropsychiatric disorders and dementia	10
1.4 Regulation of <i>SCN1A</i> and <i>SCN8A</i>	11
1.4.1 Pharmacological modulation of Na _v 1.1 and Na _v 1.6 activity.....	11
1.4.2 Transcriptional regulation of <i>SCN1A</i> and <i>SCN8A</i> expression.....	12
1.4.3 Detecting additional putative functional genomic elements	13
1.5 Summary and goals of dissertation	17
CHAPTER 2: Towards the identification of transcriptional regulatory elements for the voltage-gated sodium channel gene, <i>SCN1A</i>	19
2.1 Abstract	19
2.2 Introduction	20
2.3 Materials and Methods.....	21
2.3.1 Identification of putative functional genomic elements (FGEs) in the <i>SCN1A</i> locus..	21
2.3.2 Generation of luciferase reporter vectors	22
2.3.3 SH-SY5Y cell culture and transfection	24
2.3.4 Quantitative real-time PCR (qRT-PCR).....	25
2.3.5 Statistical analysis	25
2.4 Results	27
2.4.1 Open chromatin and transcription factor ChIP-seq data predict 32 putative functional genomic elements (FGEs) within the <i>SCN1A</i> locus.....	27
2.4.2 FGE2 and FGE17 moderately enhance luciferase reporter activity.....	30
2.4.3 <i>SCN1A</i> FGEs may jointly contribute to transcriptional regulation of reporter activity32	
2.4.4 Epilepsy-associated SNPs do not robustly affect luciferase reporter activity.....	34
2.5 Discussion	36

2.6 Acknowledgments.....	38
CHAPTER 3: Transcriptomic and epigenomic dynamics associated with development of human iPSC-derived GABAergic interneurons	39
3.1 Abstract	39
3.2 Introduction	40
3.3 Materials and Methods.....	42
3.3.1 <i>In vitro</i> differentiation to GABAergic interneurons (GINs)	42
3.3.2 Immunostaining for neuronal markers	43
3.3.3 RNA-seq and data analysis.....	44
3.3.4 Quantitative real-time PCR (qRT-PCR).....	46
3.3.5 Assay for transposase-accessible chromatin (ATAC-seq) and data analysis.....	46
3.3.6 Transcription factor (TF) motif analysis	48
3.3.7 Statistical analysis	48
3.3.8 Data availability	49
3.4 Results	50
3.4.1 Human induced pluripotent stem cells (iPSCs) are differentiated to GABAergic interneurons (GINs) with high efficiency	50
3.4.2 RNA-seq confirms enrichment of genes and pathways associated with GIN function.....	52
3.4.3 HC1- and HC2-derived GINs exhibit similar changes in chromatin accessibility across differentiation	56
3.4.4 Changes in chromatin accessibility are correlated with GIN-specific gene expression	58
3.4.5 Motif enrichment analysis implicates distinct groups of transcription factors in GIN differentiation	60
3.4.6 A subset of DEGs may represent novel risk factors for schizophrenia.....	62
3.5 Discussion	67
3.6 Acknowledgments.....	72
CHAPTER 4: Mutations in the <i>Scn8a</i> DIIS4 voltage sensor reveal new distinctions among hypomorphic and null Na_v1.6 sodium channels	73
4.1 Abstract	73
4.2 Introduction.....	74
4.3 Materials and Methods.....	77
4.3.1 Generation of founder mice.....	77
4.3.2 Genotyping.....	77

4.3.3 Animal maintenance.....	78
4.3.4 Protein modeling	79
4.3.5 Survival and weight analysis.....	79
4.3.6 Western blot analysis.....	79
4.3.7 6 Hz psychomotor seizure induction	80
4.3.8 Flurothyl seizure induction.....	80
4.3.9 EEG surgery and analysis.....	81
4.3.10 Behavioral assessment.....	81
4.3.11 Acoustic startle response	82
4.3.12 Auditory brainstem response.....	82
4.3.13 Experimental conditions for motor assessment.....	83
4.3.14 Rotarod	83
4.3.15 Grip strength.....	83
4.3.16 Nerve conduction analysis.....	84
4.3.17 Statistical analysis	84
4.4 Results	86
4.4.1 Identification of new <i>Scn8a</i> mutants with severe motor impairments	86
4.4.2 $\Delta 9$ mutants express normal levels of $\text{Na}_v1.6$	90
4.4.3 <i>Scn8a</i> ^{$\Delta 9/+$} , <i>Scn8a</i> ^{$\nabla 3/+$} , and <i>Scn8a</i> ^{$\Delta 35/+$} heterozygous mutants are resistant to induced seizures	92
4.4.4 $\Delta 9$ and $\nabla 3$ are predicted hypomorphic alleles of <i>Scn8a</i>	94
4.4.5 <i>Scn8a</i> ^{$\Delta 9/+$} and <i>Scn8a</i> ^{$\nabla 3/+$} mutants do not exhibit increased anxiety or deficits in learning and sociability	94
4.4.6 <i>Scn8a</i> ^{$\Delta 9/+$} and <i>Scn8a</i> ^{$\nabla 3/+$} mutants exhibit a decreased acoustic startle response.....	94
4.4.7 <i>Scn8a</i> ^{$\Delta 9/+$} and <i>Scn8a</i> ^{$\nabla 3/+$} heterozygous mutants exhibit motor impairments	98
4.4.8 $\Delta 9$ and $\nabla 3$ homozygous mutants exhibit reduced nerve conduction velocity	100
4.5 Discussion	102
4.6 Acknowledgments.....	108
CHAPTER 5: Conclusions and future directions	109
5.1 Summary of dissertation research	109
5.2 The state of <i>SCN1A</i> transcriptional regulation.....	110
5.2.1 Endogenous regulation of <i>SCN1A</i> mRNA levels	110
5.2.2 dCas9-based strategies to elevate <i>SCN1A</i> expression	114

5.2.3 The shift towards single-cell analyses.....	115
5.3 Assessment of novel targets for GABAergic interneuron function	116
5.3.1 Putative genetic regulatory elements in genes relevant to GABAergic function.....	116
5.3.2 Examining the contribution of <i>CPLX2</i> and <i>TRPC4</i> to neurological disease.....	117
5.4 The phenotypic spectrum of loss-of-function mutations in <i>SCN8A</i>	118
5.4.1 Examining the phenotypic impact of hypomorphic and null <i>SCN8A</i> alleles	118
5.4.2 Future characterization of the <i>Scn8a</i> $\Delta 9$ and $\nabla 3$ alleles	120
5.4.3 The contribution of Nav1.6 to the acoustic startle response and hearing	120
5.5 Conclusions	121
<u>APPENDIX A: Supporting data for Chapter 2</u>	147
<u>APPENDIX B: Supporting data for Chapter 3</u>	152
<u>APPENDIX C: Supporting data for Chapter 4</u>	160
C.1 Supporting materials and methods	160
C.1.1 Open field test and novel object recognition	160
C.1.2 Three-chamber social interaction	160
C.1.3 Reciprocal social interaction.....	161
C.2 Supporting figures and tables	162

List of Figures

Figure 1.1. Structure of the human voltage-gated sodium channel (VGSC) proteins.....	2
Figure 1.2. 5' genomic organization of human <i>SCN1A</i> and <i>SCN8A</i>	12
Figure 1.3. Comparison of high-throughput approaches to detect accessible chromatin.....	16
Figure 2.1. Neuronal open chromatin data indicate 32 putative functional genomic elements (FGEs) in the <i>SCN1A</i> locus.	28
Figure 2.2. Several FGEs demonstrate cis-regulatory activity in a dual luciferase reporter assay.	29
Figure 2.3. Subdeletions of FGE2 and FGE17 exhibit complex impacts on luciferase reporter activity.	30
Figure 2.4. FGEs exhibit a combinatorial effect on luciferase reporter activity.	33
Figure 2.5. Epilepsy-associated SNPs do not elicit robust allele-dependent effects on luciferase reporter activity.	35
Figure 3.1. Distinct subtypes of GABAergic interneurons emerge after 78 days of differentiation.	51
Figure 3.2. Broad changes in neuronal gene expression across GIN differentiation.	53
Figure 3.3. iPSC-derived GINs are enriched for pathways associated with mature neuronal function.....	55
Figure 3.4. ATAC-seq reveals widespread changes in chromatin accessibility across GIN differentiation.	57
Figure 3.5. Dynamic association of chromatin accessibility and gene expression across GIN differentiation.	59
Figure 3.6. DARs with divergent changes in accessibility are enriched for distinct sets of transcription factors.....	61
Figure 3.7. DARs are significantly enriched in schizophrenia-associated genomic loci.	63
Figure 3.8. A subset of genes that are differentially expressed in the schizophrenia dorsolateral prefrontal cortex (DLPFC) exhibit opposing trends in expression across GIN differentiation. ...	66
Figure 4.1. $\Delta 9$, $\nabla 3$, and $\Delta 35$ are novel alleles in the Nav1.6 DIIS4 voltage sensor.....	87
Figure 4.2. <i>Scn8a</i> ^{$\Delta 9/\Delta 9$} , <i>Scn8a</i> ^{$\nabla 3/\nabla 3$} , and <i>Scn8a</i> ^{$\Delta 35/\Delta 35$} homozygous mutants exhibit decreased growth and premature lethality.	89

Figure 4.3. The $\Delta 9$ mutation does not alter Nav1.6 protein levels.....	91
Figure 4.4. <i>Scn8a</i> ^{A9/+} , <i>Scn8a</i> ^{V3/+} , and <i>Scn8a</i> ^{A35/+} heterozygous mutants are resistant to induced seizures.	93
Figure 4.5. <i>Scn8a</i> ^{A9/+} and <i>Scn8a</i> ^{V3/+} heterozygous mutants exhibit a reduced acoustic startle response.	96
Figure 4.6. <i>Scn8a</i> ^{A9/+} , <i>Scn8a</i> ^{V3/+} , and <i>Scn8a</i> ^{A35/+} heterozygous mutants demonstrate normal auditory brainstem response (ABR).	97
Figure 4.7. <i>Scn8a</i> ^{A9/+} and <i>Scn8a</i> ^{V3/+} heterozygous mutants exhibit impaired motor performance on a rotarod.	99
Figure 4.8. <i>Scn8a</i> ^{A9/A9} and <i>Scn8a</i> ^{V3/V3} homozygous mutants exhibit reduced nerve conduction velocity.	101
Figure 5.1. Comparison of differential gene expression and chromatin accessibility within 1 Mb of the <i>SCN1A</i> locus across GIN differentiation.	113
Figure A1. Transcription factors with predicted binding in FGE2 do not significantly alter <i>SCN1A</i> expression.	147
Figure B1. Neural progenitor cells (NPCs) emerge after 22 days of differentiation.	152
Figure B2. The genomic distribution of ATAC-seq peaks is comparable between the HC1 and HC2 lines at each stage of GABAergic interneuron (GIN) differentiation.	152
Figure B3. Differentially expressed genes (DEGs) exhibit consistent expression patterns between HC1 and HC2 cell lines.	153
Figure B4. Transcription factor motifs enriched in +A DARs with increased accessibility over GIN differentiation exhibit discernable footprints.	154
Figure B5. Transcription factor motifs enriched in -A DARs with decreased accessibility over GIN differentiation exhibit discernable footprints.	155
Figure B6. Transcription factors enriched in +A DARs are predicted to interact with 198 genes that are differentially expressed in the dorsolateral prefrontal cortex of schizophrenia patients.	156
Figure B7. Overview of comparisons between DEGs associated with GIN differentiation and the schizophrenia dorsolateral prefrontal cortex.	157
Figure C1. <i>Scn8a</i> ^{A9/A9} , <i>Scn8a</i> ^{V3/V3} , and <i>Scn8a</i> ^{A35/A35} homozygous mutants are born in the predicted Mendelian ratio.	162
Figure C2. Representative anti-Nav1.6 immunoblots.	162

Figure C3. Female <i>Scn8a</i> ^{A9/+} , <i>Scn8a</i> ^{V3/+} , and <i>Scn8a</i> ^{A35/+} heterozygous mutants are resistant to induced seizures.	163
Figure C4. Representative click-test-evoked ABR waves.	164
Figure C5. <i>Scn8a</i> ^{A9/+} , <i>Scn8a</i> ^{V3/+} , and <i>Scn8a</i> ^{A35/+} heterozygous mutants exhibit normal ABR interpeak latencies.	165

List of Tables

Table 1.1. Genomic organization and tissue-specific expression of human voltage-gated sodium channel α subunit genes.	4
Table 1.2. Subcellular distribution of neuronal voltage-gated sodium channel α subunit genes. ...	4
Table 1.3. Overview of reported <i>Scn8a</i> mouse models.	9
Table 2.1. Genome-wide association studies (GWASs) identify three epilepsy-associated SNPs in the <i>SCN1A</i> locus.	35
Table 5.1. There are no differentially accessible regions of chromatin within the <i>SCN1A</i> locus across GIN differentiation.	112
Table A1. Data accessions from the UCSC ENCODE and NCBI GEO databases used to identify putative functional genome elements (FGEs).	148
Table A2. Coordinates and annotations of FGEs in the <i>SCN1A</i> locus.	150
Table A3. List of primer sequences for molecular cloning and quantitative real-time PCR (qRT-PCR).	151
Table B1. List of primer sequences for quantitative real-time PCR (qRT-PCR) analyses.	158
Table B2. List of the 10 most significant biological process gene ontology (GO) pathways identified by gene set enrichment analysis (GSEA).	159
Table C1. <i>Scn8a</i> ^{A9/+} heterozygous mutants do not exhibit deficits in several behavioral paradigms.	166
Table C2. <i>Scn8a</i> ^{V3/+} heterozygous mutants do not exhibit deficits in several behavioral paradigms.	167
Table C3. <i>Scn8a</i> $\Delta 9$, $\Delta 3$, and $\Delta 35$ heterozygous and homozygous mutant mice exhibit several phenotypic differences from WT littermates.	168

CHAPTER 1: Introduction

1.1 The voltage-gated sodium channel gene family

The voltage-gated sodium channel (VGSC) gene family is comprised of nine α subunits and four accessory β subunits that collectively initiate and propagate action potentials in a variety of excitable cell types, such neurons and myocytes (**Table 1.1**) (1,2). VGSC α subunits consist of four repeat domains (denoted DI-DIV), each of which is composed of six transmembrane segments (S1-S6; **Fig. 1.1**) (3,4). The S4 voltage sensor segment in each repeat domain is enriched for positively charged amino acid residues, and plays an important role in voltage-dependent channel gating (**Fig. 1.1A**) (4). The S5-S6 extracellular linkers constitute the channel pore-forming loop and establish a sodium cation selectivity filter (**Fig. 1.1A**) (3,4). In response to membrane depolarization, the channel will open and permit the influx of sodium cations into the cell (5-7). This depolarizing sodium current is sustained until the transmembrane potential reaches approximately +30 mV, at which point the channel closes and temporarily enters a refractory period of activity as the membrane is repolarized (5,6,8). While VGSCs α subunits were initially reported to act as monomers, recent work has demonstrated that α subunits also form homodimers (9,10). In contrast, the accessory β subunits are monomeric proteins consisting of a single, type I transmembrane domain, with an extracellular immunoglobulin-like hook (**Fig. 1.1A**) (3,11). Up to two β subunit proteins (β 1 or β 3, with β 2 or β 4) may interact with VGSC α subunits to modulate membrane localization and channel kinetics (11-14).

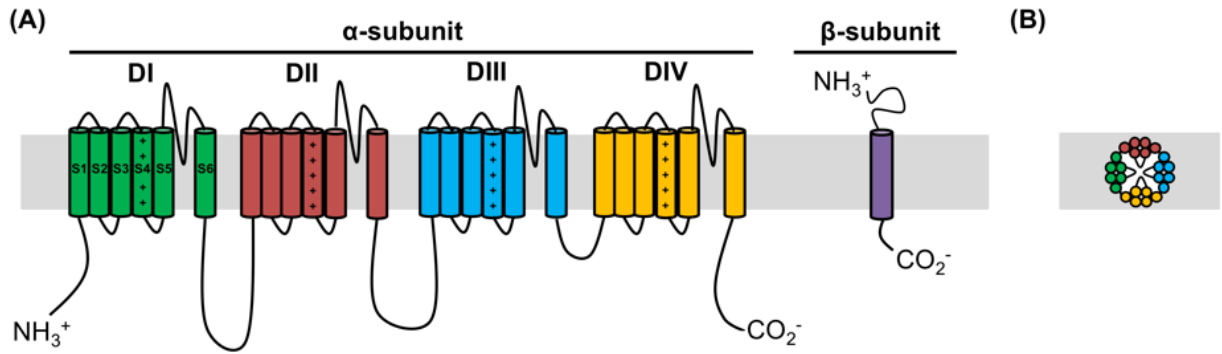


Figure 1.1. Structure of the human voltage-gated sodium channel (VGSC) proteins. (A) The VGSC α subunit is comprised of four repeat domains (DI-DIV), each consisting of six transmembrane segments (S1-S6). Plus signs (+) indicate the positively charged S4 voltage sensor segment in each domain. The VGSC β subunit consists of a single type I transmembrane domain. **(B)** Topological view of the VGSC α subunit tertiary structure in the plasma membrane.

1.2 Voltage-gated sodium channels in the central nervous system

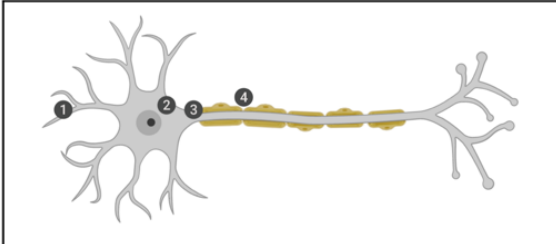
1.2.1 Overview of the neuronal voltage-gated sodium channels

Four VGSC α subunit genes are predominantly expressed in the central nervous system: *SCN1A* (encoding $Na_v1.1$), *SCN2A* ($Na_v1.2$), *SCN3A* ($Na_v1.3$), and *SCN8A* ($Na_v1.6$, **Tables 1.1-1.2**) (3,15). These four genes are broadly expressed throughout the brain, with weaker expression in the retina and spinal cord (16,17). *SCN3A* expression peaks during embryogenesis and declines after birth, whereas *SCN1A*, *SCN2A*, and *SCN8A* mRNA levels increase throughout gestation and early life (16,18). Expression of these VGSCs is not mutually exclusive, as each channel exhibits unique electrophysiological properties and subcellular distribution (**Table 1.2**). $Na_v1.3$ is predominantly localized to the soma, while $Na_v1.1$, $Na_v1.2$, and $Na_v1.6$ exhibit more variable distribution across neuronal membranes (**Table 1.2**) (17,19). $Na_v1.1$ and $Na_v1.2$ are broadly expressed throughout the neuron, though $Na_v1.1$ is primarily localized to the soma and axon initial segment and $Na_v1.2$ is enriched at unmyelinated nodes of Ranvier (**Table 1.2**) (17,19). As axons become fully myelinated, $Na_v1.6$ replaces $Na_v1.2$ to become the primary VGSC at the mature nodes of Ranvier (3,20-22). $Na_v1.6$ also plays an important role at the axon initial segment, where it contributes to repetitive action potential firing (**Table 1.2**) (3,20,21).

Table 1.1. Genomic organization and tissue-specific expression of human voltage-gated sodium channel α subunit genes. CNS and PNS denote expression the central nervous system and peripheral nervous system, respectively.

Gene	Chromosome	Protein	Tissue Expression
SCN1A	chr2	Na _v 1.1	CNS PNS
SCN2A	chr2	Na _v 1.2	CNS PNS
SCN3A	chr2	Na _v 1.3	CNS PNS
SCN4A	chr17	Na _v 1.4	Skeletal muscle
SCN5A	chr3	Na _v 1.5	Cardiac muscle
SCN8A	chr12	Na _v 1.6	CNS PNS
SCN9A	chr2	Na _v 1.7	PNS
SCN10A	chr3	Na _v 1.8	PNS
SCN11A	chr3	Na _v 1.9	PNS

Table 1.2. Subcellular distribution of neuronal voltage-gated sodium channel α subunit genes. Circled numbers denote channel localization to the dendrites (1), soma (2), axon initial segment (3), or nodes of Ranvier (4).



Gene	Protein	Subcellular Localization
SCN1A	Na _v 1.1	Dendrites ¹ Soma ² Axon initial segment ³ Nodes of Ranvier ⁴
SCN2A	Na _v 1.2	Soma ² Axon initial segment ³ Nodes of Ranvier ⁴
SCN3A	Na _v 1.3	Soma ²
SCN8A	Na _v 1.6	Dendrites ¹ Axon initial segment ³ Nodes of Ranvier ⁴

1.2.2 *SCN1A*, *SCN8A*, and the excitatory-inhibitory balance

SCN1A and *SCN8A* demonstrate salient contributions to the normal control of neuronal excitability. Though both channels are detectable in a variety of neuronal subtypes, *SCN1A* is preferentially expressed in inhibitory cells, particularly GABAergic interneurons (GINs) (19,22-27). Conditional deletion of *Scn1a* in GINs and inhibitory Purkinje neurons of mice is sufficient to reduce the excitability of these cells, but excitability of pyramidal cells is not significantly altered following *Scn1a* deletion (26,28). In contrast, conditional expression of a gain-of-function *Scn8a* allele in excitatory neurons, but not GINs, is sufficient to induce seizures and premature lethality in mice (29). Taken together, these findings support the hypothesis that *SCN1A* expression is essential for proper inhibitory neuronal signaling, whereas aberrant *SCN8A* activity may drive neuronal hyperexcitability (3,20,21). *SCN1A* and *SCN8A* therefore contribute to the delicate balance between neuronal excitation and inhibition, which is often disrupted in neurological disease (17). Accordingly, aberrant $\text{Na}_v1.1$ and $\text{Na}_v1.6$ expression or activity have been implicated in several neurological disorders, including migraine, epilepsy, and Alzheimer's disease (17,30-32).

1.3 *SCN1A* and *SCN8A* dysfunction in neurological disease

1.3.1 Familial hemiplegic migraine

Familial hemiplegic migraine (FHM) is an autosomal dominant form of migraine with aura accompanied by paralysis of one side of the body (33,34). FHM is classified into one of three subtypes, based on the causative gene: FHM1 (*CACNA1A*), FHM2 (*ATP1A2*), and FHM3 (*SCN1A*) (33,34). To date, over ten pathogenic mutations in *SCN1A* have been identified in

patients with FHM3, representing both gain-of-function, as well as loss-of-function variants that induce folding defects in the tertiary structure of Na_v1.1 (30,33-35).

1.3.2 *SCN1A*-derived epilepsy

Epilepsy is a neurological disorder characterized by recurrent, spontaneous seizures that affects over 50 million people worldwide (36). Since the first epilepsy mutation in *SCN1A* was described in 2000, over 1,250 additional pathogenic mutations have been identified in patients with multiple forms of early-onset epilepsy (37-39). *SCN1A* mutations are responsible for at least 10% of cases of genetic epilepsy with febrile seizures plus (GEFS+), which is marked by both febrile and afebrile seizures that begin in adolescence and persist beyond six years of age (14,40). Heterozygous loss-of-function mutations in *SCN1A* account for 70-80% of cases of Dravet syndrome, a refractory, severe early-life epileptic encephalopathy (14,41). In addition to seizures, patients with *SCN1A*-derived epilepsy exhibit a spectrum of additional clinical phenotypes, including intellectual disability, developmental delay, sleep disturbances, gastrointestinal distress, impaired mobility or ataxia, and autistic features (41,42).

1.3.3 *SCN8A*-derived epilepsy

In contrast to *SCN1A*, the first *SCN8A* mutation in a patient with epilepsy was only reported in 2012 (31). Since this initial report, over 150 additional pathogenic mutations have been identified in *SCN8A*, spanning multiple forms of severe, refractory epilepsy (31,43-48). Though several loss-of-function alleles have been identified in patients in epilepsy, most reported cases of *SCN8A*-derived epilepsy are due to gain-of-function mutations in *SCN8A* (49-55). Patients with *SCN8A*-derived epilepsy also exhibit a range of clinical comorbidities, including

developmental delay, intellectual disability, autism, tremor, ataxia, reduced bone density, and hypotonia (43,46,56-58).

1.3.3.1 The contribution of Na_v1.6 voltage sensors to epilepsy

The phenotypic spectrum of patients with *SCN8A* mutations is diverse, even among individuals with mutations that impact the same regions of Na_v1.6, such as the S4 voltage sensor domains (44,47,48,52,55,59-62). To date, 21 pathogenic mutations have been identified in the four Na_v1.6 voltage sensor domains in epilepsy patients (4,47,48,61,62). Patients with these mutations exhibit early-onset refractory epilepsy and a spectrum of additional clinical phenotypes including developmental delay (p.R223G, DIS4), tremor and intellectual disability (p.F846S, DIIS4), and hypotonia (p.R850Q, DIIS4) (46,57,58). This phenotypic variability also extends to patients with mutations within the same S4 voltage sensor. For instance, both p.R1617Q and p.R1620L occur in the DIVS4 voltage sensor; however, whereas p.R1617Q was identified in a patient with refractory seizures, intellectual disability and impaired motor function, p.R1620L was found in a patient with autism, intellectual disability, dyskinesia, and attention deficit hyperactivity disorder without severe epilepsy (58,63,64).

1.3.3.2 Phenotypic variability among mouse models of *Scn8a* dysfunction

Rodent models offer a powerful tool to study the impact of specific *SCN8A* mutations on seizure, behavior, and motor phenotypes. Since the first mouse model expressing a *Scn8a* mutation (*med-jo*) was reported in 1965, over 20 additional models of *Scn8a* dysfunction have been generated (**Table 1.3**) (65). Mice that are homozygous for *Scn8a* mutant alleles exhibit motor abnormalities and/or reduced survival relative to wild-type or heterozygous mutant littermates (**Table 1.3**)

(53,65-69). Mice that are heterozygous for gain-of-function *SCN8A* alleles may also exhibit mild deficits in motor coordination relative to wild-type littermates, and develop convulsive, spontaneous seizures that contribute to premature lethality (**Table 1.3**) (29,69). In contrast, mice that are heterozygous for loss-of-function *Scn8a* alleles often demonstrate comparable motor function and survival to wild-type littermates, though they are more resistant to induced seizures (**Table 1.3**) (70-72).

There are broad phenotypic differences in terms of survival, behavior, and motor phenotypes between mice with loss-of-function *Scn8a* mutations (**Table 1.3**). The severity of motor impairment varies between lines, ranging from mild tremor (*med-jo*) or lurching gait (*9J*) to progressive hind-limb paralysis (*med*; **Table 1.3**) (53,65,73). Motor phenotypes may also vary between lines with mutations in the same region of the Na_v1.6 channel protein. For instance, the *nmf2*, *nmf5*, and *nmf58* missense mutations all affect the Na_v1.6 DIII pore-forming loop, yet while *Scn8a^{nmf2/nmf2}* and *Scn8a^{nmf5/nmf5}* homozygous mutants exhibit hind-limb paralysis, *Scn8a^{nmf58/nmf58}* animals demonstrate milder dystonia (**Table 1.3**) (67). Seizure phenotypes and survival are also dependent on the genetic background of the mutant animals. For instance, *Scn8a^{med-jo/+}*, *Scn8a^{med/+}*, or *Scn8a^{8J/+}* heterozygous mutants develop absence seizures when bred onto the C3HeB/FeJ, but not C57BL/6J, genetic background (74). Similarly, *Scn8a^{med-j/med-j}* homozygous mutants exhibit neonatal lethality when bred on the C57BL/6J background, but survive to adulthood when crossed onto the C3HeB/FeJ, A/J, DBA/2J, or 129S6 genetic backgrounds (75,76). Given the contribution of genetic background to observed phenotypes in mutant animals, it is crucial to compare the phenotypic impacts of alleles between mice bred on the same genetic background.

Table 1.3. Overview of reported *Scn8a* mouse models. Phenotypes refer to wild-type (WT), heterozygous (m/+) or homozygous (m/m) mutant mice.

Allele	Type of Mutation	Effect on Na _v 1.6	Location	Reference(s)	Phenotypes
<i>med</i>	LINE insertion	Null	Exon 2	Duchen 1970, <i>J. Neurol. Neurosurg. Psychiatry</i>	m/+: enhanced fear conditioning freezing, absence seizures, elevated resistance to induced seizures m/m: hind-limb paralysis, premature lethality
<i>med-Tg</i>	Transgene insertion	Null	[Undetermined]	Kohrmann et al. 1995, <i>Genomics</i> McKinney et al. 2008, <i>Genes, Brain Behav.</i>	
<i>dmu</i>	Frameshift deletion	Null	Exon 10	De Repentigny et al. 2001, <i>Hum. Mol. Genet.</i>	
<i>ataxia3</i>	Missense (p.S21P)	Null	N-terminus	Sharkey et al. 2009, <i>J. Neurosci</i>	
<i>8J</i>	Missense (p.V929F)	Null	DII pore-forming loop	Papale et al. 2009, <i>Hum. Mol. Genet.</i>	
<i>Δ35</i>	Frameshift deletion	Null	Intron 14	Inglis et al. 2019, <i>Genes, Brain Behav.</i>	
<i>Scn8a^{fl}</i>	Conditional knockout	Null	Exon 1	Levin & Meisler et al. 2004, <i>Genesis</i> Woodruff-Pak et al. 2006, <i>Behav. Neurosci.</i> Levin et al. 2006, <i>J. Neurophysiol.</i> Makinson et al. 2017, <i>Neuron</i> Chen et al. 2018, <i>Sci. Rep.</i>	Pcp2-Cre, m/m: ataxia and tremor, impaired spatial memory, impaired motor coordination Gabra6-Cre, m/m: impaired motor coordination Pcp2/Gabra6-Cre, m/m: ataxia and tremor, impaired motor coordination Ppp1r2-Cre, m/+: absence seizures Foxg1-Cre, m/+: elevated resistance to induced seizures Emx1-Cre, m/+: elevated resistance to induced seizures Camk2a-Cre, m/+: elevated resistance to induced seizures Dlx5/Dlx6-Cre, m/+: absence seizures Emx1/Dlx5/Dlx6-Cre, m/+: absence seizures, elevated resistance to induced seizures Scn10a-Cre, m/m: comparable to WT littermates
<i>med-jo</i>	Missense (p.A1071T)	Hypomorph	DIII S4-S5 linker	Dickie 1965, <i>Mouse News Lett.</i>	m/+: absence seizures, m/m: tremor, ataxia
<i>med-j</i>	Splice site mutation	Hypomorph	Intron 2	Kohrman et al. 1996, <i>J. Biol. Chem</i>	m/m: dystonia, muscle weakness
<i>jolting2J</i>	[Undetermined]	Hypomorph	[Undetermined]	Thompson et al. 2004, <i>MGI Direct Data Submission</i>	m/m: shortened lifespan, tremors, unsteady gait, reduced auditory brainstem response
<i>nmf2</i>	Missense (p.N1370T)	Hypomorph	DIII pore-forming loop	Buchner et al. 2004, <i>Mamm. Genome.</i>	m/m: hind-limb paralysis
<i>nmf5</i>	Missense (p.I1392F)	Hypomorph	DIII pore-forming loop	Buchner et al. 2004, <i>Mamm. Genome.</i>	m/m: retinal degeneration, hind-limb paralysis
<i>nmf58</i>	Missense (p.L1404H)	Hypomorph	DIII pore-forming loop	Buchner et al. 2004, <i>Mamm. Genome.</i>	m/m: dystonia
<i>tremorD</i>	Missense (p.W935L)	Hypomorph	DII pore-forming loop	Timms et al. 2008, <i>MGI Direct Data Submission</i>	m/+: mild, sporadic tremor m/m: persistent tremor, abnormal gait
<i>cth</i>	Missense (p.D981V)	Hypomorph	DIIS6	Mackenzie et al. 2009, <i>Genes, Brain Behav.</i>	m/m: hearing loss, tremor
<i>9J</i>	In-frame deletion	Hypomorph	DIVS6	Jones et al. 2016, <i>Neurobiol. Dis.</i>	m/m: lurching gait, shortened lifespan, reduced size
<i>R1627H</i>	Missense (p.R1627H)	Hypomorph	DIVS4	Makinson et al. 2016, <i>Exp. Neurol.</i>	m/m: impaired motor coordination, audiogenic seizures, reduced auditory brainstem response
<i>Δ9</i>	In-frame deletion	Hypomorph	DIIS4	Inglis et al. 2019, <i>Genes, Brain Behav.</i>	m/+: impaired motor coordination, absent acoustic startle response, elevated resistance to induced seizures m/m: ataxic gait with frequent loss of posture, premature lethality, reduced size
<i>Γ3</i>	In-frame insertion	Hypomorph	DIIS4	Inglis et al. 2019, <i>Genes, Brain Behav.</i>	m/+: reduced grip strength, impaired motor coordination, absent acoustic startle response, elevated resistance to induced seizures m/m: ataxic gait with frequent loss of posture, mild tremor, premature lethality, reduced size
<i>R1620L</i>	Missense (p.R1620L)	Hypomorph	DIVS4	Wong et al., under review	m/+: elevated motor activity, impaired object recognition, abnormal social interaction, increased susceptibility to induced seizures, spontaneous seizures, absent freezing behavior m/m: premature lethality
<i>N1768D</i>	Missense (p.N1768D)	Gain-of-function	C-terminus	Wagnon et al. 2015, <i>Hum. Mol. Genet.</i> Lopez-Santiago et al. 2017, <i>PNAS</i>	m/+: spontaneous seizures, premature lethality, impaired social discrimination m/m: SUDEP, premature lethality, tremor
<i>R1872W</i>	Conditional knock-in (p.R1872W)	Gain-of-function	C-terminus	Bunton-Stasyshyn & Wagnon et al. 2019, <i>Brain</i>	Ella-Cre, m/+: reduced survival, spontaneous seizures Emx1-Cre, m/+: reduced survival, spontaneous seizures Gad2-Cre, m/+: comparable to WT littermates

1.3.4 Neuropsychiatric disorders and dementia

Patients with epilepsy demonstrate increased risk of neuropsychiatric disease relative to the general population, with ~20% greater risk of developing autism spectrum disorder or 10-25% risk of major depressive disorder (77,78). The inverse is also true, as patients with Alzheimer's disease (AD) and dementia experience a 10-fold elevated risk of developing epilepsy (79). One common clinical feature of neuropsychiatric disorders, dementia, and epilepsy is impaired cognition or executive function (80-83). These cognitive symptoms may arise independently of epilepsy, as several *SCN8A* mutations have been identified in patients with autism or intellectual disability, but no seizures (52,63). Patients with AD also exhibit decreased levels of $\text{Na}_v1.1$, and patients with schizophrenia demonstrate reduced activity from the GINs that preferentially express *SCN1A* (80-83). Ciccone et al. recently reported that $\text{Na}_v1.6$ is upregulated in hippocampal neurons following exposure to $\text{A}\beta_{1-42}$ *in vitro*, suggesting that heightened network excitability in AD patients is also linked to $\text{Na}_v1.6$ dysfunction (84). Several studies have also demonstrated that broad pharmacological inhibition of VGSC activity with phenytoin, or siRNA-mediated knockdown of *Scn1a*, can impair context-dependent and spatial memory (32,80). Altogether, these results suggest that altered VGSC activity, and specifically reduced *SCN1A* expression, can contribute toward cognitive decline. Furthermore, these cognitive phenotypes may be a result of aberrant activity from GINs that rely on $\text{Na}_v1.1$ function (80,85,86). For example, by injecting $\text{Na}_v1.1$ -overexpressing GINs into AD model mice or crossing hAPP animals onto a $\text{Na}_v1.1$ -BAC transgenic background, researchers were able to elevate inhibitory neurotransmission, prolong survival, improve cognitive performance in the Morris water maze, and reduce hyperactive behavior (80,85).

1.4 Regulation of *SCN1A* and *SCN8A*

1.4.1 Pharmacological modulation of $\text{Na}_v1.1$ and $\text{Na}_v1.6$ activity

Given the contribution of $\text{Na}_v1.1$ and $\text{Na}_v1.6$ to several neurological diseases, the ability to selectively modulate activity of either VGSC α subunit could have translational relevance.

Common pharmacological treatments for epilepsy or migraine include phenytoin, valproic acid, carbamazepine, and lamotrigine, all of which broadly inhibit VGSC activity by prolonging the channel refractory period (87,88). However, given that these drugs also inhibit $\text{Na}_v1.1$ activity, they are not viable treatments for patients with loss-of-function mutations in *SCN1A*. Recently, the Hm1a venom peptide was demonstrated to reduce hyperexcitability and seizure frequency in the *Scn1a*^{+/-} model of Dravet syndrome, reportedly due to activity as a $\text{Na}_v1.1/\text{Na}_v1.3$ -selective agonist (89). However, mice were only observed for 4 days post-treatment, making it unclear whether Hm1a would be efficacious as a long-term treatment (89). The VGSC antagonist GS967/Prax330 has also been demonstrated to extend the lifespan of mutants in animal models of *Scn1a*, *Scn2a*, and *Scn8a* epileptic encephalopathy (29,90-92). However, the efficacy of GS967 is highly variable, as a majority of animals with a global knock-in of the *SCN8A* p.R1872W epilepsy mutation exhibited only one additional week of survival relative to vehicle-treated littermates, compared to an additional two months in *Scn8a*^{N1768D/+} mutant animals (29,91).

1.4.2 Transcriptional regulation of *SCN1A* and *SCN8A* expression

1.4.2.1 Regulation of transcription initiation

Both *SCN1A* and *SCN8A* exhibit complex 5' genomic regions that span 72-75 kb upstream of the first coding exon (**Fig. 1.2**) (93-95). *SCN1A* possesses seven alternative noncoding exons (denoted a-g) and three alternative promoters (denoted 1A, 1B, and 1C) within this region, while *SCN8A* has three alternative noncoding exons (a-c) and a single characterized promoter (**Fig. 1.2**) (93-95). Of the three *SCN1A* promoters, only 1C is known to have a proximal genetic regulatory element, which is bound by the transcriptional repressor, RACK1 (96). *SCN8A* possesses a conserved silencer element in intron 1, which is bound by the chromatin remodeler protein, CDYL (97). While there are no confirmed transcriptional enhancer elements for either gene in humans, Hsiao et al. reported a long, noncoding RNA with a transcription start site downstream of *SCN1A* that, when knocked down using antisense RNAs, led to an increase in *SCN1A* mRNA and Nav1.1 protein levels (98). Several studies have also observed that the VGSC $\beta 2$ subunit undergoes sequential cleavage by β - and γ -secretases, thereby releasing an intracellular domain ($\beta 2$ -ICD) that localizes to the nucleus of cells (99,100). When the $\beta 2$ -ICD is overexpressed *in vitro*, there is a subsequent increase in *SCN1A* mRNA levels, though it is unclear whether this effect is due to $\beta 2$ -ICD binding within the *SCN1A* locus or a more indirect mechanism (99,100).

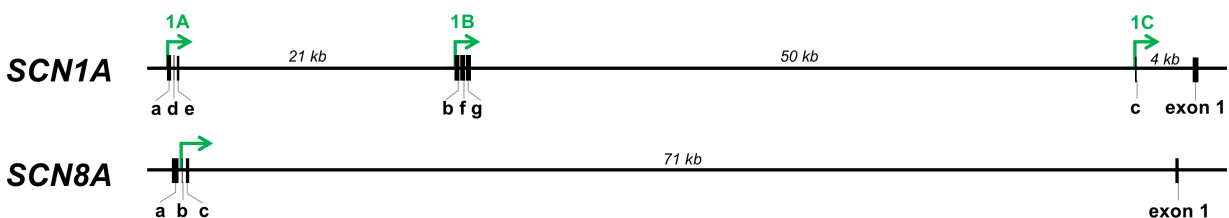


Figure 1.2. 5' genomic organization of human *SCN1A* and *SCN8A*. The horizontal black line denotes human *SCN1A* or *SCN8A*, in which noncoding (lettered, a-g) and coding (numbered, 1) exons are indicated by vertical bars. Green arrows denote promoters.

1.4.2.2 Post-transcriptional regulation

Both *SCN1A* and *SCN8A* exhibit alternative splicing of several coding exons (101-105). *SCN1A* and *SCN8A* exhibit two developmentally-regulated forms of exon 5, resulting in distinct protein isoforms which differ by two amino acids (101-103). Exon 5N is preferentially included in transcripts during early development, but is largely replaced by exon 5A after birth (101-103). *SCN1A* and *SCN8A* also possess unique alternative exons that result in truncated, nonfunctional VGSC proteins, namely “poison” exon 20N in *SCN1A* and exon 18N in *SCN8A* (104,105). *SCN1A* and *SCN8A* transcript stability is also regulated by the RNA binding proteins GAPDH and PUM2, respectively, thereby leading to reduced Na_v1.1 or Na_v1.6 protein levels (106-108). Given that GAPDH and PUM2 have wide-ranging activity throughout the nervous system, it is unclear whether modulation of these proteins would be beneficial in the context of treating VGSC-derived neurological disease. PUM2 alone is known to bind at least 875 distinct mRNAs in the mouse brain, and altered expression can significantly impair neurogenesis, while GAPDH is a critical glycolytic enzyme involved in ATP production (106,109).

1.4.3 Detecting additional putative functional genomic elements

1.4.3.1 Evolutionary conservation of noncoding sequences

While progress has been made in identifying silencers of *SCN1A* and *SCN8A* expression, there are no identified transcriptional enhancer elements for either gene in humans. Previous strategies to detect genetic regulatory elements in VGSCs have largely relied on the analysis of evolutionarily-conserved noncoding regions of the genome (94-97,106,110). By definition, noncoding genomic regions are not translated into protein and are therefore spared from

purifying selection, leading to sequence variation across species as a result of genetic drift (111). Therefore, noncoding regions that have been conserved across evolution may indicate genetic elements that play a functional role in gene expression (111). While conservation-based analyses have been successful in identifying promoter elements for both *SCN1A* and *SCN8A*, they have yet to identify *cis*-regulatory enhancers or silencers that may also influence transcription (94,112). It is also unclear whether genetic elements that tightly control neuron-specific gene expression would be conserved across species, given the substantial changes in brain morphology across mammalian evolution (113). For instance, the 5' genomic organization of *SCN1A* varies substantially between mice and humans: only two promoters (1A and 1B) and three noncoding exons (a-c) are evolutionarily conserved between species (**Fig. 1.2**) (95,110).

1.4.3.2 Accessible chromatin as a marker of functional genomic elements

An additional approach to identify putative regulatory elements is the use of epigenomic markers of accessible chromatin, such as post-translational modifications of histones (114-116). In eukaryotes, chromosomal DNA is tightly packaged into nucleosomes that consist of 147 bp DNA wrapped around a histone protein octamer (117). The conformation of nucleosomes directly impacts gene expression and is influenced by post-translational modifications of individual histones, particularly methylation or acetylation of histones H3 and H4 (117,118).

Transcriptionally inactive DNA is marked by histone modifications, such as H3K9me3 or H3K27me3, that promote a condensed heterochromatin state in which DNA is inaccessible to regulatory proteins (118,119). In contrast, actively transcribed genes are marked by histone modifications such as H3K27ac and H3K36me3, which relax nucleosome packaging to promote an “open” chromatin state conducive to transcription factor binding (118,119). *Cis*-regulatory

functional genomic elements are also associated with specific histone post-translational modifications, such as H3K4me1 (transcriptional enhancers) and H3K4me3 (promoters) (119).

1.4.3.3 Techniques to detect accessible regions of chromatin

With the advent of next-generation sequencing, several techniques have been developed to detect the epigenomic signatures of chromatin that is accessible to proteins such as transcription factors (**Fig. 1.3**) (114-116). Chromatin immunoprecipitation sequencing (ChIP-seq) relies on the use of antibodies to enrich for DNA associated with specific histone post-translational modifications (e.g. H3K4me1, H3K27ac), thereby indicating putative transcriptional regulatory elements (119). In contrast, other sequencing-based technologies involve a step to digest and isolate accessible chromatin, rather than sequences linked to specific histone modifications. DNase-seq utilizes the DNase I endonuclease to digest exposed DNA, whereas formaldehyde-assisted isolation of regulatory elements (FAIRE-seq) involves a phenol-chloroform separation step to enrich for DNA that is not tightly associated with a nucleosome (115,116). The assay for transposase-accessible chromatin (ATAC-seq) is a more recent technique that isolates open chromatin based on the ability of the Tn5 transposase to integrate into DNA (114).

However, each technique comes with its own set of limitations. ChIP-seq results are entirely contingent on the fidelity of the antibody, and require several independent controls to account for the immunoprecipitation step or the absence of nucleosomes (119,120). While DNase-seq, FAIRE-seq, and ATAC-seq are capable of detecting open chromatin, they do not distinguish between enhancer and promoter elements, which possess unique epigenomic signatures (121). While ATAC-seq enables high-resolution detection of open chromatin with as

few as 500 cells, ChIP-seq, FAIRE-seq, and DNase-seq may require upwards of 100,000 cells, making them less practical approaches when the cellular input is limited (114,122).

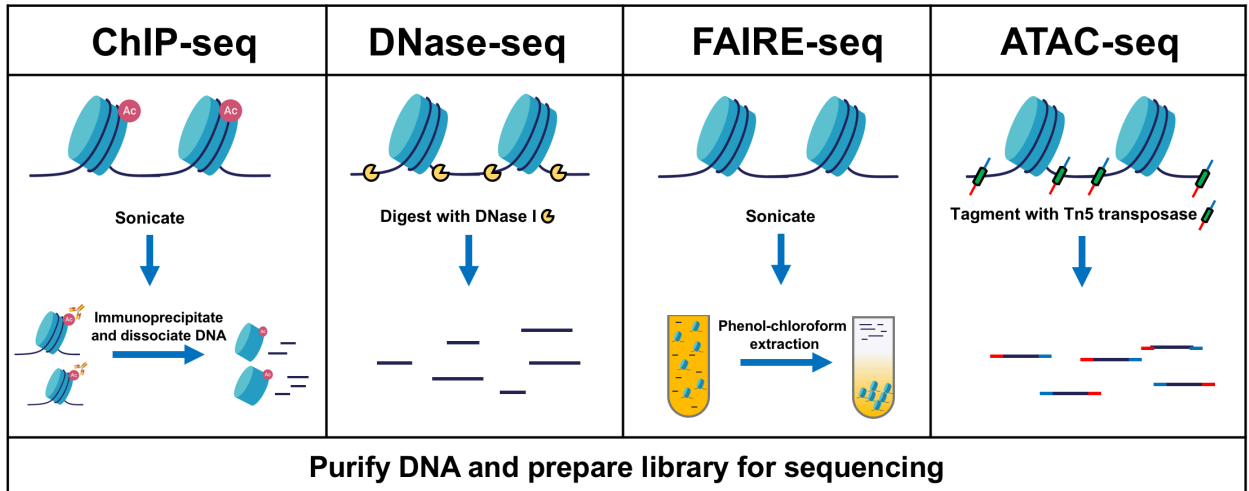


Figure 1.3. Comparison of high-throughput approaches to detect accessible chromatin. “Ac” denotes the H3K27ac post-translational modification associated with active transcription. Adapted by permission from Springer Nature Customer Service Centre GmbH: Nature, *Nat. Rev. Genet.* (123).

1.5 Summary and goals of dissertation

The *SCN1A* and *SCN8A* VGSC genes are critical for the normal control of neuronal excitability, making them important targets for the treatment of neurological disease. In particular, loss-of-function mutations in *SCN1A* are the primary cause of the severe childhood epilepsy, Dravet syndrome, and reduced Na_v1.1 levels may broadly contribute to cognitive dysfunction by impairing GIN activity. Therefore, methods that could increase expression of *SCN1A* or enhance GIN function could have translational relevance to several disorders. In contrast, both loss-of-function and gain-of-function mutations in *SCN8A* result in a diverse spectrum of clinical phenotypes, even among patients with mutations affecting the same region of the Na_v1.6 channel. Though there are several existing animal models of *SCN8A* dysfunction, the fact that they are on separate genetic backgrounds may confound comparisons between mouse lines. Furthermore, despite the clinical variability observed among patients with mutations in the Na_v1.6 voltage sensor domains, there are no existing comparisons of how mutations within the same voltage sensor affect phenotypic outcomes in mice.

The overarching goals of this dissertation research were: (1) to identify noncoding genetic elements that contribute to *SCN1A* transcriptional regulation and (2) to characterize how mutations within the same domain of the Na_v1.6 channel protein elicit unique behavioral and motor phenotypes. First, I discuss my initial approach to identifying putative functional genomic elements (FGEs) underlying *SCN1A* transcription through the use of publicly available neuronal open chromatin data (**Chapter 2**). Though we did not identify any FGEs with robust *cis*-regulatory activity, an alternative strategy would be to examine transcriptomic and epigenomic changes in developing human GINs, which preferentially express *SCN1A* (**Chapter 3**). Finally, to assess how altered Na_v1.6 contributes to diverse phenotypic outcomes, we characterized three

mouse lines on the C57BL/6J genetic background with distinct mutations in the Nav1.6 DIIS4 voltage sensor domain (**Chapter 4**). As a result of this study, we identified that hypomorphic and null *Scn8a* mutations may result in unique clinical consequences. Altogether, these studies have provided a deeper understanding of the genetic elements underlying neuronal inhibition, and how altered Nav1.6 function contributes toward varied clinical phenotypes (**Chapter 5**).

CHAPTER 2: Towards the identification of transcriptional regulatory elements for the voltage-gated sodium channel gene, *SCN1A*

2.1 Abstract

Aberrant function or expression of the voltage-gated sodium channel α subunit gene, *SCN1A* (encoding the protein $\text{Na}_v1.1$), is associated with multiple neurological disorders, most prominently epilepsy. In particular, *SCN1A* heterozygous loss-of-function mutations cause 70-80% of cases of Dravet syndrome (DS), a catastrophic, early-life encephalopathy. Despite the important role of *SCN1A* in epilepsy and, more broadly, in the normal regulation of neuronal excitability, little is currently known about the machinery underlying the regulation of *SCN1A* transcription. By integrating neuronal open chromatin and transcription factor ChIP-seq data from a variety of primary human tissues and immortalized cell lines, we identified 32 regions within the *SCN1A* locus that may indicate functional genomic elements (FGEs), such as transcriptional enhancers. While none of these FGEs individually elicit a robust increase in reporter activity in a dual luciferase assay, at least two FGEs may act synergistically to enhance transcription.

2.2 Introduction

Mutations in the voltage-gated sodium channel α subunit gene *SCN1A* (encoding the protein, Na_v1.1) cause several neurological disorders, particularly epilepsy and migraine (35,40,124-126). Heterozygous loss-of-function *SCN1A* mutations alone account for 70-80% of cases of Dravet syndrome (DS), a severe childhood form of epilepsy(124,125,127-130). DS is characterized by spontaneous and recurrent febrile and afebrile seizures that begin within the first year of life, which are resistant to treatment by most anti-epileptic drugs (2,14,124,131,132). Despite ongoing research into novel pharmacological treatments for DS, many patients currently do not achieve adequate seizure control (133). Strategies by which *SCN1A* expression could be increased from the intact, wild-type allele would be predicted to be efficacious in DS. Previous strategies used to postnatally increase *Scn1a* mRNA levels in DS mouse models resulted in reduced seizure frequency and severity, thereby supporting the predicted benefits of elevating *SCN1A* transcription in the context of epilepsy (98,134). Given that *SCN1A* is preferentially expressed in inhibitory GABAergic interneurons (GINs), modulating *SCN1A* transcription may also have translational relevance to other neurological disorders associated with impaired neuronal inhibition, such as schizophrenia or Alzheimer's disease (19,23-25,85,135-137). Despite the association of *SCN1A* with DS, and, more broadly, GIN function, there has been little progress towards identifying the transcriptional machinery that contributes to *SCN1A* regulation. To date, only one protein inhibitor of *SCN1A* transcription (RACK1) has been identified (96).

Underlying the current gap in knowledge of *SCN1A* transcription is the poor characterization of noncoding genetic regulatory elements for *SCN1A*, such as enhancers. These functional genomic elements (FGEs) are critical for tissue-specific transcriptional control of gene expression through interactions with proteins such as transcription factors (TFs). Enhancer

elements are marked by open chromatin and are thereby accessible to TFs that mediate transcriptional regulation (114,116). FGEs have been identified through the use of techniques that can detect regions of open chromatin, including DNase-seq, FAIRE-seq, ATAC-seq, or ChIP-seq for the histone modifications H3K27ac, H3K4me1, and H3K4me3 (114,116,138). Disease-associated SNPs may also affect gene expression by altering or creating binding motifs for TFs, and have previously been utilized to identify FGEs (139-142). Genome-wide association studies (GWASs) of common forms of epilepsy have identified three SNPs in the *SCN1A* locus, which may also mark putative FGEs (143,144).

Here, we report 32 putative FGEs within the *SCN1A* locus that possess signatures of open chromatin in neuronal cells, two of which encompass epilepsy-associated SNPs: rs11890028 in FGE6 (5'-UTR) and rs6732655 in FGE20 (intron 16) (143,144). We have evaluated these FGEs in a dual luciferase assay for potential regulatory activity, and identified several elements that may collectively contribute toward *SCN1A* transcriptional regulation.

2.3 Materials and Methods

2.3.1 Identification of putative functional genomic elements (FGEs) in the *SCN1A* locus

We previously defined the *SCN1A* locus as the genomic interval from 115 kb upstream of the *SCN1A* translation start site to 15 kb downstream of the poly(A) termination site (95). Publicly available neuronal open chromatin and transcription factor (TF) ChIP-seq data were obtained from the NIH ENCODE and NCBI Gene Expression Omnibus (GEO) databases, as detailed in **Table A1** (145-158). Sequencing reads from GEO data sets were aligned to the hg19 annotation of the human genome using Bowtie2, and peaks of enriched signal were determined using

HOMER software (159,160). Intersection of open chromatin markers and TF binding were determined using the BEDTools suite of command line programs (161). FGE1-17 were identified based on evidence of at least one marker of open chromatin and TF binding from neuronal ChIP-seq data, while FGE18-32 were identified by the presence of ≥ 2 markers of open chromatin. Coordinates for each FGE along with identifying open chromatin markers or putative TFs from ChIP-seq data are listed in **Table A2**.

2.3.2 Generation of luciferase reporter vectors

The evolutionarily-conserved 1B *SCN1A* promoter was PCR-amplified from human genomic DNA (gDNA) using primers tagged with 5'-*SacI* or -*XhoI* restriction sites, then digested and cloned into the pNL1.1 NanoLuc luciferase reporter vector (Invitrogen), such that the *SCN1A* promoter drove NanoLuc expression (96,112). A second reporter vector was generated by subcloning the constitutive thymidine kinase (*TK*) promoter from pGL4.54[luc2/*TK*] (Promega) to drive NanoLuc expression. These reporter vectors are denoted as p*SCN1A* and p*TK*, respectively.

To facilitate high-throughput molecular cloning of putative FGEs, a gene cassette containing *attR* sites for Gateway destination cloning was PCR-amplified from pDEST26 (ThermoFisher) using primers with 5'-*SacI* restriction sites and cloned directly upstream of the respective promoter in the p*SCN1A* and p*TK* reporter vectors. FGEs within the *SCN1A* locus were individually PCR-amplified from human gDNA with forward primers containing a 5'-CACC tag, for directional cloning into the pENTR™/D-TOPO® Gateway entry vector (Invitrogen). FGEs were subsequently integrated into p*SCN1A* or p*TK* utilizing the Gateway LR clonase II system to generate recombinant FGE NanoLuc reporter vectors (Invitrogen). Vectors

containing the minor allelic variants of epilepsy-associated SNPs were subsequently generated with the QuikChange II XL site-directed mutagenesis kit (Agilent), by using pTK vectors with the major SNP allele as a template. Vectors were transformed into subcloning efficiency DH5 α competent (ThermoFisher) or XL10-Gold ultracompetent cells (Agilent), and plasmids were isolated utilizing the PureLink™ Quick Plasmid Miniprep or HiPure Plasmid Filter Midiprep kits (Thermofisher).

For initial amplification of the *SCN1A* and *TK* promoters, as well as the Gateway destination cloning gene cassette, PCR was carried out in a 25 μ L volume containing 5 \times Green GoTaq Reaction Buffer (Promega), 0.2 mM dNTPs (Promega), 10 μ M primers, and 1 unit *Taq* DNA polymerase (Promega). The reaction parameters were: 1 cycle with 3 min at 95°C; 30 cycles with 30 s at 95°C, 30 s at 58°C, 1 min/kb at 72°C; then a final extension step of 5 min at 72°C. Subsequent amplification of FGEs was carried out in a 20 μ L volume containing 5 \times Phusion HF Buffer (Invitrogen), 0.2 mM dNTPs (Promega), 10 μ M primers, and 1 unit Phusion HotStart II Polymerase (Invitrogen). The reaction parameters were: 1 cycle with 30 s at 98°C; 30 cycles with 10 s at 98°C, 30 s/kb at 72°C; 1 cycle with 5 min at 72°C. Mutagenesis PCR reactions were carried out in a 50 μ L volume containing 10 \times reaction buffer (Agilent), 10 ng template plasmid, 125 ng primers, 0.2 mM dNTPs (Agilent), 6% QuikSolution reagent (Agilent), and 1 unit *PfuUltra* HF DNA polymerase (Agilent). The reaction parameters were: 1 cycle with 1 min at 95°C; 18 cycles with 50 s at 95°C, 50 s at 60°C, 1 min/kb at 68°C; 1 cycle with 7 min at 68°C. Amplification products were treated with *DpnI* restriction enzyme to digest the template plasmid containing the major SNP allele. Vector integrity was confirmed by Sanger sequencing, through Psomagen Inc. (<http://macrogenusa.com/>). All primer sequences are listed in **Table A3**.

2.3.3 SH-SY5Y cell culture and transfection

SH-SY5Y human neuroblastoma cells (ATCC) were cultured at 37°C with 5% CO₂ in DMEM (Invitrogen) supplemented with 10% fetal bovine serum (Invitrogen). Cells were regularly tested for mycoplasma infection, and discarded after passage number 20.

For dual luciferase reporter assays, 2.5-3.0×10⁵ cells were seeded onto each well of a 24-well dish in Opti-MEM Reduced Serum Medium (Invitrogen) and co-transfected with 900 ng NanoLuc vector (pNL1.1, p*SCN1A*, p*TK*, etc.) and 100 ng pGL4.54[luc2/*TK*] (Promega) using TransFast transfection reagent (Promega). At 24 hrs post-transfection, NanoLuc and firefly luciferase activity were measured on a Synergy H1 Hybrid Multi-Mode Microplate Reader (BioTek) using the Nano-Glo® Dual-Luciferase® Reporter Assay System (Promega). NanoLuc luminescence was normalized to firefly luciferase expressed from pGL4.54[luc2/*TK*] in order to control for transfection efficiency.

To assess the impact of TF overexpression on *SCN1A* mRNA levels, 1.5-2.0×10⁶ SH-SY5Y cells were seeded onto each well of a 12-well dish in Opti-MEM Reduced Serum Medium (Invitrogen). Cells were then individually transfected with 1.8 µg of a vector which constitutively expressed Pbx3 (pcDNA3-mPbx3), MEF2A (pCAGMS-hMEF2A), or FRA2 (pCMV-FRA2), using TransFast transfection reagent (Promega) (162-164). To determine transfection efficiency, cells were co-transfected with 0.2 µg pcDNA3.1-EGFP (AddGene), which constitutively expresses a fluorescent EGFP reporter. As a control, additional pools of cells were solely transfected with 2 µg pcDNA3.1-EGFP (AddGene). At 48 hrs post-transfection, cells were dissociated using 0.05% Trypsin-EDTA (Invitrogen) and RNA was isolated using a PureLink RNA Mini kit (Invitrogen). We consistently observed 10-15% transfection efficiency across all experiments.

2.3.4 Quantitative real-time PCR (qRT-PCR)

The concentration and quality of RNA isolated from SH-SY5Y cells were determined utilizing a NanoDrop 2000 spectrophotometer (ThermoFisher). RNA samples were then incubated with amplification-grade DNase I (Invitrogen) for 15 min at 25°C to digest genomic DNA. DNase I was inactivated by adding 25 mM EDTA solution to each sample and incubating at 65°C for 10 min. DNase-treated RNA samples were then reverse-transcribed into cDNA using a SuperScript III first-strand cDNA synthesis kit with random hexamer primers (Invitrogen).

qRT-PCR was carried out in technical triplicate in a 20 μ L volume containing iQ SYBR Green SuperMix (Bio-Rad) and 5 μ M primers, on a CFX96 Real-Time PCR Detection System (Bio-Rad). The reaction parameters were: 1 cycle with 2 min at 95°C; 40 cycles with 15 s at 95°C, 30 s at 60/61°C; 1 cycle with 10 s at 95°C. To prevent amplification of genomic DNA, qRT-PCR primers were designed to span exon-exon junctions, using Primer3 software (<http://primer3.ut.ee/>; **Table A3**) (165). The optimal annealing temperature to generate standard curves with 90-100% amplification efficiency was determined for each primer pair. *SCN1A* expression was normalized to *ACTB* (encoding β -actin) using the Pfaffl equation, as previously described (166,167).

2.3.5 Statistical analysis

Statistical comparisons were calculated using Prism v8.1.2 software (GraphPad, San Diego, CA, USA). One-way ANOVA with Dunnett's post-hoc multiple comparisons was used to compare normalized NanoLuc reporter activity in recombinant FGE NanoLuc vectors relative to p*SCN1A* or p*TK*. One-way ANOVA with Dunnett's post-hoc multiple comparisons was also used to

compare normalized *SCN1A* expression between cells transfected with vectors expressing EGFP, Pbx3, MEF2A, or FRA2. One-way ANOVA with Tukey's post-hoc multiple comparisons was used to compare normalized NanoLuc reporter activity between p*SCN1A*, p*TK*, and a recombinant p*TK* vector containing the F16 enhancer element (168). All error bars in figures indicate \pm standard error of the mean (SEM).

2.4 Results

2.4.1 Open chromatin and transcription factor ChIP-seq data predict 32 putative functional genomic elements (FGEs) within the *SCN1A* locus

By analyzing public data sets for markers of open chromatin in various human neuronal cell lines and brain tissue from the UCSC ENCODE and NCBI GEO databases, we generated a comprehensive map of open chromatin regions in the *SCN1A* locus (**Fig. 2.1, Table A1**) (145,169). We previously defined the *SCN1A* locus as the genomic interval from 115 kb upstream of the *SCN1A* translation start site to 15 kb downstream of the poly(A) termination site (95). From our analysis of existing data, we identified 32 regions of open chromatin ranging in size from ~100-2200 bp, which could potentially represent functional genomic elements (FGEs) that contribute to *SCN1A* transcription. We identified FGE1-FGE17 based on evidence of at least one marker of open chromatin and TF binding from neuronal ChIP-seq data (**Fig. 2.1, Table A2**). In contrast, FGE18-FGE32 were identified by the presence of two or more markers of open chromatin (**Fig. 2.1, Table A2**). FGE10 and FGE12 coincided with the evolutionarily-conserved 1A and 1B *SCN1A* promoters, thereby supporting the ability of this approach to identify genetic regulatory elements (**Fig. 2.1, Table A2**) (112).

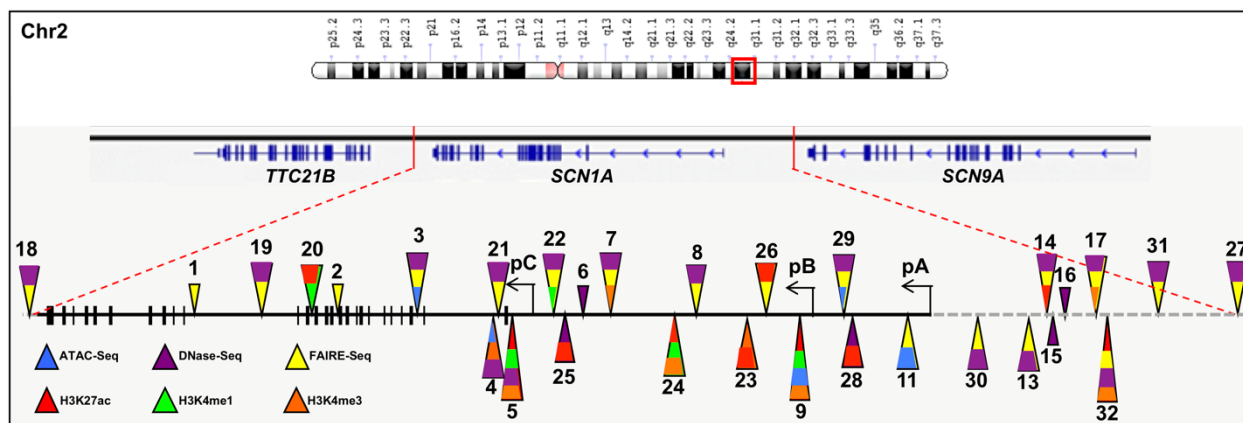


Figure 2.1. Neuronal open chromatin data indicate 32 putative functional genomic elements (FGEs) in the *SCN1A* locus. Each FGE is represented by a triangle, in which the colors indicate relevant open chromatin markers in neuronal cells (key in bottom left, source data sets described in Tables A1-A2). Black arrows denote the alternative *SCN1A* promoters: 1A, 1B, and 1C²⁰. The horizontal black line denotes the *SCN1A* gene, in which coding exons are indicated by vertical bars. The dashed grey line denotes the region upstream of the 1A *SCN1A* promoter, but within the genomic interval considered for this study. Coordinates refer to the hg19 annotation of the human genome (Feb 2009)^{37,38}.

We collectively evaluated 30 of these 32 FGEs in a dual luciferase assay for regulatory activity. FGE10 and FGE12, which contain known *SCN1A* promoters, were excluded from analysis (96,112). We first cloned the major human *SCN1A* promoter (1B) into the pNL1.1 NanoLuc luciferase expression vector (Promega, **Fig. 2.2A**) (112). In this new vector, denoted p*SCN1A*, NanoLuc expression was driven by the *SCN1A* promoter (**Fig. 2.2A**). Next, we generated additional recombinant NanoLuc vectors by individually cloning each FGE upstream of the promoter in p*SCN1A* (**Fig. 2.2A**). These recombinant vectors were individually transfected into SH-SY5Y human neuroblastoma cells to assess whether each FGE altered luciferase reporter activity, relative to p*SCN1A*. To account for transfection efficiency, we co-transfected each FGE vector into SH-SY5Y cells with pGL4.54[luc2/*TK*] (Promega), which expresses firefly luciferase. Of the 30 FGEs tested, only FGE29 elicited a significant decrease in NanoLuc activity (**Fig. 2.2B**). In contrast, FGE2, 17, 23, and 26 all evoked significant increases in luciferase reporter activity, suggesting these four FGEs may possess transcriptional enhancer activity (**Fig. 2.2B**).

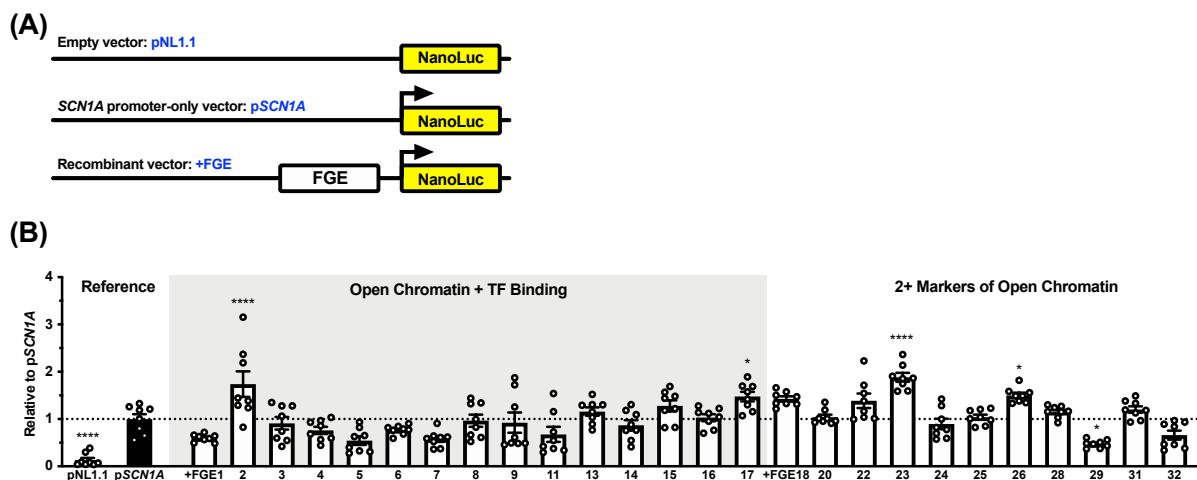


Figure 2.2. Several FGEs demonstrate cis-regulatory activity in a dual luciferase reporter assay. (A) Diagrams of NanoLuc reporter vectors. **(B)** FGEs were individually cloned upstream of the *SCN1A* promoter driving NanoLuc expression, then expressed in SH-SY5Y cells (n=8). NanoLuc values were normalized to firefly luciferase to account for transfection efficiency, and

are presented relative to the p*SCN1A* vector (black bar). Asterisks (*) denote statistical comparisons to p*SCN1A*. Mean \pm SEM. * $p < 0.05$, **** $p < 0.0001$.

2.4.2 FGE2 and FGE17 moderately enhance luciferase reporter activity

Out of the four FGEs that significantly increased luciferase reporter activity, FGE2 and FGE17 were in part identified by TF binding from neuronal ChIP-seq data (**Table A2**). Specifically, ChIP-seq data indicated that FGE2 was bound by PBX3, MEF2A, and FRA2, while FGE17 was bound by the chromatin looping factors RAD21 and CTCF (**Table A2**) (145,146,170). As a first step to evaluate whether these TFs may alter *SCN1A* expression, we transfected SH-SY5Y human neuroblastoma cells with plasmid vectors expressing EGFP or one of the three TFs bound to FGE2, then used qRT-PCR to quantify *SCN1A* expression (**Fig. A1**). However, we did not observe any significant changes in *SCN1A* expression between cells transfected with each individual TF or EGFP, suggesting that PBX3, MEF2A, and FRA2 do not affect *SCN1A* transcription.

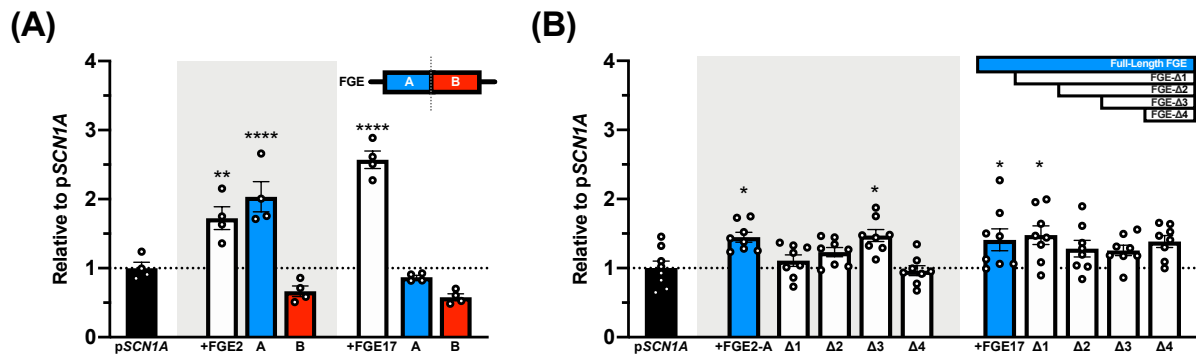


Figure 2.3. Subdeletions of FGE2 and FGE17 exhibit complex impacts on luciferase reporter activity. (A) Two equivalent subdeletions of FGE2 and FGE17 (from 5'-3', A-B) were cloned into p*SCN1A* and transfected into SH-SY5Y cells to identify a minimal region necessary for regulatory activity (n=4). (B) Additional recombinant FGE NanoLuc vectors were generated by sequentially deleting 64-200 bp from the 5' end of FGE2 and FGE17 (n=8). NanoLuc values were normalized to firefly luciferase to account for transfection efficiency, and are presented relative to the p*SCN1A* vector (black bar). Asterisks (*) denote statistical comparisons to p*SCN1A*. Mean \pm SEM. * $p < 0.05$, ** $p < 0.01$, **** $p < 0.0001$.

To examine the minimal genomic region necessary to elicit a significant change in luciferase reporter activity, we cloned equivalent subdeletions of FGE2 and FGE17 (denoted -A or -B) into p*SCN1A* and evaluated the new vectors in a dual luciferase assay in SH-SY5Y cells (**Fig. 2.3A**). Both the full-length inserts of FGE2 and FGE17 reproducibly elicited significant increases in NanoLuc activity relative to p*SCN1A* (**Fig. 2.3A**). Furthermore, the recombinant vector containing the 5'-proximal FGE2-A element reproduced the significant increase in reporter activity observed in our initial screen, whereas the vector containing the 3'-proximal FGE2-B was comparable to p*SCN1A* (**Fig. 2.3A**). In contrast, neither the FGE17-A or FGE17-B vectors elicited a significant change in NanoLuc activity from p*SCN1A* (**Fig. 2.3A**). Altogether, these results suggest that FGE2-A contains the minimal genomic region necessary for FGE2-mediated regulatory activity, whereas the element underlying FGE17-mediated activity may span both the FGE17-A and FGE17-B subdeletions.

To further narrow the minimal regions necessary for FGE2- and FGE17-mediated regulatory activity, we generated a series of four additional NanoLuc vectors in which 64-200 bp was sequentially deleted from the 5' end of each FGE (denoted Δ 1- Δ 4, **Fig. 2.3B**). Given that FGE2-A elicited a significant increase in reporter activity, we performed serial deletions on this element, rather than full-length FGE2. While FGE2-A and FGE17 continued to elicit a significant increase in luciferase reporter activity relative to p*SCN1A*, there was some variability observed among the deletion constructs (**Fig. 2.3B**). While FGE2-A- Δ 1 and FGE2-A- Δ 2 exhibited comparable activity to p*SCN1A*, the smaller FGE2-A- Δ 3 construct exhibited significantly greater NanoLuc activity than p*SCN1A* (**Fig. 2.3B**). In contrast, FGE17- Δ 1 was the only FGE17 deletion vector to significantly increase reporter activity relative to p*SCN1A* (**Fig. 2.3B**). However, neither the FGE2-A- Δ 3 or FGE17- Δ 1 vectors individually demonstrated

significantly greater NanoLuc activity from any of their respective FGE2-A or FGE17 deletion constructs, suggesting that any changes in reporter activity were modest.

2.4.3 *SCN1A* FGEs may jointly contribute to transcriptional regulation of reporter activity

To assess whether FGE2, 17, 23, or 26 could elicit an additive effect on reporter activity, we first generated a vector in which the constitutive thymidine kinase (*TK*) promoter drove NanoLuc expression, denoted *pTK* (**Fig. 2.4A**). As a positive control, we also cloned into *pTK* the F16 enhancer element, which was previously reported to increase reporter activity in SH-SY5Y cells (168) (**Fig. 2.4A**). Importantly, *pTK* exhibited ~8-fold higher NanoLuc activity relative to *pSCN1A*, confirming that *TK* is a more robust promoter (**Fig. 2.4A**). Furthermore, *pTK* containing the F16 element exhibited a significant increase in reporter activity relative to both *pSCN1A* and *pTK*, thereby indicating that expression from the *TK* promoter can still be modulated by transcriptional enhancer elements (**Fig. 2.4B**).

Next, we generated two sets of luciferase vectors, which contained either one (1F) or two (2F) FGEs (**Fig. 2.4.C**). Specifically, 1F vectors contained FGE2-A, 17, 23, or 26 directly upstream of the *TK* promoter (**Fig. 2.4.C**). The 2F vectors contained two copies of FGE2-A, or a single copy of FGE2-A along with FGE17, 23 or 26 (**Fig. 2.4.C**). There were no significant differences in NanoLuc activity between *pTK* and any of the 1F vectors (**Fig. 2.4D**). However, the 2F vector containing both FGE2-A and FGE26 elicited a significant increase in reporter activity relative to the *pTK* (**Fig. 2.4D**). Furthermore, reporter activity was significantly greater than the 1F vector that solely contained FGE26 (**Fig. 2.4D**).

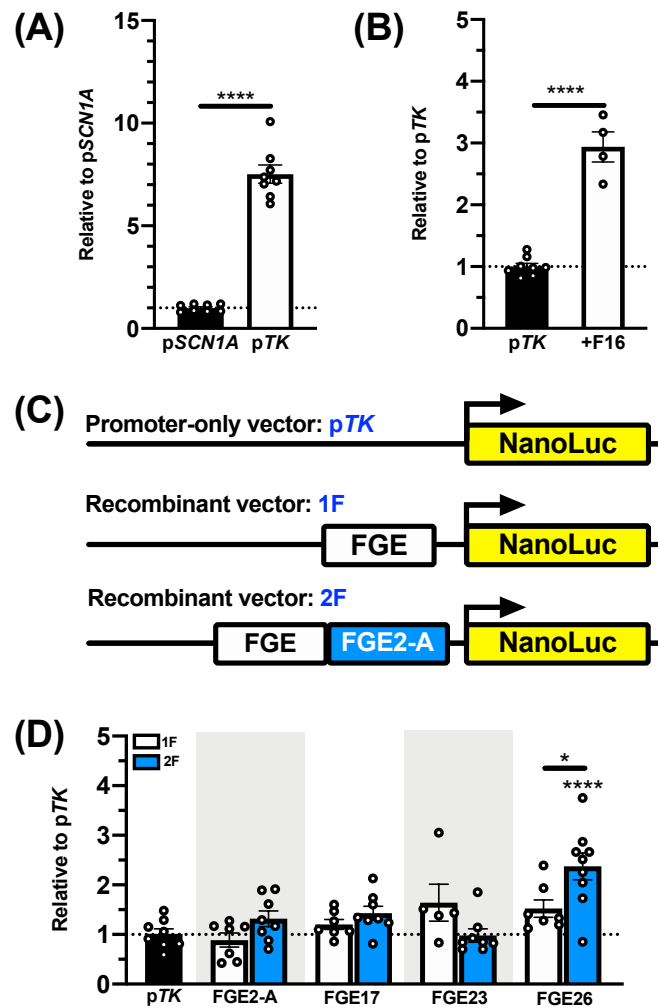


Figure 2.4. FGEs exhibit a combinatorial effect on luciferase reporter activity. (A) The thymidine kinase (*TK*) promoter drives significantly greater NanoLuc activity than the *SCN1A* 1B promoter (black bar). (B) The *MECP2*-proximal F16 enhancer element drives a further increase in NanoLuc activity relative to *pTK* ($n=4$) (168). (C) Recombinant 1F vectors contained a single FGE (2-A, 17, 23, or 26) upstream of the *TK* promoter driving NanoLuc expression, whereas recombinant 2F vectors contained FGE2-A in addition to a secondary FGE. (D) SH-SY5Y cells transfected with a recombinant 2F vector containing both FGE2-A and FGE26 exhibited significantly greater NanoLuc activity compared to *pTK* promoter or the 1F vector solely containing FGE26 ($n=5-9$). Unless noted with a horizontal black line, asterisks (*) denote statistical comparisons relative to (A) *pSCN1A* or (B,D) *pTK*. Mean \pm SEM. * $p < 0.05$, **** $p < 0.0001$.

2.4.4 Epilepsy-associated SNPs do not robustly affect luciferase reporter activity

In addition to open chromatin data, disease-associated SNPs have previously been utilized to identify putative FGEs (139-142). Genome-wide association studies (GWASs) previously identified three SNPs in the *SCN1A* locus that are associated with common forms of epilepsy (**Table 2.1**) (143,144). Two of these SNPs fell within predicted regions of open chromatin: rs11890028 in FGE6 (5'-UTR) and rs6732655 in FGE20 (intron 16, **Table 2.1**). In contrast, rs12987787 (intron 23) did not overlap with any neuronal open chromatin data. While neither FGE6 nor FGE20 elicited significant changes in luciferase reporter activity in our initial screen, these p*SCN1A* vectors both contained the major SNP alleles that were not associated with disease (**Fig. 2.2B**). To determine whether there were allele-dependent effects on reporter activity, we evaluated additional p*TK* constructs with the major or minor allelic variants of all three epilepsy-associated SNPs in a dual luciferase assay. While there were no significant changes in NanoLuc activity between constructs with the major or minor allelic variants of each SNP, we did observe a significant decrease in reporter activity from the rs11890028 constructs derived from FGE6 (**Fig. 2.5**). Therefore, while rs11890028 may not have an allele-dependent effect, FGE6 as a whole may act as a transcriptional silencer element. Interestingly, we also observed a significant increase in NanoLuc activity from the vector containing the rs12987787 major SNP allele relative to p*TK* (**Fig 2.5**). However, there was no significant difference between the vector containing the rs12987787 minor SNP allele ($p = 0.0612$), suggesting that any changes in activity may be modest (**Fig. 2.5**).

Table 2.1. Genome-wide association studies (GWASs) identify three epilepsy-associated SNPs in the *SCN1A* locus. The major and minor SNP allele frequencies are listed in parentheses, and asterisks (*) denote the disease-associated allele (143,144).

SNP ID	GWAS	Location	Phenotype	Major Allele	Minor Allele
rs6732655	ILAE 2014, <i>Lancet Neurol.</i>	Intron 16	All Epilepsy	T (0.78)	A* (0.22)
rs12987787	ILAE 2014, <i>Lancet Neurol.</i>	Intron 23	Focal Epilepsy	T (0.79)	C* (0.21)
rs11890028	Steffens et al. 2012, <i>Hum. Mol. Gen.</i>	5'-UTR	Genetic Generalized Epilepsy	T (0.74)	G* (0.26)

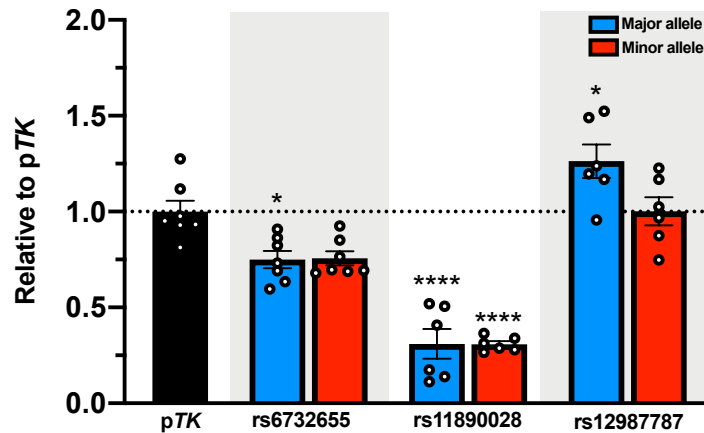


Figure 2.5. Epilepsy-associated SNPs do not elicit robust allele-dependent effects on luciferase reporter activity. SH-SY5Y cells were individually transfected with a recombinant NanoLuc vector containing either the major or minor allelic variant for the epilepsy-associated SNPs rs6732655, rs11890028, or rs12987787 (n=6-7). NanoLuc values were normalized to firefly luciferase to account for transfection efficiency, and are presented relative to the pTK vector (black bar). Asterisks (*) denote statistical comparisons to p*SCN1A*. Mean ± SEM. * $p < 0.05$, **** $p < 0.0001$.

2.5 Discussion

In this preliminary study, we integrated publicly available human neuronal open chromatin and transcription factor ChIP-seq data to identify 32 putative FGEs in the *SCN1A* locus. Two of these FGEs intersected with the epilepsy-associated SNPs, rs11890028 (FGE6) and rs6732655 (FGE20), though neither variant demonstrated an allele-specific effect on NanoLuc reporter activity in a dual luciferase assay. While there was some evidence that the major allele of epilepsy-associated SNP rs12987787 may significantly increase NanoLuc reporter activity, it did not significantly vary from the vector containing the minor SNP allele. These results suggest that any regulatory impact of rs12987787 may therefore be modest.

Out of the 32 FGEs we identified, only one element, FGE29, exhibited transcriptional silencer activity on the *SCN1A* promoter in our initial dual luciferase assay. In contrast, four elements elicited statistically significant increases in reporter activity: FGE2, 17, 23, and 26. When FGE26 was evaluated in a 2F reporter vector containing an additional copy of FGE2-A, we observed a significant increase in NanoLuc reporter activity relative to pTK. *SCN1A* possesses an intricate 5' genomic region comprised of seven alternative noncoding exons and three alternative promoters (95,96). Our results suggest that transcriptional regulation of *SCN1A* may be equally complex, and involve the joint contribution of multiple FGEs to drive *SCN1A* expression. Future studies are necessary to examine the contribution of these FGEs to endogenous *SCN1A* expression in cells, and whether any synergistic regulatory activity is limited to FGE2-A and FGE26, among other combinations of FGEs.

It is worth noting that, in the same assay with the 2F FGE26 vector, we did not observe a significant increase in reporter activity from 1F vectors containing a single FGE. Given that the control F16 enhancer element was capable of eliciting an approximately 3-fold increase in pTK

NanoLuc activity, the *TK* promoter was not limited by an inherent ceiling effect on reporter expression (168). However, *SCNIA* expression is largely restricted to parvalbumin-positive GABAergic interneurons (GINs), suggesting that *SCNIA* transcriptional regulatory elements may exert moderate effect on *SCNIA* expression in comparison to FGEs from other, more ubiquitously, expressed genes (14,23). Considering that the *TK* promoter drives ~8-fold greater NanoLuc expression relative to the *SCNIA* promoter, it may therefore be less sensitive to positive modulation by these FGEs. In contrast, the *TK* promoter may have heightened sensitivity to FGEs that act as transcriptional silencer elements. For instance, while FGE6, which contained rs11890028, was comparable to p*SCNIA* in our initial screen for regulatory activity, it significantly reduced NanoLuc expression when cloned into a p*TK* vector.

Ultimately, while we were able to identify several potential FGEs involved in *SCNIA* transcriptional regulation, our approach was limited by the heterogeneity of available open chromatin data sets. While *SCNIA* expression in the brain is largely observed in inhibitory GINs, existing open chromatin data was only available from brain regions consisting of multiple neuronal or even glial cell types, or immortalized neuroblastoma lines that display substantial morphological and molecular differences from primary neurons (14,23,171). Therefore, open chromatin studies in primary GINs may also identify novel, unique FGEs, and would be an important next step in identifying putative *SCNIA* transcriptional regulatory elements.

2.6 Acknowledgments

The research reported in this chapter was supported by the National Institute of Neurological Disorders and Stroke of the National Institutes of Health under award number R21NS108760 (A.E.) and the predoctoral training grant appointments T32GM008490 (G.A.S.I.) and T32NS007480 (G.A.S.I.). The content of this study is solely the responsibility of the authors and does not necessarily reflect the official views of the National Institutes of Health. We also thank Dr. Haiyan Fu (Emory University), Dr. Robert Slany (University of Erlangen-Nuremberg), Dr. Cheng-Ming Chiang (University of Texas: Southwestern), and Dr. Ichiro Manabe (Chiba University) for kindly sharing plasmid vectors utilized in this study.

CHAPTER 3: Transcriptomic and epigenomic dynamics associated with development of human iPSC-derived GABAergic interneurons

3.1 Abstract

GABAergic interneurons (GINs) are a heterogeneous class of inhibitory neurons that collectively contribute to the maintenance of normal neuronal excitability and network activity. Identification of the genetic regulatory elements and transcription factors that contribute toward GIN function may provide new insight into the pathways underlying proper GIN activity, while also indicating potential therapeutic targets for GIN-associated disorders, such as epilepsy and schizophrenia. In this study, we examined temporal changes in gene expression and chromatin accessibility by collecting human iPSC-derived GINs at three time points during development for transcriptomic and epigenomic analysis: neural progenitor cells at 22 days post-differentiation (D22), then GINs at D50 and D78. We observed 13,221 differentially accessible regions (DARs) of chromatin that associate with temporal changes in gene expression observed in D78 GINs. We also classified families of transcription factors that are increasingly enriched at DARs during differentiation, indicating regulatory networks that likely drive GIN development. By comparing our data set with a previous study of dysregulated gene expression in the dorsolateral prefrontal cortex of schizophrenia patients, we identified several candidate genes that might have relevance to GIN dysfunction in schizophrenia patients. Collectively, these data provide a resource for examining the molecular networks regulating GIN functionality.

3.2 Introduction

GABAergic interneurons (GINs) comprise a heterogeneous population of inhibitory neurons that play a critical role in regulating neuronal excitability (172-174). GINs have been characterized based on their unique electrophysiological properties, cellular morphology, and expression of specific calcium-binding proteins or neuropeptides (174-177). Collectively, these diverse GINs help shape the complex neural circuitry underlying proper network activity and, when disrupted, can cause neurological disorders such as epilepsy, Alzheimer's disease, and schizophrenia (26,83,178-184). Schizophrenia alone affects ~1% of the global population, and patients exhibit a wide spectrum of clinical phenotypes, including depression, psychosis, and impaired cognition (184,185). Patients with schizophrenia often share comparable numbers of GINs with healthy controls, yet exhibit reduced expression of genes involved in GABA synthesis (*GADI* and *GAD2*) or fast-spiking inhibition (*PVALB*, encoding parvalbumin), thereby suggesting that schizophrenic phenotypes, or negative symptoms, may partially stem from altered functional development of GINs (81-83,186).

Several homeobox and basic helix-loop-helix transcription factors are known to contribute to neural patterning and early GIN fate specification, including *DLX1/DLX2*, *NKX2.1*, *ASCL1*, and *MASH1* (172,173,181,187). However, much less is known about the networks of transcription factors and genetic elements that contribute to mature GIN function. Identification of these regulatory components may provide new insight into the pathways underlying proper GIN activity, while also denoting potential therapeutic targets for GIN-associated disorders. Though some progress has been made in describing the chromatin and transcriptomic signatures of GIN subtypes in mice, efforts to relate these findings to humans are confounded by the divergence in GIN complexity and development through primate evolution

(173,188-191). While there are several existing methods to culture human-derived GINs or related brain organoids *in vitro*, studies have only profiled these cells utilizing RNA-seq or, in one case, anti-NKX2.1 ChIP-seq (173,189,192-194). Altogether, there is a current knowledge gap in the epigenomic dynamics of developing GINs, which may direct interneuron-specific expression patterns.

In the current study, we differentiated human induced pluripotent stem cells (iPSCs) derived from two healthy male controls into GINs with 81-85% efficiency. To examine temporal changes in gene expression and chromatin accessibility, cells were collected at three time points for RNA-seq and ATAC-seq analysis: neural progenitor cells (NPCs) at 22 days post-differentiation (D22), then GINs at D50 and D78. By comparing differentially accessible regions (DARs) of chromatin that were shared between the two iPSC lines, we identified 13,221 genomic regions that correlated with temporal changes in gene expression unique to mature GINs. We also classified several transcription factors (TFs) that are increasingly enriched at DARs during differentiation, indicating regulatory networks that underlie GIN function. Furthermore, we identified several genes that may be especially relevant to mature GIN function in schizophrenia patients. Collectively, these data represent a comprehensive analysis of transcriptomic and epigenomic changes that occur during GIN development.

3.3 Materials and Methods

3.3.1 *In vitro* differentiation to GABAergic interneurons (GINs)

The HC1 and HC2 human induced pluripotent stem cell (iPSC) lines were previously generated using skin biopsy samples from two healthy adult males (195). iPSCs (passage ≤ 35) were cultured on irradiated mouse embryonic fibroblasts (MEFs) in human iPSC media consisting of DMEM/F12 (#11320082, Invitrogen) supplemented with 20% KnockOut Serum Replacement (#10828028, Invitrogen), 2 mM GlutaMAX (#35050079, Invitrogen), 100 μ M non-essential amino acids (NEAA, #11140050, Invitrogen), 100 μ M 2-mercaptoethanol (#21985023, Invitrogen), and 10 ng/mL human basic FGF (#100-18B, PeproTech, Rocky Hill, NJ, USA) as previously described (196). Media were changed daily and iPSC lines were passaged by incubation for 1 hr at 37°C in DMEM/F12 media with 1 mg/ml collagenase (#17018029, Invitrogen). For differentiation of iPSCs into cortical GABAergic interneurons (GINs), iPSC colonies were detached from the feeder layer with collagenase and resuspended in EB medium, comprised of FGF2-free human iPSC media supplemented with 2 μ M dorsomorphin (#3093, Tocris Bioscience, Bristol, UK) and 2 μ M A-83-01 (#2939, Tocris Bioscience). Cells were grown in non-treated polystyrene plates for 6 days, and media was changed daily. On day 7 (D7) of the differentiation protocol, floating embryoid bodies (EBs) were transferred to Matrigel-coated 6-well plates (#354432, Corning). Cells were first grown in NPC1 media, consisting of DMEM/F12 with 1 \times N-2 supplement (#17502001, Invitrogen), 1 \times NEAA, 2 μ g/ml heparin (#H3149, MilliporeSigma), and 1 μ g/ml of recombinant human SHH (#100-45, PeproTech). On D11, the NPC1 media was replaced with NPC2 medium, comprised of DMEM/F12 with 1 \times N-2 supplement, 1 \times NEAA, 2 μ g/ml heparin, and 1.5 μ M Purmorphamine (#4551, Tocris

Bioscience). From D7-D22, the media was changed once every two days. On D22, neural rosettes were mechanically picked and transferred to low-attachment plates (#3471, Corning) in NPC2 media supplemented with 1× B-27 (#17504044, Invitrogen). For further differentiation, neural progenitor spheres were dissociated by incubation with Accutase (#A1110501, Invitrogen) for 10 min at 37°C, then resuspended in Neuron medium, comprised of Neurobasal medium (#21103049, Invitrogen) supplemented with 2 mM GlutaMAX, 1× B-27, 1 μM cAMP (#D0260, MilliporeSigma), 200 ng/mL L-ascorbic acid (#A4403, MilliporeSigma), 10 ng/mL recombinant BDNF (#450-02, PeproTech), and 10 ng/mL recombinant GDNF (#450-10, PeproTech). For quantification of GIN subtypes, additional cells were passaged onto coverslips coated with 50 μg/ml poly-D-lysine (#P6407, MilliporeSigma) and 10 μg/ml laminin (#L2020, MilliporeSigma). Cells were continuously cultured in Neuron media from D22-D78, and half of the media was replaced weekly. At D22, D50, and D78, cells were dissociated with Accutase and gently pelleted by centrifugation at 1,500 rpm for 5 min. Cells were resuspended in 1 mL TRIzol reagent (#15596026, ThermoFisher) for RNA-seq and qRT-PCR, or 1× PBS for ATAC-seq library preparation.

3.3.2 Immunostaining for neuronal markers

Cells at D36, D50, or D78 were fixed with 4% paraformaldehyde (#1574, Electron Microscopy Sciences, Hatfield, PA, USA) for 15 min at room temperature. Samples were permeabilized and blocked with 0.25% Triton X-100 (#X100, MilliporeSigma) and 10% donkey serum (#017-000-121, Jackson ImmunoResearch, West Grove, PA, USA) in PBS for 20 min as previously described (195). Samples were then incubated with primary antibodies at 4°C overnight, followed by incubation with secondary antibodies for 1 hr at room temperature. The following

primary antibodies were used: rabbit polyclonal anti-NESTIN (1:800; #AB5922, MilliporeSigma), mouse monoclonal anti-NKX2.1 (1:500; #MAB5460, MilliporeSigma), rabbit polyclonal anti-GABA (1:1000; #A2052, MilliporeSigma), mouse monoclonal anti-calbindin (1:500; #300, Swant, Marly, Switzerland), rabbit polyclonal anti-calretinin (1:500; #7699/4, Swant), rabbit polyclonal anti-parvalbumin (1:300; #PV27, Swant), rabbit monoclonal anti-somatostatin (1:500; #MA5-17182, ThermoFisher), rabbit polyclonal anti-NPY (1:300; #T-4068.0500, Peninsula Laboratories, San Carlos, CA, USA), and chicken polyclonal anti-MAP2 (1:500; #nb300-213, Novus Biologicals, Centennial, CO, USA). The following secondary antibodies were used: donkey anti-chicken Alexa Fluor 488 (1:1000; #703-545-155, Jackson ImmunoResearch), donkey anti-mouse Alexa Fluor 568 (1:1000; #A10037, ThermoFisher), and donkey anti-rabbit Alexa Fluor 568 (1:1000; #A10042, ThermoFisher). Antibodies were prepared in PBS containing 0.25% Triton X-100 and 10% donkey serum. Slides were mounted using VECTASHIELD antifade medium with DAPI (#H-1200, Vector Laboratories, Burlingame, CA, USA). Images were taken using a Nikon Eclipse Ti-E microscope, and analyzed with ImageJ (<https://imagej.nih.gov/ij/>) (197).

3.3.3 RNA-seq and data analysis

Total RNA was isolated from TRIzol preparations of HC1-derived GINs following manufacturer guidelines (ThermoFisher). Briefly, 200 µl chloroform (#C298-500, Fisher Scientific) was added to each TRIzol sample, and samples were incubated on ice for 15 minutes, followed by an initial 15 min centrifugation step at 13,200 rpm and 4°C. The aqueous phase containing RNA was transferred to a new nuclease-free tube and gently mixed with 500 µl isopropanol (#BP2618-1, Fisher Scientific). Tubes were incubated for an additional 15 min on ice before a second 15 min

centrifugation step at 13,200 rpm and 4°C. Precipitated RNA was aspirated and resuspended in 1 mL of 75% ethanol, then centrifuged for 15 minutes at 13,200 rpm and 4°C. The precipitated RNA pellet was then aspirated and dissolved in 50 µl nuclease-free water via a 10 min incubation step at 60°C. RNA concentration and quality was determined utilizing a 2100 Bioanalyzer (Agilent Technologies, Santa Clara, CA, USA). 2 µg total RNA per sample was used to create libraries with a Kapa Biosystems stranded RNA-seq kit with capture beads (#KK8421, Kapa Biosystems, Wilmington, MA, USA). Libraries were pooled at equimolar concentrations and sequenced on a NextSeq 500 system (Illumina, San Diego, CA, USA), using 75 bp paired-end chemistry.

Raw sequence reads were trimmed for Illumina adapters utilizing Trimmomatic v.0.38, and then aligned to the hg38 human reference genome utilizing TopHat2 v2.1.1 (198,199). HTSeq v0.11.0 was used to determine gene counts from uniquely-mapped, paired reads (200). DESeq2 was utilized to normalize gene counts and determine changes in gene expression between cells at D22, D50, and D78 (201). Genes were considered to have detectable expression if at least two samples within a given time point (D22, D50, or D78) exhibited a DESeq2-normalized expression value > 3 . Differentially expressed genes (DEGs) were determined by a false discovery rate (FDR) < 0.05 and absolute fold change (FC) > 2 .

Spatial gene set enrichment (SGSE) within the human prenatal brain was performed with the brainImageR package in Bioconductor, using the 4,840 DEGs between D78 and D22 as input (202). All genes with detectable expression were pre-ranked for gene set enrichment analysis (GSEA) based on the equation: $-\log_{10}\text{FDR} \times \log_2\text{FC}$. GSEA was performed utilizing GSEA v3.0 software, with default settings (1000 permutations, weighted enrichment statistic, and meandiv

normalization) (203). Pathways with FDR (q) < 0.05 were considered statistically significant. The ten most significant GSEA pathways observed starting at D50 are detailed in **Table B2**.

3.3.4 Quantitative real-time PCR (qRT-PCR)

Total RNA from HC1 and HC2 cells were incubated with amplification-grade DNase I (#18068015, Invitrogen) for 15 min at 25°C to eliminate residual genomic DNA. DNase I was inactivated by adding 25 mM EDTA solution to each sample and incubating at 65°C for 10 min. DNase-treated RNA was then reverse-transcribed into cDNA using a SuperScript III first-strand cDNA synthesis kit with random hexamer primers (#18080051, Invitrogen).

qRT-PCR was carried out in technical triplicate in a 20 μ L volume containing iQ SYBR Green SuperMix (#1708880, Bio-Rad) and 5 μ M primers, on a CFX96 Real-Time PCR Detection System (Bio-Rad). The reaction parameters were: 1 cycle with 2 min at 95°C; 40 cycles with 15 s at 95°C, 30 s at 58°C or 60°C; 1 cycle with 10 s at 95°C. To prevent amplification of any residual genomic DNA, Primer3 software (<http://primer3.ut.ee/>) was used to design qRT-PCR primers that spanned exon-exon junctions (165). The optimal annealing temperature to generate standard curves with 90-100% amplification efficiency was determined for each primer pair (**Table B1**). The expression level of each gene was normalized to *ACTB* (encoding β -actin) using the Pfaffl method, as previously described (166,167).

3.3.5 Assay for transposase-accessible chromatin (ATAC-seq) and data analysis

ATAC-seq was performed as previously described by Guo et al. (204). Briefly, differentiated cells were gently pelleted in 1 \times PBS and resuspended in a 25 μ L tagmentation reaction consisting of 1 \times TD buffer (10 mM TAPS-NaOH pH 8.1, 5 mM MgCl₂, 10% DMF), 2.5 μ L Tn5

transposase, 0.1% TWEEN 20, and 0.02% Digitonin, then incubated for 1 hr at 37 °C. Tagmented nuclei were diluted two-fold and incubated for 30 min at 40°C in lysis buffer, comprised of 300 mM NaCl, 100 mM EDTA, 0.6% SDS, 1.6 µg proteinase K. Transposed DNA was isolated by size selection using SPRI-beads and PCR-amplified using 2× KAPA HiFi HotStart ReadyMix (#7958927001, Roche) and Nextera Indexing Primers (#FC-131-2003, Illumina, San Diego, CA, USA). Following PCR amplification, the size-selection step was repeated to enrich for low molecular weight DNA. Sample quality was assessed on a 2100 Bioanalyzer (Agilent Technologies), and libraries were pooled at an equimolar ratio for sequencing on a HiSeq2500 system (Illumina) with 50 bp paired-end chemistry.

Raw sequencing reads were trimmed for sequencing adapters utilizing the CutAdapt package in Python, then mapped to the hg38 human reference genome using Bowtie2 v2.2.4 (205,206). MACS2 v.2.1.0 was used to call peaks, and counts were normalized to reads per peak per million (rppm) using the equation: $(\text{total reads} \times 10^6) / (\text{unique reads} \times \text{fraction of reads in peaks})$ (122). Peaks were annotated to the nearest transcription start site (TSS) using HOMER v.4.8.2 software, and distribution of raw ATAC peaks across the genome was determined using ChIPseeker (160,207). edgeR was utilized to determine changes in chromatin accessibility between samples at D22, D50, and D78 (208). Differentially accessible regions (DARs) of chromatin were defined by $\text{FDR} < 0.05$ and absolute fold change > 2 . Only DARs with the same signed fold change (positive or negative) between time point comparisons in both HC1 and HC2 were utilized for downstream analyses. The distribution of shared DARs in schizophrenia-associated genomic loci were visualized using karyoploteR (209,210). Visualizations of ATAC-seq rpm signal to the human genome build hg38 were generated from bigWig files using the

rtracklayer package in R/Bioconductor (211). All custom R/Bioconductor scripts are available upon request.

3.3.6 Transcription factor (TF) motif analysis

The MEME Suite v5.0.5 Analysis of Motif Enrichment (AME) tool was utilized to determine enrichment of TF binding motifs (HOCOMOCO v11 database) in shared DARs, compared to shuffled input sequences (212,213). TF footprinting in DARs was performed utilizing RGT-HINT software (214). Cytoscape v3.7.1 software was used to visualize predicted TF interaction networks (215). Similarity among HOCOMOCO v11 TF motifs was calculated using STAMP alignment software (<http://www.benoslab.pitt.edu/stamp/>), phylogenies were visualized with FigTree v1.4.4 (<http://tree.bio.ed.ac.uk>), and clades of similar TF motifs were determined using CTree v1.03 (216,217).

3.3.7 Statistical analysis

Statistical comparisons were calculated using Prism v8.1.2 software (GraphPad, San Diego, CA, USA). A two-way ANOVA with Tukey's multiple comparisons test was used to compare the distribution of ATAC-seq peaks and the percentage of cells expressing GIN markers relative to D22 or D36. Two-way ANOVA with Sidak's multiple comparisons test was used to compare differences in gene expression validated by qRT-PCR relative to D22. The Pearson's product-moment correlation between TSS accessibility and gene expression was calculated using the `cor()` function in R. The BEDtools two-tailed Fisher's exact test was used to compare enrichment of DARs in 108 schizophrenia-associated genomic loci, and enrichment of TF motifs within 693

differentially expressed genes identified in the dorsolateral prefrontal cortex of schizophrenia patients (161,218).

3.3.8 Data availability

All sequencing data are available under accession GSE145073 at the National Center for Biotechnology Information Gene Expression Omnibus (GEO, <https://www.ncbi.nlm.nih.gov/geo/>).

3.4 Results

3.4.1 Human induced pluripotent stem cells (iPSCs) are differentiated to GABAergic interneurons (GINs) with high efficiency

NKX2.1 is highly expressed in the medial ganglionic eminence (MGE) of the ventral telencephalon where the majority of inhibitory progenitors arise during development (219). By using sonic hedgehog (SHH) and its agonist, Purmorphamine, neural progenitor cells (NPCs) were patterned to the ventral forebrain fate, and >90% of cells express NKX2.1, and the neural progenitor marker, NESTIN, by 22 days post-differentiation (D22, **Fig. B1**) (220-222). These NPCs were further differentiated into MAP2⁺/GABA⁺ neurons with high (>99%) efficiency (**Fig. 3.1**). We collected iPSC-derived cells for RNA-seq and ATAC-seq analysis at three time points during GIN differentiation: D22, D50, and D78 (**Fig. 3.1A**). Cells were further assessed for the emergence of GIN subtypes at D36, with ~19% and ~16% staining positive for the calcium-binding proteins calbindin (CB⁺) and calretinin (CR⁺), respectively (**Fig. 3.1B-E**). In contrast, less than ~4% of cells at D36 stained for the GIN subtype markers somatostatin (SST⁺), parvalbumin (PV⁺), or neuropeptide Y (NPY⁺; **Fig. 3.1B-E**). There was a significant increase in the total proportion of GABA⁺ cells by D50, as indicated by elevated percentages of CB⁺ (~22-25% increase), CR⁺ (~11% increase), and SST⁺ (~12% increase) cells (**Fig. 3.1B-E**). There was also a significant increase in the percentage of PV⁺ (~13-14%) cells by D78, though the proportion of NPY⁺ cells remained constant across differentiation (**Fig. 3.1B-E**). Altogether, 81-85% of cells exhibited GABA immunoreactivity by D78, including 26-31% SST⁺ and 15-16% PV⁺ cells, suggesting a robust conversion of iPSCs from both the HC1 and HC2 cell lines into GINs (**Fig. 3.1B-E**).

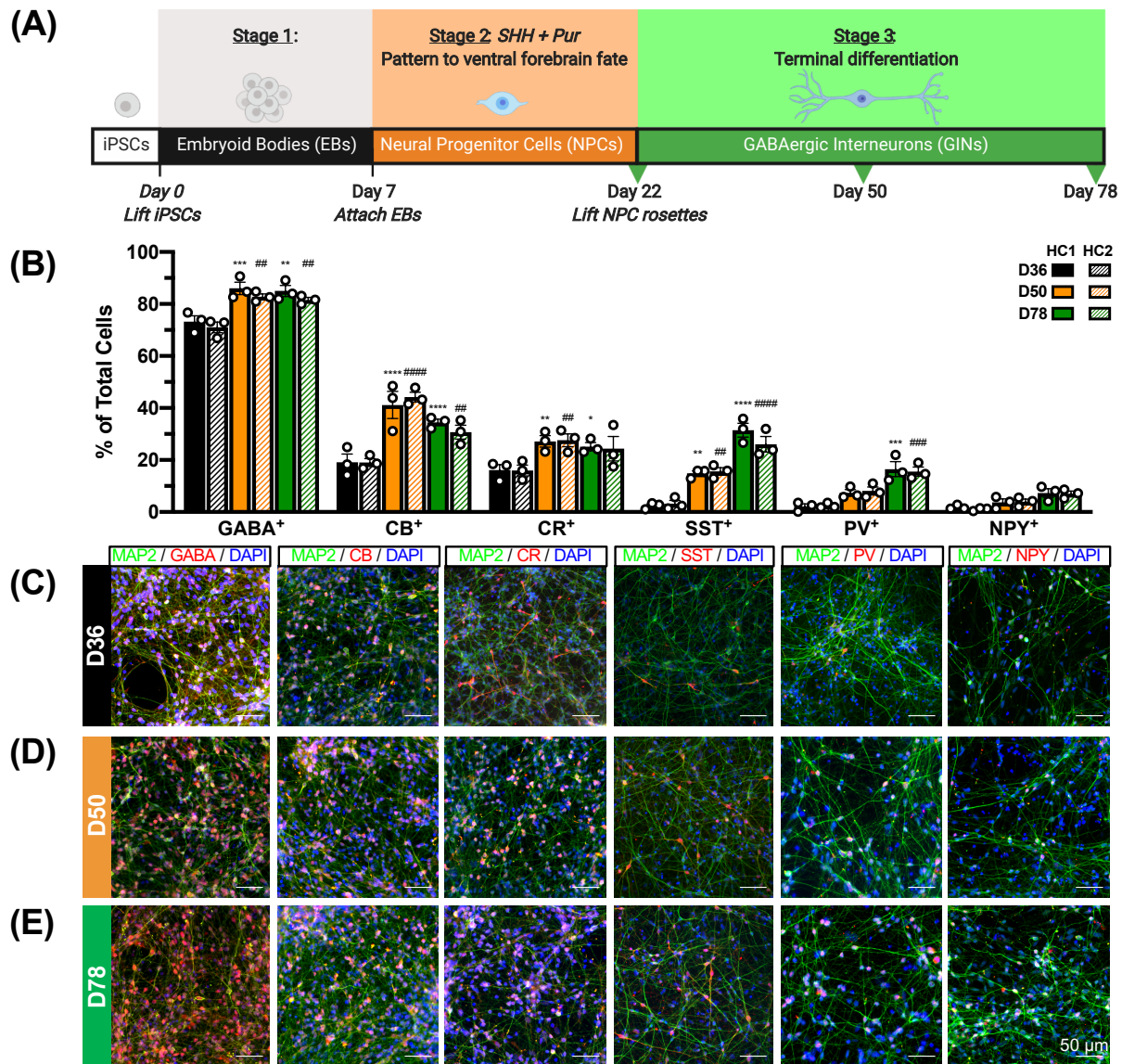


Figure 3.1. Distinct subtypes of GABAergic interneurons emerge after 78 days of differentiation. (A) Human iPSC lines derived from two healthy male controls (denoted HC1 and HC2) were patterned to the ventral forebrain fate and subsequently differentiated to GINs. Samples were collected for RNA-seq and ATAC-seq at three time points: 22 days post-differentiation (D22), D50, and D78. Created with BioRender. (B) Cells were differentiated into GINs with ~81-85% efficiency, marked by GABA immunoreactivity (GABA⁺) and the emergence of GIN subtypes expressing the markers calbindin (CB⁺), calretinin (CR⁺), somatostatin (SST⁺), parvalbumin (PV⁺), and neuropeptide Y (NPY⁺; n=3). Asterisks (*) denote statistical comparisons relative to D36 in HC1, while pound signs (#) denote statistical comparisons to D36 in HC2. Mean \pm SEM. * $p < 0.05$, **/## $p < 0.01$, ***/### $p < 0.001$, ****/#### $p < 0.0001$. (C-E) Representative immunostaining images of cells at (C) D36, (D) D50, and (E) D78 (scale bars: 50 μ m).

3.4.2 RNA-seq confirms enrichment of genes and pathways associated with GIN function

As a first step to characterize GIN development, we performed RNA-seq on 2-3 replicates of HC1 cells at D22, D50, and D78. We identified a total of 5,776 unique differentially expressed genes (DEGs) across all three time point comparisons, as defined by a >2-fold change in gene expression and false discovery rate (FDR) < 0.05 (**Fig. 3.2A**). The most variation in gene expression (4,840 DEGs) was observed between D78 and D22, with comparable numbers of downregulated and upregulated genes (**Fig. 3.2B-C**).

To validate the trends in gene expression observed in RNA-seq, we performed quantitative real-time PCR (qRT-PCR) for selected DEGs related to GIN function and development (**Fig. 3.2D-G, Table B1**). For instance, both *SCN1A* and *NEUROD1* are significantly upregulated by D78, relative to D22 (**Fig. 3.2D-E**). While *SCN1A* is crucial for fast-spiking GABAergic inhibition in PV⁺ GINs, *NEUROD1* encodes a basic helix-loop-helix transcription factor (TF) that induces neuronal differentiation (23,26,223,224). Consistent with the RNA-seq data, there was a significant increase in *SCN1A* expression by D78, and *NEUROD1* expression by D50 in the HC1 cell line (**Fig. 3.2D-E**). qRT-PCR also affirmed RNA-seq results from DEGs that were significantly downregulated over GIN differentiation, such as *DLX3* and *CHL1* (**Fig. 3.2F-G**). *DLX3* is a member of the homeobox TF family, and has previously been reported to repress neural gene expression (**Fig. 3.2F**) (225). *CHL1* encodes a neural adhesion molecule which is expressed in interneuron precursors and negatively regulates NPC proliferation (**Fig. 3.2G**) (226). Accordingly, qRT-PCR results confirmed that both *DLX3* and *CHL1* expression were significantly reduced by D50 in HC1 cells (**Fig. 3.2F-G**). These trends in expression were consistent in HC2 cells, which exhibited a significant increase in *SCN1A* expression, and a significant decrease in *DLX3* and *CHL1* expression, by D50 (**Fig. 3.2D,F-G**). While *NEUROD1* was significantly

upregulated in both HC1 and HC2 cells during GIN differentiation, induction of *NEUROD1* expression occurred earlier in HC1 cells (D50) than HC2 cells (D78, **Fig. 3.2E**). This variability between cell lines underscores the importance of utilizing multiple iPSC lines.

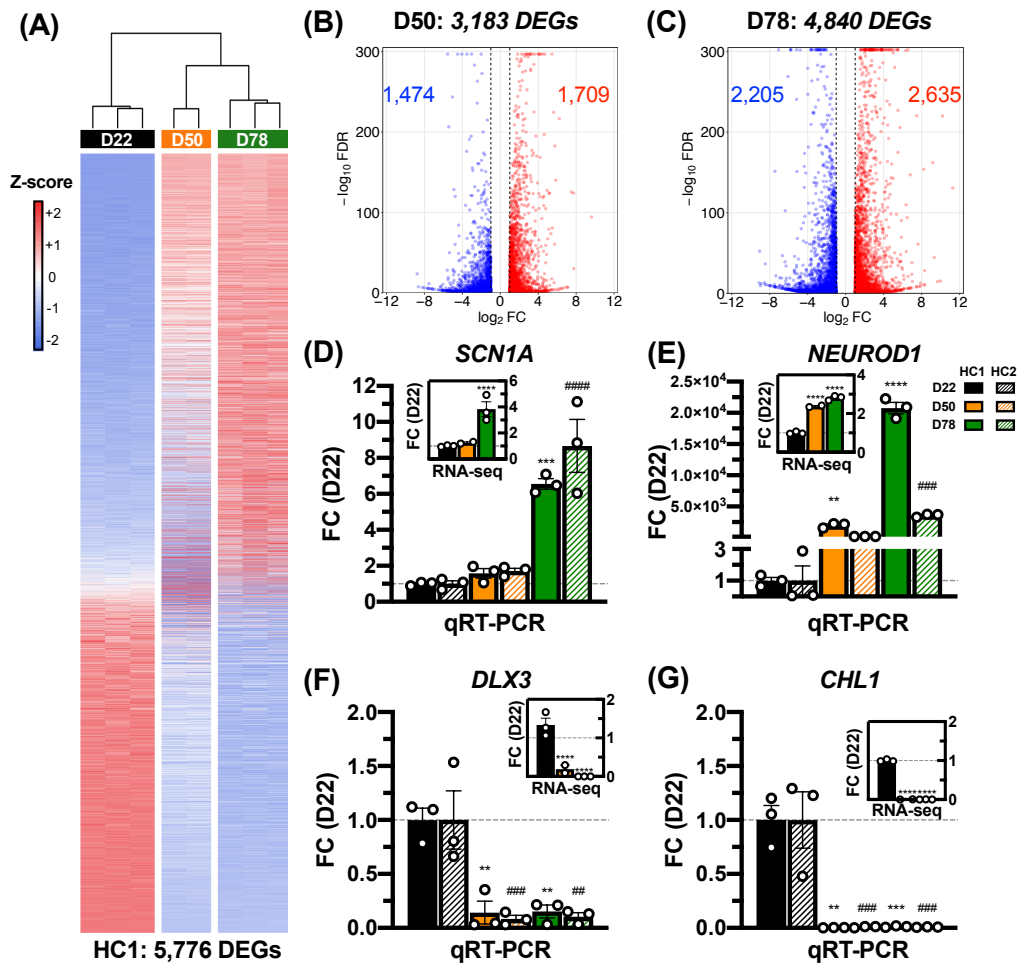


Figure 3.2. Broad changes in neuronal gene expression across GIN differentiation. (A) There are 5,776 differentially expressed genes (DEGs) across GIN differentiation in HC1 cells (n=2-3). Cell colors indicate row Z-scores of DESeq2-normalized gene expression values (blue: low, red: high). (B-C) Summary of upregulated and downregulated DEGs at (B) D50 and (C) D78, relative to D22. (D-G) Both (D-E) upregulated and (F-G) downregulated DEGs detected by RNA-seq exhibit comparable trends in expression between HC1 and HC2 across differentiation. qRT-PCR results are normalized to *ACTB*, and expression is presented as fold change (FC) relative to D22 (n=3). DESeq2-normalized RNA-seq results are presented in the corner of each panel, relative to D22 (n=2-3). Asterisks (*) denote statistical comparisons to D22 in HC1, while pound signs (#) denote statistical comparisons to D22 in HC2. Mean \pm SEM. **/### $p < 0.01$, ***/#### $p < 0.001$, ****/##### $p < 0.0001$.

Spatial gene set enrichment (SGSE) revealed that the 4,840 DEGs with altered expression between D78 and D22 were most associated with the MGE, which is the primary source of cortical GINs (**Fig. 3.3A**) (178,189,202). These DEGs were also associated with the lateral ganglionic eminence (LGE), ventricular zone (VZ), and the horizontal portion of the rostral migratory stream (RMS), all of which generate cortical or olfactory bulb GINs (**Fig. 3.3A**) (227,228). SGSE analysis also noted a strong association between these DEGs and the putamen, which relies on the integration of GINs and cholinergic interneurons for proper function (**Fig. 3.3A**) (229). There was minimal association of DEGs with the subventricular zone (SVZ) and marginal zone (MZ), which are important sources of excitatory cortical neurons and glia, respectively (**Fig. 3.3A**) (230-232).

Gene set enrichment analysis (GSEA) of all detected genes was utilized to identify molecular pathways associated with changes in gene expression at D50 and D78 relative to D22 (**Fig. 3.3B-C, Table B2**) (203). The expression patterns of cells at D50 and D78 were significantly enriched for genes associated with pathways linked to neuronal maturation and, importantly, GABAergic function (**Fig. 3.3B-C**). For instance, the GABA receptor subunit genes (*GABRA3*, *GABRB2*, and *GABRG2*) and GABA reuptake transporter gene (*SLC6A1*) were among the DEGs enriched in the “GABAergic synaptic transmission” gene ontology (GO) term (**Fig. 3.3B-C**). All of these genes are highly expressed in GINs, and GABA receptor subunit or transporter dysfunction is associated with epilepsy and schizophrenia-like phenotypes (233-235). Similarly, *SYT1*, *SV2A*, and *VAMP2* were all enriched in the “vesicle-mediated transport in synapse” GO pathway (**Fig. 3.3B-C**). While *SYT1* encodes a calcium-binding protein involved in fast-releasing inhibitory transmitter release, *SV2A* and *VAMP2* encode proteins involved in vesicular release and docking, respectively (236-239). All three DEGs are noted to have enriched

expression and function in developing GINs (236-239). Genes involved in synapse organization were also significantly enriched in cells at D50 and D78, including *NGEF*, which plays a specialized role in GABAergic inhibition by facilitating neurite outgrowth and the localization of GABA_A receptor subunits to inhibitory synapses (**Fig. 3.3B-C**) (240,241). Altogether, these results support that differentiated cells adopt a GIN-like fate by D78.

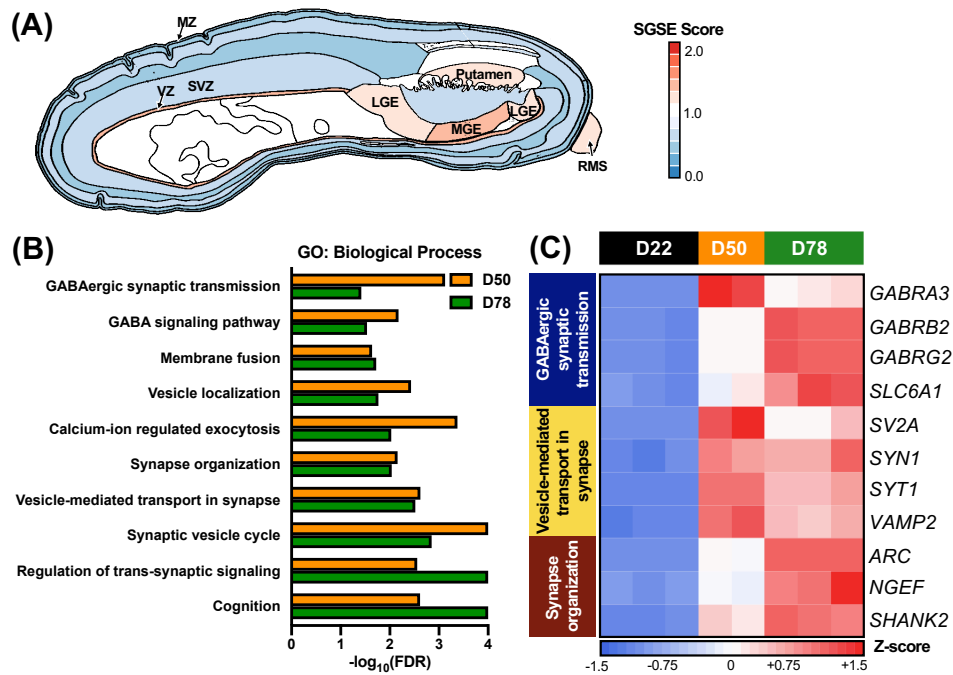


Figure 3.3. iPSC-derived GINs are enriched for pathways associated with mature neuronal function. (A) The 4,840 DEGs at D78 relative to D22 are primarily associated with the medial ganglionic eminence (MGE) in the developing human brain. DEGs are also associated with the lateral ganglionic eminence (LGE), horizontal portion of the rostral migratory stream (RMS), putamen, and ventricular zone (VZ), but not the subventricular zone (SVZ) or marginal zone (MZ). Colors indicate the spatial gene set enrichment (SGSE) score for each brain region (blue: low, red: high). Image of the fetal human brain at 15 post-coital weeks was derived from the Allen Brain Atlas using brainImageR (202). (B) The ten most significant biological process gene ontology (GO) terms identified by gene set enrichment analysis (GSEA) indicate enrichment of DEGs involved in GABAergic synapse formation and neuronal function across GIN differentiation. Genes were pre-ranked based on changes in expression relative to D22. Normalized enrichment scores and FDR q -values for each GSEA comparison are listed in Table S3. (C) Heatmap of representative DEGs in GO categories identified by GSEA analysis. Cell colors indicate row Z-scores of DESeq2-normalized gene expression values (blue: low, red: high).

3.4.3 HC1- and HC2-derived GINs exhibit similar changes in chromatin accessibility across differentiation

To generate a comprehensive map of accessible regions of chromatin across GIN differentiation, ATAC-seq was performed on 2-3 replicates of cells derived from the HC1 and HC2 lines at each of the three time points (**Fig. 3.4, Fig. B2**). Out of the 35,703 ATAC-seq peaks detected across all samples, 16,492 peaks in HC1 cells (46% of all peaks) and 15,583 in HC2 cells (44%) demonstrated significant changes in accessibility over GIN differentiation, as defined by >2-fold change in accessibility and $FDR < 0.05$ (**Fig. 3.4A-B**). Collectively, 13,515 differentially accessible regions (DARs) of chromatin were present in both the HC1 and HC2 lines (**Fig. 3.4C**). To identify ATAC-seq peaks that were broadly representative of epigenomic changes in GIN development, we focused on the 13,221 DARs that exhibited consistent changes in accessibility between both cell lines and across specific stages of GIN differentiation. Principal component analysis of these 13,221 DARs indicated that samples at the same time point exhibited the least variation, regardless of cell line (**Fig. 3.4D**). Consistent with our RNA-seq results, the greatest amount of variation was observed between D78 and D22 (**Fig. 3.4D**). In comparison to D50, nearly twice as many DARs are present at D78 relative to D22, with a majority (71%) increasing in accessibility over GIN differentiation (**Fig. 3.4E-F**).

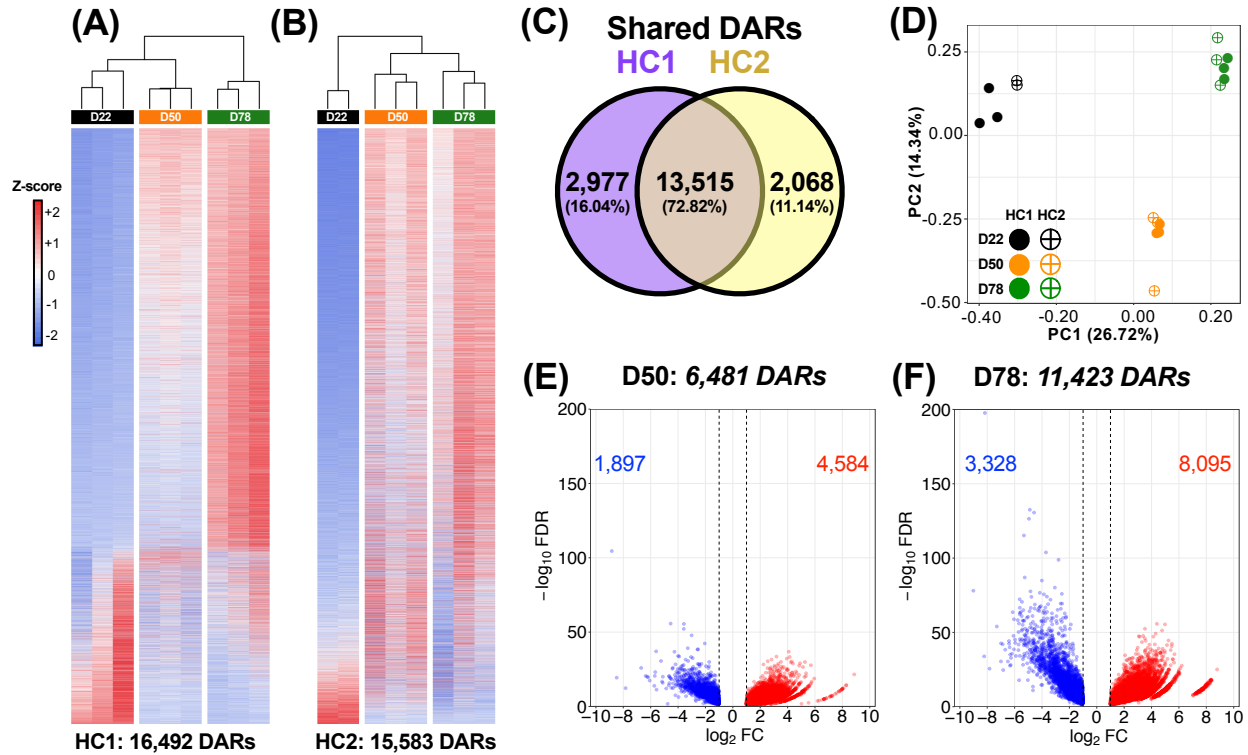


Figure 3.4. ATAC-seq reveals widespread changes in chromatin accessibility across GIN differentiation. (A-B) HC1 exhibits a total of 16,492 differentially accessible regions (DARs) of chromatin across differentiation, while HC2 exhibits 15,583 DARs (n=2-3 per time point). Cell colors indicate row Z-scores of reads per million (rpm) for each DAR (blue: low, red: high). (C) 13,515 regions are differentially accessible in both the HC1 and HC2 lines, though only 13,221 DARs exhibit similar changes in accessibility between time point comparisons. (D) Principal component (PC) analysis of ATAC-seq rpm values across the 13,221 shared DARs. The percentage of variance explained by PC1 or PC2 is listed in parentheses. (E-F) Summary of the 13,221 shared DARs with decreasing or increasing accessibility across differentiation at (E) D50 and (F) D78, relative to D22.

3.4.4 Changes in chromatin accessibility are correlated with GIN-specific gene expression

Epigenomic changes in chromatin structure directly impact gene expression, and increased accessibility is often linked to elevated transcription (114). We observed a significant, positive correlation between changes in accessibility of DARs proximal to the transcription start site (TSS) and gene expression at D50 and D78, relative to D22 (**Fig. 3.5A-B**). For instance, *B3GAT2* encoding a glucuronyltransferase which is involved in synapse formation and the maintenance of extracellular perineuronal nets, was confirmed by RNA-seq and qRT-PCR to be significantly upregulated by D78 (**Fig. 3.5C, Fig. B3A**) (242). While there was no significant change in accessibility at the characterized *B3GAT2* TSS, there were three proximal (within 3 kb) DARs with increased accessibility over GIN differentiation that may contribute to elevated *B3GAT2* expression (**Fig. 3.5C**). Consistent with previous reports that cell type-specific gene expression is driven by elements outside of the TSS, only 6.6% of shared DARs were within 3 kb of a TSS (192,243-245). Therefore, the chromatin remodeling that occurs across differentiation may reveal novel genetic regulatory elements that contribute toward expression of GIN-specific genes. For instance, *SLC6A1*, which encodes the GAT-1 transporter responsible for reuptake of GABA at mature inhibitory synapses, is significantly upregulated by D50, yet demonstrates no significant change in TSS accessibility (**Fig. 5D, Fig. B3B**) (235). However, one DAR within *SLC6A1* intron 1 (7.5 kb downstream of the TSS) significantly increased in accessibility by D50, and therefore may represent a regulatory enhancer element (**Fig. 3.5D**).

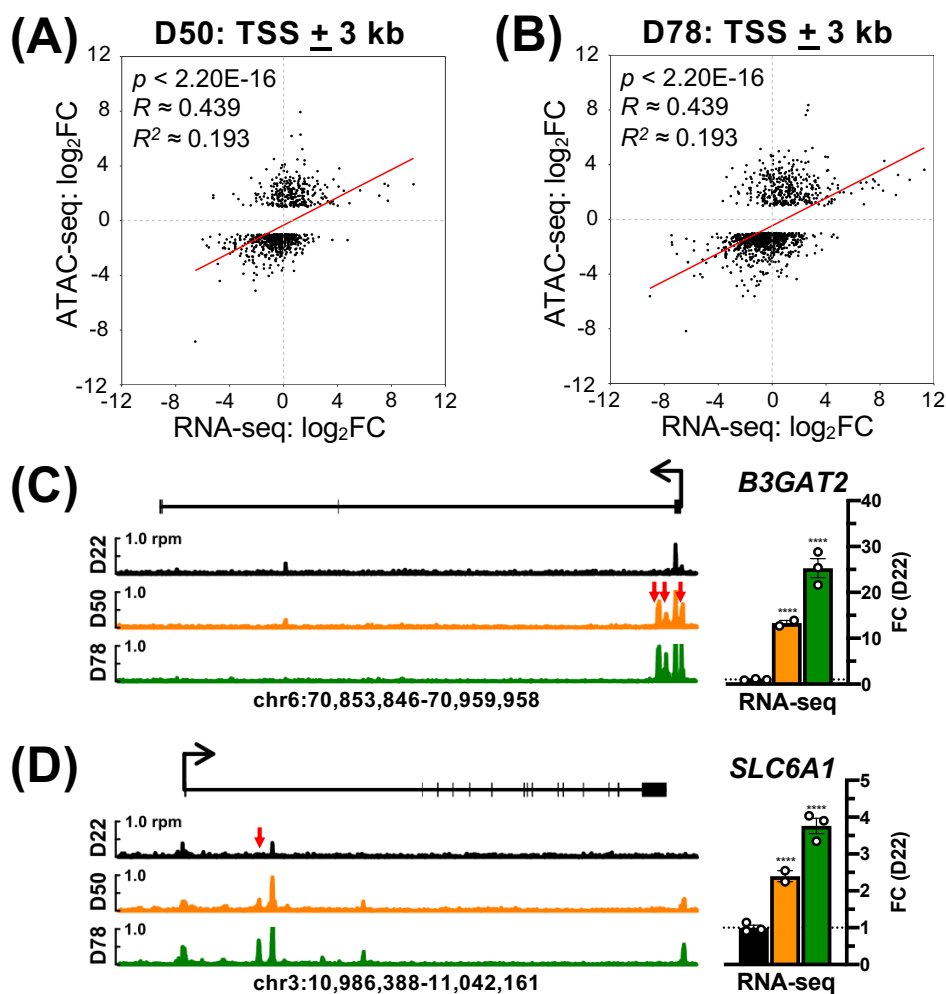


Figure 3.5. Dynamic association of chromatin accessibility and gene expression across GIN differentiation. (A-B) DARs within 3 kb of the transcription start site (TSS \pm 3 kb) are positively correlated with changes in gene expression. \log_2FC denotes fold change in chromatin accessibility (ATAC-seq) or gene expression (RNA-seq) relative to D22. Pearson's product-moment correlation. (C-D) Examples of DEGs with DARs that may contribute to changes in expression. Genome plots represent composite ATAC-seq data from HC1 and HC2 cells, where shared DARs with increased accessibility are denoted by red arrows (rpm: reads per million). Coordinates refer to the hg38 annotation of the human genome (Dec. 2013) (246). DESeq2-normalized RNA-seq data from HC1 cells are presented to the right of each genome plot. Asterisks (*) denote statistical comparisons to D22. Mean \pm SEM. **** $p < 0.0001$.

3.4.5 Motif enrichment analysis implicates distinct groups of transcription factors in GIN differentiation

One mechanism by which DARs mediate changes in gene expression is through interactions with transcription factors (TFs) (114). We classified DARs into one of two groups, based on whether they increased (denoted +A) or decreased (-A) in accessibility across GIN differentiation. Next, we utilized the MEME Suite Analysis of Motif Enrichment (AME) tool to predict the 20 most significant TF binding motifs that were enriched in either +A or -A DARs (**Fig. 3.6**) (212). There was no overlap between the 20 most significant binding motifs enriched in either group, indicating that distinct groups of TFs that interact with +A and -A DARs (**Fig. 3.6**). There were also discernable TF footprints at each predicted binding motif, supporting the physical occupation of predicted motifs by their respective TFs (**Fig. B4, B5**). Furthermore, a majority of TFs enriched in +A DARs (HOXA2, IRF3, etc.) exhibited more prominent footprints at D78 than D22 (**Fig. B4**). The reverse was true for TFs enriched in -A DARs, which demonstrated more prominent footprints at D22 than D78 (**Fig. B5**).

Using the STAMP tool for TF motif comparison, enriched TFs in +A and -A DARs were clustered into subfamilies based on consensus binding motif similarity (**Fig. 3.6**) (216). Notably, +A DARs were enriched for TFs containing a basic helix-loop-helix (bHLH) domain, which have previously been associated with neuronal development, including NEUROD2, which promotes inhibitory synapse formation (**Fig. 3.6**) (247-249). Several bHLH TFs previously linked to glutamatergic differentiation were also enriched in +A DARs, including NEUROG2, EMX1, and EMX2 (**Fig. 3.6**) (250,251). Other clusters included homeobox- (HOX) family TFs such as HOXA2, which is involved in dorsoventral patterning and neurogenesis, or NKX6.2, which

contributes to CR⁺ and SST⁺ GIN cell fate specification ⁸¹(252) (**Fig. 3.6**). In contrast, motifs for Krüppel-like family (KLF) members were enriched in -A DARs, including the KLF5 and KLF15 proteins known to maintain pluripotency or repress neurite outgrowth (**Fig. 3.6, Fig. B5**) (253-255). These diverse TF clusters also included motifs for the SRY-related protein, SOX2, and the zinc finger nuclease (ZnF), ZNF281, which contribute toward the multipotent state of NPCs (**Fig. 3.6**) (256,257). Interestingly, one +A DAR cluster included TFs in the nBAF, IRF, and ETS protein families, which have defined roles outside of neuronal development: BCL11A, IRF3, and ETS2 (**Fig. 3.6**) (258,259). Of the three enriched TFs within this cluster, BCL11A demonstrated the most prominent change in motif occupancy between D78 and D22 (**Fig. B4**). Altogether, these results suggest that +A DARs interact with TFs that promote GIN development, whereas -A DARs represent targets of TFs that suppress neuronal differentiation.

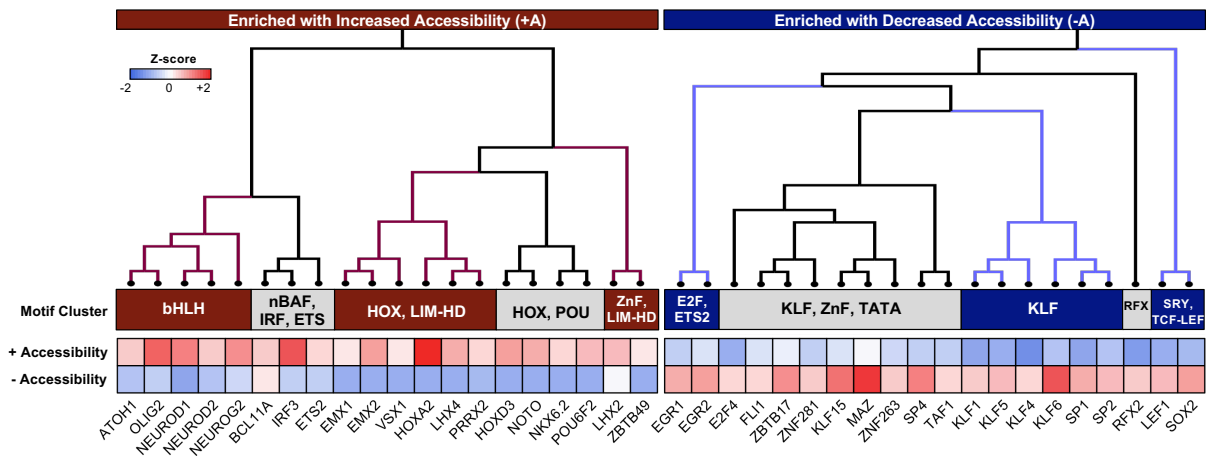


Figure 3.6. DARs with divergent changes in accessibility are enriched for distinct sets of transcription factors. Heatmap of the 20 most significant transcription factor (TF) binding motifs enriched in DARs with increasing (+A) or decreasing (-A) accessibility across GIN differentiation. TFs enriched in +A or -A DARs are clustered into subfamilies by consensus binding motif similarity, as determined by STAMP alignment software (216). Cell colors indicate column Z-scores of the $-\log(\text{rank})$ of TF motif as determined by the MEME Suite AME tool (blue: less enriched, red: highly enriched) (212).

3.4.6 A subset of DEGs may represent novel risk factors for schizophrenia

Given the contribution of GIN dysfunction to schizophrenia, we also examined whether DARs coincided with the 108 schizophrenia-associated genomic loci initially reported by the Schizophrenia Working Group of the Psychiatric Genomics Consortium (210). In total, 111 out of the 13,221 DARs shared between HC1- and HC2-derived GINs localize to 56 of these schizophrenia-associated genomic loci, indicating a significant enrichment ($p = 8.2108E-09$, two-tailed Fisher's exact test; **Fig. 3.7**). We next examined whether the predicted binding sites of TFs enriched in +A DARs also coincided with genes that are differentially expressed in schizophrenia patients (**Fig. B6**) (181). Specifically, we utilized the 693 DEGs reported by Fromer et al. in the post-mortem dorsolateral prefrontal cortex (DLPFC) of 258 schizophrenia cases against 279 healthy controls (218). TFs associated with +A DARs are predicted to interact with 198 (28.6%) of these schizophrenia DEGs, 44 of which are also upregulated throughout GIN differentiation, thereby indicating a significant enrichment ($p = 0.0348$, two-tailed Fisher's exact test; **Fig. B5, B6**). These results therefore suggest that TFs associated with +A DARs could contribute to the normal regulation of genes that are aberrantly expressed in schizophrenia patients (**Fig. B6**).

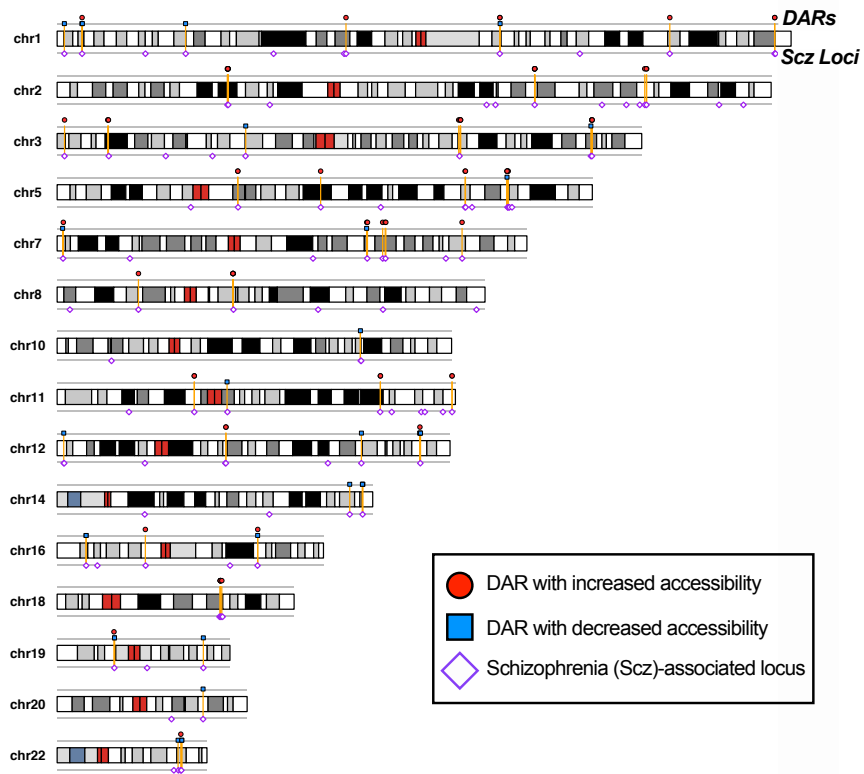


Figure 3.7. DARs are significantly enriched in schizophrenia-associated genomic loci. 111 DARs are located within with 56/108 schizophrenia-associated genomic loci identified by the Schizophrenia Working Group of the Psychiatric Genomics Consortium (210). Red circles and blue squares indicate DARs with increased or decreased accessibility by D78, respectively, while purple diamonds denote schizophrenia-associated genomic loci.

Of the 693 DEGs identified in the schizophrenia DLPFC by Fromer et al., 361 were downregulated, and 332 were upregulated relative to healthy controls (218). We compared the expression of these 693 genes in the Fromer et al. data set to expression patterns between D78 and D22 in developing GINs, and subsequently grouped them into one of four categories: (1) genes with the same expression level at both D22 and D78, (2) DEGs upregulated at D78 relative to D22, (3) DEGs downregulated at D78 relative to D22, and (4) genes with undetectable expression at both time points (**Fig. B7A,C**). A majority of downregulated (62%) and upregulated (72%) genes in the schizophrenia DLPFC exhibited constant expression from D22 to D78 (**Fig. B7A,C**). In contrast, ~8% of the 693 schizophrenia DEGs were not detected by RNA-seq in differentiating GINs (**Fig. B7A,C**).

We posed two hypotheses to identify candidate schizophrenia genes with potential relevance to developing GINs. First, that genes important for GIN function would be downregulated in schizophrenia patients relative to control cases, yet upregulated throughout normal GIN differentiation. Second, that genes that contribute toward GIN dysfunction would be upregulated in a schizophrenia disease state, yet downregulated across differentiation. While it is also possible that genes with constant expression over GIN differentiation could still contribute to a disease state when dysregulated, it is difficult to speculate whether these effects could be linked to altered GIN activity, or broader neuronal dysfunction. Altogether, we identified 83 DEGs that met these criteria: 65 genes that were upregulated in schizophrenia patients and downregulated in GINs, and 18 genes which were downregulated in patients but upregulated in GINs (**Fig. B7A,C**, relevant groups denoted by arrows) (218).

To identify genes with roles specific to developing GINs, we focused on the 25 DEGs with DARs indicative of relevant genetic enhancer elements that drive cell type-specific gene

expression: 17 genes with DARs that increased in accessibility, and 8 with DARs that decreased in accessibility (**Fig. 3.8A, Fig. B7B,D**) (245). A majority of genes with differential accessibility exhibited DARs distal from the TSS. For instance, *CPLX2* was significantly upregulated by D50 in GINs and exhibits three distal DARs (one upstream of the TSS, two downstream of the TES), all of which significantly increase in accessibility during GIN differentiation (**Fig. 3.8B, Fig. B3C**). Similarly, *NTNG2* was upregulated by D78 in GINs, and exhibits two DARs: one of which is upstream of the TSS and significantly increased in accessibility by D78 (**Fig. 3.8C**). Alternatively, *TRPC4* exhibits significantly decreased expression over GIN differentiation, along with four corresponding DARs, all of which also decrease in accessibility (**Fig. 3.8D, Fig. B3D**). Collectively, these 25 genes and their adjacent DARs may represent novel risk factors for schizophrenia, and candidates targets for treatment.

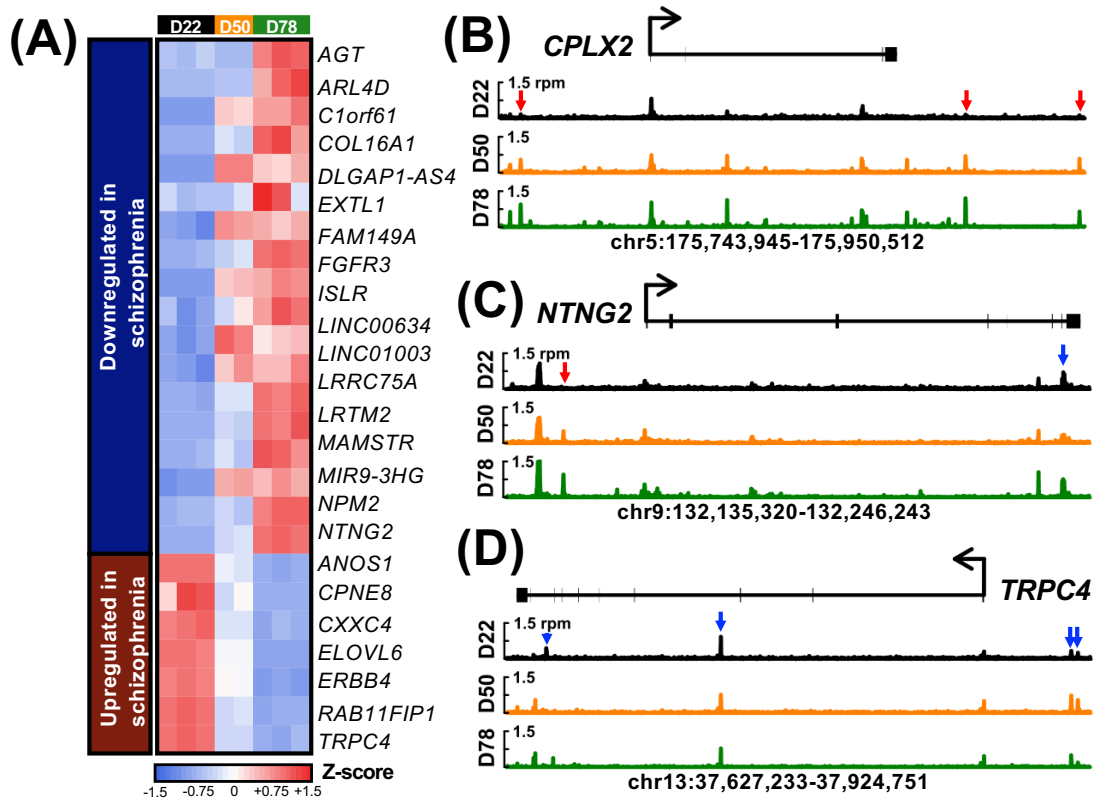


Figure 3.8. A subset of genes that are differentially expressed in the schizophrenia dorsolateral prefrontal cortex (DLPFC) exhibit opposing trends in expression across GIN differentiation. (A) 25 genes that are upregulated across GIN differentiation yet downregulated in the schizophrenia DLPFC, or vice-versa, exhibit DARs ($n=2-3$). Cell colors indicate row Z-scores of DESeq2-normalized gene expression values (blue: low, red: high). **(B-D)** Examples of DEGs with expression patterns that diverge between the schizophrenia DLPFC and across GIN differentiation (218). Genome plots represent composite ATAC-seq data from HC1 and HC2 cells, where shared DARs are denoted by colored arrows (red: increased accessibility, blue: decreased accessibility, rpm: reads per million). Coordinates refer to hg38 annotation of the human genome (Dec. 2013) (246).

3.5 Discussion

In this study, we differentiated iPSCs to a heterogeneous population of GINs with 81-85% efficiency, as confirmed by positive immunostaining for GABA and GIN markers such as PV, SST, and CR. SGSE and GSEA analyses indicated that these cells adopt a GIN fate by D78. While previous studies have also examined transcriptomic changes during GIN differentiation, this is the first study to profile changes in chromatin accessibility of developing human GINs (173,175,178,183). Furthermore, we have combined both RNA-seq and ATAC-seq to explore the temporal dynamics of GIN development, thereby facilitating comparisons between altered chromatin accessibility and gene expression. By utilizing two independent iPSC lines, we were also able to identify accessible regions of chromatin and biological pathways that were consistently altered across different genetic backgrounds, indicating shared programming during GIN differentiation.

The regions of open chromatin detected by ATAC-seq mark potential binding sites for TFs that mediate changes in gene expression. We detected significant enrichment for distinct families of TF motifs in DARs with increased (+A) or decreased (-A) accessibility over GIN differentiation. In +A DARs, these motifs suggest binding of several TFs with previously characterized roles in GIN fate specification, including the bHLH family proteins NEUROD1, NEUROD2, and NKX6.2 (224,247,248). +A DARs were also enriched for binding motifs of TFs with roles outside of neurons, such as IRF3 (toll-like receptor signaling), HOXD3 (angiogenesis), and BCL11A (hemoglobin switching) thereby suggesting novel roles in GIN development and function (258-260). Though BCL11A was originally characterized as a developmental regulator of hemoglobin production in erythroid cells, Wiegrefe et al. reported that *Bcl11a* is highly expressed in projection neurons and GINs of the developing neocortex, and

we observed a significant increase in *BCL11A* expression across GIN differentiation (258,261). Several missense or truncating loss-of-function mutations in *BCL11A* have also been identified in patients with intellectual disability, and heterozygous-null *Bcl11a* mice exhibit impaired long-term memory in a social discrimination task (262). Altogether, these results suggest that *BCL11A* plays an important role in GIN function and cognition.

Of the TFs identified in our motif enrichment analysis, only *KLF5* (enriched in -A DARs) was differentially expressed in the DLPFC of schizophrenia patients (218). Though we did not observe a significant change in *KLF5* RNA levels across GIN differentiation, previous studies (including Fromer et al.) have reported a significant increase in *KLF5* expression in schizophrenia cases relative to controls (218,263). *KLF5* does not have a well-characterized function in brain development, though it is known to contribute to cellular proliferation and the maintenance of a pluripotent state (253,255). We speculate that dysregulation of *KLF5* expression may impair GIN differentiation or function, thereby contributing to the pathogenesis of schizophrenia.

Interestingly, we observed that several bHLH TF binding motifs associated with glutamatergic differentiation also were enriched in +A DARs: *NEUROG2*, *EMX1*, and *EMX2* (250,251,264,265). Though our differentiation protocol consistently generated GINs with 81-85% efficiency, a minority of cells may also adopt a glutamatergic fate (172). Furthermore, our bulk RNA-seq methodology cannot be deconvoluted to determine the contribution of specific cell types to the observed epigenomic or transcriptomic changes during differentiation. Therefore, the enrichment of consensus binding motifs for TFs associated with glutamatergic neuronal development may reflect the presence of DARs that are unique to a subset of non-GABAergic cells. Alternatively, though *NEUROG2* is often linked to glutamatergic

differentiation, Pereira et al. observed that coordinated overexpression of *Neurog2* and *Neurod2* enabled the conversion of mouse striatal glia into PV⁺ GINs with ~30% efficiency (224,251,265). Similarly, Parras et al. noted that deficits in GIN development and migration in the cortex of *Mash1*-null mice could be rescued by overexpressing *Neurog2* (250). Beyond their role in glutamatergic development, *Emx1* and *Emx2* are also involved in early corticogenesis from neural precursors (251,265,266). It is possible, then, that these glutamatergic TFs may also partially contribute toward human GIN development through cortical patterning or other mechanisms.

We observed a significant enrichment of both DARs within schizophrenia-associated genomic loci, and +A TFs with genes that are differentially expressed between the DLPFC of patients with schizophrenia and healthy controls. Given the crucial role of GINs in maintaining cortical network activity, GIN dysfunction in the DLPFC is believed to contribute to the cognitive and behavioral deficits observed in schizophrenia patients (83,184,267). Therefore, it is possible that genes with increased expression in developing GINs, but decreased expression in the schizophrenia DLPFC could represent novel risk factors for schizophrenia. Genes that are upregulated over the course of development are typically associated with cell type-specific functionality. It stands to reason, then, that downregulation of these same genes in mature neurons could be deleterious. For example, *SCN1A* expression is significantly upregulated during GIN development, and is directly linked to PV⁺ GIN function (23). Bender et al. demonstrated that siRNA-mediated knockdown of *Scn1a* in the brain of adult rats resulted in impaired spatial memory, presumably due to reduced GABAergic activity (32). Likewise, it is possible that genes that are typically downregulated during differentiation may elicit a deleterious effect when upregulated. While genes with constant expression over differentiation could also be damaging

when dysregulated, it is less clear whether these effects would be driven by dysfunction of a specific cell type.

Of the DEGs with increased expression in developing GINs and decreased expression in the schizophrenia DLPFC, or vice-versa, 25 genes possess adjacent DARs that may contribute to cell type-specific alterations in gene expression (218). While several of these DEGs, such as *NTNG2* and *ERBB4*, have previously been linked to schizophrenia, we report DARs indicative of novel genetic *cis*-regulatory elements (268,269). For instance, there is a DAR upstream of the TSS for *NTNG2* that significantly increases in accessibility by D78. Given that *NTNG2* also exhibits a significant increase in gene expression by D78, this DAR potentially indicates a transcriptional enhancer element. The remaining DEGs can be separated into three groups: (1) genes with unclear roles in any tissue, (2) genes with characterized roles in non-neuronal tissues, and (3) genes with known neuronal functions. The first group includes the DEGs *LRTM2*, *LINC00634*, and *LRRC75A*, all of which are known to be expressed in the adult brain (270). However, the function of these three genes remains uncharacterized, thereby complicating efforts to link changes in expression to neuronal function or a disease state. The second group contains genes such as *MAMSTR* and *FGFR3*, both of which have previously been associated with bone development (271,272). However, *MAMSTR* also acts as a cofactor of *MEF2C*, an important transcription factor in inhibitory neurons and synaptic development, suggesting that it may also contribute to GABAergic function (271,273). Likewise, *Fgfr3*-null mice exhibit reduced dopaminergic neurons relative to control littermates, thereby indicating a potential role in neuronal development (274). The third group contains genes such as *CPLX2* and *TRPC4*, both of which exhibit defined roles in mature neurons, yet have not been extensively examined in the context of schizophrenia. *CPLX2*, which is upregulated during GIN differentiation, is a member

of the complexin family of genes involved in synaptic vesicle release. While *Cplx2*-null mice appear phenotypically normal, Yamauchi et al. reported that *Cplx2*-null mice exhibit a greater response to maternal deprivation stress than WT littermates (275,276). Specifically, the stressed *Cplx2*-null mice exhibited reduced performance in the Morris water maze relative to stressed WT littermates, whereas the *Cplx2*-null littermates that were not subjected to maternal stress were comparable to WT (276). Similarly, Begemann et al reported that 4-week-old *Cplx2*-null mice that received a parietal cortical cryolesion, but not the sham group, exhibited an increased latency to discover the platform in the Morris water maze when tested at 10 months of age (277). Altogether, Begemann et al. suggested that while loss of *CPLX2* expression does not inherently cause schizophrenia-like phenotypes, it may act as a risk factor following exposure to a stressor (275,278). Furthermore, our results suggest that loss of *CPLX2* expression may impact GIN function. Alternatively, the nonselective cation channel gene, *TRPC4*, is downregulated during GIN differentiation, and upregulated in the schizophrenia DLPFC (218). While there are no reported animal models in which *Trpc4* is overexpressed, *Trpc4*-null mice exhibit anxiolytic phenotypes in the elevated plus maze and open field test behavioral paradigms (279). Additionally, Klipec et al. reported that while *Trpc4*-null rats exhibited normal cognition and performance in the alternating Y-maze and reversal shift-learning paradigms, they demonstrated reduced addictive behavior in a cocaine self-administration task (280). Considering that elevated anxiety and anhedonia (linked to addiction) are prominent phenotypes among patients with schizophrenia, these studies suggest that reduced *TRPC4* expression could be protective in the context of associated negative symptoms. Altogether, these genes and their adjacent DARs represent potential targets for the treatment of schizophrenia, and merit further study.

In summary, our ATAC-seq and RNA-seq data reveal novel TFs and genetic regulatory elements that may broadly regulate the expression of genes critical for GIN development. Furthermore, we have identified several genes that may be of translational relevance to GIN dysfunction in schizophrenia. Together, these data will be a useful resource for examining the molecular networks regulating mature GIN functionality and schizophrenia-associated genes.

3.6 Acknowledgments

The research reported in this chapter was supported by the National Institute of Neurological Disorders and Stroke of the National Institutes of Health under award numbers R01NS107505 (Z.W.), R21NS108760 (A.E.), U19AI131130 (Z.W.), and F31NS110193 (G.A.S.I.). Further funding was provided by predoctoral training grant appointment T32NS007480 (G.A.S.I.), the Department of Defense under award number W81XWH1910353 (Z.W.), and the Edward Mallinckrodt, Jr. Foundation (Z.W.). RNA-seq was performed with the Georgia Genomics and Bioinformatics Core at the University of Georgia, while ATAC-seq libraries were sequenced at the NYU Genome Technology Center. We are grateful for feedback from Dr. Peng Jin.

CHAPTER 4: Mutations in the *Scn8a* DIIS4 voltage sensor reveal new distinctions among hypomorphic and null $\text{Na}_v1.6$ sodium channels

Reproduced with permission from:

Inglis GAS, Wong JC, Butler KM, Thelin JT, Mistretta OC, Wu X, Lin X, English AW, Escayg A. *Mutations in the *Scn8a* DIIS4 voltage sensor reveal new distinctions among hypomorphic and null $\text{Na}_v1.6$ sodium channels*. *Genes, Brain and Behavior*. 2019:e12612. Epub 2019/10/13. doi: 10.1111/gbb.12612. PubMed PMID: 31605437.

4.1 Abstract

Mutations in the voltage-gated sodium channel gene *SCN8A* cause a broad range of human diseases, including epilepsy, intellectual disability, and ataxia. Here we describe three mouse lines on the C57BL/6J background with novel, overlapping mutations in the *Scn8a* DIIS4 voltage sensor: an in-frame 9 bp deletion ($\Delta 9$), an in-frame 3 bp insertion ($\nabla 3$) and a 35 bp deletion that results in a frameshift and the generation of a null allele ($\Delta 9$). *Scn8a* ^{$\Delta 9/+$} and *Scn8a* ^{$\nabla 3/+$} heterozygous mutants display subtle motor deficits, reduced acoustic startle response, and are resistant to induced seizures, suggesting that these mutations reduce activity of the *Scn8a* channel protein, $\text{Na}_v1.6$. Heterozygous *Scn8a* ^{$\Delta 35/+$} mutants show no alterations in motor function or acoustic startle response, but are resistant to induced seizures. Homozygous mutants from each line exhibit premature lethality and severe motor impairments, ranging from uncoordinated gait with tremor ($\Delta 9$ and $\nabla 3$) to loss of hindlimb control ($\Delta 35$). *Scn8a* ^{$\Delta 9/\Delta 9$} and *Scn8a* ^{$\nabla 3/\nabla 3$} homozygous mutants also exhibit impaired nerve conduction velocity, while normal nerve conduction was observed in *Scn8a* ^{$\Delta 35/\Delta 35$} homozygous mice. Our results suggest that hypomorphic mutations that reduce $\text{Na}_v1.6$ activity will likely result in different clinical phenotypes compared to null alleles. These three mouse lines represent a valuable opportunity to examine the phenotypic impacts of hypomorphic and null *Scn8a* mutations without the confound of strain-specific differences.

4.2 Introduction

The voltage-gated sodium channel (VGSC) gene family consists of nine α subunits and four β subunits that collectively function to regulate neuronal excitability (2,281). All VGSC α subunits share a common tertiary structure: four repeat domains (DI-DIV), each consisting of six transmembrane segments (S1-S6) (4). The fourth (S4) segment in each domain, known as the voltage sensor, is enriched for positively charged amino acids that are crucial to voltage-dependent channel gating (4). The neuronal VGSC *SCN8A*, which encodes the $\text{Na}_v1.6$ α subunit, is primarily expressed at axon initial segments and the nodes of Ranvier (3,20,21,282). $\text{Na}_v1.6$ is known to facilitate persistent sodium current and repetitive action potential firing, and its activity at the nodes of Ranvier contributes to normal nerve conduction (3,20,21).

To date, over 200 pathogenic *SCN8A* mutations have been identified in patients with epilepsy, intellectual disability, ataxia, and autism (31,44-46,52,54,61,283-285). Patients exhibit a range of clinical phenotypes, ranging from mild or no seizures to severe, refractory epilepsy, along with several comorbidities including tremor, developmental delay, intellectual disability, and hypotonia (46,57,58,63,285). This phenotypic variability extends to patients with mutations within the same region of the $\text{Na}_v1.6$ protein. For instance, both p.R1617Q and p.R1620L occur in the DIVS4 voltage sensor (58,63). Whereas p.R1617Q was identified in a patient with refractory seizures, intellectual disability and impaired motor function, p.R1620L was found in a patient with autism, intellectual disability, dyskinesia, and attention deficit hyperactivity disorder without severe epilepsy (58,63,64).

Several of the seizure and behavioral phenotypes seen in patients with *SCN8A* mutations have been recapitulated in mouse models (69,70,286). Mutant mice heterozygous for the gain-of-function p.N1768D or p.R1872W human epilepsy mutations develop spontaneous seizures

within the first 2 months of life (69,70,286). *Scn8a*^{N1768D/+} heterozygous mutants also exhibit premature lethality, reduced social discrimination, and impaired motor coordination (69). In contrast, loss of Nav1.6 activity is associated with greater seizure resistance in mice (72,74,287). Likewise, patients with hypomorphic Nav1.6 mutations may not develop epilepsy, but instead exhibit clinical phenotypes such as intellectual disability, developmental delay, autism, or motor dysfunction (44,52,54,284). While existing mouse models that are heterozygous for loss-of-function *Scn8a* alleles, like *9J* and *med-Tg*, do not express specific human mutations, they do exhibit behavioral abnormalities such as increased anxiety or decreased spatial memory (70,288). Depending on their genetic background, loss-of-function heterozygous mutants may also develop absence seizures (27,74). Furthermore, when bred to homozygosity, hypomorphic *Scn8a* alleles are known to cause severe motor phenotypes, including persistent tremor, lurching gait, dystonia, and ataxia (65,66,72,288,289).

In the process of using CRISPR/Cas9 to introduce specific human *SCN8A* mutations into the mouse *Scn8a* locus, we generated three additional mouse lines with unplanned *Scn8a* mutations that affected the Nav1.6 DIIS4 voltage sensor, denoted as $\Delta 9$, $\nabla 3$ and $\Delta 35$. The $\Delta 9$ and $\nabla 3$ mutations represent an in-frame 9 bp deletion and 3 bp insertion, respectively, while $\Delta 35$ is a 35 bp deletion that causes a frameshift and a null *Scn8a* allele. All three mutations are predicted to affect the same positively charged arginine residue at position 848 within the mouse Nav1.6 DIIS4 voltage sensor. Homozygous mutants from each line display a spectrum of motor deficits, including mild tremor and uncoordinated ataxic gait with frequent loss of posture. Heterozygous *Scn8a* ^{$\Delta 9$ /+} and *Scn8a* ^{$\nabla 3$ /+} mutants also exhibit subtle motor deficits and an impaired acoustic startle response. Furthermore, all three mutations are on the same C57BL/6J genetic background, thereby allowing genotype/phenotype

comparisons without the confound of strain-specific differences. Collectively, these mouse models offer a unique opportunity to examine the phenotypic impacts of distinct mutations within the same region of the $\text{Na}_v1.6$ channel.

4.3 Materials and Methods

4.3.1 Generation of founder mice

The *Scn8a* $\Delta 9$, $\nabla 3$, and $\Delta 35$ mutations were generated on the C57BL/6J background (strain #000664, The Jackson Laboratory, Bar Harbor, Maine) by the Mouse Transgenic and Gene Targeting Core at Emory University, using CRISPR/Cas9 with a gRNA targeted to *Scn8a* exon 15. After isolating genomic DNA from tail biopsies of founder mice, *Scn8a* exon 15 was PCR-amplified using forward primer 5'-ACAGTCTGCGACACGATCAG and reverse primer 5'-ATCTGGGCCAGGAAAGAGTT. PCR was carried out in a 25 μ L volume containing 5X Green GoTaq Reaction Buffer (#M7911, Promega), 0.2 mM dNTPs (#U1515, Promega), 10 μ M primers and 1 unit *Taq* DNA polymerase (#M3005, Promega). The reaction parameters were: 1 cycle with 3 minutes at 95°C; 34 cycles with 30 seconds at 95°C, 30 seconds at 58°C, 1 minute at 72°C; then 1 final extension cycle with 5 minutes at 72°C. Purified PCR products were submitted to Psomagen Inc. (<http://macrogenusa.com/>) for Sanger sequencing and compared to the reference mm9 sequence (UCSC Genome Browser, <https://genome.ucsc.edu/>).

4.3.2 Genotyping

For routine genotyping, mutant mice were identified by amplification of a 569 bp genomic fragment (using primers and the protocol described above). The $\Delta 9$, $\nabla 3$, and $\Delta 35$ mutations all disrupt a *HinfI* restriction site in *Scn8a* exon 15. Therefore, digestion of the PCR product with *HinfI* (#ER0801, Thermo Fisher Scientific) generates two fragments (157 and 412 bp) from the WT allele, whereas the mutant alleles are undigested (569 bp band). Restriction fragments

were detected by electrophoresis on 1.2% agarose gels after staining with ethidium bromide (#BP1302-10, Thermo Fisher Scientific).

4.3.3 Animal maintenance

Heterozygous mutant males from each line were backcrossed to C57BL/6J females for four generations (N4) prior to experimentation. N4 heterozygotes from each line were subsequently bred to produce wild-type (WT), heterozygous (m/+) and homozygous (m/m) offspring (N4F1). Behavioral analysis, motor analysis, acoustic startle and auditory brainstem response are optimally performed with adult mice, beyond the age at which we observed lethality in the homozygous mutants. Therefore, heterozygous mutant and WT littermates at the N4 generation were used for these assays and seizure profiling in order to increase the efficiency of generating sufficient mice for testing. Survival and weight measurements, $Na_v1.6$ expression, and nerve conduction velocity were compared between homozygous and heterozygous mutants and WT littermates at the N4F1 generation. For genetic complementation testing, heterozygous *Scn8a*^{49/+}, *Scn8a*^{73/+}, and *Scn8a*^{435/+} mutants on the C57BL/6J background were crossed to heterozygous-null *Scn8a*^{med/+} mice on the C3H/HeJ background (strain #000659, The Jackson Laboratory) to generate (C57BL/6J x C3H/HeJ) F1 mice (72,290). All mice were group-housed on a 12-hour light/dark cycle with ad libitum access to food and water and cared for following NIH guidelines, with approval by the Emory University Institutional Animal Care and Use Committee.

4.3.4 Protein modeling

The impact of each mutation on Na_v1.6 structure was modeled using the Phyre2 toolkit (<http://www.sbg.bio.ic.ac.uk/phyre2/>), based on the template sodium channel crystal structure from *Periplaneta americana* (fold library ID c5x0mA, protein database ID 5X0M) (4,291).

Protein structures of the $\nabla 3$ and $\Delta 9$ mutant channel proteins were visualized and the root-mean-square deviation (RMSD) from WT Na_v1.6 was calculated using PyMOL v2.0 software (Schrödinger, LLC, <https://pymol.org/2/>).

4.3.5 Survival and weight analysis

N4F1 male and female mice from the *Scn8a* $\Delta 9$, $\nabla 3$, and $\Delta 35$ lines were weighed daily from postnatal days (P) 7-24 (P7-24), and then every 3-5 days afterward until P90. Mice were observed daily for general health and survival. Sample sizes per genotype, where *m* denotes a mutant allele: WT: *N* = 5 to 11, *m*/+: *N* = 14 to 21, *m*/*m*: *N* = 6 to 11 (from eight to 14 litters per line/sex).

4.3.6 Western blot analysis

Whole-brain lysates from N4F1 male and female mice aged P14-17 (*N* = 5-6, from four to eight litters per line) were enriched for membrane-bound proteins by ultracentrifugation at 38000g for 30 minutes. Protein extracts (75-100 μ g) were denatured in 4X Laemmli buffer (#1610747, Bio-Rad) with 5% β -mercaptoethanol (#444203, MilliporeSigma) and loaded on a precast 7.5% mini-PROTEAN TGX stain-free polyacrylamide gel (#4568023, Bio-Rad). Blots were probed with 1:200 dilution polyclonal anti-Na_v1.6 (#AB5580-200UL, MilliporeSigma), and visualized with 1:5000 dilution HRP-conjugated polyclonal anti-IgG (#NA934, GE Healthcare, Chicago,

Illinois). Band intensities were analyzed using Image Lab software (v5.2.1, Bio-Rad) and normalized to total protein. For the homozygous *Scn8a*^{A35/A35} mutants, which lacked a Na_v1.6 band, the background signal corresponding to 260 kDa was quantified and plotted.

4.3.7 6 Hz psychomotor seizure induction

6 Hz psychomotor seizures were induced as previously described (292,293). N4 male and female mice (2-5 months old, N = 5-14, from five to nine litters per line/sex) from each line were individually restrained and provided 0.5% proparacaine hydrochloride ophthalmic solution (#07-892-9554, Patterson Veterinary, Greeley, Colorado) as a topical anesthetic. A brief corneal stimulus (6 Hz, 0.2-ms pulse width, 3 seconds, 27 mA) was applied using a constant current device (ECT Unit 57800; Ugo Basile, Cornerio, Italy). Behavioral seizure responses were scored by an experimenter blinded to genotype on a modified Racine's scale: 0 (no abnormal behavior), 1 (immobile for ≥ 3 seconds), 2 (forelimb clonus or head nodding), 3 (rearing and falling) (294).

4.3.8 Flurothyl seizure induction

Seizures were induced with the chemical convulsant, Bis(2,2,2-trifluoroethyl) ether (flurothyl, #287571-5G, MilliporeSigma), as previously described (293,295). Briefly, 2 to 5-month-old N4 male and female mice from each line (N = 10-16, from four to 12 litters per line/sex) were individually placed in a clear, Plexiglas chamber, and flurothyl was continuously introduced into the chamber at a rate of 20 μ L/min. Latencies to the first myoclonic jerk (MJ) and generalized tonic-clonic seizure (GTCS) were recorded by an experimenter blinded to genotype.

4.3.9 EEG surgery and analysis

N4 male *Scn8a*^{Δ9/+} mutants (3-5 months old, n = 5, from two litters) were implanted with four cortical electrodes (Vintage Machine Supplies, Medina, Ohio), as previously described (166). The electrodes were implanted at the following coordinates relative to bregma: anterior-posterior (AP) +2.0 mm and medial-lateral (ML) +1.2 mm, AP -1.5 mm and ML +1.2 mm, AP +0.5 mm and ML -2.2 mm, and AP -3.5 mm and ML -2.2 mm. EMG recordings were collected by two fine-wire electrodes implanted into the neck muscle. Each mouse was allowed 3 days to recover from the surgery prior to EEG recordings. EEG was recorded continuously for 116 hours from one mouse prior to death due to unknown cause. The remaining four mice each had 316-319 hours of EEG recordings. EEG/EMG signals were collected and analyzed with Somnologica EEG software. Seizures were manually identified by the presence of high-frequency and high-amplitude EEG signals that were at least twice the background and lasted for at least 3 seconds.

4.3.10 Behavioral assessment

Behavioral analyses were conducted on 3 to 5-month-old N4 male WT and heterozygous littermates from the Δ9 and ∇3 lines. All testing was conducted under consistent lighting conditions (452 lx) during the animals' light cycle, between the hours of 9 am to 4 pm. Mice were given 2 hours to acclimate to the experimental space before testing. The same cohort of Δ9 mice (N = 12-13, from six litters) was used for open field testing and novel object recognition. A separate cohort of Δ9 mice (N = 9-15, from eight litters) was used for three-chamber social interaction, then reciprocal social interaction. The same cohort of ∇3 mice was used for open field testing, novel object recognition, then reciprocal social interaction (N = 8-13, from four litters). Mice were given at least 1 week to recover between each paradigm. All

behavior was scored using ANY-maze Behavior Tracking Software (Stoelting, Wood Dale, Illinois) by a user blinded to genotype. Protocols for each paradigm are detailed in **Appendix C1**.

4.3.11 Acoustic startle response

N4 male WT and heterozygous mutant (3-5 months old, N = 8-15, from seven to 13 litters per line) from each of the three mouse lines were individually placed into a Plexiglas cylinder fitted over a motion sensor (SR-LAB Startle Response System, San Diego Instruments, San Diego, California) and acclimated to a 67 dB background white noise for 5 minutes. Mice were then exposed to white noise or a 4 kHz acoustic stimulus at one of 10 different intensities (70, 72, 76, 80, 85, 93, 102, 108, 117 or 120 dB) for 40 ms. A total of 55 trials (five per stimulus or white noise) were run in a randomized order, with a 5-30 seconds interval between trials. Maximum voltage (V_{\max}), a metric of the peak acoustic startle response, was automatically recorded in the 100 ms following each stimulus. The average V_{\max} across five trials per stimulus intensity was calculated for each mouse by an experimenter blinded to genotype.

4.3.12 Auditory brainstem response

N4 male WT and heterozygous mutant mice (1-3 months old, N = 3-6, from two to three litters per line) from each of the three mouse lines were anesthetized with ketamine (80 mg/kg) and xylazine (10 mg/kg), and electrodes were implanted in the forehead, left ear, and right ear to determine ABR thresholds. Using RZ6 Tucker-Davis system III hardware (Tucker-Davis Technologies, Alachua, Florida), ABR clicks or tone bursts (10-ms duration, 0.5-ms rise-fall time) were presented to both ears. Each click consisted of 1 to 4 kHz stimuli, presented at an

intensity of 10 to 90 dB, in 10 dB increments. Tone bursts ranged in frequency (4, 8, 12, 18, 24 or 32 kHz) and intensity (10-90 dB, again in 10 dB increments). ABR threshold was determined from appearance of ABR waves I, II, III and V using BioSigRz software (Tucker-Davis Technologies, Alachua, Florida) by an experimenter blinded to genotype. The lowest stimulus level that elicited a repeatable two-phase waveform was considered to be the ABR threshold.

4.3.13 Experimental conditions for motor assessment

Motor assessments were conducted on 3 to 5-month-old N4 male heterozygous mutant and WT littermates from each line (N = 8-18, from 6 to 13 litters per line). All testing was performed by an experimenter blinded to genotype, between the hours of 9 AM TO 4 PM, with 2 hours of acclimation to the experimental space before assessment.

4.3.14 Rotarod

Each mouse was tested on a rotarod (Rotamex, Columbus Instruments, Columbus, Ohio) for 10 minutes on four consecutive days, with three trials per day. The rotarod gradually accelerated at a rate of 0.1 RPM over a 10-minute period, to a max speed of 40 RPM. Latency to fall was automatically recorded for each trial by photobeam break.

4.3.15 Grip strength

Each mouse was placed on the mesh grid of a force meter (Chatillon, Ametek, Berwyn, Pennsylvania), and gently pulled by the tail until all four limbs were released. The average grip strength (in general force/GF units) was recorded across five consecutive trials per mouse.

4.3.16 Nerve conduction analysis

N4F1 male and female P14-17 heterozygous and homozygous mutants and WT littermates from the $\Delta 9$, $\Delta 3$, and $\Delta 35$ lines were anesthetized with isoflurane, and a segment of the sciatic nerve was exposed in the posterior mid-thigh (N = 4-7, from four to nine litters per line). Two stimulating monopolar needle electrodes (#74325-36/40, 28G, Ambu, Copenhagen, Denmark), were placed on the exposed sciatic nerve, and two fine-wire EMG electrodes were inserted into the foot using a 25G 5/8" hypodermic needle. The fine-wire EMG electrodes were constructed from enamel-coated steel wires (#M468240, California Fine Wire Company, Grover Beach, California), in which the insulation was removed from the distal 1 mm of the recording tips. The sciatic nerve was stimulated with 0.1-ms constant voltage pulses, each spaced 3 seconds apart to avoid muscle fatigue. The average latency to the onset of a direct muscle (M) response evoked in foot muscles was recorded using custom LabView software (National Instruments, Austin, Texas), and analyzed by an experimenter blinded to genotype. Conduction velocity was calculated by dividing the distance between the stimulating and EMG electrodes by the average M-response latency. This procedure was also performed on F1 littermates from the *Scn8a med* line.

4.3.17 Statistical analysis

Statistical comparisons were calculated using Prism v8.1.2 software (GraphPad, San Diego, California). A χ^2 test was used to compare the number of observed N4F1 WT, heterozygous, and homozygous mutant births to the predicted 1:2:1 Mendelian ratio. A log-rank (Mantel-Cox) test was used to compare survival rates among N4F1 male and female homozygous mutant littermates within each line. A Kruskal-Wallis test with Dunn's multiple comparisons test was used to compare normalized protein levels from Western blots. A parametric one-way ANOVA

followed by Tukey's multiple comparisons test was used to compare the time spent in the center in the open field behavioral task and nerve conduction velocity. A one-sample parametric *t*-test was used to compare interaction with the novel object against 50% random chance in the novel object recognition paradigm, as well as interaction with the empty cage, “novel” mouse, or “stranger” mouse against 50% random chance in three-chamber social interaction. A two-tailed unpaired parametric Student's *t*-test was used to compare speed and distance traveled in the open field test, total interaction time and latency to interact in reciprocal social interaction, grip strength, and latency to each seizure event following flurothyl induction. The unpaired nonparametric Mann-Whitney *U*-test was used to compare Racine scores in the 6 Hz seizure induction paradigm. Two-way rANOVA with Sidak's multiple comparisons was first used to compare the latency to fall from the rotarod between genotypes on each day of testing, then between Day 1 and Day 4 of testing for mice of a given genotype. Two-way rANOVA with Sidak's multiple comparisons was also used to compare the acoustic startle V_{\max} for mice of given a genotype relative to the no-stimulus (N/S) condition, as well as V_{\max} , ABR thresholds, and interpeak latencies between genotypes. All error bars in figures represent \pm standard error of the mean (SEM).

4.4 Results

4.4.1 Identification of new *Scn8a* mutants with severe motor impairments

The $\Delta 9$, $\nabla 3$, and $\Delta 35$ mutations occur in *Scn8a* exon 15, which encodes the Nav1.6 DIIS4 voltage sensor domain (**Fig. 4.1A**). $\Delta 9$ is a 9 bp in-frame deletion that removes three amino acid residues, including the positively charged R848 predicted to contribute to normal voltage sensor function in mouse Nav1.6 (**Fig. 4.1B**) (296-298). $\nabla 3$ is an in-frame 3 bp insertion that introduces an aspartate residue (p.D849) adjacent to p.R848 (**Fig. 4.1B**). Based on the root-mean-square deviation (RMSD) from WT Nav1.6 protein, neither the $\Delta 9$ or $\nabla 3$ mutations are predicted to disrupt overall channel structure (**Fig. 4.1C-E**) (299). $\Delta 35$ is a 35 bp deletion that extends from *Scn8a* intron 14 into exon 15, resulting in a frameshift that is predicted to generate a null *Scn8a* allele (**Fig. 4.1B**). Prior to evaluating the phenotypic consequences of these three mutations, male heterozygous mutants for each allele were backcrossed to female C57BL/6J mice for four generations.

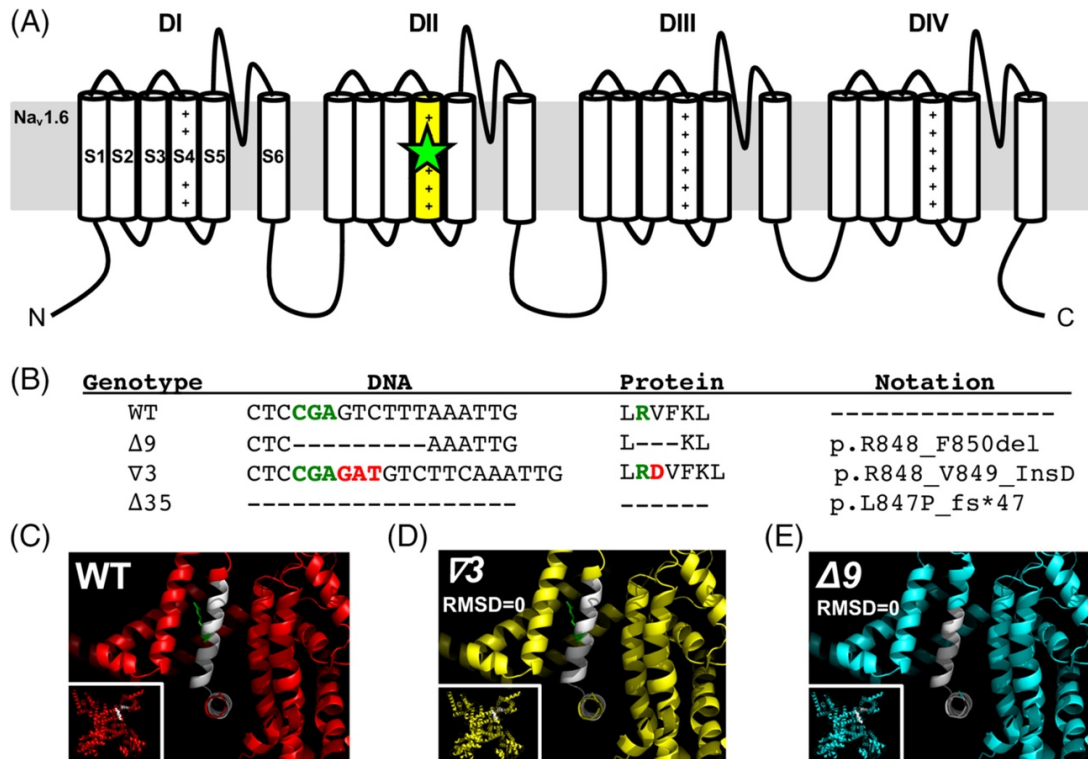


Figure 4.1. $\Delta 9$, $\nabla 3$, and $\Delta 35$ are novel alleles in the Na_v1.6 DIIS4 voltage sensor. (A) The *Scn8a* $\Delta 9$ and $\nabla 3$ mutations overlap within *Scn8a* exon 15, and impact the same region (green star) of the DIIS4 voltage sensor domain (yellow). The $\Delta 35$ mutation extends from *Scn8a* intron 14 into exon 15, and is predicted to generate a null allele. (B) DNA and protein sequence comparison between the WT *Scn8a* allele and each of the three mutant alleles. Green, arginine/R 848 residue predicted to contribute to normal channel function. Red, aspartate/D residue insertion at position 849 in the $\nabla 3$ allele. The $\Delta 35$ deletion spans the described sequence and causes a premature stop codon. (C-E) 3D representations of the DIIS4 voltage sensor domain (white α helix) in WT and mutant Na_v1.6 proteins. The entire Na_v1.6 channel protein is presented in the bottom left corner of each panel. Root-mean-square deviation (RMSD) of atomic positions suggests no structural divergence between WT Na_v1.6 and the $\nabla 3$ or $\Delta 9$ mutant channel proteins. The critical R848 residue is presented as a green wire plot (C,D). This R848 residue is deleted by the $\Delta 9$ mutation (E).

N4F1 wild-type (WT), heterozygous (m/+), and homozygous (m/m) mutants from each *Scn8a* line were born at the predicted 1:2:1 Mendelian ratio (**Fig. C1**; $\Delta 9$: $\chi^2 = 0.0465/P = .977$; $\nabla 3$: $\chi^2 = 2.640/P = .267$; $\Delta 35$: $\chi^2 = 1.783/P = .410$); however, all homozygous mutants exhibited abnormal motor phenotypes beginning in the second week of life. Both the *Scn8a* ^{$\Delta 9/\Delta 9$} and *Scn8a* ^{$\nabla 3/\nabla 3$} mutants displayed an uncoordinated ataxic gait, with episodic tremor and frequent loss of posture, phenotypes that were more pronounced in the *Scn8a* ^{$\nabla 3/\nabla 3$} mice. Consistent with previous *Scn8a* null models, such as *Scn8a*^{*med/med*}, the *Scn8a* ^{$\Delta 35/\Delta 35$} mutants exhibited progressive hindlimb paralysis (53,289,300-303).

Homozygous mutants from each line are visibly smaller than their WT and heterozygous littermates by P14 (**Fig. 4.2A-C**). Compared to their WT and heterozygous littermates, homozygous mutants fail to gain weight and exhibit premature lethality (**Fig. 4.2**). While 100% of the *Scn8a* ^{$\nabla 3/\nabla 3$} and *Scn8a* ^{$\Delta 35/\Delta 35$} mutants die by P36 (**Fig. 4.2E-F**), 15-20% of *Scn8a* ^{$\Delta 9/\Delta 9$} mutants survive to adulthood (**Fig. 4.2D**). There are no significant differences in survival rates between male and female homozygous mutants within each line ($\Delta 9$: $\chi^2 = 1.265/P = .2607$; $\nabla 3$: $\chi^2 = 3.083/P = .0791$; $\Delta 35$: $\chi^2 = 0.2424/P = .6225$). Though *Scn8a* ^{$\nabla 3/+$} mutants are visually indistinguishable from their WT littermates and demonstrate normal growth, 10% to 15% exhibit premature lethality (**Fig. 4.2E**).

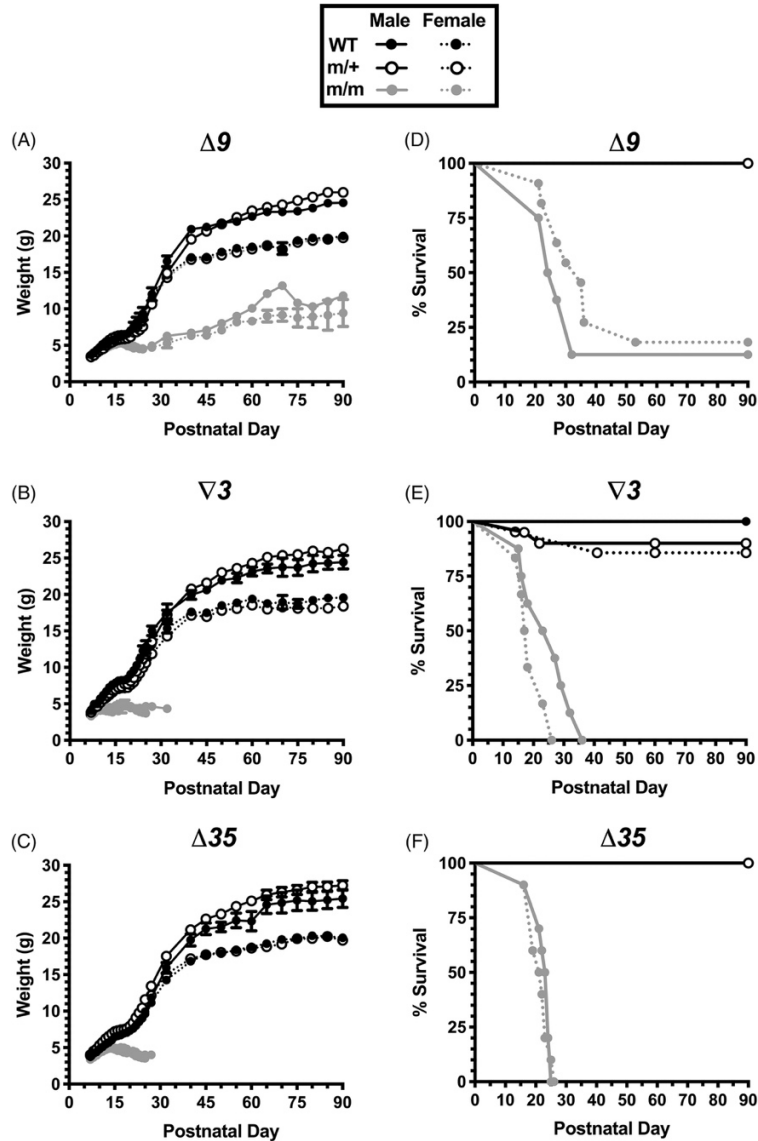


Figure 4.2. *Scn8a* ^{$\Delta 9/\Delta 9$} , *Scn8a* ^{$\nabla 3/\nabla 3$} , and *Scn8a* ^{$\Delta 35/\Delta 35$} homozygous mutants exhibit decreased growth and premature lethality. *Scn8a* ^{$\Delta 9/\Delta 9$} , *Scn8a* ^{$\nabla 3/\nabla 3$} and *Scn8a* ^{$\Delta 35/\Delta 35$} homozygous mutants exhibit (A-C) decreased growth (indicated by body weight) and (D-F) decreased survival relative to WT and heterozygous mutant littermates. No premature lethality was observed in WT or heterozygous mutant littermates from the (D) $\Delta 9$ and (F) $\Delta 35$ lines. Sample sizes per sex and line, where *m* denotes a mutant allele: $\Delta 9$ males (WT: n = 5, m/+ : n = 20, m/m : n = 8, from eight litters), $\Delta 9$ females (WT: n = 9, m/+ : n = 14, m/m : n = 11, from eight litters), $\nabla 3$ males (WT: n = 7, m/+ : n = 20, m/m : n = 8, from 13 litters), $\nabla 3$ females (WT: n = 11, m/+ : n = 21, m/m : n = 6, from 14 litters), $\Delta 35$ males (WT: n = 6, m/+ : n = 15, m/m : n = 10, from 12 litters), $\Delta 35$ females (WT: n = 10, m/+ : n = 14, m/m : n = 10, from 11 litters). Mean \pm SEM.

4.4.2 $\Delta 9$ mutants express normal levels of $\text{Na}_v1.6$

To evaluate whether the motor phenotypes observed in homozygous mutant mice were a result of altered $\text{Na}_v1.6$ protein levels, we performed immunoblotting on total brain protein that was isolated from N4F1 mice (P14-17). There was no significant difference in $\text{Na}_v1.6$ expression between genotypes within the $\Delta 9$ line ($H = 1.170/P = .5782$), suggesting the $\Delta 9$ allele does not impact the stability of the channel protein (**Fig. 4.3A, Fig. C2A**). While there is statistical evidence for differences in $\text{Na}_v1.6$ levels between genotypes within the $\nabla 3$ line ($H = 6.020/P = .0431$), none of the Dunn's post hoc comparisons were statistically significant, suggesting that the effect of genotype on protein levels was modest (**Fig. 4.3B, Fig. C2B**). In contrast, there was a highly significant effect of genotype on $\text{Na}_v1.6$ expression in the $\Delta 35$ line (**Fig. 4.3C, Fig. C2C**; $H = 12.50/P < .0001$), which was also reflected in post hoc multiple comparisons between WT littermates and homozygous *Scn8a* ^{$\Delta 35/\Delta 35$} mutants (**Fig. 4.3C**; $H = 9.50/P = .0021$). There was no detectable $\text{Na}_v1.6$ in homozygous *Scn8a* ^{$\Delta 35/\Delta 35$} mice, thereby confirming $\Delta 35$ is a null allele (**Fig. 4.3C, Fig. C2C**).

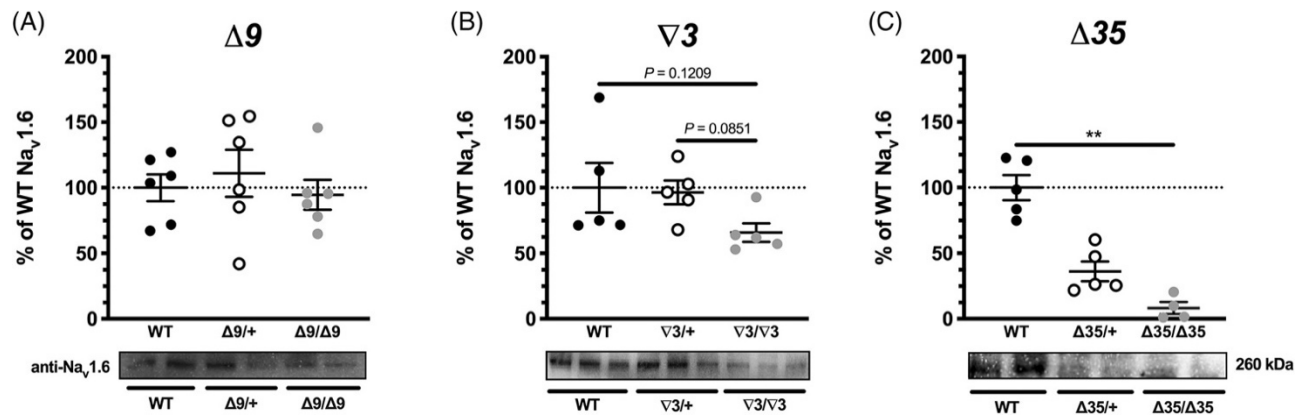


Figure 4.3. The $\Delta 9$ mutation does not alter $Na_v1.6$ protein levels. (A) $Na_v1.6$ expression levels are comparable across genotypes within the $\Delta 9$ line. (B) There is a significant effect of genotype on $Na_v1.6$ expression within the $\nabla 3$ line, though none of the Dunn's post hoc comparisons were statistically significant. (C) $Na_v1.6$ expression is significantly reduced in $Scn8a^{\Delta 35/\Delta 35}$ mutant mice relative to their WT littermates. Results are normalized to total protein, and presented relative to the average WT value. The 260 kDa $Na_v1.6$ band is outlined on each representative blot. Sample sizes per line: $\Delta 9$ (N = 6, from seven litters), $\nabla 3$ (N = 5, from four litters), $\Delta 35$ (N = 5, from eight litters). Mean \pm SEM. $**P < .01$

4.4.3 *Scn8a*^{Δ9/+}, *Scn8a*^{∇3/+}, and *Scn8a*^{Δ35/+} heterozygous mutants are resistant to induced seizures

We used two seizure induction paradigms to evaluate the seizure susceptibility of *Scn8a*^{Δ9/+}, *Scn8a*^{∇3/+}, and *Scn8a*^{Δ35/+} heterozygous mutants. In the 6 Hz paradigm, most of the male WT littermates exhibited seizures that were scored as a 2 on a modified Racine's scale (marked by forelimb clonus or head nodding), whereas most of the heterozygous mutants did not seize (**Fig. 4.4A-C**; Δ9: U = 6.5/*P* < .0001; ∇3: U = 15.0/*P* < .0001; Δ35: U = 26.0/*P* < .0001). (294). Following flurothyl administration, male heterozygous mutants exhibited significantly greater latencies to the first myoclonic jerk (MJ; Δ9: *t*₂₄ = 5.873/*P* < .0001; ∇3: *t*₂₄ = 5.298/*P* < .0001; Δ35: *t*₂₄ = 4.982/*P* < .0001) and generalized tonic-clonic seizure (GTCS; Δ9: *t*₂₄ = 8.732/*P* < .0001; ∇3: *t*₂₄ = 11.15/*P* < .0001; Δ35: *t*₂₄ = 7.257/*P* < .0001) when compared to WT littermates (**Fig. 4.4D-F**). No sex differences were observed (**Fig. C3**). To determine whether the heterozygous mutants exhibit spontaneous seizures, we implanted four cortical electrodes into five adult *Scn8a*^{Δ9/+} males and recorded EEG activity for 2 weeks. No spontaneous seizures were observed during the recording period.

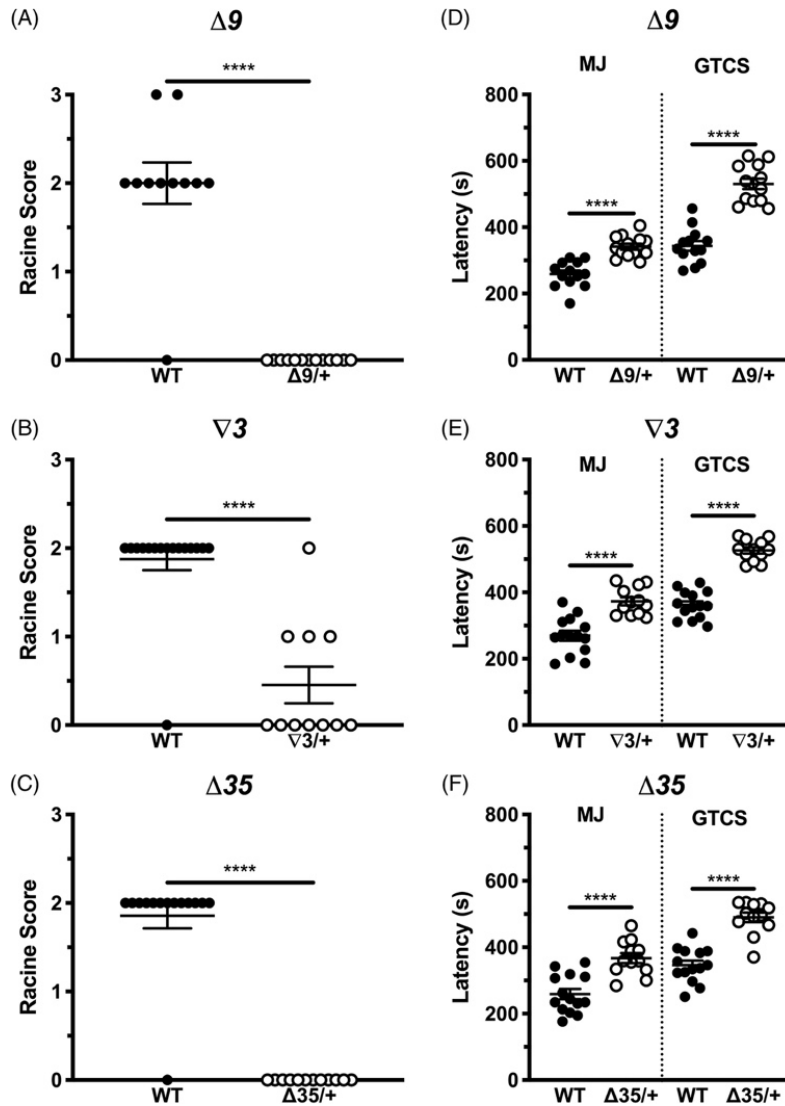


Figure 4.4. *Scn8a*^{Δ9/+}, *Scn8a*^{∇3/+}, and *Scn8a*^{Δ35/+} heterozygous mutants are resistant to induced seizures. (A-C) Male *Scn8a*^{Δ9/+}, *Scn8a*^{∇3/+}, and *Scn8a*^{Δ35/+} mutants are more resistant to 6 Hz seizures at a current of 27 mA compared to WT littermates. Sample sizes per line, where *m* denotes a mutant allele: Δ9 (WT: n = 13, m/+ : n = 13, from seven litters), ∇3 (WT: n = 14, m/+ : n = 12, from nine litters), Δ35 (WT: n = 14, m/+ : n = 12, from six litters). (D-F) Male *Scn8a*^{Δ9/+}, *Scn8a*^{∇3/+}, and *Scn8a*^{Δ35/+} mutants demonstrate increased latencies to the flurothyl-induced myoclonic jerk (MJ) and first generalized tonic-clonic seizure (GTCS) relative to WT littermates. Sample sizes per line: Δ9 (WT: n = 11, m/+ : n = 13, from seven litters), ∇3 (WT: n = 16, m/+ : n = 11, from 11 litters), Δ35 (WT: n = 14, m/+ : n = 12, from 12 litters). Mean ± SEM. ***P* < .0001**

4.4.4 $\Delta 9$ and $\nabla 3$ are predicted hypomorphic alleles of *Scn8a*

To test whether the $\Delta 9$, $\nabla 3$, and $\Delta 35$ alleles could rescue the hindlimb paralysis observed in homozygous *Scn8a*-null mice, heterozygous mutants from each line were crossed to heterozygous-null *Scn8a^{med/+}* mice on the C3H/HeJ genetic background (72). The resulting hemizygous *Scn8a ^{$\Delta 9$ /med}* and *Scn8a ^{$\nabla 3$ /med}* mice exhibited similar movement abnormalities as homozygous *Scn8a ^{$\Delta 9/\Delta 9$}* and *Scn8a ^{$\nabla 3/\nabla 3$}* mutants. In contrast, *Scn8a ^{$\Delta 35$ /med}* mutants exhibited the hindlimb paralysis characteristic of homozygous *Scn8a*-null mutants. This partial rescue of the *Scn8a*-null phenotype by the $\Delta 9$ and $\nabla 3$ alleles suggests that these mutations are hypomorphic and possess residual Na_v1.6 activity.

4.4.5 *Scn8a ^{$\Delta 9$ /+}* and *Scn8a ^{$\nabla 3$ /+}* mutants do not exhibit increased anxiety or deficits in learning and sociability

To determine whether *Scn8a ^{$\Delta 9$ /+}* or *Scn8a ^{$\nabla 3$ /+}* mutants exhibit behavioral abnormalities, we performed an initial battery of behavioral assessments on heterozygous mutants and WT littermates from each line (Tables C1-C2). Performance was comparable between *Scn8a ^{$\Delta 9$ /+}* and *Scn8a ^{$\nabla 3$ /+}* heterozygous mutants and their respective WT littermates in all behavioral assessments, with the exception of reciprocal social interaction, in which heterozygous mutants spent significantly more time interacting with each other compared to WT littermates (Tables C1-C2: $\Delta 9$: $t_{14} = 2.438/P = .0287$; $\nabla 3$: $t_8 = 2.309/P = .0497$).

4.4.6 *Scn8a ^{$\Delta 9$ /+}* and *Scn8a ^{$\nabla 3$ /+}* mutants exhibit a decreased acoustic startle response

We also examined the acoustic startle response in WT and heterozygous mutant mice from each of the three lines. Beginning at the 102 dB stimulus intensity, WT mice from each line

demonstrated significantly greater acoustic startle responses relative to the baseline, no stimulus (N/S) condition (**Fig. 4.5**). However, *Scn8a*^{Δ9/+} and *Scn8a*^{∇3/+} mutants demonstrated significantly reduced acoustic startle responses compared to WT littermates between the 102-120 dB stimulus intensities (**Fig. 4.5A-B**; Δ9: main effect of genotype, $F_{1,18} = 35.33, P < .0001$; main effect of intensity, $F_{10,180} = 27.62/P < .0001$; interaction of stimulus intensity and genotype, $F_{10,180} = 16.43/P < .0001$; ∇3: main effect of genotype, $F_{1,16} = 44.00/P < .0001$; main effect of intensity, $F_{10,160} = 15.86/P < .0001$; interaction of stimulus intensity and genotype, $F_{10,160} = 11.83/P < .0001$). Interestingly, *Scn8a*^{Δ35/+} mutants exhibited comparable acoustic startle response to WT littermates (**Fig. 4.5C**; main effect of genotype, $F_{1,25} = 0.0122/P = .913$; main effect of intensity, $F_{10,250} = 39.40/P < .0001$; interaction of stimulus intensity and genotype, $F_{10,250} = 0.278/P < .986$). To determine whether the reduced acoustic startle response was due to hearing loss, we compared the minimum sound intensity necessary to evoke an auditory brainstem response (ABR) between heterozygous mutants from each line and their respective WT littermates at several frequencies (**Fig. 4.6**). While the ABR threshold of mice from each line varied based on the frequency presented (main effect of frequency, Δ9: $F_{6,54} = 103.4/P < .0001$; ∇3: $F_{6,30} = 38.26/P < .0001$; Δ35: $F_{6,30} = 43.77/P < .0001$), there were no differences in ABR threshold between *Scn8a*^{Δ9/+}, *Scn8a*^{∇3/+} or *Scn8a*^{Δ35/+} mutants and their respective WT littermates, demonstrating that the mutants do not have hearing deficits (**Fig. 4.6, Fig. C4**; Δ9: main effect of genotype, $F_{1,9} = 1.185/P = .305$; interaction of stimulus frequency and genotype $F_{6,54} = 1.589/P = .168$; ∇3: main effect of genotype, $F_{1,5} = 0.339/P = .586$; interaction of ABR frequency and genotype, $F_{6,30} = 0.619/P = .713$; Δ35: main effect of genotype, $F_{1,5} = 0.2360/P = .6477$; interaction of ABR frequency and genotype, $F_{6,30} = 0.753/P = .612$).

Furthermore, there were no differences in interpeak latencies between ABR waves, suggesting overall normal auditory signaling (Fig. C5).

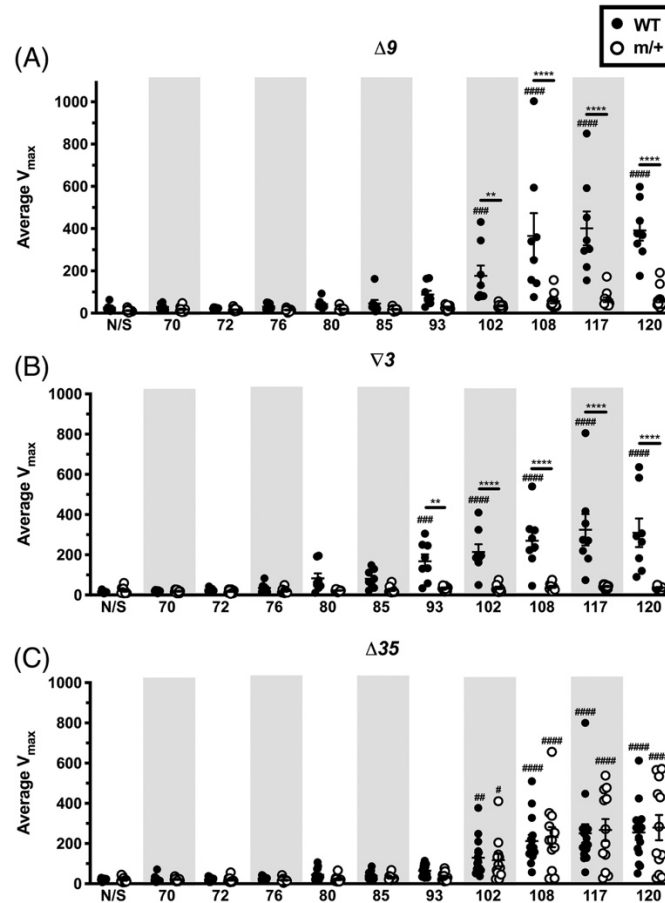


Figure 4.5. *Scn8a* ^{$\Delta 9/+$} and *Scn8a* ^{$\nabla 3/+$} heterozygous mutants exhibit a reduced acoustic startle response. (A-B) *Scn8a* ^{$\Delta 9/+$} and *Scn8a* ^{$\nabla 3/+$} mutants exhibit a significantly reduced startle response relative to WT littermates, and do not exhibit a significant increase in acoustic startle response at any stimulus intensity relative to the N/S (no stimulus) condition. (C) *Scn8a* ^{$\Delta 35/+$} mutants demonstrate a comparable startle response to WT littermates. Data is presented as the average V_{\max} of five trials per stimulus intensity. Sample sizes per line, where m denotes a mutant allele: $\Delta 9$ (WT: $n = 8$, $m/+$: $n = 12$, from nine litters), $\nabla 3$ (WT: $n = 8$, $m/+$: $n = 10$, from seven litters), $\Delta 35$ (WT: $n = 15$, $m/+$: $n = 12$, from 13 litters). Mean \pm SEM. Asterisks (*) denote comparisons between genotypes at the same stimulus intensity, while pound signs (#) denote comparisons within a genotype relative to the N/S condition. # $P < .05$, **/# $P < .01$, ### $P < .001$, **/##### $P < .0001$**

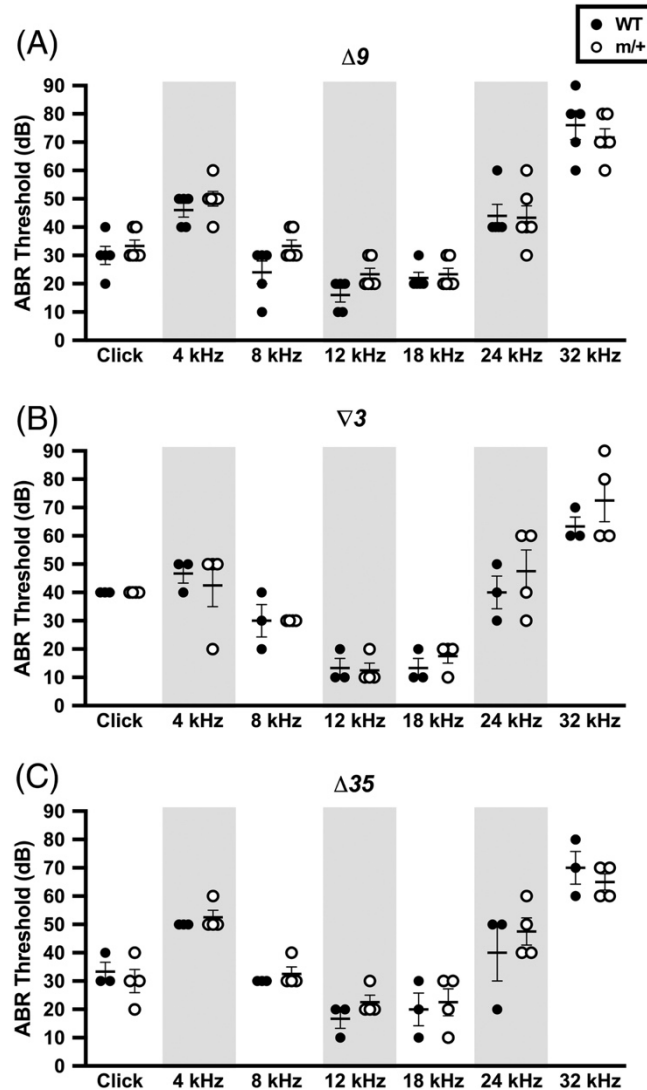


Figure 4.6. *Scn8a* ^{$\Delta 9$ /+}, *Scn8a* ^{$\nabla 3$ /+}, and *Scn8a* ^{$\Delta 35$ /+} heterozygous mutants demonstrate normal auditory brainstem response (ABR). The ABR threshold, or the lowest intensity at which an acoustic stimulus evokes an ABR wave, is comparable between *Scn8a* ^{$\Delta 9$ /+}, *Scn8a* ^{$\nabla 3$ /+}, and *Scn8a* ^{$\Delta 35$ /+} mutants and their respective WT littermates. “Click” denotes the ABR click test, which presents multiple acoustic stimuli ranging from 1 to 4 kHz. All other columns represent the ABR tone-burst test, which presents a single frequency between 4 and 32 kHz. Sample sizes per line, where *m* denotes a mutant allele: $\Delta 9$ (WT: *n* = 5, *m*/+ : *n* = 6, from three litters), $\nabla 3$ (WT: *n* = 3, *m*/+ : *n* = 4, from two litters), $\Delta 35$ (WT: *n* = 3, *m*/+ : *n* = 4, from three litters). Mean \pm SEM.

4.4.7 *Scn8a*^{Δ9/+} and *Scn8a*^{∇3/+} heterozygous mutants exhibit motor impairments

While homozygous mutants from each line exhibit severe motor abnormalities, heterozygous mutants are visually indistinguishable from their WT littermates. We first examined motor coordination and learning in heterozygous *Scn8a*^{Δ9/+}, *Scn8a*^{∇3/+}, and *Scn8a*^{Δ35/+} mutants and their respective WT littermates using a rotarod apparatus. WT and heterozygous mutant littermates from each line demonstrated similar proficiency on the rotarod on Day 1 of testing (**Fig. 4.7A-C**). WT and heterozygous littermates from each line exhibited a significant improvement in performance on the rotarod over the 4-day testing period (**Fig. 4.7A-C**; main effect of time, Δ9: $F_{3,84} = 78.90/P < .0001$; ∇3: $F_{3,72} = 63.06/P < .0001$; Δ35: $F_{3,84} = 50.07/P < .0001$). While the *Scn8a*^{Δ9/+} and *Scn8a*^{∇3/+} mutants did improve over time, they were unable to achieve the same degree of performance (marked by a shorter latency to fall) as their WT littermates (**Fig. 4.7A-B**; Δ9: main effect of genotype, $F_{1,28} = 22.73/P < .0001$; interaction of time and genotype, $F_{3,84} = 12.17/P < .0001$; ∇3: main effect of genotype, $F_{1,24} = 6.042/P = .0216$; interaction of time and genotype, $F_{3,72} = 2.034/P = .117$). In contrast, the *Scn8a*^{Δ35/+} mutants did not demonstrate any deficits in rotarod performance relative to WT littermates (**Fig. 4.7C**; main effect of genotype, $F_{1,28} = 2.118/P = .1567$; interaction of time and genotype, $F_{3,84} = 1.320/P = .2733$). To examine potential deficits in muscle strength, we used a force meter to measure grip strength in mice from each line. While the *Scn8a*^{Δ9/+} and *Scn8a*^{Δ35/+} mutants had comparable grip strength to their WT littermates, the *Scn8a*^{∇3/+} mutants exhibited significantly lower grip strength, suggesting an allele-specific deficit in strength (**Fig. 4.7D-F**; Δ9: $t_{23} = 0.283/P = .780$; ∇3: $t_{18} = 2.230/P = .0339$; Δ35: $t_{28} = 1.031/P = .311$).

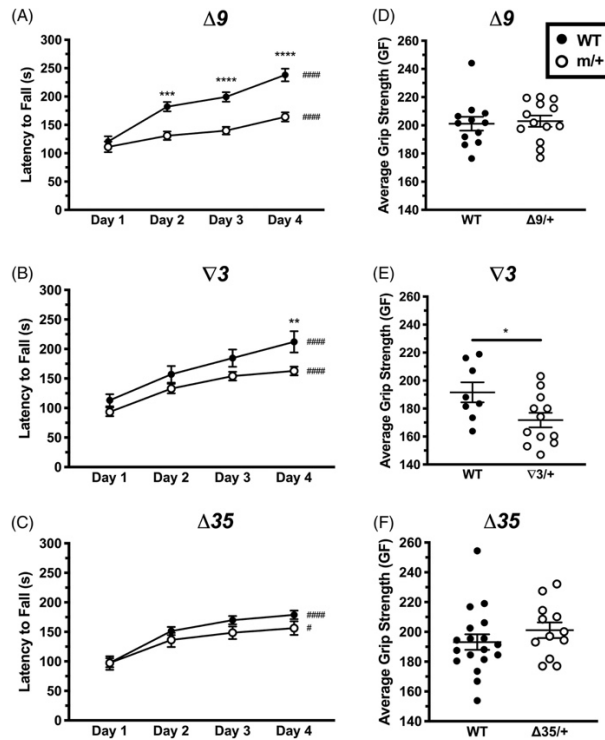


Figure 4.7. *Scn8a* ^{$\Delta 9/+$} and *Scn8a* ^{$\nabla 3/+$} heterozygous mutants exhibit impaired motor performance on a rotarod. (A-C) The rotarod performance of WT and heterozygous littermates from each line significantly improved over the 4-day testing period. Data is presented as the average of three trials per day of testing. **(A-B)** *Scn8a* ^{$\Delta 9/+$} and *Scn8a* ^{$\nabla 3/+$} mice exhibit significantly impaired performance on the rotarod over time relative to WT littermates by Day 4 of testing. **(C)** *Scn8a* ^{$\Delta 35/+$} mutants demonstrate comparable latency to fall from the rotarod over time relative to WT littermates. Asterisks (*) denote statistical comparisons between genotypes on the same day of testing, while pound signs (#) denote statistical comparisons between Day 1 and Day 4 of testing within a genotype. Sample sizes per line, where *m* denotes a mutant allele: $\Delta 9$ (WT: *n* = 15, *m/+*: *n* = 15, from nine litters), $\nabla 3$ (WT: *n* = 10, *m/+*: *n* = 16, from nine litters), $\Delta 35$ (WT: *n* = 18, *m/+*: *n* = 13, from 13 litters). **(D-F)** *Scn8a* ^{$\Delta 9/+$} and *Scn8a* ^{$\Delta 35/+$} mice exhibit comparable grip strength to WT littermates, whereas *Scn8a* ^{$\nabla 3/+$} mutants demonstrate significantly reduced grip strength (GF, general force units). Asterisks (*) denote statistical comparisons between genotypes. Sample sizes per line: $\Delta 9$ (WT: *n* = 12, *m/+*: *n* = 13, from seven litters), $\nabla 3$ (WT: *n* = 8, *m/+*: *n* = 12, from six litters), $\Delta 35$ (WT: *n* = 18, *m/+*: *n* = 12, from 12 litters). Mean \pm SEM. */#*P* < .05, ***P* < .01, ****P* < .001, ****/#*P* < .0001

4.4.8 $\Delta 9$ and $\nabla 3$ homozygous mutants exhibit reduced nerve conduction velocity

Consistent with the role of $\text{Na}_v1.6$ at the nodes of Ranvier, previous studies have demonstrated that *Scn8a* mutants with reduced $\text{Na}_v1.6$ activity also exhibit decreased nerve conduction velocity (75,288,304). We measured sciatic nerve conduction velocity in N4F1 mice from each line to examine whether nerve conduction is also altered by each mutation. Due to the premature lethality observed in homozygous mutants, nerve conduction was assessed in mice aged P14-17. Nerve conduction velocity was significantly reduced in both *Scn8a* ^{$\Delta 9/\Delta 9$} and *Scn8a* ^{$\nabla 3/\nabla 3$} mice relative to their WT and heterozygous mutant littermates (**Fig. 4.8A-B**; $\Delta 9$: $F_{2,15} = 10.19/P = .0016$; $\nabla 3$: $F_{2,11} = 0.3621/P = .0008$). There were no significant differences in nerve conduction velocity between genotypes within the $\Delta 35$ line, consistent with age-matched mice from the *Scn8a*-null *med* line, suggesting that *Scn8a*-null mice within this age range do not exhibit deficits in nerve conduction velocity (**Fig. 4.8C-D**; $\Delta 35$: $F_{2,15} = 1.452/P = .2652$; *med*: $F_{2,14} = 1.521/P = .2525$).

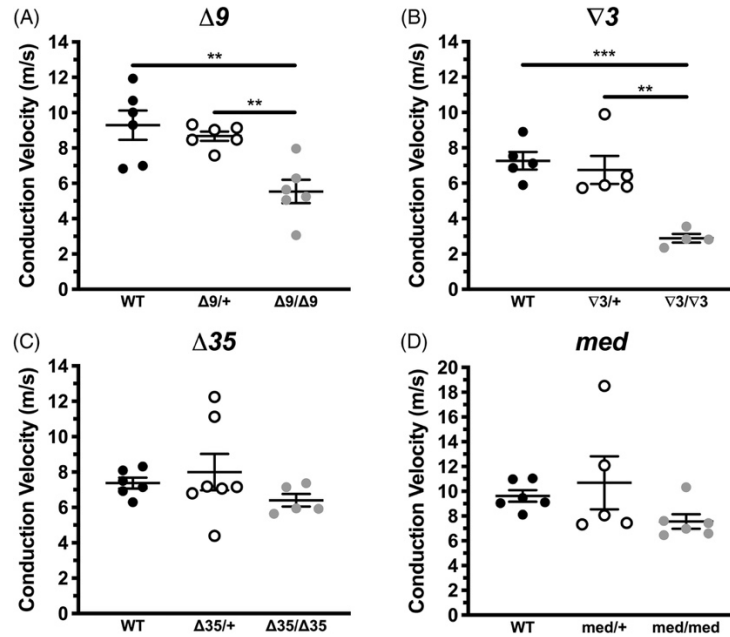


Figure 4.8. *Scn8a* ^{$\Delta 9/\Delta 9$} and *Scn8a* ^{$\nabla 3/\nabla 3$} homozygous mutants exhibit reduced nerve conduction velocity. (A-B) *Scn8a* ^{$\Delta 9/\Delta 9$} and *Scn8a* ^{$\nabla 3/\nabla 3$} homozygous mutants exhibit a significant reduction in sciatic nerve conduction velocity relative to their WT and heterozygous littermates. (C-D) There are no significant differences in conduction velocity between genotypes within the *Scn8a*-null $\Delta 35$ or *med* lines. Sample sizes per line, where *m* denotes a mutant allele: $\Delta 9$ (WT: n = 6, *m*/+: n = 6, *m*/*m*: n = 6, from nine litters), $\nabla 3$ (WT: n = 5, *m*/+: n = 5, *m*/*m*: n = 4, from five litters), $\Delta 35$ (WT: n = 6, *m*/+: n = 7, *m*/*m*: n = 5, from six litters), *med* (WT: n = 6, *m*/+: n = 5, *m*/*m*: n = 6, from four litters). Mean \pm SEM. *P* < .01, ****P* < .001**

4.5 Discussion

We previously showed that the hypomorphic *med-jo* and null *med Scn8a* alleles confer increased seizure resistance, and that shRNA-mediated knockdown of *Scn8a* in the hippocampus prevents the development of spontaneous seizures in a mouse model of mesial temporal lobe epilepsy (72,287). Similarly, both the *Scn8a*^{Δ9/+} and *Scn8a*^{∇3/+} heterozygous mutants exhibit increased resistance to 6 Hz- and flurothyl-induced seizures, and *Scn8a*^{Δ9/+} mutants do not exhibit behavioral or absence seizures. Altogether, these results suggest that the Δ9 and ∇3 mutations reduce the activity of Na_v1.6 channels.

Mutations in *Scn8a* have also been associated with recessive movement disorders in mice, including ataxia, dystonia, tremor and abnormal gait (65,75,76,288-290). *Scn8a*^{Δ35/Δ35} mutants recapitulate the progressive hindlimb paralysis observed in *Scn8a*-null mice, whereas both the *Scn8a*^{Δ9/Δ9} and *Scn8a*^{∇3/∇3} homozygous mutants exhibit an unsteady, ataxic gait resulting in frequent loss of posture (53,289,300-303). Homozygous mutant mice from each line also exhibit premature lethality relative to their WT and heterozygous littermates. The cause of death appears secondary to these motor complications, as 15-20% of *Scn8a*^{Δ9/Δ9} homozygous mutants survive to adulthood without demonstrating improvement in their gait. De Repentigny et al reported that null *Scn8a*^{dmu/dmu} mice possess smaller hearts than WT littermates and exhibit labored breathing, while Noujaim et al noted that null *Scn8a*^{S21P/S21P} mutants exhibit abnormal electrocardiograph waveforms relative to WT littermates (303,305). These observations suggest that the increased mortality observed in *Scn8a* homozygous mutants may result from autonomic nervous system dysfunction, as a consequence of reduced Na_v1.6 activity.

In contrast to *Scn8a*^{Δ9/Δ9} mutants, all *Scn8a*^{∇3/∇3} mice die within the first 6 weeks of life, indicating that the *Scn8a*^{∇3/∇3} mutants are more severely affected. Unlike the Δ9 allele, which removes an arginine residue, the ∇3 allele introduces a negatively charged aspartate residue which could potentially interact with multiple cationic residues within the DIIS4 voltage sensor. Furthermore, the ∇3 allele has a mild effect on Na_v1.6 protein levels, indicating that the *Scn8a*^{∇3/∇3} mutants also exhibit reduced Na_v1.6 levels relative to WT littermates. This additional slight decrease in Na_v1.6 expression might increase the risk of the autonomic dysfunction in *Scn8a*^{∇3/∇3} mutants as previously reported for *Scn8a*-null mutants (303,305). However, both the Δ9 and ∇3 alleles partially rescue the *Scn8a*-null *med* phenotype in hemizygous mutants, indicating that these two alleles retain some residual activity and likely generate hypomorphic (rather than null) Na_v1.6 channels. It is also possible that the differences in motor phenotypes and survival rates between *Scn8a*^{Δ9/Δ9} and *Scn8a*^{∇3/∇3} mutants arise as a result of allele-specific neomorphic effects on channel activity. However, electrophysiological analysis will be required to identify possible differences in biophysical properties of Na_v1.6 channels from the two lines.

Interestingly, we observed reduced performance on the rotarod in heterozygous *Scn8a*^{Δ9/+} and *Scn8a*^{∇3/+} mutants compared to their respective WT littermates. Furthermore, *Scn8a*^{∇3/+} mutants also demonstrated reduced grip strength. Given that the heterozygous mutants are visually indistinguishable from their WT littermates, these results raise the possibility that *Scn8a*^{Δ9/+} and *Scn8a*^{∇3/+} mutants may exhibit additional distinct, albeit subtle, motor deficits. In contrast to Δ9 and ∇3 mice, the *Scn8a*^{Δ35/+} mutants exhibited normal grip strength and rotarod performance. Similarly, McKinney et al observed comparable rotarod performance between heterozygous-null *Scn8a*^{med-Tg/+} mutants and WT littermates (70). Despite

previous reports of mild cognitive and behavioral disabilities in heterozygous-null *Scn8a*^{med-Tg/+} and hypomorphic *Scn8a*^{9J/+} mutants, we saw no significant behavioral abnormalities in the *Scn8a*^{Δ9/+} or *Scn8a*^{∇3/+} mutants (70,288).

Strikingly, while *Scn8a*^{Δ35/+} mutants demonstrated an acoustic startle response similar to WT littermates, both *Scn8a*^{Δ9/+} and *Scn8a*^{∇3/+} heterozygous mutants exhibited significantly reduced acoustic startle. This phenotype is not due to hearing loss, given that *Scn8a*^{Δ9/+} and *Scn8a*^{∇3/+} mutants exhibit ABR thresholds and waveforms comparable to their WT littermates. A similar absence of acoustic startle was reported previously in another voltage-gated ion channel mutant, the *Cacng2* stargazer model of absence epilepsy (306). Consistent with the *Scn8a*^{Δ9/+} and *Scn8a*^{∇3/+} heterozygous mutants, homozygous stargazer mutants do not display a startle response above baseline to acoustic stimuli ranging from 90-120 dB (306). In line with our findings, the stargazer mutants also exhibit ABR thresholds and hearing comparable to control littermates (306,307). Abnormal morphology of vestibular sensory epithelia was observed in stargazer mutants, suggesting that impaired vestibular signal transduction may underlie the ablated acoustic startle response (306). This morphology is consistent with the extensive vestibular dysfunction observed in the stargazer mutants, including a failure to stay on a rotarod and impaired righting reflexes (306). However, the *Scn8a*^{Δ9/+} and *Scn8a*^{∇3/+} mutants demonstrate baseline rotarod performance similar to WT littermates and do not exhibit the hallmark circling or abnormal righting reflexes indicative of vestibular dysfunction (308). Therefore, further studies will be necessary to elucidate the specific mechanisms underlying the observed acoustic startle phenotypes in the *Scn8a*^{Δ9/+} and *Scn8a*^{∇3/+} mutants.

Given the important function of Nav1.6 at the nodes of Ranvier, it is unsurprising that reduced Nav1.6 activity has previously been linked to decreased nerve conduction velocity in the hypomorphic *Scn8a*^{9J/9J} and *Scn8a*^{medj/medj} homozygous mutants (20,75,288). Similarly, both *Scn8a*^{Δ9/Δ9} and *Scn8a*^{∇3/∇3} homozygous mutants exhibited a significant decrease in nerve conduction velocity, which suggests that impaired nerve conduction may partially contribute to the observed motor phenotypes. However, despite their progressive hindlimb paralysis, null *Scn8a*^{Δ35/Δ35} and *Scn8a*^{med/med} homozygous mutants did not exhibit altered conduction velocity. Similarly, Angaut-Petit et al previously reported that conduction velocity is comparable between *Scn8a*^{med/med} mutants and phenotypic control mice (either WT or heterozygous littermates) from P3 to 16 (304). To avoid potential confounds from weight loss and muscle atrophy, we only tested N4F1 Δ35 and *med* mice aged P14 to 17. Angaut-Petit et al noted a significant decrease in conduction velocity in *Scn8a*^{med/med} mutants aged P17 to 23, the time frame during which most *Scn8a*-null mice die (304). It is possible, then, that *Scn8a*-null mice exhibit normal nerve conduction within the first 2 to 3 weeks of life. However, as *Scn8a*-null mice age, nerve conduction could steadily worsen, in part due to abnormal expansion of the nodes of Ranvier and decreased paranodal myelination (75,309).

Notably, homozygous mutant mice expressing the hypomorphic Δ9 and ∇3 alleles exhibited deficits in nerve conduction velocity, whereas age-matched null Δ35 mutants were comparable to WT littermates. This result raises the possibility that loss of *Scn8a* expression in Δ35 mutants may trigger compensatory upregulation of other VGSCs at the nodes of Ranvier, thereby maintaining normal nerve conduction. In contrast to the Δ35 mutation, our results indicate that the Δ9 and ∇3 mutations do not result in null alleles. Therefore, we hypothesize that these two hypomorphic mutations may not induce changes in expression of paralogs VGSC

genes, such as *Scn1a* or *Scn2a*. Without this increase in levels of WT VGSCs at the nodes of Ranvier, the *Scn8a*^{Δ9/Δ9} and *Scn8a*^{∇3/∇3} homozygous mutants would demonstrate impaired nerve conduction. Though additional Western blotting and immunostaining would be necessary to confirm this hypothesis, previous studies have demonstrated that loss of *Scn8a* expression leads to the compensatory recruitment of other VGSC proteins, particularly Na_v1.2 (encoded by *Scn2a*), to the mature nodes of Ranvier and axon initial segment (75,310,311). In further support of this hypothesis, Vega et al reported that Na_v1.2 protein levels are significantly upregulated in null *Scn8a*^{med-Tg/med-Tg} mutants relative to WT littermates (312).

With the recent discovery that VGSC proteins can dimerize, it is also possible that the hypomorphic Δ9 or ∇3 alleles might exert a dominant-negative effect on WT Na_v1.6 by forming mutant-WT heterodimers (9,313). For instance, mutant isoforms of the VGSC Na_v1.5 have been reported to exert a dominant-negative effect on sodium current via heterodimerization (313). Therefore, Na_v1.6 mutant-WT heterodimers may also exhibit biophysical properties that are distinct from a WT homodimer, thereby contributing to the motor deficits and impaired acoustic startle response we observed in the *Scn8a*^{Δ9/+} and *Scn8a*^{∇3/+} mutants. Given that Δ35 is a null allele, *Scn8a*^{Δ35/+} mutants will only be able to express homodimers of WT Na_v1.6, accounting for the similar motor and acoustic startle presentation between Δ35 mutants and WT littermates. We have previously demonstrated that a reduction in Na_v1.6 activity or expression increases seizure resistance (72,287,314). Therefore, we speculate that while *Scn8a*^{Δ35/+} mutants exhibit increased seizure resistance due to loss of *Scn8a* expression, heterodimerization may also contribute to the increased seizure resistance in *Scn8a*^{Δ9/+} and *Scn8a*^{∇3/+} mutants.

In summary, we have identified several phenotypes in mice expressing the hypomorphic *Scn8a* Δ9 and ∇3 alleles that were not observed in mice with the null Δ35 allele. In

particular, we found that mutants from the $\Delta 9$ and $\nabla 3$ lines exhibit impaired rotarod performance, decreased nerve conduction velocity, and a reduced acoustic startle response (**Table C3**). While further work is required to address the mechanisms underlying these phenotypic differences, our observations suggest that the clinical consequences of hypomorphic *SCN8A* mutations may differ from null *SCN8A* alleles.

4.6 Acknowledgments

The research reported in this chapter was supported by the National Institute of Neurological Disorders and Stroke of the National Institutes of Health under award numbers R01NS090319 (A.E.) and F31NS110193 (G.A.S.I.). Further funding was provided by predoctoral training grant appointments T32GM008490 (G.A.S.I., K.M.B.), T32NS007480 (G.A.S.I.) and the American Epilepsy Society (J.C.W.). This study was supported in part by the Mouse Transgenic and Gene Targeting Core, which is subsidized by the School of Medicine, Emory University and is one of the Emory Integrated Core Facilities. Additional support for the Mouse Transgenic and Gene Targeting Core was provided by the Georgia Clinical & Translational Science Alliance of the National Institutes of Health (award number UL1TR002378). Editorial assistance was provided by Cheryl T. Strauss.

CHAPTER 5: Conclusions and future directions

5.1 Summary of dissertation research

Given the relevance of *SCN1A* and *SCN8A* to normal neuronal excitability and human disease, the overarching goals of my dissertation research were: (1) to identify genetic elements or pathways contributing to transcriptional regulation of *SCN1A* and (2) to characterize the phenotypic impacts of novel *Scn8a* mutations.

Our initial approach to identify putative functional genomic elements (FGEs) in *SCN1A* utilized publicly available neuronal open chromatin and ChIP-seq data sets (**Chapter 2**). However, none of these FGEs individually evoked a reproducible or robust increase in luciferase reporter activity. While this strategy relied on chromatin accessibility in immortalized neuroblastoma lines or heterogeneous brain regions to identify putative FGEs, *SCN1A* is predominantly expressed in GABAergic interneurons (GINs) (19,22-27). Therefore, an alternative strategy to identify FGEs in *SCN1A* would be to evaluate chromatin accessibility in an enriched population of GINs (**Chapter 3**). We therefore performed ATAC-seq and mRNA-seq at three time points across GIN development from human iPSCs, with the aim of identifying differentially-accessible regions (DARs) of chromatin that were associated with differentially-expressed genes (DEGs). Though there were no DARs within the *SCN1A* locus, we did identify several DARs associated with altered expression of genes crucial for GIN maturation and function (**Table 5.1**). Furthermore, we identified several novel genes that may play an important role in GIN function and, by extension, the pathogenesis of disorders associated with altered GIN function, such as schizophrenia.

Another component of my dissertation research focused on *SCN8A*, which was recently identified as an important cause of severe, childhood-onset epilepsy (31). In the process of

developing a novel mouse model of *SCN8A*-derived epilepsy, we generated three additional mouse lines with varying degrees of $\text{Na}_v1.6$ activity reduction: $\Delta 9$, $\nabla 3$, and $\Delta 35$ (**Chapter 4**). Our results suggest that hypomorphic *Scn8a* alleles ($\Delta 9$ and $\nabla 3$) may exert effects on $\text{Na}_v1.6$ function that are distinct from null alleles ($\Delta 35$ and *med*), potentially due to aberrant channel heterodimerization or differences in compensatory expression of paralogous voltage-gated sodium channel (VGSC) genes (315).

Altogether, the results presented in this dissertation expand our knowledge of regulation of *SCN1A* expression, the pathways contributing toward a GIN cell fate, and $\text{Na}_v1.6$ function. In the following sections, I will further discuss the implications and future directions of this research.

5.2 The state of *SCN1A* transcriptional regulation

5.2.1 Endogenous regulation of *SCN1A* mRNA levels

There are several pieces of evidence that suggest neuronal expression of *SCN1A* is both developmentally and spatially regulated. *Scn1a* mRNA levels gradually increase throughout gestation, and peak between the second and third postnatal weeks of life in mice (16,18). Though *SCN1A* is widely expressed throughout the brain, $\text{Na}_v1.1$ levels are higher in inhibitory GABAergic neurons compared to excitatory cells (16,18,23). Furthermore, conditional deletion of *Scn1a* in GINs, but not pyramidal neurons, is sufficient to evoke spontaneous seizures in mice (26). Previous work has identified several genetic elements that likely contribute to tight control of *SCN1A* expression, including three alternative promoters, a transcriptional silencer element,

and a GAPDH-binding site in the 3'-UTR that promotes degradation of the mature *SCN1A* transcript (96,106,110).

Given that *SCN1A* possesses at least one transcriptional silencer element, we believed it may contain additional genetic regulatory elements that contribute to its observed temporospatial expression patterns. However, we did not identify any genetic elements with a robust effect on reporter activity (**Chapter 2**). Our initial approach was limited by the fact that available data sets were derived from immortalized cell lines or heterogeneous brain regions. Immortalized neuroblastoma lines are useful *in vitro* models of human neurobiology, though they lack many of the electrophysiological and molecular characteristics of primary neurons (316-318). In contrast, brain tissue contains primary neurons as well as non-neuronal cell types, such as glia. These tissue samples are highly heterogeneous, and may be comprised of cell types that weakly express *SCN1A*. Altogether, epigenomic analysis of either immortalized cell lines or post-mortem tissue may not detect regions of open chromatin that drive the robust *SCN1A* expression specifically observed in GINs.

To assess chromatin accessibility and *SCN1A* expression in more relevant cell types, we performed mRNA-seq and ATAC-seq at three time points across differentiation of human iPSC-derived neural progenitors to late-stage GINs (**Chapter 3**). Though these samples were also heterogeneous, representing at least five GIN subtypes, they were still enriched for GINs that strongly express *SCN1A* by 78 days post-differentiation (D78). However, we did not observe any DARs in the *SCN1A* locus over the course of GIN differentiation (**Table 5.1**). When considering discrete peaks of enriched ATAC-seq signal at D78 GINs, we identified eight regions of open chromatin within the *SCN1A* locus, four of which overlap with FGEs reported in **Chapter 2**: FGE9, 10, 13, and 28 (**Table 5.1**). Though Peak 6 / FGE10 corresponds to the *SCN1A* 1B

promoter, none of the remaining FGEs elicited a significant change in reporter activity in a dual luciferase reporter assay (**Fig. 2.2**). Given that transcriptional enhancer elements have previously been identified up to 1 Mb from their target promoter, it is possible that ATAC-seq peaks outside of the *SCN1A* locus, proximal to the seven genes neighboring *SCN1A* on chromosome 2, may also represent candidate FGEs (319). Upon reviewing ATAC-seq data from D78 GINs, we identified 86 peaks within 1 Mb of the *SCN1A* 1B promoter, five of which corresponded to DARs with increased accessibility over differentiation: three associated with *CSRNP3* (two intergenic, one intronic), and two associated with *SCN7A* (both intergenic; **Fig. 5.1**). Only one DAR, in *SCN2A* intron 21, exhibited a significant decrease in accessibility by D78 (**Fig. 5.1**). Considering that only three of the genes within this interval are differentially expressed over GIN differentiation (*SCN1A*, *SCN2A*, and *CSRNP3*), a subset of the remaining peaks proximal to the five genes with constant expression across differentiation (*GALNT3*, *TTC21B*, *SCN9A*, *SCN7A*, and *XIRP2*) may represent additional FGEs that contribute to *SCN1A* expression (**Fig. 5.1**).

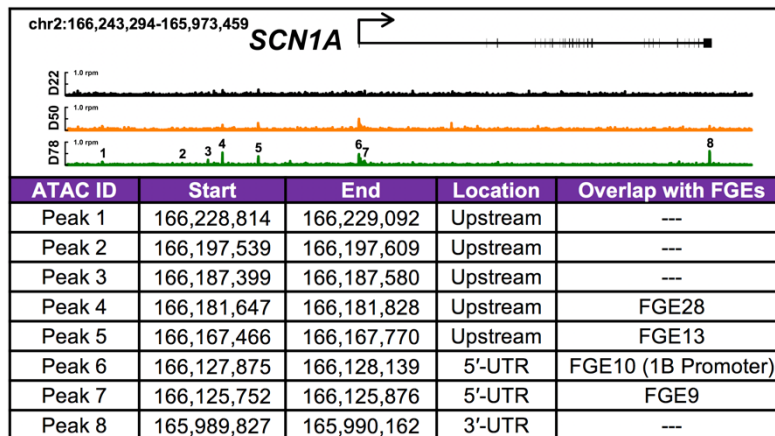


Table 5.1. There are no differentially accessible regions of chromatin within the *SCN1A* locus across GIN differentiation. We identified eight ATAC-seq peaks in the *SCN1A* locus at D78. None of these peaks are differentially accessible across GIN differentiation, though peaks 4-7 overlap with FGEs reported in **Chapter 2**. Genome plots represent ATAC-seq data from HC1 cells (rpm: reads per million), and coordinates refer to the hg38 annotation of the human genome (Dec. 2013) (246).

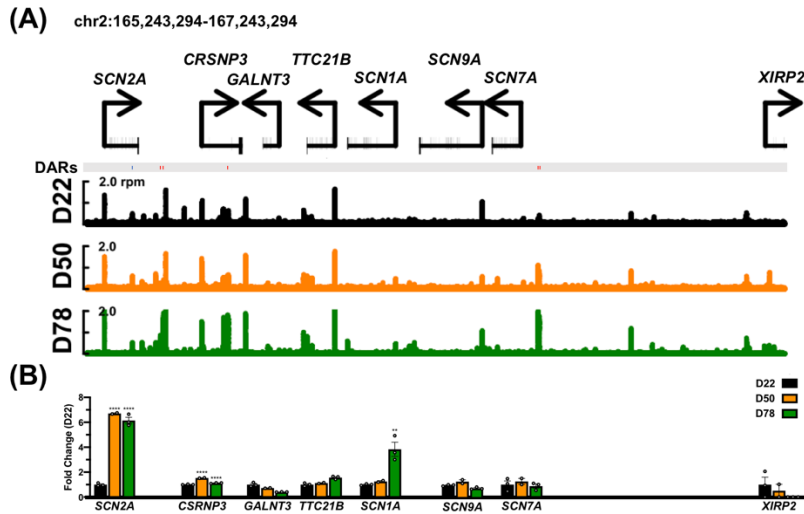


Figure 5.1. Comparison of differential gene expression and chromatin accessibility within 1 Mb of the *SCN1A* locus across GIN differentiation. (A) There are 86 ATAC-seq peaks at D78 in the interval spanning ± 1 Mb from the 1B *SCN1A* promoter, six of which exhibit differential accessibility across GIN differentiation. Genome plots represent ATAC-seq data from HC1 cells (rpm: reads per million), and coordinates refer to the hg38 annotation of the human genome (Dec. 2013) (246). DARS with increased accessibility by D78 are depicted in red, while DARS with decreased accessibility are blue. (B) Only *SCN1A*, *CSRNP3*, and *SCN2A* are differentially expressed between D22 and D78 (mean \pm SEM, $n=2-3$). One-way ANOVA with Tukey's multiple comparisons. Asterisks denote statistical significance relative to D22 (** $p<0.01$, **** $p<0.0001$).

In **Chapter 2**, we presented evidence that several genetic elements (specifically, FGE2A and FGE26) may jointly contribute toward *SCN1A* transcription. However, it is important to note several limitations of this finding. First, luciferase reporter assays do not model the endogenous organization of the *SCN1A* locus. Therefore, it is unclear whether FGE2A and FGE26 interact *in vivo* to promote elevated *SCN1A* transcription, or if our result was an artifact of cloning these elements into an exogenous vector in close proximity. Neither FGE2A nor FGE26 overlapped with any peaks of open chromatin signal in the late-stage, D78 GINs. Furthermore, none of the ATAC-seq peaks identified in D78 GINs overlapped with any of the FGEs that elicited a significant increase in reporter activity: FGE2A, 17, 23, or 26. Considering these results, the

simplest conclusion is that none of the identified putative FGEs contribute toward regulation of *SCN1A* transcription.

Though *SCN1A* is broadly expressed in GABAergic neurons, it is most associated with the function of fast-spiking parvalbumin-positive (PV⁺) GINs (26,85). However, at D78, only ~15% of cells were PV⁺ (**Fig. 4.1**). Therefore, while our data represents an enriched pool of GABAergic cells, it does not specifically reflect the specific epigenomic landscape of PV⁺ GINs. In the future, it may be necessary to isolate a more homogeneous pool of PV⁺ GINs in order to assess putative transcriptional enhancer elements. Differential expression of *SCN1A* could also be driven by alternative promoter usage among individual cell types or brain regions. Interestingly, only the 1B promoter exhibited ATAC-seq signal in D78 GINs (**Table 5.1**). Given that the 1B element is the strongest out of the three *SCN1A* promoters, it is possible that robust *SCN1A* expression in GINs may partially be a result of heightened 1B promoter activity (95,96).

5.2.2 dCas9-based strategies to elevate *SCN1A* expression

Despite the lack of known transcriptional enhancers of *SCN1A* expression, the deactivated Cas9 (dCas9) endonuclease offers a novel method to modulate *SCN1A* transcription. While dCas9 does not cleave DNA, it can be fused to transcriptional activators or silencers in order to modulate endogenous expression of target genes (320-324). For instance, dCas9 fused to four repeats of the VP16 transcriptional activation domain (dCas9^{VP64}) can significantly increase expression when targeted to a gene's promoter using a complementary guide RNA (gRNA) (321,324). A major benefit of this approach is that gene activation can be limited to specific cell types or at particular stages of development, as determined by the promoter driving dCas9 or gRNA expression. While dCas9^{VP64} requires multiple gRNAs that simultaneously tile several

activators across a promoter or enhancer to robustly increase expression, there are several variants of this technique that require only one gRNA, such as dCas9^{VP160} or dCas9^{SAM} (321,323,324). dCas9^{VP160} fuses dCas9 to ten repeats of the VP16 activation domain, while dCas9^{SAM} links a dCas9^{VP64}-gRNA complex to the p65 and HSF1 transcriptional activation domains (321,324). dCas9^{VP160} has already been utilized to successfully elevate *Scn1a* expression in a mouse model of Dravet syndrome (134). By injecting lentiviral vectors encoding dCas9^{VP160} and a gRNA complementary to the 1B *SCN1A* promoter, Colasante et al. were able to selectively increase *Scn1a* mRNA levels in primary hippocampal neurons (134). Importantly, the dCas9^{VP160} construct did not influence expression of paralogous VGSC genes (134). Furthermore, *Scn1a*^{+/-} mice injected with Cas9^{VP160} exhibited a significant increase in the excitability of cortical GINs, along with reduced seizure frequency and severity (134).

5.2.3 The shift towards single-cell analyses

Though our protocol generated GINs with 81-85% efficiency, the resultant pool of cells was still highly heterogeneous, consisting of at least five GIN subtypes. The remaining 10-15% of cells likely adopt a dopaminergic or glutamatergic fate, which may complicate efforts to definitively identify pathways specific to GINs. Ideally, we would only perform ATAC-seq and mRNA-seq on a population of cells enriched for a specific GIN subtype marker, such as parvalbumin or somatostatin. While techniques such as fluorescence-activated cell sorting and immunopanning are broadly useful in isolating individual cell types, they rely on antibodies that recognize extracellular epitopes of membrane-bound proteins. Therefore, these techniques cannot be used to enrich for GIN subtypes that are defined by intracellular calcium binding proteins and neuropeptides.

An alternative method to control for the heterogeneity of a cell population would be to use single cell (sc), rather than bulk, mRNA-seq or ATAC-seq. scRNA-seq in particular has been widely adopted as a tool to identify subpopulations of cells from iPSC-derived organoids or homogenized tissue, but is still limited by its resolution (178,189,325). There is a finite amount of RNA or DNA that can be amplified and processed from a single cell, contributing toward extensive variability between samples, even among the same cell types (325,326). Given the continuing difficulties in distinguishing between technical noise and inherent variance for weakly expressed genes, such as lncRNAs, single cell approaches are not ideal for comparing subtle changes in gene expression or accessibility across development.

5.3 Assessment of novel targets for GABAergic interneuron function

Though our approach in **Chapter 3** did not identify any robust FGEs in *SCN1A*, the mRNA-seq and ATAC-seq data we generated represent an important resource for identifying novel genes involved in GIN development and function. Given that *SCN1A* dysfunction broadly impairs neuronal inhibition, the restoration of GIN activity is predicted to be therapeutic in several neurological disorders.

5.3.1 Putative genetic regulatory elements in genes relevant to GABAergic function

One clear future direction of our work would be to examine whether DARs identified in GABAergic DEGs such as *SLC6A1* or *B3GAT2* functionally contribute toward gene expression. While we initially utilized a luciferase reporter assay to evaluate putative FGEs, dCas9^{VP64} could also be applied to endogenously validate putative enhancers, as localizing transcriptional activators to these elements will be predicted to increase gene expression (320). Furthermore, it

is unclear whether all the predicted transcription factor (TF) binding motifs enriched in DARs are physically occupied. An important next step would be to perform ChIP-seq for a subset of these TFs, in order to validate our findings and construct a more focused regulatory network. Given their previous associations with cognitive impairment and schizophrenia, respectively, our first steps would be to assess BCL11A and KLF5 binding in D78 GINs.

5.3.2 Examining the contribution of *CPLX2* and *TRPC4* to neurological disease

Among the genes with differential expression between developing GINs and schizophrenia patients, *CPLX2* and *TRPC4* exhibited the most compelling links to neurological disease. Specifically, we observed a significant increase in *CPLX2* expression by D78 in GINs, while Fromer et al. reported a significant decrease in *CPLX2* expression in schizophrenia patients (218). *Cplx2*-null mice also exhibit cognitive deficits following exposure to a stressor, suggesting that loss of *Cplx2* may predispose animals to schizophrenic-like phenotypes (276,277). Given that previous studies only examined spatial memory in *Cplx2*-null mice, it would be useful to assess whether these mutants replicate other behavioral abnormalities observed in schizophrenia patients, such as elevated anxiety or reduced sociability. Furthermore, it would be interesting to examine whether GIN-specific knockout of *Cplx2* is sufficient to induce behavioral abnormalities in mice following exposure to a stressor. Interestingly, a meta-analysis of 12 microarray studies found that *CPLX2* was consistently downregulated in the brains of epilepsy patients, suggesting that *CPLX2* may also be associated with seizure phenotypes (327). To explore the broader contribution of *CPLX2* to neurological disease, it would be interesting to examine whether *CPLX2*-null mice also exhibit altered seizure phenotypes.

In contrast to *CPLX2*, we observed a significant decrease in *TRPC4* expression by D78 in GINs, whereas Fromer et al. reported a significant increase in *TRPC4* expression in schizophrenia patients (218). Interestingly, *Trpc4*-null rodents exhibit reduced anxiety and addictive behavior, and *Trpc1/Trpc4* double knockout mice demonstrate reduced mortality in response to pilocarpine-induced seizures, suggesting that altered *TRPC4* expression may be neuroprotective (279,280,328). One future direction of our research, then, would be to observe whether acute knockdown of *Trpc4* also affects behavioral and seizure phenotypes. Another line of research would be to explore how increased *TRPC4* activity alters behavior or seizure susceptibility, given that elevated *TRPC4* expression is observed in schizophrenia patients (218). While several *TRPC4* agonists have been identified, these compounds also target or antagonize other ion channels, or exhibit variable efficacy depending on the composition of the *TRPC4* tetramer (329-332). For instance, englerin A is a partial agonist of *TRPC4*, though it also activates *TRPC5* and antagonizes *TRPA1*, *TRPV3/V4*, and *TRPM8* (330,331). Another agonist, BTB, activates the *TRPC1:TRPC5* and *TRPC4:TRPC5* heteromers, but has no effect on *TRPC1:TRPC4* heteromers or monomeric *TRPC4* (329). A more direct approach, then, would be to utilize a viral vector or dCas9^{VP160} construct to promote *TRPC4* expression.

5.4 The phenotypic spectrum of loss-of-function mutations in *SCN8A*

5.4.1 Examining the phenotypic impact of hypomorphic and null *SCN8A* alleles

Most of the discussion at this point has been guided by the contribution of *SCN1A* to proper GIN function. However, we also observed several deficits in mice expressing the hypomorphic *Scn8a* $\Delta 9$ and $\nabla 3$ alleles, but not the null $\Delta 35$ allele (**Chapter 4**). We proposed two mechanisms to

explain these phenotypes: (1) that complete loss of *Scn8a* expression may trigger compensatory upregulation of other VGSCs at the nodes of Ranvier and axon initial segment (AIS), and (2) that the hypomorphic $\Delta 9$ or $\nabla 3$ alleles might exert a dominant-negative effect on WT Na_v1.6 by forming mutant-WT heterodimers.

There are several experiments that could be performed to validate the first mechanism. While we initially performed Western blotting for Na_v1.6 in whole-brain protein isolates from *Scn8a* ^{$\Delta 9/\Delta 9$} , *Scn8a* ^{$\nabla 3/\nabla 3$} , or *Scn8a* ^{$\Delta 35/\Delta 35$} homozygous mutant mice, we could also probe for altered expression of the paralogous Na_v1.1 and Na_v1.2 VGSC proteins, relative to wild-type (WT) littermates. Alternatively, there could be differential localization, rather than expression, of paralogous VGSCs, meaning that Na_v1.1 or Na_v1.2 could be preferentially recruited to the axon initial segment (AIS) or nodes of Ranvier in the absence of Na_v1.6. To assess this possibility, we could examine the colocalization of Na_v1.1, Na_v1.2, or Na_v1.6 with markers of the AIS (ankyrin-G) or nodes of Ranvier (Caspr) in primary neurons from *Scn8a* ^{$\Delta 9/\Delta 9$} , *Scn8a* ^{$\nabla 3/\nabla 3$} , or *Scn8a* ^{$\Delta 35/\Delta 35$} homozygous mutant mice (73,312).

It is less straightforward, however, to examine the validity of the second proposed mechanism, or whether mutant-WT Na_v1.6 heterodimers exhibit unique electrophysiological properties. Clatot et al. previously used whole-cell patch clamp recordings to demonstrate that mutant Na_v1.5 channels can exhibit a dominant-negative effect on cardiac sodium channel current (10). While whole-cell patch-clamp could also reveal whether *Scn8a* ^{$\Delta 9/+$} , *Scn8a* ^{$\nabla 3/+$} , or *Scn8a* ^{$\Delta 35/+$} heterozygous mutants exhibit a total reduction in Na_v1.6-driven sodium current, it would not resolve specific changes in the biophysical properties of mutant-WT Na_v1.6 heterodimers. An alternative approach, then, would be to perform single channel patch clamp, in order to examine activity from individual Na_v1.6 complexes. However, it still would not be

possible to verify whether the channel complexes were homodimeric (WT-WT or mutant-mutant) or heterodimeric (mutant-WT).

5.4.2 Future characterization of the *Scn8a* $\Delta 9$ and $\nabla 3$ alleles

There are several remaining questions surrounding the phenotypic impact of the *Scn8a* $\Delta 9$ and $\nabla 3$ alleles. First, while our results indicate that both alleles are both hypomorphic, it is unclear how each allele alters the biophysical properties of Na_v1.6 channel protein, or whether one allele is more functional than the other. In contrast to examining whether Na_v1.6 heterodimers exhibit unique channel properties, it is markedly simpler to assess sodium current dynamics in hippocampal neurons isolated from *Scn8a* ^{$\Delta 9/\Delta 9$} or *Scn8a* ^{$\nabla 3/\nabla 3$} homozygous mutants. Furthermore, while we proposed that the $\nabla 3$ allele may be more weakly expressed than WT *Scn8a*, this result may also reflect that our protein extraction protocol enriches for membrane-bound proteins through an ultracentrifugation step. While the $\nabla 3$ allele is not predicted to alter the structure of the Na_v1.6 channel protein, the introduction of the negatively charged aspartate residue may impede integration of the channel in the plasma membrane. Therefore, it may be worthwhile to examine if surface expression of $\Delta 9$ and $\nabla 3$ Na_v1.6 are altered, relative to WT.

5.4.3 The contribution of Na_v1.6 to the acoustic startle response and hearing

One of the most striking phenotypes observed among the three *Scn8a* mutant lines was that heterozygous *Scn8a* ^{$\Delta 9/+$} and *Scn8a* ^{$\nabla 3/+$} mutants lacked an acoustic startle, whereas *Scn8a* ^{$\Delta 35/+$} mutants exhibited a startle response that was comparable to WT littermates (315). This phenotype was not due to hearing loss, as heterozygous mutants from each line exhibited comparable acoustic brainstem response (ABR) to their respective WT littermates (315). One

possibility is that the ablated acoustic startle is linked to altered activity of the dorsal cochlear nucleus, which is the terminal destination of the auditory nerve (333,334). Chen et al. reported that the hypomorphic *Scn8a*^{med-j/med-j} and *Scn8a*^{med-jo/med-jo} mutants exhibited significantly reduced spontaneous bursting activity in the dorsal cochlear nucleus relative to age-matched WT animals (335). While 51% of neurons from WT animals exhibited bursting activity, only 7% of neurons from *Scn8a*^{med-j/med-j} and 0% from *Scn8a*^{med-jo/med-jo} mutants demonstrated bursting (335). In spite of altered bursting patterns, *Scn8a*^{med-j/med-j} homozygous mutants were previously confirmed to have comparable ABR thresholds to WT littermates, though it is unclear whether *med-j* or *med-jo* mutant mice exhibit altered acoustic startle (336). Given that elevated spontaneous activity in the dorsal cochlear nucleus is associated with tinnitus, or a persistent ringing in ears, reduced bursting may impair auditory responses (334,335,337). Altogether, it would be interesting to examine bursting patterns in the dorsal cochlear nucleus of $\Delta 9$, $\Delta 3$, or $\Delta 35$ mutant mice, to compare whether hypomorphic or null animals exhibit reduced activity relative to WT littermates.

5.5 Conclusions

The studies described in this dissertation contribute toward two ongoing research goals: (1) to provide a more comprehensive analysis of *SCN1A* transcriptional regulation, especially in GINs, and (2) deepen our understanding of how Na_v1.6 mutations effect diverse clinical phenotypes. Furthermore, the mRNA-seq and ATAC-seq data reported in **Chapter 3** represent a valuable resource for examining pathways related to human GIN differentiation, as well as novel targets for the treatment of GIN-derived disorders. Altogether, these studies may contribute to improved development of future therapeutic strategies in patients with *SCN1A*- or *SCN8A*-derived disease.

REFERENCES

1. Catterall, W.A. (2014) Structure and function of voltage-gated sodium channels at atomic resolution. *Experimental physiology*, **99**, 35-51.
 2. Meisler, M.H. and Kearney, J.A. (2005) Sodium channel mutations in epilepsy and other neurological disorders. *J Clin Invest*, **115**, 2010-2017.
 3. Yu, F.H. and Catterall, W.A. (2003) Overview of the voltage-gated sodium channel family. *Genome biology*, **4**, 207.
 4. Shen, H., Zhou, Q., Pan, X., Li, Z., Wu, J. and Yan, N. (2017) Structure of a eukaryotic voltage-gated sodium channel at near-atomic resolution. *Science (New York, N.Y.)*, **355**.
 5. Bean, B.P. (2007) The action potential in mammalian central neurons. *Nature reviews. Neuroscience*, **8**, 451-465.
 6. Hodgkin, A.L. and Huxley, A.F. (1952) A quantitative description of membrane current and its application to conduction and excitation in nerve. *The Journal of physiology*, **117**, 500-544.
 7. McCormick, D.A. (2014) In Byrne, J. H., Heidelberger, R. and Waxham, M. N. (eds.), *From Molecules to Networks: An Introduction to Cellular and Molecular Neuroscience*. 3 ed. Elsevier Academic Press, pp. 351-376.
 8. Mantegazza, M. and Catterall, W.A. (2012) In th, Noebels, J. L., Avoli, M., Rogawski, M. A., Olsen, R. W. and Delgado-Escueta, A. V. (eds.), *Jasper's Basic Mechanisms of the Epilepsies*. National Center for Biotechnology Information (US)
- Michael A Rogawski, Antonio V Delgado-Escueta, Jeffrey L Noebels, Massimo Avoli and Richard W Olsen., Bethesda (MD).
9. Clatot, J., Hoshi, M., Wan, X., Liu, H., Jain, A., Shinlapawittayatorn, K., Marionneau, C., Ficker, E., Ha, T. and Deschenes, I. (2017) Voltage-gated sodium channels assemble and gate as dimers. *Nature communications*, **8**, 2077.
 10. Clatot, J., Zheng, Y., Girardeau, A., Liu, H., Laurita, K.R., Marionneau, C. and Deschenes, I. (2018) Mutant voltage-gated Na(+) channels can exert a dominant negative effect through coupled gating. *American journal of physiology. Heart and circulatory physiology*, **315**, H1250-h1257.
 11. O'Malley, H.A. and Isom, L.L. (2015) Sodium channel β subunits: emerging targets in channelopathies. *Annu Rev Physiol*, **77**, 481-504.
 12. Isom, L.L., Ragsdale, D.S., De Jongh, K.S., Westenbroek, R.E., Reber, B.F., Scheuer, T. and Catterall, W.A. (1995) Structure and function of the beta 2 subunit of brain sodium channels, a transmembrane glycoprotein with a CAM motif. *Cell*, **83**, 433-442.
 13. Morgan, K., Stevens, E.B., Shah, B., Cox, P.J., Dixon, A.K., Lee, K., Pinnock, R.D., Hughes, J., Richardson, P.J., Mizuguchi, K. *et al.* (2000) beta 3: an additional auxiliary subunit of the voltage-sensitive sodium channel that modulates channel gating with distinct kinetics. *Proceedings of the National Academy of Sciences of the United States of America*, **97**, 2308-2313.
 14. Escayg, A. and Goldin, A.L. (2010) Sodium channel SCN1A and epilepsy: mutations and mechanisms. *Epilepsia*, **51**, 1650-1658.
 15. Goldin, A.L. (2001) Resurgence of Sodium Channel Research. *Annual Review of Physiology*, **63**, 871-894.

16. Beckh, S., Noda, M., Lubbert, H. and Numa, S. (1989) Differential regulation of three sodium channel messenger RNAs in the rat central nervous system during development. *The EMBO journal*, **8**, 3611-3616.
17. Catterall, W.A., Kalume, F. and Oakley, J.C. (2010) Nav1.1 channels and epilepsy. *The Journal of physiology*, **588**, 1849-1859.
18. Felts, P.A., Yokoyama, S., Dib-Hajj, S., Black, J.A. and Waxman, S.G. (1997) Sodium channel alpha-subunit mRNAs I, II, III, NaG, Na6 and hNE (PN1): different expression patterns in developing rat nervous system. *Brain research. Molecular brain research*, **45**, 71-82.
19. Yu, F.H., Mantegazza, M., Westenbroek, R.E., Robbins, C.A., Kalume, F., Burton, K.A., Spain, W.J., McKnight, G.S., Scheuer, T. and Catterall, W.A. (2006) Reduced sodium current in GABAergic interneurons in a mouse model of severe myoclonic epilepsy in infancy. *Nat Neurosci*, **9**, 1142-1149.
20. Garcia, K.D., Sprunger, L.K., Meisler, M.H. and Beam, K.G. (1998) The sodium channel Scn8a is the major contributor to the postnatal developmental increase of sodium current density in spinal motoneurons. *J Neurosci*, **18**, 5234-5239.
21. Chen, K., Godfrey, D.A., Ilyas, O., Xu, J. and Preston, T.W. (2009) Cerebellum-related characteristics of Scn8a-mutant mice. *Cerebellum (London, England)*, **8**, 192-201.
22. Vacher, H., Mohapatra, D.P. and Trimmer, J.S. (2008) Localization and targeting of voltage-dependent ion channels in mammalian central neurons. *Physiological reviews*, **88**, 1407-1447.
23. Sun, Y., Pasca, S.P., Portmann, T., Goold, C., Worringer, K.A., Guan, W., Chan, K.C., Gai, H., Vogt, D., Chen, Y.J. *et al.* (2016) A deleterious Nav1.1 mutation selectively impairs telencephalic inhibitory neurons derived from Dravet Syndrome patients. *eLife*, **5**.
24. Ogiwara, I., Miyamoto, H., Morita, N., Atapour, N., Mazaki, E., Inoue, I., Takeuchi, T., Itohara, S., Yanagawa, Y., Obata, K. *et al.* (2007) Nav1.1 localizes to axons of parvalbumin-positive inhibitory interneurons: a circuit basis for epileptic seizures in mice carrying an Scn1a gene mutation. *J. Neurosci.*, **27**, 5903-5914.
25. Hedrich, U.B., Liautard, C., Kirschenbaum, D., Pofahl, M., Lavigne, J., Liu, Y., Theiss, S., Slotta, J., Escayg, A., Dihne, M. *et al.* (2014) Impaired action potential initiation in GABAergic interneurons causes hyperexcitable networks in an epileptic mouse model carrying a human Na(V)1.1 mutation. *J. Neurosci.*, **34**, 14874-14889.
26. Dutton, S.B., Makinson, C.D., Papale, L.A., Shankar, A., Balakrishnan, B., Nakazawa, K. and Escayg, A. (2013) Preferential inactivation of Scn1a in parvalbumin interneurons increases seizure susceptibility. *Neurobiol Dis*, **49**, 211-220.
27. Makinson, C.D., Tanaka, B.S., Sorokin, J.M., Wong, J.C., Christian, C.A., Goldin, A.L., Escayg, A. and Huguenard, J.R. (2017) Regulation of Thalamic and Cortical Network Synchrony by Scn8a. *Neuron*, **93**, 1165-1179.e1166.
28. Kalume, F., Yu, F.H., Westenbroek, R.E., Scheuer, T. and Catterall, W.A. (2007) Reduced sodium current in Purkinje neurons from Nav1.1 mutant mice: implications for ataxia in severe myoclonic epilepsy in infancy. *The Journal of neuroscience : the official journal of the Society for Neuroscience*, **27**, 11065-11074.
29. Bunton-Stasyshyn, R.K.A., Wagnon, J.L., Wengert, E.R., Barker, B.S., Faulkner, A., Wagley, P.K., Bhatia, K., Jones, J.M., Maniaci, M.R., Parent, J.M. *et al.* (2019)

- Prominent role of forebrain excitatory neurons in SCN8A encephalopathy. *Brain*, **142**, 362-375.
30. Cestèle, S., Schiavon, E., Rusconi, R., Franceschetti, S. and Mantegazza, M. (2013) Nonfunctional Na^V1.1 familial hemiplegic migraine mutant transformed into gain of function by partial rescue of folding defects. *Proceedings of the National Academy of Sciences*, **110**, 17546-17551.
 31. Veeramah, K.R., O'Brien, J.E., Meisler, M.H., Cheng, X., Dib-Hajj, S.D., Waxman, S.G., Talwar, D., Girirajan, S., Eichler, E.E., Restifo, L.L. *et al.* (2012) De novo pathogenic SCN8A mutation identified by whole-genome sequencing of a family quartet affected by infantile epileptic encephalopathy and SUDEP. *American journal of human genetics*, **90**, 502-510.
 32. Bender, A.C., Natola, H., Ndong, C., Holmes, G.L., Scott, R.C. and Lenck-Santini, P.P. (2013) Focal Scn1a knockdown induces cognitive impairment without seizures. *Neurobiol Dis*, **54**, 297-307.
 33. Fan, C., Wolking, S., Lehmann-Horn, F., Hedrich, U.B., Freilinger, T., Lerche, H., Borck, G., Kubisch, C. and Jurkat-Rott, K. (2016) Early-onset familial hemiplegic migraine due to a novel SCN1A mutation. *Cephalalgia : an international journal of headache*, **36**, 1238-1247.
 34. Shao, N., Zhang, H., Wang, X., Zhang, W., Yu, M. and Meng, H. (2018) Familial Hemiplegic Migraine Type 3 (FHM3) With an SCN1A Mutation in a Chinese Family: A Case Report. *Frontiers in Neurology*, **9**.
 35. Dhifallah, S., Lancaster, E., Merrill, S., Leroudier, N., Mantegazza, M. and Cestele, S. (2018) Gain of Function for the SCN1A/hNav1.1-L1670W Mutation Responsible for Familial Hemiplegic Migraine. *Frontiers in molecular neuroscience*, **11**, 232.
 36. Banerjee, P.N., Filippi, D. and Allen Hauser, W. (2009) The descriptive epidemiology of epilepsy-a review. *Epilepsy Res.*, **85**, 31-45.
 37. Escayg, A., MacDonald, B.T., Meisler, M.H., Baulac, S., Huberfeld, G., An-Gourfinkel, I., Brice, A., LeGuern, E., Moulard, B., Chaigne, D. *et al.* (2000) Mutations of SCN1A, encoding a neuronal sodium channel, in two families with GEFS+2. *Nat. Genet.*, **24**, 343-345.
 38. Landrum, M.J., Lee, J.M., Riley, G.R., Jang, W., Rubinstein, W.S., Church, D.M. and Maglott, D.R. (2014) ClinVar: public archive of relationships among sequence variation and human phenotype. *Nucleic acids research*, **42**, D980-985.
 39. Meng, H., Xu, H.Q., Yu, L., Lin, G.W., He, N., Su, T., Shi, Y.W., Li, B., Wang, J., Liu, X.R. *et al.* (2015) The SCN1A mutation database: updating information and analysis of the relationships among genotype, functional alteration, and phenotype. *Human mutation*, **36**, 573-580.
 40. Dutton, S.B.B., Dutt, K., Papale, L.A., Helmers, S., Goldin, A.L. and Escayg, A. (2017) Early-life febrile seizures worsen adult phenotypes in Scn1a mutants. *Experimental neurology*, **293**, 159-171.
 41. Villas, N., Meskis, M.A. and Goodliffe, S. (2017) Dravet syndrome: Characteristics, comorbidities, and caregiver concerns. *Epilepsy & behavior : E&B*, **74**, 81-86.
 42. de Lange, I.M., Gunning, B., Sonsma, A.C.M., van Gemert, L., van Kempen, M., Verbeek, N.E., Sinoo, C., Nicolai, J., Knoers, N., Koeleman, B.P.C. *et al.* (2019) Outcomes and comorbidities of SCN1A-related seizure disorders. *Epilepsy & behavior : E&B*, **90**, 252-259.

43. Johannesen, K.M., Gardella, E., Encinas, A.C., Lehesjoki, A.E., Linnankivi, T., Petersen, M.B., Lund, I.C.B., Blichfeldt, S., Miranda, M.J., Pal, D.K. *et al.* (2019) The spectrum of intermediate SCN8A-related epilepsy. *Epilepsia*, **60**, 830-844.
44. Larsen, J., Carvill, G.L., Gardella, E., Kluger, G., Schmiedel, G., Barisic, N., Depienne, C., Brilstra, E., Mang, Y., Nielsen, J.E. *et al.* (2015) The phenotypic spectrum of SCN8A encephalopathy. *Neurology*, **84**, 480-489.
45. Meisler, M.H., Helman, G., Hammer, M.F., Fureman, B.E., Gaillard, W.D., Goldin, A.L., Hirose, S., Ishii, A., Kroner, B.L., Lossin, C. *et al.* (2016) SCN8A encephalopathy: Research progress and prospects. *Epilepsia*, **57**, 1027-1035.
46. Zhang, Q., Li, J., Zhao, Y., Bao, X., Wei, L. and Wang, J. (2017) Gene mutation analysis of 175 Chinese patients with early-onset epileptic encephalopathy. *Clinical genetics*, **91**, 717-724.
47. Landrum, M.J., Lee, J.M., Benson, M., Brown, G.R., Chao, C., Chitipiralla, S., Gu, B., Hart, J., Hoffman, D., Jang, W. *et al.* (2018) ClinVar: improving access to variant interpretations and supporting evidence. *Nucleic Acids Res.*, **46**, D1062-d1067.
48. Stenson, P.D., Mort, M., Ball, E.V., Evans, K., Hayden, M., Heywood, S., Hussain, M., Phillips, A.D. and Cooper, D.N. (2017) The Human Gene Mutation Database: towards a comprehensive repository of inherited mutation data for medical research, genetic diagnosis and next-generation sequencing studies. *Hum. Genet.*, **136**, 665-677.
49. Gardella, E., Marini, C., Trivisano, M., Fitzgerald, M.P., Alber, M., Howell, K.B., Darra, F., Siliquini, S., Bolsterli, B.K., Masnada, S. *et al.* (2018) The phenotype of SCN8A developmental and epileptic encephalopathy. *Neurology*, **91**, e1112-e1124.
50. Lopez-Santiago, L.F., Yuan, Y., Wagnon, J.L., Hull, J.M., Frasier, C.R., O'Malley, H.A., Meisler, M.H. and Isom, L.L. (2017) Neuronal hyperexcitability in a mouse model of SCN8A epileptic encephalopathy. *Proceedings of the National Academy of Sciences of the United States of America*, **114**, 2383-2388.
51. Liu, Y., Schubert, J., Sonnenberg, L., Helbig, K.L., Hoei-Hansen, C.E., Koko, M., Rannap, M., Lauxmann, S., Huq, M., Schneider, M.C. *et al.* (2019) Neuronal mechanisms of mutations in SCN8A causing epilepsy or intellectual disability. *Brain*, **142**, 376-390.
52. Wagnon, J.L., Barker, B.S., Ottolini, M., Park, Y., Volkheimer, A., Valdez, P., Swinkels, M.E.M., Patel, M.K. and Meisler, M.H. (2017) Loss-of-function variants of SCN8A in intellectual disability without seizures. *Neurology. Genetics*, **3**, e170.
53. Duchen, L.W. (1970) Hereditary motor end-plate disease in the mouse: light and electron microscopic studies. *Journal of neurology, neurosurgery, and psychiatry*, **33**, 238-250.
54. Wagnon, J.L., Mencacci, N.E., Barker, B.S., Wengert, E.R., Bhatia, K.P., Balint, B., Carecchio, M., Wood, N.W., Patel, M.K. and Meisler, M.H. (2018) Partial loss-of-function of sodium channel SCN8A in familial isolated myoclonus. *Human mutation*, **39**, 965-969.
55. Blanchard, M.G., Willemsen, M.H., Walker, J.B., Dib-Hajj, S.D., Waxman, S.G., Jongmans, M.C., Kleefstra, T., van de Warrenburg, B.P., Praamstra, P., Nicolai, J. *et al.* (2015) De novo gain-of-function and loss-of-function mutations of SCN8A in patients with intellectual disabilities and epilepsy. *Journal of medical genetics*, **52**, 330-337.
56. Rolvien, T., Butscheidt, S., Jeschke, A., Neu, A., Denecke, J., Kubisch, C., Meisler, M.H., Puschel, K., Barvencik, F., Yorgan, T. *et al.* (2017) Severe bone loss and multiple fractures in SCN8A-related epileptic encephalopathy. *Bone*, **103**, 136-143.

57. de Kovel, C.G., Meisler, M.H., Brilstra, E.H., van Berkestijn, F.M., van 't Slot, R., van Lieshout, S., Nijman, I.J., O'Brien, J.E., Hammer, M.F., Estacion, M. *et al.* (2014) Characterization of a de novo SCN8A mutation in a patient with epileptic encephalopathy. *Epilepsy Res.*, **108**, 1511-1518.
58. Ohba, C., Kato, M., Takahashi, S., Lerman-Sagie, T., Lev, D., Terashima, H., Kubota, M., Kawawaki, H., Matsufuji, M., Kojima, Y. *et al.* (2014) Early onset epileptic encephalopathy caused by de novo SCN8A mutations. *Epilepsia*, **55**, 994-1000.
59. Anand, G., Collett-White, F., Orsini, A., Thomas, S., Jayapal, S., Trump, N., Zaiwalla, Z. and Jayawant, S. (2016) Autosomal dominant SCN8A mutation with an unusually mild phenotype. *Eur. J. Paediatr. Neurol.*, **20**, 761-765.
60. Gardella, E., Becker, F., Moller, R.S., Schubert, J., Lemke, J.R., Larsen, L.H., Eiberg, H., Nothnagel, M., Thiele, H., Altmuller, J. *et al.* (2016) Benign infantile seizures and paroxysmal dyskinesia caused by an SCN8A mutation. *Ann. Neurol.*, **79**, 428-436.
61. Wagnon, J.L. and Meisler, M.H. (2015) Recurrent and Non-Recurrent Mutations of SCN8A in Epileptic Encephalopathy. *Front. Neurol.*, **6**, 104.
62. Butler, K.M., da Silva, C., Shafir, Y., Weisfeld-Adams, J.D., Alexander, J.J., Hegde, M. and Escayg, A. (2017) De novo and inherited SCN8A epilepsy mutations detected by gene panel analysis. *Epilepsy Res.*, **129**, 17-25.
63. Rossi, M., El-Khechen, D., Black, M.H., Farwell Hagman, K.D., Tang, S. and Powis, Z. (2017) Outcomes of Diagnostic Exome Sequencing in Patients With Diagnosed or Suspected Autism Spectrum Disorders. *Pediatr Neurol*, **70**, 34-43.e32.
64. Liu, Y., Schubert, J., Sonnenberg, L., Helbig, K.L., Hoei-Hansen, C.E., Koko, M., Rannap, M., Lauxmann, S., Huq, M., Schneider, M.C. *et al.* (2019) Neuronal mechanisms of mutations in SCN8A causing epilepsy or intellectual disability. *Brain*, **142**, 376-390.
65. Dickie, M.M. (1965) Jolting. *Mouse News Lett.*, **32**, 44.
66. Kohrman, D.C., Smith, M.R., Goldin, A.L., Harris, J. and Meisler, M.H. (1996) A missense mutation in the sodium channel Scn8a is responsible for cerebellar ataxia in the mouse mutant jolting. *J Neurosci*, **16**, 5993-5999.
67. Buchner, D.A., Seburn, K.L., Frankel, W.N. and Meisler, M.H. (2004) Three ENU-induced neurological mutations in the pore loop of sodium channel Scn8a (Na(v)1.6) and a genetically linked retinal mutation, rd13. *Mammalian genome : official journal of the International Mammalian Genome Society*, **15**, 344-351.
68. Sharkey, L.M., Cheng, X., Drews, V., Buchner, D.A., Jones, J.M., Justice, M.J., Waxman, S.G., Dib-Hajj, S.D. and Meisler, M.H. (2009) The ataxia3 mutation in the N-terminal cytoplasmic domain of sodium channel Na(v)1.6 disrupts intracellular trafficking. *The Journal of neuroscience : the official journal of the Society for Neuroscience*, **29**, 2733-2741.
69. Wagnon, J.L., Korn, M.J., Parent, R., Tarpey, T.A., Jones, J.M., Hammer, M.F., Murphy, G.G., Parent, J.M. and Meisler, M.H. (2015) Convulsive seizures and SUDEP in a mouse model of SCN8A epileptic encephalopathy. *Human molecular genetics*, **24**, 506-515.
70. McKinney, B.C., Chow, C.Y., Meisler, M.H. and Murphy, G.G. (2008) Exaggerated emotional behavior in mice heterozygous null for the sodium channel Scn8a (Nav1.6). *Genes, brain, and behavior*, **7**, 629-638.

71. Makinson, C.D., Dutt, K., Lin, F., Papale, L.A., Shankar, A., Barela, A.J., Liu, R., Goldin, A.L. and Escayg, A. (2016) An *Scn1a* epilepsy mutation in *Scn8a* alters seizure susceptibility and behavior. *Experimental neurology*, **275 Pt 1**, 46-58.
72. Martin, M.S., Tang, B., Papale, L.A., Yu, F.H., Catterall, W.A. and Escayg, A. (2007) The voltage-gated sodium channel *Scn8a* is a genetic modifier of severe myoclonic epilepsy of infancy. *Human molecular genetics*, **16**, 2892-2899.
73. Jones, J.M., Dionne, L., Dell'Orco, J., Parent, R., Krueger, J.N., Cheng, X., Dib-Hajj, S.D., Bunton-Stasyshyn, R.K., Sharkey, L.M., Dowling, J.J. *et al.* (2016) Single amino acid deletion in transmembrane segment D4S6 of sodium channel *Scn8a* (*Nav1.6*) in a mouse mutant with a chronic movement disorder. *Neurobiology of disease*, **89**, 36-45.
74. Papale, L.A., Beyer, B., Jones, J.M., Sharkey, L.M., Tufik, S., Epstein, M., Letts, V.A., Meisler, M.H., Frankel, W.N. and Escayg, A. (2009) Heterozygous mutations of the voltage-gated sodium channel *SCN8A* are associated with spike-wave discharges and absence epilepsy in mice. *Human molecular genetics*, **18**, 1633-1641.
75. Kearney, J.A., Buchner, D.A., De Haan, G., Adamska, M., Levin, S.I., Furay, A.R., Albin, R.L., Jones, J.M., Montal, M., Stevens, M.J. *et al.* (2002) Molecular and pathological effects of a modifier gene on deficiency of the sodium channel *Scn8a* (*Na(v)1.6*). *Human molecular genetics*, **11**, 2765-2775.
76. Sprunger, L.K., Escayg, A., Tallaksen-Greene, S., Albin, R.L. and Meisler, M.H. (1999) Dystonia associated with mutation of the neuronal sodium channel *Scn8a* and identification of the modifier locus *Scnm1* on mouse chromosome 3. *Hum Mol Genet*, **8**, 471-479.
77. Besag, F.M. (2018) Epilepsy in patients with autism: links, risks and treatment challenges. *Neuropsychiatric disease and treatment*, **14**, 1-10.
78. Tellez-Zenteno, J.F., Patten, S.B., Jette, N., Williams, J. and Wiebe, S. (2007) Psychiatric comorbidity in epilepsy: a population-based analysis. *Epilepsia*, **48**, 2336-2344.
79. Sen, A., Capelli, V. and Husain, M. (2018) Cognition and dementia in older patients with epilepsy. *Brain*, **141**, 1592-1608.
80. Verret, L., Mann, E.O., Hang, G.B., Barth, A.M., Cobos, I., Ho, K., Devidze, N., Masliah, E., Kreitzer, A.C., Mody, I. *et al.* (2012) Inhibitory interneuron deficit links altered network activity and cognitive dysfunction in Alzheimer model. *Cell*, **149**, 708-721.
81. Chung, D.W., Fish, K.N. and Lewis, D.A. (2016) Pathological Basis for Deficient Excitatory Drive to Cortical Parvalbumin Interneurons in Schizophrenia. *The American journal of psychiatry*, **173**, 1131-1139.
82. Volk, D.W., Edelson, J.R. and Lewis, D.A. (2016) Altered expression of developmental regulators of parvalbumin and somatostatin neurons in the prefrontal cortex in schizophrenia. *Schizophrenia research*, **177**, 3-9.
83. Lewis, D.A., Curley, A.A., Glausier, J.R. and Volk, D.W. (2012) Cortical parvalbumin interneurons and cognitive dysfunction in schizophrenia. *Trends in neurosciences*, **35**, 57-67.
84. Ciccone, R., Franco, C., Piccialli, I., Boscia, F., Casamassa, A., de Rosa, V., Cepparulo, P., Cataldi, M., Annunziato, L. and Pannaccione, A. (2019) Amyloid beta-Induced Upregulation of *Nav1.6* Underlies Neuronal Hyperactivity in *Tg2576* Alzheimer's Disease Mouse Model. *Sci Rep*, **9**, 13592.

85. Martinez-Losa, M., Tracy, T.E., Ma, K., Verret, L., Clemente-Perez, A., Khan, A.S., Cobos, I., Ho, K., Gan, L., Mucke, L. *et al.* (2018) Nav1.1-Overexpressing Interneuron Transplants Restore Brain Rhythms and Cognition in a Mouse Model of Alzheimer's Disease. *Neuron*, **98**, 75-89.e75.
86. Bender, A.C., Luikart, B.W. and Lenck-Santini, P.P. (2016) Cognitive Deficits Associated with Nav1.1 Alterations: Involvement of Neuronal Firing Dynamics and Oscillations. *PloS one*, **11**, e0151538.
87. Brodie, M.J. (2017) Sodium Channel Blockers in the Treatment of Epilepsy. *CNS drugs*, **31**, 527-534.
88. Rosenberg, G. (2007) The mechanisms of action of valproate in neuropsychiatric disorders: can we see the forest for the trees? *Cellular and Molecular Life Sciences*, **64**, 2090-2103.
89. Richards, K.L., Milligan, C.J., Richardson, R.J., Jancovski, N., Grunnet, M., Jacobson, L.H., Undheim, E.A.B., Mobli, M., Chow, C.Y., Herzig, V. *et al.* (2018) Selective Na^V1.1 activation rescues Dravet syndrome mice from seizures and premature death. *Proceedings of the National Academy of Sciences*, **115**, E8077-E8085.
90. Anderson, L.L., Hawkins, N.A., Thompson, C.H., Kearney, J.A. and George, A.L. (2017) Unexpected Efficacy of a Novel Sodium Channel Modulator in Dravet Syndrome. *Scientific Reports*, **7**, 1682.
91. Baker, E.M., Thompson, C.H., Hawkins, N.A., Wagnon, J.L., Wengert, E.R., Patel, M.K., George, A.L., Jr., Meisler, M.H. and Kearney, J.A. (2018) The novel sodium channel modulator GS-458967 (GS967) is an effective treatment in a mouse model of SCN8A encephalopathy. *Epilepsia*, **59**, 1166-1176.
92. Anderson, L.L., Thompson, C.H., Hawkins, N.A., Nath, R.D., Petersohn, A.A., Rajamani, S., Bush, W.S., Frankel, W.N., Vanoye, C.G., Kearney, J.A. *et al.* (2014) Antiepileptic activity of preferential inhibitors of persistent sodium current. *Epilepsia*, **55**, 1274-1283.
93. Drews, V.L., Lieberman, A.P. and Meisler, M.H. (2005) Multiple transcripts of sodium channel SCN8A (Na(V)1.6) with alternative 5'- and 3'-untranslated regions and initial characterization of the SCN8A promoter. *Genomics*, **85**, 245-257.
94. Drews, V.L., Shi, K., de Haan, G. and Meisler, M.H. (2007) Identification of evolutionarily conserved, functional noncoding elements in the promoter region of the sodium channel gene SCN8A. *Mammalian genome : official journal of the International Mammalian Genome Society*, **18**, 723-731.
95. Martin, M.S., Tang, B., Ta, N. and Escayg, A. (2007) Characterization of 5' untranslated regions of the voltage-gated sodium channels SCN1A, SCN2A, and SCN3A and identification of cis-conserved noncoding sequences. *Genomics*, **90**, 225-235.
96. Dong, Z.F., Tang, L.J., Deng, G.F., Zeng, T., Liu, S.J., Wan, R.P., Liu, T., Zhao, Q.H., Yi, Y.H., Liao, W.P. *et al.* (2014) Transcription of the human sodium channel SCN1A gene is repressed by a scaffolding protein RACK1. *Molecular neurobiology*, **50**, 438-448.
97. Liu, Y., Lai, S., Ma, W., Ke, W., Zhang, C., Liu, S., Zhang, Y., Pei, F., Li, S., Yi, M. *et al.* (2017) CDYL suppresses epileptogenesis in mice through repression of axonal Nav1.6 sodium channel expression. *Nature communications*, **8**, 355.
98. Hsiao, J., Yuan, T.Y., Tsai, M.S., Lu, C.Y., Lin, Y.C., Lee, M.L., Lin, S.W., Chang, F.C., Liu Pimentel, H., Olive, C. *et al.* (2016) Upregulation of Haploinsufficient Gene

- Expression in the Brain by Targeting a Long Non-coding RNA Improves Seizure Phenotype in a Model of Dravet Syndrome. *EBioMedicine*, **9**, 257-277.
99. Kim, D.Y., Gersbacher, M.T., Inquimbert, P. and Kovacs, D.M. (2011) Reduced sodium channel Na(v)1.1 levels in BACE1-null mice. *The Journal of biological chemistry*, **286**, 8106-8116.
 100. Kim, D.Y., Carey, B.W., Wang, H., Ingano, L.A., Binshtok, A.M., Wertz, M.H., Pettingell, W.H., He, P., Lee, V.M., Woolf, C.J. *et al.* (2007) BACE1 regulates voltage-gated sodium channels and neuronal activity. *Nature cell biology*, **9**, 755-764.
 101. Thompson, C.H., Kahlig, K.M. and George, A.L., Jr. (2011) SCN1A splice variants exhibit divergent sensitivity to commonly used antiepileptic drugs. *Epilepsia*, **52**, 1000-1009.
 102. Gazina, E.V., Richards, K.L., Mokhtar, M.B., Thomas, E.A., Reid, C.A. and Petrou, S. (2010) Differential expression of exon 5 splice variants of sodium channel alpha subunit mRNAs in the developing mouse brain. *Neuroscience*, **166**, 195-200.
 103. Copley, R.R. (2004) Evolutionary convergence of alternative splicing in ion channels. *Trends in genetics : TIG*, **20**, 171-176.
 104. Carvill, G.L., Engel, K.L., Ramamurthy, A., Cochran, J.N., Roovers, J., Stamberger, H., Lim, N., Schneider, A.L., Hollingsworth, G., Holder, D.H. *et al.* (2018) Aberrant Inclusion of a Poison Exon Causes Dravet Syndrome and Related SCN1A-Associated Genetic Epilepsies. *American journal of human genetics*, **103**, 1022-1029.
 105. O'Brien, J.E., Drews, V.L., Jones, J.M., Dugas, J.C., Barres, B.A. and Meisler, M.H. (2012) Rbfox proteins regulate alternative splicing of neuronal sodium channel SCN8A. *Molecular and cellular neurosciences*, **49**, 120-126.
 106. Lin, G.W., Lu, P., Zeng, T., Tang, H.L., Chen, Y.H., Liu, S.J., Gao, M.M., Zhao, Q.H., Yi, Y.H. and Long, Y.S. (2017) GAPDH-mediated posttranscriptional regulations of sodium channel Scn1a and Scn3a genes under seizure and ketogenic diet conditions. *Neuropharmacology*, **113**, 480-489.
 107. Zeng, T., Dong, Z.F., Liu, S.J., Wan, R.P., Tang, L.J., Liu, T., Zhao, Q.H., Shi, Y.W., Yi, Y.H., Liao, W.P. *et al.* (2014) A novel variant in the 3' UTR of human SCN1A gene from a patient with Dravet syndrome decreases mRNA stability mediated by GAPDH's binding. *Human genetics*, **133**, 801-811.
 108. Driscoll, H.E., Muraro, N.I., He, M. and Baines, R.A. (2013) Pumilio-2 regulates translation of Nav1.6 to mediate homeostasis of membrane excitability. *The Journal of neuroscience : the official journal of the Society for Neuroscience*, **33**, 9644-9654.
 109. Zhang, M., Chen, D., Xia, J., Han, W., Cui, X., Neuenkirchen, N., Hermes, G., Sestan, N. and Lin, H. (2017) Post-transcriptional regulation of mouse neurogenesis by Pumilio proteins. *Genes & development*, **31**, 1354-1369.
 110. Long, Y.-S., Shi, Y.-W. and Liao, W.-P. (2009) Conservation-based prediction of the transcription regulatory region of the SCN1A gene. *Progress in Natural Science*, **19**, 1675-1681.
 111. Xie, J., Qian, K., Si, J., Xiao, L., Ci, D. and Zhang, D. (2018) Conserved noncoding sequences conserve biological networks and influence genome evolution. *Heredity*, **120**, 437-451.
 112. Nakayama, T., Ogiwara, I., Ito, K., Kaneda, M., Mazaki, E., Osaka, H., Ohtani, H., Inoue, Y., Fujiwara, T., Uematsu, M. *et al.* (2010) Deletions of SCN1A 5' genomic region with promoter activity in Dravet syndrome. *Human mutation*, **31**, 820-829.

113. Bae, B.I., Jayaraman, D. and Walsh, C.A. (2015) Genetic changes shaping the human brain. *Developmental cell*, **32**, 423-434.
114. Buenrostro, J.D., Giresi, P.G., Zaba, L.C., Chang, H.Y. and Greenleaf, W.J. (2013) Transposition of native chromatin for fast and sensitive epigenomic profiling of open chromatin, DNA-binding proteins and nucleosome position. *Nature methods*, **10**, 1213-1218.
115. Tsompana, M. and Buck, M.J. (2014) Chromatin accessibility: a window into the genome. *Epigenetics & chromatin*, **7**, 33.
116. Song, L., Zhang, Z., Grasfeder, L.L., Boyle, A.P., Giresi, P.G., Lee, B.K., Sheffield, N.C., Graf, S., Huss, M., Keefe, D. *et al.* (2011) Open chromatin defined by DNaseI and FAIRE identifies regulatory elements that shape cell-type identity. *Genome research*, **21**, 1757-1767.
117. Cutter, A.R. and Hayes, J.J. (2015) A brief review of nucleosome structure. *FEBS letters*, **589**, 2914-2922.
118. Bannister, A.J. and Kouzarides, T. (2011) Regulation of chromatin by histone modifications. *Cell research*, **21**, 381-395.
119. Calo, E. and Wysocka, J. (2013) Modification of enhancer chromatin: what, how, and why? *Molecular cell*, **49**, 825-837.
120. Barski, A., Cuddapah, S., Cui, K., Roh, T.Y., Schones, D.E., Wang, Z., Wei, G., Chepelev, I. and Zhao, K. (2007) High-resolution profiling of histone methylations in the human genome. *Cell*, **129**, 823-837.
121. Davie, K., Jacobs, J., Atkins, M., Potier, D., Christiaens, V., Halder, G. and Aerts, S. (2015) Discovery of Transcription Factors and Regulatory Regions Driving In Vivo Tumor Development by ATAC-seq and FAIRE-seq Open Chromatin Profiling. *PLOS Genetics*, **11**, e1004994.
122. Scharer, C.D., Blalock, E.L., Barwick, B.G., Haines, R.R., Wei, C., Sanz, I. and Boss, J.M. (2016) ATAC-seq on biobanked specimens defines a unique chromatin accessibility structure in naive SLE B cells. *Scientific reports*, **6**, 27030.
123. Furey, T.S. (2012) ChIP-seq and beyond: new and improved methodologies to detect and characterize protein-DNA interactions. *Nature Reviews Genetics*, **13**, 840-852.
124. Kearney, J.A., Wiste, A.K., Stephani, U., Trudeau, M.M., Siegel, A., RamachandranNair, R., Elterman, R.D., Muhle, H., Reinsdorf, J., Shields, W.D. *et al.* (2006) Recurrent de novo mutations of SCN1A in severe myoclonic epilepsy of infancy. *Pediatr Neurol*, **34**, 116-120.
125. Ragsdale, D.S. (2008) How do mutant Nav1.1 sodium channels cause epilepsy? *Brain Res Rev*, **58**, 149-159.
126. Cestele, S., Labate, A., Rusconi, R., Tarantino, P., Mumoli, L., Franceschetti, S., Annesi, G., Mantegazza, M. and Gambardella, A. (2013) Divergent effects of the T1174S SCN1A mutation associated with seizures and hemiplegic migraine. *Epilepsia*, **54**, 927-935.
127. Suls, A., Velizarova, R., Yordanova, I., Deprez, L., Van Dyck, T., Wauters, J., Guergueltcheva, V., Claes, L.R., Kremensky, I., Jordanova, A. *et al.* (2010) Four generations of epilepsy caused by an inherited microdeletion of the SCN1A gene. *Neurology*, **75**, 72-76.
128. Surovy, M., Soltysova, A., Kolnikova, M., Sykora, P., Ilencikova, D., Ficek, A., Radvanszky, J. and Kadasi, L. (2016) Novel SCN1A variants in Dravet syndrome and

- evaluating a wide approach of patient selection. *General physiology and biophysics*, **35**, 333-342.
129. Takaori, T., Kumakura, A., Ishii, A., Hirose, S. and Hata, D. (2017) Two mild cases of Dravet syndrome with truncating mutation of SCN1A. *Brain & development*, **39**, 72-74.
 130. Thompson, C.H., Porter, J.C., Kahlig, K.M., Daniels, M.A. and George, A.L., Jr. (2012) Nontruncating SCN1A mutations associated with severe myoclonic epilepsy of infancy impair cell surface expression. *The Journal of biological chemistry*, **287**, 42001-42008.
 131. Catterall, W.A. (2012) In Noebels, J. L., Avoli, M., Rogawski, M. A., Olsen, R. W. and Delgado-Escueta, A. V. (eds.), *Jasper's Basic Mechanisms of the Epilepsies*. 4th ed, Bethesda (MD).
 132. Hawkins, N.A., Martin, M.S., Frankel, W.N., Kearney, J.A. and Escayg, A. (2011) Neuronal voltage-gated ion channels are genetic modifiers of generalized epilepsy with febrile seizures plus. *Neurobiol Dis*, **41**, 655-660.
 133. Catarino, C.B., Liu, J.Y., Liagkouras, I., Gibbons, V.S., Labrum, R.W., Ellis, R., Woodward, C., Davis, M.B., Smith, S.J., Cross, J.H. *et al.* (2011) Dravet syndrome as epileptic encephalopathy: evidence from long-term course and neuropathology. *Brain*, **134**, 2982-3010.
 134. Colasante, G., Lignani, G., Brusco, S., Di Berardino, C., Carpenter, J., Giannelli, S., Valassina, N., Bido, S., Ricci, R., Castoldi, V. *et al.* (2019) dCas9-Based Scn1a Gene Activation Restores Inhibitory Interneuron Excitability and Attenuates Seizures in Dravet Syndrome Mice. *Molecular Therapy*.
 135. Han, S., Yu, F.H., Schwartz, M.D., Linton, J.D., Bosma, M.M., Hurley, J.B., Catterall, W.A. and de la Iglesia, H.O. (2012) Na(V)1.1 channels are critical for intercellular communication in the suprachiasmatic nucleus and for normal circadian rhythms. *Proc Natl Acad Sci U S A*, **109**, E368-377.
 136. Rudy, B., Fishell, G., Lee, S. and Hjerling-Leffler, J. (2011) Three groups of interneurons account for nearly 100% of neocortical GABAergic neurons. *Dev. Neurobiol.*, **71**, 45-61.
 137. Volk, D.W., Sampson, A.R., Zhang, Y., Edelson, J.R. and Lewis, D.A. (2016) Cortical GABA markers identify a molecular subtype of psychotic and bipolar disorders. *Psychological medicine*, **46**, 2501-2512.
 138. Hon, G.C., Hawkins, R.D. and Ren, B. (2009) Predictive chromatin signatures in the mammalian genome. *Hum. Mol. Genet.*, **18**, R195-201.
 139. Roman, T.S., Cannon, M.E., Vadlamudi, S., Buchkovich, M.L., Wolford, B.N., Welch, R.P., Morken, M.A., Kwon, G.J., Varshney, A., Kursawe, R. *et al.* (2017) A Type 2 Diabetes-Associated Functional Regulatory Variant in a Pancreatic Islet Enhancer at the *Adcy5* Locus. *Diabetes*.
 140. Mesrian Tanha, H., Rahgozar, S. and Mojtavavi Naeini, M. (2017) ABCC4 functional SNP in the 3' splice acceptor site of exon 8 (G912T) is associated with unfavorable clinical outcome in children with acute lymphoblastic leukemia. *Cancer Chemother. Pharmacol.*, **80**, 109-117.
 141. Davis, J.P., Vadlamudi, S., Roman, T.S., Zeynalzadeh, M., Iyengar, A.K. and Mohlke, K.L. (2018) Enhancer deletion and allelic effects define a regulatory molecular mechanism at the VLDLR cholesterol GWAS locus. *Human molecular genetics*, **28**, 888-895.

142. Meng, F., Yuan, G., Zhu, X., Zhou, Y., Wang, D. and Guo, Y. (2018) Functional Variants Identified Efficiently through an Integrated Transcriptome and Epigenome Analysis. *Scientific Reports*, **8**, 2959.
143. Steffens, M., Leu, C., Ruppert, A.K., Zara, F., Striano, P., Robbiano, A., Capovilla, G., Tinuper, P., Gambardella, A., Bianchi, A. *et al.* (2012) Genome-wide association analysis of genetic generalized epilepsies implicates susceptibility loci at 1q43, 2p16.1, 2q22.3 and 17q21.32. *Hum. Mol. Genet.*, **21**, 5359-5372.
144. (2014) Genetic determinants of common epilepsies: a meta-analysis of genome-wide association studies. *Lancet Neurol.*, **13**, 893-903.
145. Barrett, T., Wilhite, S.E., Ledoux, P., Evangelista, C., Kim, I.F., Tomashevsky, M., Marshall, K.A., Phillippy, K.H., Sherman, P.M., Holko, M. *et al.* (2013) NCBI GEO: archive for functional genomics data sets--update. *Nucleic acids research*, **41**, D991-995.
146. Davis, C.A., Hitz, B.C., Sloan, C.A., Chan, E.T., Davidson, J.M., Gabdank, I., Hilton, J.A., Jain, K., Baymuradov, U.K., Narayanan, A.K. *et al.* (2018) The Encyclopedia of DNA elements (ENCODE): data portal update. *Nucleic acids research*, **46**, D794-d801.
147. Boulay, G., Awad, M.E., Riggi, N., Archer, T.C., Iyer, S., Boonseng, W.E., Rossetti, N.E., Naigles, B., Rengarajan, S., Volorio, A. *et al.* (2017) OTX2 Activity at Distal Regulatory Elements Shapes the Chromatin Landscape of Group 3 Medulloblastoma. *Cancer discovery*, **7**, 288-301.
148. Vermunt, M.W., Reinink, P., Korving, J., de Bruijn, E., Creyghton, P.M., Basak, O., Geeven, G., Toonen, P.W., Lansu, N., Meunier, C. *et al.* (2014) Large-scale identification of coregulated enhancer networks in the adult human brain. *Cell reports*, **9**, 767-779.
149. Oldridge, D.A., Wood, A.C., Weichert-Leahey, N., Crimmins, I., Sussman, R., Winter, C., McDaniel, L.D., Diamond, M., Hart, L.S., Zhu, S. *et al.* (2015) Genetic predisposition to neuroblastoma mediated by a LMO1 super-enhancer polymorphism. *Nature*, **528**, 418-421.
150. Vermunt, M.W., Tan, S.C., Castelijn, B., Geeven, G., Reinink, P., de Bruijn, E., Kondova, I., Persengiev, S., Bontrop, R., Cuppen, E. *et al.* (2016) Epigenomic annotation of gene regulatory alterations during evolution of the primate brain. *Nature neuroscience*, **19**, 494-503.
151. Liu, F., Hon, G.C., Villa, G.R., Turner, K.M., Ikegami, S., Yang, H., Ye, Z., Li, B., Kuan, S., Lee, A.Y. *et al.* (2015) EGFR Mutation Promotes Glioblastoma through Epigenome and Transcription Factor Network Remodeling. *Molecular cell*, **60**, 307-318.
152. Henrich, K.O., Bender, S., Saadati, M., Dreidax, D., Gartlgruber, M., Shao, C., Herrmann, C., Wiesenfarth, M., Parzonka, M., Wehrmann, L. *et al.* (2016) Integrative Genome-Scale Analysis Identifies Epigenetic Mechanisms of Transcriptional Deregulation in Unfavorable Neuroblastomas. *Cancer research*, **76**, 5523-5537.
153. Araujo, D.J., Anderson, A.G., Berto, S., Runnels, W., Harper, M., Ammanuel, S., Rieger, M.A., Huang, H.C., Rajkovich, K., Loerwald, K.W. *et al.* (2015) FoxP1 orchestration of ASD-relevant signaling pathways in the striatum. *Genes & development*, **29**, 2081-2096.
154. Ying, M., Tilghman, J., Wei, Y., Guerrero-Cazares, H., Quinones-Hinojosa, A., Ji, H. and Latta, J. (2014) Kruppel-like factor-9 (KLF9) inhibits glioblastoma stemness through global transcription repression and integrin alpha6 inhibition. *The Journal of biological chemistry*, **289**, 32742-32756.
155. Heynen, G.J., Nevedomskaya, E., Palit, S., Jagalur Basheer, N., Liefink, C., Schlicker, A., Zwart, W., Bernards, R. and Bajpe, P.K. (2016) Mastermind-Like 3 Controls

- Proliferation and Differentiation in Neuroblastoma. *Molecular cancer research : MCR*, **14**, 411-422.
156. Hsu, C.L., Chang, H.Y., Chang, J.Y., Hsu, W.M., Huang, H.C. and Juan, H.F. (2016) Unveiling MYCN regulatory networks in neuroblastoma via integrative analysis of heterogeneous genomics data. *Oncotarget*, **7**, 36293-36310.
 157. Kleine-Kohlbrecher, D., Christensen, J., Vandamme, J., Abarategui, I., Bak, M., Tommerup, N., Shi, X., Gozani, O., Rappsilber, J., Salcini, A.E. *et al.* (2010) A functional link between the histone demethylase PHF8 and the transcription factor ZNF711 in X-linked mental retardation. *Molecular cell*, **38**, 165-178.
 158. Ataman, B., Boulting, G.L., Harmin, D.A., Yang, M.G., Baker-Salisbury, M., Yap, E.L., Malik, A.N., Mei, K., Rubin, A.A., Spiegel, I. *et al.* (2016) Evolution of Osteocrin as an activity-regulated factor in the primate brain. *Nature*, **539**, 242-247.
 159. Langmead, B. and Salzberg, S.L. (2012) Fast gapped-read alignment with Bowtie 2. *Nature Methods*, **9**, 357.
 160. Heinz, S., Benner, C., Spann, N., Bertolino, E., Lin, Y.C., Laslo, P., Cheng, J.X., Murre, C., Singh, H. and Glass, C.K. (2010) Simple combinations of lineage-determining transcription factors prime cis-regulatory elements required for macrophage and B cell identities. *Molecular cell*, **38**, 576-589.
 161. Quinlan, A.R. and Hall, I.M. (2010) BEDTools: a flexible suite of utilities for comparing genomic features. *Bioinformatics (Oxford, England)*, **26**, 841-842.
 162. Garcia-Cuellar, M.-P., Steger, J., Füller, E., Hetzner, K. and Slany, R.K. (2015) Pbx3 and Meis1 cooperate through multiple mechanisms to support Hox-induced murine leukemia. *Haematologica*, **100**, 905-913.
 163. Oishi, Y., Manabe, I., Imai, Y., Hara, K., Horikoshi, M., Fujiu, K., Tanaka, T., Aizawa, T., Kadowaki, T. and Nagai, R. (2010) Regulatory polymorphism in transcription factor KLF5 at the MEF2 element alters the response to angiotensin II and is associated with human hypertension. *FASEB journal : official publication of the Federation of American Societies for Experimental Biology*, **24**, 1780-1788.
 164. Wang, W.M., Lee, A.Y. and Chiang, C.M. (2008) One-step affinity tag purification of full-length recombinant human AP-1 complexes from bacterial inclusion bodies using a polycistronic expression system. *Protein expression and purification*, **59**, 144-152.
 165. Untergasser, A., Cutcutache, I., Koressaar, T., Ye, J., Faircloth, B.C., Remm, M. and Rozen, S.G. (2012) Primer3--new capabilities and interfaces. *Nucleic Acids Res*, **40**, e115.
 166. Lamar, T., Vanoye, C.G., Calhoun, J., Wong, J.C., Dutton, S.B.B., Jorge, B.S., Velinov, M., Escayg, A. and Kearney, J.A. (2017) SCN3A deficiency associated with increased seizure susceptibility. *Neurobiol Dis*, **102**, 38-48.
 167. Pfaffl, M.W. (2001) A new mathematical model for relative quantification in real-time RT-PCR. *Nucleic Acids Res*, **29**, e45.
 168. Liu, J. and Francke, U. (2006) Identification of cis-regulatory elements for MECP2 expression. *Human molecular genetics*, **15**, 1769-1782.
 169. Rosenbloom, K.R., Armstrong, J., Barber, G.P., Casper, J., Clawson, H., Diekhans, M., Dreszer, T.R., Fujita, P.A., Guruvadoo, L., Haeussler, M. *et al.* (2015) The UCSC Genome Browser database: 2015 update. *Nucleic Acids Res.*, **43**, D670-681.

170. Guillou, E., Ibarra, A., Coulon, V., Casado-Vela, J., Rico, D., Casal, I., Schwob, E., Losada, A. and Mendez, J. (2010) Cohesin organizes chromatin loops at DNA replication factories. *Genes & development*, **24**, 2812-2822.
171. Gordon, J., Amini, S. and White, M.K. (2013) General overview of neuronal cell culture. *Methods in molecular biology (Clifton, N.J.)*, **1078**, 1-8.
172. Sun, A.X., Yuan, Q., Tan, S., Xiao, Y., Wang, D., Khoo, A.T., Sani, L., Tran, H.D., Kim, P., Chiew, Y.S. *et al.* (2016) Direct Induction and Functional Maturation of Forebrain GABAergic Neurons from Human Pluripotent Stem Cells. *Cell reports*, **16**, 1942-1953.
173. Meganathan, K., Lewis, E.M.A., Gontarz, P., Liu, S., Stanley, E.G., Elefanty, A.G., Huettner, J.E., Zhang, B. and Kroll, K.L. (2017) Regulatory networks specifying cortical interneurons from human embryonic stem cells reveal roles for CHD2 in interneuron development. *Proceedings of the National Academy of Sciences of the United States of America*, **114**, E11180-e11189.
174. Rossignol, E. (2011) Genetics and function of neocortical GABAergic interneurons in neurodevelopmental disorders. *Neural plasticity*, **2011**, 649325.
175. Liu, Y., Liu, H., Sauvey, C., Yao, L., Zarnowska, E.D. and Zhang, S.C. (2013) Directed differentiation of forebrain GABA interneurons from human pluripotent stem cells. *Nature protocols*, **8**, 1670-1679.
176. Marin, O. (2012) Interneuron dysfunction in psychiatric disorders. *Nature reviews. Neuroscience*, **13**, 107-120.
177. Arber, C. and Li, M. (2013) Cortical interneurons from human pluripotent stem cells: prospects for neurological and psychiatric disease. *Frontiers in cellular neuroscience*, **7**, 10.
178. Xiang, Y., Tanaka, Y., Patterson, B., Kang, Y.J., Govindaiah, G., Roselaar, N., Cakir, B., Kim, K.Y., Lombroso, A.P., Hwang, S.M. *et al.* (2017) Fusion of Regionally Specified hPSC-Derived Organoids Models Human Brain Development and Interneuron Migration. *Cell stem cell*, **21**, 383-398.e387.
179. Shao, Z., Noh, H., Bin Kim, W., Ni, P., Nguyen, C., Cote, S.E., Noyes, E., Zhao, J., Parsons, T., Park, J.M. *et al.* (2019) Dysregulated protocadherin-pathway activity as an intrinsic defect in induced pluripotent stem cell-derived cortical interneurons from subjects with schizophrenia. *Nature neuroscience*, **22**, 229-242.
180. Sun, Q., Li, X., Ren, M., Zhao, M., Zhong, Q., Ren, Y., Luo, P., Ni, H., Zhang, X., Zhang, C. *et al.* (2019) A whole-brain map of long-range inputs to GABAergic interneurons in the mouse medial prefrontal cortex. *Nature neuroscience*, **22**, 1357-1370.
181. Volk, D.W. and Lewis, D.A. (2014) Early developmental disturbances of cortical inhibitory neurons: contribution to cognitive deficits in schizophrenia. *Schizophrenia bulletin*, **40**, 952-957.
182. Jacob, J. (2016) Cortical interneuron dysfunction in epilepsy associated with autism spectrum disorders. *Epilepsia*, **57**, 182-193.
183. Nicholas, C.R., Chen, J., Tang, Y., Southwell, D.G., Chalmers, N., Vogt, D., Arnold, C.M., Chen, Y.J., Stanley, E.G., Elefanty, A.G. *et al.* (2013) Functional maturation of hPSC-derived forebrain interneurons requires an extended timeline and mimics human neural development. *Cell stem cell*, **12**, 573-586.
184. Mouchlianitis, E., McCutcheon, R. and Howes, O.D. (2016) Brain-imaging studies of treatment-resistant schizophrenia: a systematic review. *The lancet. Psychiatry*, **3**, 451-463.

185. Tandon, R., Gaebel, W., Barch, D.M., Bustillo, J., Gur, R.E., Heckers, S., Malaspina, D., Owen, M.J., Schultz, S., Tsuang, M. *et al.* (2013) Definition and description of schizophrenia in the DSM-5. *Schizophrenia research*, **150**, 3-10.
186. Bicks, L.K., Yamamuro, K., Flanigan, M.E., Kim, J.M., Kato, D., Lucas, E.K., Koike, H., Peng, M.S., Brady, D.M., Chandrasekaran, S. *et al.* (2020) Prefrontal parvalbumin interneurons require juvenile social experience to establish adult social behavior. *Nature communications*, **11**, 1003.
187. Hansen, D.V., Lui, J.H., Flandin, P., Yoshikawa, K., Rubenstein, J.L., Alvarez-Buylla, A. and Kriegstein, A.R. (2013) Non-epithelial stem cells and cortical interneuron production in the human ganglionic eminences. *Nature neuroscience*, **16**, 1576-1587.
188. Clowry, G.J. (2015) An enhanced role and expanded developmental origins for gamma-aminobutyric acidergic interneurons in the human cerebral cortex. *Journal of anatomy*, **227**, 384-393.
189. Close, J.L., Yao, Z., Levi, B.P., Miller, J.A., Bakken, T.E., Menon, V., Ting, J.T., Wall, A., Krostag, A.R., Thomsen, E.R. *et al.* (2017) Single-Cell Profiling of an In Vitro Model of Human Interneuron Development Reveals Temporal Dynamics of Cell Type Production and Maturation. *Neuron*, **93**, 1035-1048.e1035.
190. Mo, A., Mukamel, E.A., Davis, F.P., Luo, C., Henry, G.L., Picard, S., Urich, M.A., Nery, J.R., Sejnowski, T.J., Lister, R. *et al.* (2015) Epigenomic Signatures of Neuronal Diversity in the Mammalian Brain. *Neuron*, **86**, 1369-1384.
191. Anastasiades, P.G., Marques-Smith, A., Lyngholm, D., Lickiss, T., Raffiq, S., Katzel, D., Miesenbock, G. and Butt, S.J. (2016) GABAergic interneurons form transient layer-specific circuits in early postnatal neocortex. *Nature communications*, **7**, 10584.
192. Gallegos, D.A., Chan, U., Chen, L.F. and West, A.E. (2018) Chromatin Regulation of Neuronal Maturation and Plasticity. *Trends in neurosciences*, **41**, 311-324.
193. Noh, H., Shao, Z., Coyle, J.T. and Chung, S. (2017) Modeling schizophrenia pathogenesis using patient-derived induced pluripotent stem cells (iPSCs). *Biochimica et biophysica acta. Molecular basis of disease*, **1863**, 2382-2387.
194. Schuster, J., Laan, L., Klar, J., Jin, Z., Huss, M., Korol, S., Noraddin, F.H., Sobol, M., Birnir, B. and Dahl, N. (2019) Transcriptomes of Dravet syndrome iPSC derived GABAergic cells reveal dysregulated pathways for chromatin remodeling and neurodevelopment. *Neurobiol Dis*, 104583.
195. Wen, Z., Nguyen, H.N., Guo, Z., Lalli, M.A., Wang, X., Su, Y., Kim, N.S., Yoon, K.J., Shin, J., Zhang, C. *et al.* (2014) Synaptic dysregulation in a human iPSC model of mental disorders. *Nature*, **515**, 414-418.
196. Chiang, C.H., Su, Y., Wen, Z., Yoritomo, N., Ross, C.A., Margolis, R.L., Song, H. and Ming, G.L. (2011) Integration-free induced pluripotent stem cells derived from schizophrenia patients with a DISC1 mutation. *Molecular psychiatry*, **16**, 358-360.
197. Rueden, C.T., Schindelin, J., Hiner, M.C., DeZonia, B.E., Walter, A.E., Arena, E.T. and Eliceiri, K.W. (2017) ImageJ2: ImageJ for the next generation of scientific image data. *BMC Bioinformatics*, **18**, 529.
198. Bolger, A.M., Lohse, M. and Usadel, B. (2014) Trimmomatic: a flexible trimmer for Illumina sequence data. *Bioinformatics (Oxford, England)*, **30**, 2114-2120.
199. Trapnell, C., Pachter, L. and Salzberg, S.L. (2009) TopHat: discovering splice junctions with RNA-Seq. *Bioinformatics (Oxford, England)*, **25**, 1105-1111.

200. Anders, S., Pyl, P.T. and Huber, W. (2015) HTSeq--a Python framework to work with high-throughput sequencing data. *Bioinformatics (Oxford, England)*, **31**, 166-169.
201. Love, M.I., Huber, W. and Anders, S. (2014) Moderated estimation of fold change and dispersion for RNA-seq data with DESeq2. *Genome biology*, **15**, 550.
202. Linker, S.B., Hsu, J.Y., Pfaff, A., Amatya, D., Ko, S.M., Voter, S., Wong, Q. and Gage, F.H. (2019) BrainImageR: spatiotemporal gene set analysis referencing the human brain. *Bioinformatics (Oxford, England)*, **35**, 343-345.
203. Subramanian, A., Tamayo, P., Mootha, V.K., Mukherjee, S., Ebert, B.L., Gillette, M.A., Paulovich, A., Pomeroy, S.L., Golub, T.R., Lander, E.S. *et al.* (2005) Gene set enrichment analysis: a knowledge-based approach for interpreting genome-wide expression profiles. *Proceedings of the National Academy of Sciences of the United States of America*, **102**, 15545-15550.
204. Guo, M., Price, M.J., Patterson, D.G., Barwick, B.G., Haines, R.R., Kania, A.K., Bradley, J.E., Randall, T.D., Boss, J.M. and Scharer, C.D. (2018) EZH2 Represses the B Cell Transcriptional Program and Regulates Antibody-Secreting Cell Metabolism and Antibody Production. *Journal of immunology (Baltimore, Md. : 1950)*, **200**, 1039-1052.
205. Martin, M. (2011) Cutadapt removes adapter sequences from high-throughput sequencing reads. *2011*, **17**, 3.
206. Langmead, B. and Salzberg, S.L. (2012) Fast gapped-read alignment with Bowtie 2. *Nature methods*, **9**, 357-359.
207. Yu, G., Wang, L.G. and He, Q.Y. (2015) ChIPseeker: an R/Bioconductor package for ChIP peak annotation, comparison and visualization. *Bioinformatics (Oxford, England)*, **31**, 2382-2383.
208. Robinson, M.D., McCarthy, D.J. and Smyth, G.K. (2010) edgeR: a Bioconductor package for differential expression analysis of digital gene expression data. *Bioinformatics (Oxford, England)*, **26**, 139-140.
209. Gel, B. and Serra, E. (2017) karyoploteR: an R/Bioconductor package to plot customizable genomes displaying arbitrary data. *Bioinformatics (Oxford, England)*, **33**, 3088-3090.
210. Ripke, S., Neale, B.M., Corvin, A., Walters, J.T.R., Farh, K.-H., Holmans, P.A., Lee, P., Bulik-Sullivan, B., Collier, D.A., Huang, H. *et al.* (2014) Biological insights from 108 schizophrenia-associated genetic loci. *Nature*, **511**, 421-427.
211. Lawrence, M., Gentleman, R. and Carey, V. (2009) rtracklayer: an R package for interfacing with genome browsers. *Bioinformatics (Oxford, England)*, **25**, 1841-1842.
212. Bailey, T.L., Boden, M., Buske, F.A., Frith, M., Grant, C.E., Clementi, L., Ren, J., Li, W.W. and Noble, W.S. (2009) MEME SUITE: tools for motif discovery and searching. *Nucleic Acids Res*, **37**, W202-208.
213. Kulakovskiy, I.V., Vorontsov, I.E., Yevshin, I.S., Sharipov, R.N., Fedorova, A.D., Rumynskiy, E.I., Medvedeva, Y.A., Magana-Mora, A., Bajic, V.B., Papatsenko, D.A. *et al.* (2018) HOCOMOCO: towards a complete collection of transcription factor binding models for human and mouse via large-scale ChIP-Seq analysis. *Nucleic Acids Res*, **46**, D252-d259.
214. Li, Z., Schulz, M.H., Look, T., Begemann, M., Zenke, M. and Costa, I.G. (2019) Identification of transcription factor binding sites using ATAC-seq. *Genome biology*, **20**, 45.

215. Shannon, P., Markiel, A., Ozier, O., Baliga, N.S., Wang, J.T., Ramage, D., Amin, N., Schwikowski, B. and Ideker, T. (2003) Cytoscape: a software environment for integrated models of biomolecular interaction networks. *Genome research*, **13**, 2498-2504.
216. Mahony, S. and Benos, P.V. (2007) STAMP: a web tool for exploring DNA-binding motif similarities. *Nucleic Acids Res*, **35**, W253-258.
217. Archer, J. and Robertson, D.L. (2007) CTree: comparison of clusters between phylogenetic trees made easy. *Bioinformatics (Oxford, England)*, **23**, 2952-2953.
218. Fromer, M., Roussos, P., Sieberts, S.K., Johnson, J.S., Kavanagh, D.H., Perumal, T.M., Ruderfer, D.M., Oh, E.C., Topol, A., Shah, H.R. *et al.* (2016) Gene expression elucidates functional impact of polygenic risk for schizophrenia. *Nature neuroscience*, **19**, 1442-1453.
219. Campbell, K. (2003) Dorsal-ventral patterning in the mammalian telencephalon. *Current opinion in neurobiology*, **13**, 50-56.
220. Liu, Y., Weick, J.P., Liu, H., Krencik, R., Zhang, X., Ma, L., Zhou, G.M., Ayala, M. and Zhang, S.C. (2013) Medial ganglionic eminence-like cells derived from human embryonic stem cells correct learning and memory deficits. *Nat Biotechnol*, **31**, 440-447.
221. Maroof, A.M., Keros, S., Tyson, J.A., Ying, S.W., Ganat, Y.M., Merkle, F.T., Liu, B., Goulburn, A., Stanley, E.G., Elefanty, A.G. *et al.* (2013) Directed differentiation and functional maturation of cortical interneurons from human embryonic stem cells. *Cell stem cell*, **12**, 559-572.
222. Park, D., Xiang, A.P., Mao, F.F., Zhang, L., Di, C.G., Liu, X.M., Shao, Y., Ma, B.F., Lee, J.H., Ha, K.S. *et al.* (2010) Nestin is required for the proper self-renewal of neural stem cells. *Stem cells (Dayton, Ohio)*, **28**, 2162-2171.
223. Pang, Z.P., Yang, N., Vierbuchen, T., Ostermeier, A., Fuentes, D.R., Yang, T.Q., Citri, A., Sebastiano, V., Marro, S., Sudhof, T.C. *et al.* (2011) Induction of human neuronal cells by defined transcription factors. *Nature*, **476**, 220-223.
224. Pereira, M., Birtele, M., Shrigley, S., Benitez, J.A., Hedlund, E., Parmar, M. and Ottosson, D.R. (2017) Direct Reprogramming of Resident NG2 Glia into Neurons with Properties of Fast-Spiking Parvalbumin-Containing Interneurons. *Stem cell reports*, **9**, 742-751.
225. Beanan, M.J. and Sargent, T.D. (2000) Regulation and function of Dlx3 in vertebrate development. *Dev Dyn*, **218**, 545-553.
226. Schmalbach, B., Lepsveridze, E., Djogo, N., Papashvili, G., Kuang, F., Leshchyn'ska, I., Sytnyk, V., Nikonenko, A.G., Dityatev, A., Jakovcevski, I. *et al.* (2015) Age-dependent loss of parvalbumin-expressing hippocampal interneurons in mice deficient in CHL1, a mental retardation and schizophrenia susceptibility gene. *Journal of neurochemistry*, **135**, 830-844.
227. Vergano-Vera, E., Yusta-Boyo, M.J., de Castro, F., Bernad, A., de Pablo, F. and Vicario-Abejon, C. (2006) Generation of GABAergic and dopaminergic interneurons from endogenous embryonic olfactory bulb precursor cells. *Development (Cambridge, England)*, **133**, 4367-4379.
228. Radonjić, N.V., Ayoub, A.E., Memi, F., Yu, X., Maroof, A., Jakovcevski, I., Anderson, S.A., Rakic, P. and Zecevic, N. (2014) Diversity of cortical interneurons in primates: the role of the dorsal proliferative niche. *Cell reports*, **9**, 2139-2151.
229. Bernácer, J., Prensa, L. and Giménez-Amaya, J.M. (2007) Cholinergic Interneurons Are Differentially Distributed in the Human Striatum. *PLOS ONE*, **2**, e1174.

230. Yu, X. and Zecevic, N. (2011) Dorsal radial glial cells have the potential to generate cortical interneurons in human but not in mouse brain. *The Journal of neuroscience : the official journal of the Society for Neuroscience*, **31**, 2413-2420.
231. Costa, M.R. and Muller, U. (2014) Specification of excitatory neurons in the developing cerebral cortex: progenitor diversity and environmental influences. *Frontiers in cellular neuroscience*, **8**, 449.
232. Costa, M.R., Kessarlis, N., Richardson, W.D., Götz, M. and Hedin-Pereira, C. (2007) The Marginal Zone/Layer I as a Novel Niche for Neurogenesis and Gliogenesis in Developing Cerebral Cortex. *The Journal of Neuroscience*, **27**, 11376.
233. Yeung, R.K., Xiang, Z.H., Tsang, S.Y., Li, R., Ho, T.Y.C., Li, Q., Hui, C.K., Sham, P.C., Qiao, M.Q. and Xue, H. (2018) Gabrb2-knockout mice displayed schizophrenia-like and comorbid phenotypes with interneuron-astrocyte-microglia dysregulation. *Translational psychiatry*, **8**, 128.
234. Niturad, C.E., Lev, D., Kalscheuer, V.M., Charzewska, A., Schubert, J., Lerman-Sagie, T., Kroes, H.Y., Oegema, R., Traverso, M., Specchio, N. *et al.* (2017) Rare GABRA3 variants are associated with epileptic seizures, encephalopathy and dysmorphic features. *Brain : a journal of neurology*, **140**, 2879-2894.
235. Mattison, K.A., Butler, K.M., Inglis, G.A.S., Dayan, O., Boussidan, H., Bhambhani, V., Philbrook, B., da Silva, C., Alexander, J.J., Kanner, B.I. *et al.* (2018) SLC6A1 variants identified in epilepsy patients reduce gamma-aminobutyric acid transport. *Epilepsia*, **59**, e135-e141.
236. Bouhours, B., Gjoni, E., Kochubey, O. and Schneggenburger, R. (2017) Synaptotagmin2 (Syt2) Drives Fast Release Redundantly with Syt1 at the Output Synapses of Parvalbumin-Expressing Inhibitory Neurons. *The Journal of Neuroscience*, **37**, 4604-4617.
237. Batista-Brito, R., Machold, R., Klein, C. and Fishell, G. (2008) Gene expression in cortical interneuron precursors is prescient of their mature function. *Cerebral cortex (New York, N.Y. : 1991)*, **18**, 2306-2317.
238. Bragina, L., Giovedi, S., Barbaresi, P., Benfenati, F. and Conti, F. (2010) Heterogeneity of glutamatergic and GABAergic release machinery in cerebral cortex: analysis of synaptogyrin, vesicle-associated membrane protein, and syntaxin. *Neuroscience*, **165**, 934-943.
239. Tokudome, K., Okumura, T., Shimizu, S., Mashimo, T., Takizawa, A., Serikawa, T., Terada, R., Ishihara, S., Kunisawa, N., Sasa, M. *et al.* (2016) Synaptic vesicle glycoprotein 2A (SV2A) regulates kindling epileptogenesis via GABAergic neurotransmission. *Scientific reports*, **6**, 27420.
240. Blackmore, M.G., Moore, D.L., Smith, R.P., Goldberg, J.L., Bixby, J.L. and Lemmon, V.P. (2010) High content screening of cortical neurons identifies novel regulators of axon growth. *Molecular and cellular neurosciences*, **44**, 43-54.
241. Nakamura, Y., Morrow, D.H., Modgil, A., Huyghe, D., Deeb, T.Z., Lumb, M.J., Davies, P.A. and Moss, S.J. (2016) Proteomic Characterization of Inhibitory Synapses Using a Novel pHluorin-tagged gamma-Aminobutyric Acid Receptor, Type A (GABAA), alpha2 Subunit Knock-in Mouse. *The Journal of biological chemistry*, **291**, 12394-12407.
242. Kahler, A.K., Djurovic, S., Rimol, L.M., Brown, A.A., Athanasiu, L., Jonsson, E.G., Hansen, T., Gustafsson, O., Hall, H., Giegling, I. *et al.* (2011) Candidate gene analysis of the human natural killer-1 carbohydrate pathway and perineuronal nets in schizophrenia:

- B3GAT2 is associated with disease risk and cortical surface area. *Biological psychiatry*, **69**, 90-96.
243. Nord, A.S. and West, A.E. (2019) Neurobiological functions of transcriptional enhancers. *Nature neuroscience*.
244. Shima, Y., Sugino, K., Hempel, C.M., Shima, M., Taneja, P., Bullis, J.B., Mehta, S., Lois, C. and Nelson, S.B. (2016) A Mammalian enhancer trap resource for discovering and manipulating neuronal cell types. *eLife*, **5**, e13503.
245. Heinz, S., Romanoski, C.E., Benner, C. and Glass, C.K. (2015) The selection and function of cell type-specific enhancers. *Nature reviews. Molecular cell biology*, **16**, 144-154.
246. Haussler, M., Zweig, A.S., Tyner, C., Speir, M.L., Rosenbloom, K.R., Raney, B.J., Lee, C.M., Lee, B.T., Hinrichs, A.S., Gonzalez, J.N. *et al.* (2019) The UCSC Genome Browser database: 2019 update. *Nucleic Acids Res*, **47**, D853-d858.
247. Sousa, V.H., Miyoshi, G., Hjerling-Leffler, J., Karayannis, T. and Fishell, G. (2009) Characterization of Nkx6-2-derived neocortical interneuron lineages. *Cerebral cortex (New York, N.Y. : 1991)*, **19 Suppl 1**, i1-10.
248. Pieper, A., Rudolph, S., Wieser, G.L., Gotze, T., Miessner, H., Yonemasu, T., Yan, K., Tzvetanova, I., Castillo, B.D., Bode, U. *et al.* (2019) NeuroD2 controls inhibitory circuit formation in the molecular layer of the cerebellum. *Scientific reports*, **9**, 1448.
249. Skinner, M.K., Rawls, A., Wilson-Rawls, J. and Roalson, E.H. (2010) Basic helix-loop-helix transcription factor gene family phylogenetics and nomenclature. *Differentiation; research in biological diversity*, **80**, 1-8.
250. Parras, C.M., Schuurmans, C., Scardigli, R., Kim, J., Anderson, D.J. and Guillemot, F. (2002) Divergent functions of the proneural genes Mash1 and Ngn2 in the specification of neuronal subtype identity. *Genes & development*, **16**, 324-338.
251. Chan, C.H., Godinho, L.N., Thomaidou, D., Tan, S.S., Gulisano, M. and Parnavelas, J.G. (2001) Emx1 is a marker for pyramidal neurons of the cerebral cortex. *Cerebral cortex (New York, N.Y. : 1991)*, **11**, 1191-1198.
252. Davenne, M., Maconochie, M.K., Neun, R., Pattyn, A., Chambon, P., Krumlauf, R. and Rijli, F.M. (1999) Hoxa2 and Hoxb2 control dorsoventral patterns of neuronal development in the rostral hindbrain. *Neuron*, **22**, 677-691.
253. Aksoy, I., Giudice, V., Delahaye, E., Wianny, F., Aubry, M., Mure, M., Chen, J., Jauch, R., Bogu, G.K., Nolden, T. *et al.* (2014) Klf4 and Klf5 differentially inhibit mesoderm and endoderm differentiation in embryonic stem cells. *Nature communications*, **5**, 3719.
254. Moore, D.L., Apará, A. and Goldberg, J.L. (2011) Krüppel-like transcription factors in the nervous system: novel players in neurite outgrowth and axon regeneration. *Molecular and cellular neurosciences*, **47**, 233-243.
255. Dong, J.-T. and Chen, C. (2009) Essential role of KLF5 transcription factor in cell proliferation and differentiation and its implications for human diseases. *Cellular and Molecular Life Sciences*, **66**, 2691-2706.
256. Zhang, S. and Cui, W. (2014) Sox2, a key factor in the regulation of pluripotency and neural differentiation. *World journal of stem cells*, **6**, 305-311.
257. Pieraccioli, M., Nicolai, S., Pitolli, C., Agostini, M., Antonov, A., Malewicz, M., Knight, R.A., Raschella, G. and Melino, G. (2018) ZNF281 inhibits neuronal differentiation and is a prognostic marker for neuroblastoma. *Proceedings of the National Academy of Sciences of the United States of America*, **115**, 7356-7361.

258. Liu, N., Hargreaves, V.V., Zhu, Q., Kurland, J.V., Hong, J., Kim, W., Sher, F., Macias-Trevino, C., Rogers, J.M., Kurita, R. *et al.* (2018) Direct Promoter Repression by BCL11A Controls the Fetal to Adult Hemoglobin Switch. *Cell*, **173**, 430-442.e417.
259. Marsh, B., Stevens, S.L., Packard, A.E.B., Gopalan, B., Hunter, B., Leung, P.Y., Harrington, C.A. and Stenzel-Poore, M.P. (2009) Systemic Lipopolysaccharide Protects the Brain from Ischemic Injury by Reprogramming the Response of the Brain to Stroke: A Critical Role for IRF3. *The Journal of Neuroscience*, **29**, 9839-9849.
260. Chen, Y., Xu, B., Arderiu, G., Hashimoto, T., Young, W.L., Boudreau, N. and Yang, G.Y. (2004) Retroviral delivery of homeobox D3 gene induces cerebral angiogenesis in mice. *Journal of cerebral blood flow and metabolism : official journal of the International Society of Cerebral Blood Flow and Metabolism*, **24**, 1280-1287.
261. Wiegrefe, C., Simon, R., Peschkes, K., Kling, C., Strehle, M., Cheng, J., Srivatsa, S., Liu, P., Jenkins, Nancy A., Copeland, Neal G. *et al.* (2015) Bcl11a (Ctip1) Controls Migration of Cortical Projection Neurons through Regulation of *Sema3c*. *Neuron*, **87**, 311-325.
262. Dias, C., Estruch, S.B., Graham, S.A., McRae, J., Sawiak, S.J., Hurst, J.A., Joss, S.K., Holder, S.E., Morton, J.E.V., Turner, C. *et al.* (2016) BCL11A Haploinsufficiency Causes an Intellectual Disability Syndrome and Dysregulates Transcription. *Am J Hum Genet*, **99**, 253-274.
263. Yanagi, M., Hashimoto, T., Kitamura, N., Fukutake, M., Komure, O., Nishiguchi, N., Kawamata, T., Maeda, K. and Shirakawa, O. (2008) Expression of Kruppel-like factor 5 gene in human brain and association of the gene with the susceptibility to schizophrenia. *Schizophrenia research*, **100**, 291-301.
264. Zhang, S., Moy, W., Zhang, H., Leites, C., McGowan, H., Shi, J., Sanders, A.R., Pang, Z.P., Gejman, P.V. and Duan, J. (2018) Open chromatin dynamics reveals stage-specific transcriptional networks in hiPSC-based neurodevelopmental model. *Stem cell research*, **29**, 88-98.
265. Gorski, J.A., Talley, T., Qiu, M., Puellas, L., Rubenstein, J.L.R. and Jones, K.R. (2002) Cortical Excitatory Neurons and Glia, But Not GABAergic Neurons, Are Produced in the Emx1-Expressing Lineage. *The Journal of Neuroscience*, **22**, 6309-6314.
266. Stocker, A.M. and O'Leary, D.D.M. (2016) Emx1 Is Required for Neocortical Area Patterning. *PLOS ONE*, **11**, e0149900.
267. Roberts, R.C., Barksdale, K.A., Roche, J.K. and Lahti, A.C. (2015) Decreased synaptic and mitochondrial density in the postmortem anterior cingulate cortex in schizophrenia. *Schizophrenia research*, **168**, 543-553.
268. Law, A.J., Kleinman, J.E., Weinberger, D.R. and Weickert, C.S. (2007) Disease-associated intronic variants in the ErbB4 gene are related to altered ErbB4 splice-variant expression in the brain in schizophrenia. *Human molecular genetics*, **16**, 129-141.
269. Eastwood, S.L. and Harrison, P.J. (2010) Markers of glutamate synaptic transmission and plasticity are increased in the anterior cingulate cortex in bipolar disorder. *Biological psychiatry*, **67**, 1010-1016.
270. Uhlén, M., Fagerberg, L., Hallström, B.M., Lindskog, C., Oksvold, P., Mardinoglu, A., Sivertsson, Å., Kampf, C., Sjöstedt, E., Asplund, A. *et al.* (2015) Tissue-based map of the human proteome. *Science (New York, N.Y.)*, **347**, 1260419.

271. Creemers, E.E., Sutherland, L.B., Oh, J., Barbosa, A.C. and Olson, E.N. (2006) Coactivation of MEF2 by the SAP domain proteins myocardin and MASTR. *Molecular cell*, **23**, 83-96.
272. Colvin, J.S., Bohne, B.A., Harding, G.W., McEwen, D.G. and Ornitz, D.M. (1996) Skeletal overgrowth and deafness in mice lacking fibroblast growth factor receptor 3. *Nature genetics*, **12**, 390-397.
273. Harrington, A.J., Raissi, A., Rajkovich, K., Berto, S., Kumar, J., Molinaro, G., Raduazzo, J., Guo, Y., Loerwald, K., Konopka, G. *et al.* (2016) MEF2C regulates cortical inhibitory and excitatory synapses and behaviors relevant to neurodevelopmental disorders. *eLife*, **5**.
274. Timmer, M., Cesnulevicius, K., Winkler, C., Kolb, J., Lipokatic-Takacs, E., Jungnickel, J. and Grothe, C. (2007) Fibroblast Growth Factor (FGF)-2 and FGF Receptor 3 Are Required for the Development of the Substantia Nigra, and FGF-2 Plays a Crucial Role for the Rescue of Dopaminergic Neurons after 6-Hydroxydopamine Lesion. *The Journal of Neuroscience*, **27**, 459-471.
275. Reim, K., Mansour, M., Varoqueaux, F., McMahon, H.T., Sudhof, T.C., Brose, N. and Rosenmund, C. (2001) Complexins regulate a late step in Ca²⁺-dependent neurotransmitter release. *Cell*, **104**, 71-81.
276. Yamauchi, Y., Qin, L.H., Nishihara, M., Sawada, K., Kato, K. and Inoue, S. (2005) Vulnerability of synaptic plasticity in the complexin II knockout mouse to maternal deprivation stress. *Brain research*, **1056**, 59-67.
277. Begemann, M., Grube, S., Papiol, S., Malzahn, D., Krampe, H., Ribbe, K., Friedrichs, H., Radyushkin, K.A., El-Kordi, A., Benseler, F. *et al.* (2010) Modification of cognitive performance in schizophrenia by complexin 2 gene polymorphisms. *Archives of general psychiatry*, **67**, 879-888.
278. Radyushkin, K., El-Kordi, A., Boretius, S., Castaneda, S., Ronnenberg, A., Reim, K., Bickeboller, H., Frahm, J., Brose, N. and Ehrenreich, H. (2010) Complexin2 null mutation requires a 'second hit' for induction of phenotypic changes relevant to schizophrenia. *Genes, brain, and behavior*, **9**, 592-602.
279. Riccio, A., Li, Y., Tsvetkov, E., Gapon, S., Yao, G.L., Smith, K.S., Engin, E., Rudolph, U., Bolshakov, V.Y. and Clapham, D.E. (2014) Decreased anxiety-like behavior and Galphaq/11-dependent responses in the amygdala of mice lacking TRPC4 channels. *The Journal of neuroscience : the official journal of the Society for Neuroscience*, **34**, 3653-3667.
280. Klipec, W.D., Burrow, K.R., O'Neill, C., Cao, J.L., Lawyer, C.R., Ostertag, E., Fowler, M., Bachtell, R.K., Illig, K.R. and Cooper, D.C. (2016) Loss of the trpc4 gene is associated with a reduction in cocaine self-administration and reduced spontaneous ventral tegmental area dopamine neuronal activity, without deficits in learning for natural rewards. *Behavioural brain research*, **306**, 117-127.
281. Chatelier, A., Zhao, J., Bois, P. and Chahine, M. (2010) Biophysical characterisation of the persistent sodium current of the Nav1.6 neuronal sodium channel: a single-channel analysis. *Pflugers Arch*, **460**, 77-86.
282. Osorio, N., Cathala, L., Meisler, M.H., Crest, M., Magistretti, J. and Delmas, P. (2010) Persistent Nav1.6 current at axon initial segments tunes spike timing of cerebellar granule cells. *J Physiol*, **588**, 651-670.

283. O'Brien, J.E. and Meisler, M.H. (2013) Sodium channel SCN8A (Nav1.6): properties and de novo mutations in epileptic encephalopathy and intellectual disability. *Front Genet*, **4**, 213.
284. Trudeau, M.M., Dalton, J.C., Day, J.W., Ranum, L.P. and Meisler, M.H. (2006) Heterozygosity for a protein truncation mutation of sodium channel SCN8A in a patient with cerebellar atrophy, ataxia, and mental retardation. *J Med Genet*, **43**, 527-530.
285. Johannesen, K.M., Gardella, E., Encinas, A.C., Lehesjoki, A.E., Linnankivi, T., Petersen, M.B., Lund, I.C.B., Blichfeldt, S., Miranda, M.J., Pal, D.K. *et al.* (2019) The spectrum of intermediate SCN8A-related epilepsy. *Epilepsia*.
286. Bunton-Stasyshyn, R.K.A., Wagnon, J.L., Wengert, E.R., Barker, B.S., Faulkner, A., Wagley, P.K., Bhatia, K., Jones, J.M., Maniaci, M.R., Parent, J.M. *et al.* (2019) Prominent role of forebrain excitatory neurons in SCN8A encephalopathy. *Brain*.
287. Wong, J.C., Makinson, C.D., Lamar, T., Cheng, Q., Wingard, J.C., Terwilliger, E.F. and Escayg, A. (2018) Selective targeting of Scn8a prevents seizure development in a mouse model of mesial temporal lobe epilepsy. *Sci Rep*, **8**, 126.
288. Jones, J.M., Dionne, L., Dell'Orco, J., Parent, R., Krueger, J.N., Cheng, X., Dib-Hajj, S.D., Bunton-Stasyshyn, R.K., Sharkey, L.M., Dowling, J.J. *et al.* (2016) Single amino acid deletion in transmembrane segment D4S6 of sodium channel Scn8a (Nav1.6) in a mouse mutant with a chronic movement disorder. *Neurobiol Dis*, **89**, 36-45.
289. Dick, D.J., Boakes, R.J. and Harris, J.B. (1985) A cerebellar abnormality in the mouse with motor end-plate disease. *Neuropathol Appl Neurobiol*, **11**, 141-147.
290. Kohrman, D.C., Harris, J.B. and Meisler, M.H. (1996) Mutation detection in the med and medJ alleles of the sodium channel Scn8a. Unusual splicing due to a minor class AT-AC intron. *J Biol Chem*, **271**, 17576-17581.
291. Kelley, L.A., Mezulis, S., Yates, C.M., Wass, M.N. and Sternberg, M.J. (2015) The Phyre2 web portal for protein modeling, prediction and analysis. *Nature protocols*, **10**, 845-858.
292. Barton, M.E., Klein, B.D., Wolf, H.H. and White, H.S. (2001) Pharmacological characterization of the 6 Hz psychomotor seizure model of partial epilepsy. *Epilepsy Res*, **47**, 217-227.
293. Wong, J.C., Dutton, S.B., Collins, S.D., Schachter, S. and Escayg, A. (2016) Huperzine A Provides Robust and Sustained Protection against Induced Seizures in Scn1a Mutant Mice. *Frontiers in Pharmacology*, **7**, 357.
294. Gilchrist, J., Dutton, S., Diaz-Bustamante, M., McPherson, A., Olivares, N., Kalia, J., Escayg, A. and Bosmans, F. (2014) Nav1.1 modulation by a novel triazole compound attenuates epileptic seizures in rodents. *ACS chemical biology*, **9**, 1204-1212.
295. Dutton, S.B., Sawyer, N.T., Kalume, F., Jumbo-Lucioni, P., Borges, K., Catterall, W.A. and Escayg, A. (2011) Protective effect of the ketogenic diet in Scn1a mutant mice. *Epilepsia*, **52**, 2050-2056.
296. Catterall, W.A. (2010) Ion channel voltage sensors: structure, function, and pathophysiology. *Neuron*, **67**, 915-928.
297. Kontis, K.J. and Goldin, A.L. (1997) Sodium channel inactivation is altered by substitution of voltage sensor positive charges. *J Gen Physiol*, **110**, 403-413.
298. Stuhmer, W., Conti, F., Suzuki, H., Wang, X.D., Noda, M., Yahagi, N., Kubo, H. and Numa, S. (1989) Structural parts involved in activation and inactivation of the sodium channel. *Nature*, **339**, 597-603.

299. Kufareva, I. and Abagyan, R. (2012) Methods of protein structure comparison. *Methods Mol Biol*, **857**, 231-257.
300. Duchen, L.W. and Stefani, E. (1971) Electrophysiological studies of neuromuscular transmission in hereditary 'motor end-plate disease' of the mouse. *J Physiol*, **212**, 535-548.
301. Burgess, D.L., Kohrman, D.C., Galt, J., Plummer, N.W., Jones, J.M., Spear, B. and Meisler, M.H. (1995) Mutation of a new sodium channel gene, *Scn8a*, in the mouse mutant 'motor endplate disease'. *Nature genetics*, **10**, 461-465.
302. Kohrman, D.C., Plummer, N.W., Schuster, T., Jones, J.M., Jang, W., Burgess, D.L., Galt, J., Spear, B.T. and Meisler, M.H. (1995) Insertional mutation of the motor endplate disease (med) locus on mouse chromosome 15. *Genomics*, **26**, 171-177.
303. De Repentigny, Y., Cote, P.D., Pool, M., Bernier, G., Girard, S., Vidal, S.M. and Kothary, R. (2001) Pathological and genetic analysis of the degenerating muscle (dmu) mouse: a new allele of *Scn8a*. *Human molecular genetics*, **10**, 1819-1827.
304. Angaut-Petit, D., McArdle, J.J., Mallart, A., Bournaud, R., Pincon-Raymond, M. and Rieger, F. (1982) Electrophysiological and morphological studies of a motor nerve in 'motor endplate disease' of the mouse. *Proceedings of the Royal Society of London. Series B, Biological sciences*, **215**, 117-125.
305. Noujaim, S.F., Kaur, K., Milstein, M., Jones, J.M., Furspan, P., Jiang, D., Auerbach, D.S., Herron, T., Meisler, M.H. and Jalife, J. (2012) A null mutation of the neuronal sodium channel *NaV1.6* disrupts action potential propagation and excitation-contraction coupling in the mouse heart. *FASEB journal : official publication of the Federation of American Societies for Experimental Biology*, **26**, 63-72.
306. Khan, Z., Carey, J., Park, H.J., Lehar, M., Lasker, D. and Jinnah, H.A. (2004) Abnormal motor behavior and vestibular dysfunction in the stargazer mouse mutant. *Neuroscience*, **127**, 785-796.
307. Noebels, J.L., Qiao, X., Bronson, R.T., Spencer, C. and Davisson, M.T. (1990) Stargazer: a new neurological mutant on chromosome 15 in the mouse with prolonged cortical seizures. *Epilepsy Res*, **7**, 129-135.
308. Jones, S.M. and Jones, T.A. (2014) Genetics of peripheral vestibular dysfunction: lessons from mutant mouse strains. *Journal of the American Academy of Audiology*, **25**, 289-301.
309. Rieger, F., Pincon-Raymond, M., Lombet, A., Ponzio, G., Lazdunski, M. and Sidman, R.L. (1984) Paranodal dysmyelination and increase in tetrodotoxin binding sites in the sciatic nerve of the motor end-plate disease (med/med) mouse during postnatal development. *Dev Biol*, **101**, 401-409.
310. Ye, M., Yang, J., Tian, C., Zhu, Q., Yin, L., Jiang, S., Yang, M. and Shu, Y. (2018) Differential roles of *NaV1.2* and *NaV1.6* in regulating neuronal excitability at febrile temperature and distinct contributions to febrile seizures. *Sci Rep*, **8**, 753.
311. Katz, E., Stoler, O., Scheller, A., Khrapunsky, Y., Goebbels, S., Kirchhoff, F., Gutnick, M.J., Wolf, F. and Fleidervish, I.A. (2018) Role of sodium channel subtype in action potential generation by neocortical pyramidal neurons. *Proc Natl Acad Sci U S A*, **115**, E7184-e7192.
312. Vega, A.V., Henry, D.L. and Matthews, G. (2008) Reduced expression of *Na(v)1.6* sodium channels and compensation by *Na(v)1.2* channels in mice heterozygous for a null mutation in *Scn8a*. *Neuroscience letters*, **442**, 69-73.

313. Clatot, J., Zheng, Y., Girardeau, A., Liu, H., Laurita, K.R., Marionneau, C. and Deschenes, I. (2018) Mutant voltage-gated sodium channels can exert a dominant-negative effect through coupled gating. *American journal of physiology. Heart and circulatory physiology*.
314. Makinson, C.D., Tanaka, B.S., Lamar, T., Goldin, A.L. and Escayg, A. (2014) Role of the hippocampus in Nav1.6 (Scn8a) mediated seizure resistance. *Neurobiol Dis*, **68**, 16-25.
315. Inglis, G.A.S., Wong, J.C., Butler, K.M., Thelin, J.T., Mistretta, O.C., Wu, X., Lin, X., English, A.W. and Escayg, A. (2019) Mutations in the Scn8a DIIS4 voltage sensor reveal new distinctions among hypomorphic and null Nav 1.6 sodium channels. *Genes, brain, and behavior*, e12612.
316. Santillo, S., Schiano Moriello, A. and Di Maio, V. (2014) Electrophysiological variability in the SH-SY5Y cellular line. *General physiology and biophysics*, **33**, 121-129.
317. Constantinescu, R., Constantinescu, A.T., Reichmann, H. and Janetzky, B. (2007) Neuronal differentiation and long-term culture of the human neuroblastoma line SH-SY5Y. *Journal of neural transmission. Supplementum*, 17-28.
318. Biedler, J.L., Helson, L. and Spengler, B.A. (1973) Morphology and growth, tumorigenicity, and cytogenetics of human neuroblastoma cells in continuous culture. *Cancer research*, **33**, 2643-2652.
319. Ron, G., Globerson, Y., Moran, D. and Kaplan, T. (2017) Promoter-enhancer interactions identified from Hi-C data using probabilistic models and hierarchical topological domains. *Nature communications*, **8**, 2237.
320. Frank, C.L., Liu, F., Wijayatunge, R., Song, L., Biegler, M.T., Yang, M.G., Vockley, C.M., Safi, A., Gersbach, C.A., Crawford, G.E. *et al.* (2015) Regulation of chromatin accessibility and Zic binding at enhancers in the developing cerebellum. *Nat. Neurosci.*, **18**, 647-656.
321. Hilton, I.B., D'Ippolito, A.M., Vockley, C.M., Thakore, P.I., Crawford, G.E., Reddy, T.E. and Gersbach, C.A. (2015) Epigenome editing by a CRISPR-Cas9-based acetyltransferase activates genes from promoters and enhancers. *Nat. Biotechnol.*, **33**, 510-517.
322. Kearns, N.A., Pham, H., Tabak, B., Genga, R.M., Silverstein, N.J., Garber, M. and Maehr, R. (2015) Functional annotation of native enhancers with a Cas9-histone demethylase fusion. *Nat Methods*, **12**, 401-403.
323. Konermann, S., Brigham, M.D., Trevino, A.E., Joung, J., Abudayyeh, O.O., Barcena, C., Hsu, P.D., Habib, N., Gootenberg, J.S., Nishimasu, H. *et al.* (2015) Genome-scale transcriptional activation by an engineered CRISPR-Cas9 complex. *Nature*, **517**, 583-588.
324. Perez-Pinera, P., Kocak, D.D., Vockley, C.M., Adler, A.F., Kabadi, A.M., Polstein, L.R., Thakore, P.I., Glass, K.A., Ousterout, D.G., Leong, K.W. *et al.* (2013) RNA-guided gene activation by CRISPR-Cas9-based transcription factors. *Nat Methods*, **10**, 973-976.
325. Chen, G., Ning, B. and Shi, T. (2019) Single-Cell RNA-Seq Technologies and Related Computational Data Analysis. *Frontiers in Genetics*, **10**.
326. Pott, S. and Lieb, J.D. (2015) Single-cell ATAC-seq: strength in numbers. *Genome biology*, **16**, 172.
327. Mirza, N., Vasieva, O., Marson, A.G. and Pirmohamed, M. (2011) Exploring the genomic basis of pharmacoresistance in epilepsy: an integrative analysis of large-scale

- gene expression profiling studies on brain tissue from epilepsy surgery. *Human molecular genetics*, **20**, 4381-4394.
328. Phelan, K.D., Mock, M.M., Kretz, O., Shwe, U.T., Kozhemyakin, M., Greenfield, L.J., Dietrich, A., Birnbaumer, L., Freichel, M., Flockerzi, V. *et al.* (2012) Heteromeric canonical transient receptor potential 1 and 4 channels play a critical role in epileptiform burst firing and seizure-induced neurodegeneration. *Molecular pharmacology*, **81**, 384-392.
 329. Beckmann, H., Richter, J., Hill, K., Urban, N., Lemoine, H. and Schaefer, M. (2017) A benzothiadiazine derivative and methylprednisolone are novel and selective activators of transient receptor potential canonical 5 (TRPC5) channels. *Cell calcium*, **66**, 10-18.
 330. Minard, A., Bauer, C.C., Wright, D.J., Rubaiy, H.N., Muraki, K., Beech, D.J. and Bon, R.S. (2018) Remarkable Progress with Small-Molecule Modulation of TRPC1/4/5 Channels: Implications for Understanding the Channels in Health and Disease. *Cells*, **7**, 52.
 331. Carson, C., Raman, P., Tullai, J., Xu, L., Henault, M., Thomas, E., Yeola, S., Lao, J., McPate, M., Verkuyl, J.M. *et al.* (2015) Englerin A Agonizes the TRPC4/C5 Cation Channels to Inhibit Tumor Cell Line Proliferation. *PloS one*, **10**, e0127498.
 332. Freichel, M., Tsvilovskyy, V. and Camacho-Londono, J.E. (2014) TRPC4- and TRPC4-containing channels. *Handbook of experimental pharmacology*, **222**, 85-128.
 333. Middlebrooks, J. (2015).
 334. Baizer, J.S., Manohar, S., Paolone, N.A., Weinstock, N. and Salvi, R.J. (2012) Understanding tinnitus: the dorsal cochlear nucleus, organization and plasticity. *Brain research*, **1485**, 40-53.
 335. Chen, K., Sprunger, L.K., Meisler, M.H., Waller, H.J. and Godfrey, D.A. (1999) Reduced spontaneous activity in the dorsal cochlear nucleus of Scn8a mutant mice. *Brain research*, **847**, 85-89.
 336. Koay, G., Heffner, R. and Heffner, H. (2002) Behavioral audiograms of homozygous med(J) mutant mice with sodium channel deficiency and unaffected controls. *Hearing research*, **171**, 111-118.
 337. Pilati, N., Large, C., Forsythe, I.D. and Hamann, M. (2012) Acoustic over-exposure triggers burst firing in dorsal cochlear nucleus fusiform cells. *Hearing research*, **283**, 98-106.
 338. Frasier, C.R., Zhang, H., Offord, J., Dang, L.T., Auerbach, D.S., Shi, H., Chen, C., Goldman, A.M., Eckhardt, L.L., Bezzerides, V.J. *et al.* (2018) Channelopathy as a SUDEP Biomarker in Dravet Syndrome Patient-Derived Cardiac Myocytes. *Stem cell reports*, **11**, 626-634.

APPENDIX A: Supporting data for Chapter 2

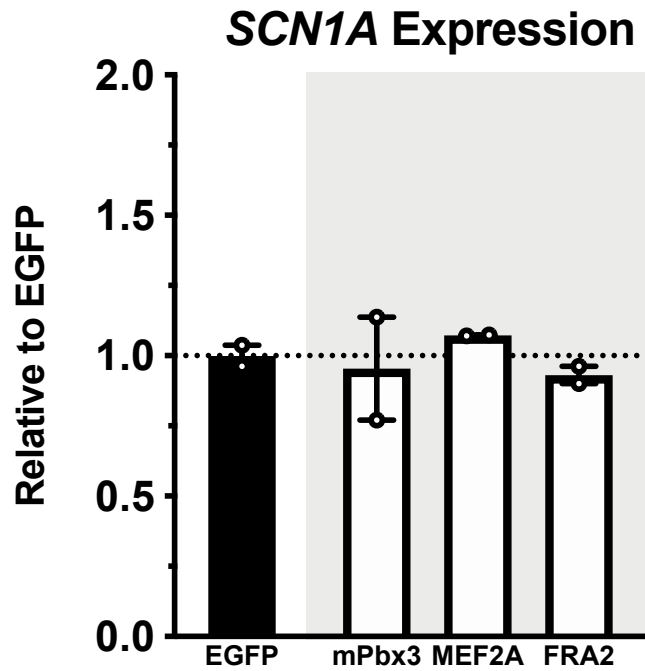


Figure A1. Transcription factors with predicted binding in FGE2 do not significantly alter *SCN1A* expression. SH-SY5Y cells were individually transfected with plasmid vectors that constitutively express the transcription factors Pbx3, MEF2A, or FRA2 (162-164). qRT-PCR results are normalized to *ACTB*, and expression is presented as fold change relative to SH-SY5Y cells transfected with an EGFP expression vector (n=2). Mean \pm SEM.

Table A1. Data accessions from the UCSC ENCODE and NCBI GEO databases used to identify putative functional genome elements (FGEs). Related to Figures 2.1-2.2.

Source	Type	Data Type	Database	Accession
Medulloblastoma	Primary tissue	ATAC-seq	GEO	GSE92584
Hippocampus	Primary tissue	ChIP-seq: H3K27ac	GEO	GSE40465
Cerebellum	Primary tissue	ChIP-seq: H3K27ac	GEO	GSE40465
SH-SY5Y	Cell line	ChIP-seq: H3K27ac	GEO	GSE65664
BE2_C	Cell line	ChIP-seq: H3K27ac	GEO	GSE65664
Cerebellum	Primary tissue	ChIP-seq: H3K27ac	GEO	GSE67978
Hippocampus	Primary tissue	ChIP-seq: H3K27ac	GEO	GSE72468
Hippocampus	Primary tissue	ChIP-seq: H3K4me1	GEO	GSE72468
Hippocampus	Primary tissue	ChIP-seq: H3K4me3	GEO	GSE72468
SH-SY5Y	Cell line	ChIP-seq: H3K27ac	GEO	GSE80197
SH-SY5Y	Cell line	ChIP-seq: H3K4me1	GEO	GSE80197
SH-SY5Y	Cell line	ChIP-seq: H3K4me3	GEO	GSE80197
NPCs	Cell line	ChIP-seq: FOXP1	GEO	GSE62718
SH-SY5Y	Cell line	ChIP-seq: GATA3	GEO	GSE65664
BE2_C	Cell line	ChIP-seq: GATA3	GEO	GSE65664
Glioblastoma	Cell line	ChIP-seq: KLF9	GEO	GSE62211
SK-N-SH	Cell line	ChIP-seq: MAML3	GEO	GSE69119
SH-SY5Y	Cell line	ChIP-seq: MAML3	GEO	GSE69119
BE2_C	Cell line	ChIP-seq: MYCN	GEO	GSE72640
D283	Cell line	ChIP-seq: NEUROD1	GEO	GSE92584
D341	Cell line	ChIP-seq: NEUROD1	GEO	GSE92584
SH-SY5Y	Cell line	ChIP-seq: PHF8	GEO	GSE20673
SH-SY5Y	Cell line	ChIP-seq: ZNF711	GEO	GSE20673
SK-N-SH	Cell line	ChIP-seq: RAD21	GEO	GSE76815
SK-N-SH	Cell line	ChIP-seq: RARA	GEO	GSE69119
SH-SY5Y	Cell line	ChIP-seq: RARA	GEO	GSE69119
DAOY	Cell line	ChIP-seq: ZFX	GEO	GSE45394
Fetal brain tissue	Primary tissue	ChIP-seq: H3K4me1	GEO	GSE78688
Fetal brain tissue	Primary tissue	ChIP-seq: H3K4me3	GEO	GSE78688
Fetal brain tissue	Primary tissue	ChIP-seq: H3K27ac	GEO	GSE78688
Cerebellum	Primary tissue	DNase-seq	ENCODE	---
Cerebrum	Primary tissue	DNase-seq	ENCODE	---
Frontal cortex	Primary tissue	DNase-seq	ENCODE	---
Frontal cortex	Primary tissue	FAIRE-seq	ENCODE	---
Glioblastoma	Primary tissue	DNase-seq	ENCODE	---
Glioblastoma	Primary tissue	FAIRE-seq	ENCODE	---
Medulloblastoma	Primary tissue	DNase-seq	ENCODE	---
Medulloblastoma	Primary tissue	FAIRE-seq	ENCODE	---
SK-N-SH	Cell line	DNase-seq	ENCODE	---
SK-N-SH	Cell line	ChIP-seq: H3K4me3	ENCODE	---
SK-N-SH	Cell line	ChIP-seq: H3K36me3	ENCODE	---
SK-N-MC	Cell line	DNase-seq	ENCODE	---
SK-N-MC	Cell line	ChIP-seq: H3K4me3	ENCODE	---
BE2_C	Cell line	DNase-seq	ENCODE	---
SK-N-SH	Cell line	ChIP-seq: CHD2	ENCODE	---
BE2_C	Cell line	ChIP-seq: CTCF	ENCODE	---
Cerebellum	Primary tissue	ChIP-seq: CTCF	ENCODE	---
SK-N-SH	Cell line	ChIP-seq: ELF1	ENCODE	---
SK-N-SH	Cell line	ChIP-seq: FOXM1	ENCODE	---
SK-N-MC	Cell line	ChIP-seq: FOXP2	ENCODE	---
SK-N-SH	Cell line	ChIP-seq: FRA2	ENCODE	---
SK-N-SH	Cell line	ChIP-seq: GABPA	ENCODE	---
SK-N-SH	Cell line	ChIP-seq: GATA3	ENCODE	---
SK-N-SH	Cell line	ChIP-seq: IRF3	ENCODE	---

Source	Type	Data Type	Database	Accession
SK-N-SH	Cell line	ChIP-seq: JUND	ENCODE	---
SK-N-SH	Cell line	ChIP-seq: MAX	ENCODE	---
SK-N-SH	Cell line	ChIP-seq: MEF2A	ENCODE	---
SK-N-SH	Cell line	ChIP-seq: MXI1	ENCODE	---
SK-N-SH	Cell line	ChIP-seq: NFIC	ENCODE	---
SK-N-SH	Cell line	ChIP-seq: NRF1	ENCODE	---
SK-N-SH	Cell line	ChIP-seq: P300	ENCODE	---
SK-N-SH	Cell line	ChIP-seq: PBX3	ENCODE	---
SK-N-SH	Cell line	ChIP-seq: RAD21	ENCODE	---
SK-N-SH	Cell line	ChIP-seq: REST	ENCODE	---
SK-N-SH	Cell line	ChIP-seq: RFX5	ENCODE	---
SK-N-SH	Cell line	ChIP-seq: SIN3A	ENCODE	---
SK-N-SH	Cell line	ChIP-seq: SMC3	ENCODE	---
SK-N-SH	Cell line	ChIP-seq: TAF1	ENCODE	---
SK-N-SH	Cell line	ChIP-seq: TCF12	ENCODE	---
SK-N-SH	Cell line	ChIP-seq: TEAD4	ENCODE	---
SK-N-SH	Cell line	ChIP-seq: USF1	ENCODE	---
SK-N-SH	Cell line	ChIP-seq: USF2	ENCODE	---
SK-N-SH	Cell line	ChIP-seq: YY1	ENCODE	---
SK-N-SH	Cell line	ChIP-seq: ZBTB33	ENCODE	---
SH-SY5Y	Cell line	ChIP-seq: GATA2	ENCODE	---
SK-N-SH	Cell line	ChIP-seq: NRSF	ENCODE	---
SK-N-SH	Cell line	ChIP-seq: CTCF	ENCODE	---

Table A2. Coordinates and annotations of FGEs in the SCN1A locus. Related to Figures 2.1-2.2. Dashes (---) indicate there was no detectable transcription factor (TF) binding at the FGE listed from the ChIP-seq data sets detailed in Table A1.

	Open Chromatin Marker(s)	TF Binding	Coordinates (hg19)	Size (bp)	Location
FGE1	FAIRE-seq	GATA3	166,873,787 - 166,874,095	308	Intron 18
FGE2	FAIRE-seq	FRA2, MEF2A, PBX3	166,898,882 - 166,899,935	1053	Intron 13
FGE3	FAIRE-seq, DNase-seq, ATAC-seq	CTCF, NFIC, PBX3, RAD21	166,913,884 - 166,914,907	1014	Intron 4
FGE4	DNase-seq, ATAC-seq, H3K4me3 ChIP-seq	GATA2, GATA3, MAML3	166,926,760 - 166,928,010	238	Intron 2
FGE5	DNase-seq, H3K4me1, H3K4me3, H3K27ac ChIP-seq	GATA2, GATA3, MAML3	166,930,205 - 166,931,219	2279	5'-UTR
FGE6	DNase-seq	GATA3	166,943,280 - 166,943,518	526	5'-UTR
FGE7	FAIRE-seq, DNase-seq, H3K4me3 ChIP-seq	OLIG2	166,946,845 - 166,949,124	1922	5'-UTR
FGE8	FAIRE-seq, DNase-seq	CTCF, RAD21, SMC3	166,962,872 - 166,963,398	1398	5'-UTR
FGE9	ATAC-seq, H3K4me1, H3K4me3, H3K27ac ChIP-seq	OLIG2	166,981,775 - 166,983,697	2240	5'-UTR
FGE10	FAIRE-seq, DNase-seq, H3K4me3, H3K27ac ChIP-seq	CTCF, OLIG2, RAD21, SMC3	166,983,840 - 166,985,238	409	5'-UTR
FGE11	FAIRE-seq, ATAC-seq	NRSF	167,004,493 - 167,006,733	223	5'-UTR
FGE12	FAIRE-seq	NFIC	167,016,348 - 167,016,757	527	Upstream
FGE13	FAIRE-seq, DNase-seq	FOXP2	167,024,047 - 167,024,270	512	Upstream
FGE14	FAIRE-seq, DNase-seq, H3K27ac ChIP-seq	CTCF, FRA2, JUND, P300, PBX3	167,026,790 - 167,027,317	1592	Upstream
FGE15	DNase-seq	P300, PBX3	167,027,660 - 167,028,172	448	Upstream
FGE16	DNase-seq	OLIG2	167,029,617 - 167,031,209	1592	Upstream
FGE17	FAIRE-seq, DNase-seq, H3K4me3 ChIP-seq	CTCF, RAD21	167,035,694 - 167,036,142	448	Upstream
FGE18	FAIRE-seq, DNase-seq	---	166,837,258 - 166,837,341	83	Downstream
FGE19	FAIRE-seq, DNase-seq	---	166,884,750-166,884,780	30	Intron 18
FGE20	H3K4me3, H3K27ac ChIP-seq	---	166,894,657-166,895,293	636	Intron 16
FGE21	FAIRE-seq, DNase-seq	---	166,928,910-166,929,109	199	Intron 3
FGE22	FAIRE-seq, DNase-seq, H3K4me1 ChIP-seq	---	166,937,563-166,938,119	556	5'-UTR
FGE23	DNase-seq, H3K27ac ChIP-seq	---	16,6940,692-166,941,192	500	5'-UTR
FGE24	H3K4me1, H3K4me3, H3K27ac ChIP-seq	---	166,959,544-166,960,098	554	5'-UTR
FGE25	H3K4me3, H3K27ac ChIP-seq	---	166,974,919-166,975,419	500	5'-UTR
FGE26	FAIRE-seq, H3K27ac ChIP-seq	---	166,976,143-166,976,923	780	5'-UTR
FGE27	FAIRE-seq, DNase-seq	---	167,043,303-167,043,349	46	Downstream
FGE28	DNase-seq, H3K27ac ChIP-seq	---	166,994,720-166,995,388	668	5'-UTR
FGE29	FAIRE-seq, DNase-seq, ATAC-seq	---	166,989,665-166,991,397	1732	5'-UTR
FGE30	FAIRE-seq, H3K27ac ChIP-seq	---	167,011,500-167,012,396	896	Upstream
FGE31	FAIRE-seq, DNase-seq	---	167,018,260-167,018,410	150	Upstream
FGE32	FAIRE-seq, DNase-seq, H3K4me3, H3K27ac ChIP-seq	---	167,037,608-167,038,408	800	Upstream

Table A3. List of primer sequences for molecular cloning and quantitative real-time PCR (qRT-PCR). Related to Figures 2.2-2.5, Figure A1.

Insert	Forward Primer (5'-3')	Reverse Primer (5'-3')	Length (bp)	5' Tags	Template
<i>SCN1A</i> (1B) Promoter	ACTCTCGAGTAAGTGTGTTAGATGGC	TCACTCGAGGCACCAGAGACCTCTGC	1084	SacI/XhoI	gDNA
<i>TK</i> Promoter	CTTCGAGCTGGCCGGTACCTGAGTCT	CTCGAGCCAAACAGTACCGGATTGCCA	557	XhoI	pGL4.54[luc2/TK]
Gateway Cloning Cassette	CGAAGCGAGCTCCATCCACGCTGTTTGACCT	CGAAGCGAGCTCCTATGACCTCGCATGCACG	1845	SacI	pDEST26
FGE1	CACCTGGGTGATGAAATGTTGCTCAC	TCTGGGTCCATATCTAGTTGCC	657	Gateway	gDNA
FGE2	CACCCCTTGTGAGCATCCGTTGGC	ACGTGGAAAGAACCTTGACCTTCT	1677	Gateway	gDNA
FGE2-A	CACCAGTCTCTGCACAAACCTGA	GTTTAGAAATTCCTCATCTGAGTA	448	Gateway	gDNA
FGE2-B	CACCAGATGCTGCCTCTTCTAGA	TGTTAGAAATGCTGGCTATACTCA	746	Gateway	gDNA
FGE2-A-Δ1	CACCCTATATACCCACACTGAAT	GTTTAGAAATTCCTCATCTGAGTA	357	Gateway	gDNA
FGE2-A-Δ2	CACCATGTAATAAATCTTCC	GTTTAGAAATTCCTCATCTGAGTA	265	Gateway	gDNA
FGE2-A-Δ3	CACCCCTAGTACTCATATTTT	GTTTAGAAATTCCTCATCTGAGTA	167	Gateway	gDNA
FGE2-A-Δ4	CACCACAGACAGATAAAATAATTG	GTTTAGAAATTCCTCATCTGAGTA	81	Gateway	gDNA
FGE3	CACCTGGTGTAGAATTTTCAGTGAGCA	AGGCCACTTATCTGCAATATTGT	1334	Gateway	gDNA
FGE4	CACCTCAGTTGACAGTGGTACTAGGA	CTCAATCATGTGTTCTAAGCACA	1309	Gateway	gDNA
FGE5	CACCACITGAGTCTCCCTCTTTTGA	GGCTCTTCAATAGCCCAA	1392	Gateway	gDNA
FGE6 (rs11890028)	CACCGGATCCACCATGACCCAAA	TGCTTCCCAACCTGTCAGAA	476	Gateway	gDNA
FGE7	CACCGGCTGAGTTGGCACCTATCA	TGAGCCATTTGTATCCAGCAAGA	2582	Gateway	gDNA
FGE8	CACCCCTCTTAGCTCTCTTTGGTAGC	AGTAAAGGTAGAGGACTCAAAGA	622	Gateway	gDNA
FGE9	CACCTGCCAACTCCTATTGAGCCAC	GCAAGAGGGGCATGTAAC	648	Gateway	gDNA
FGE12	CACCTTCTAGGATGATGATGGCTT	TGTGGATAATTGAAGGTCTGGGA	596	Gateway	gDNA
FGE13	CACCTCTTTCAACTAAGTCTTCCCA	TCCTCCACTTATGAACAGTTCCA	385	Gateway	gDNA
FGE14	CACCAGACAAGTATATATTCAGCGGCT	TATGCTCCTACTGGAATGC	650	Gateway	gDNA
FGE15	CACCGCAATGAAGTGGGAAGTGGG	TGGGCTAAGTAGTAAGAAGACCC	663	Gateway	gDNA
FGE16	CACCGGGCTAGTTTAATCCAATCTCC	CCCGAAGTAAAATCAGTTGGCA	1656	Gateway	gDNA
FGE17	CACCAGGGTCCAAAGTAACCAATGTGA	AACAATTCGGGGTGAGGAGA	557	Gateway	gDNA
FGE17-A	CACCAGGGTCCAAAGTAACCAATGTGA	CCCCAAAAAACTACGTTTCTCTTTT	310	Gateway	gDNA
FGE17-B	CACCATGTAAGTTTTTAAAAATCTTT	AACAATTCGGGGTGAGGAGA	243	Gateway	gDNA
FGE17-Δ1	CACCAAAATATTACTTCTTTTTCATGT	AACAATTCGGGGTGAGGAGA	357	Gateway	gDNA
FGE17-Δ2	CACCGGGATGTAAGTTTTTA	AACAATTCGGGGTGAGGAGA	247	Gateway	gDNA
FGE17-Δ3	CACCTCAGTACGAGTCAAAAAG	AACAATTCGGGGTGAGGAGA	139	Gateway	gDNA
FGE17-Δ4	CACCTTCTACTGAGAATTTTAC	AACAATTCGGGGTGAGGAGA	75	Gateway	gDNA
FGE18	CACCAGATGCATACCATACCTGTAAGA	ACAGATTTAAAATGGCAAGCTCA	191	Gateway	gDNA
FGE19	CACCTGCATTTGGTTCTAGCTTGGG	CGATAGGTCACATAAACTTCTGT	176	Gateway	gDNA
FGE20 (rs6732655)	CACCTCAGGGCTCAGTATGATGTTAC	ACTTGAAAACCTCCGAGCTGG	691	Gateway	gDNA
FGE21	CACCACTGGAAATACTTGGAAATCTCAA	TGAACGGTTGGATGCTTAACA	354	Gateway	gDNA
FGE22	CACCAAGTTGTGGATGCTGGGTGT	TCGGGAGACTTACAAGATCAGA	726	Gateway	gDNA
FGE23	CACCGCCATACAACCATGAGTCTGAA	GTCTATTCTCTTCCCCTTCTCGA	601	Gateway	gDNA
FGE24	CACCACCATTTTCAGCTCTCACCT	CGAGCTATTTTGGATAATGCA	682	Gateway	gDNA
FGE25	CACCCCACTCCCAACAATGTCC	TGCTATTCCACAGAGATTTCAGGA	754	Gateway	gDNA
FGE26	CACCAATGGCTAAATAAATCATAGTCTAGGC	ATTCGTGCTGAGTTCTAAAGAGA	973	Gateway	gDNA
FGE27	CACCGGCCGTGATCCTAGCTC	ACTTATTTGCTGCTGCTGTC	195	Gateway	gDNA
FGE28	CACCTGCTTTCAGGGTACAGA	CCCATTCTGAGGAGAAAGTAGCTG	674	Gateway	gDNA
FGE29	CACCCCTCTGTGGCAATAGATATGGA	AGGCTTTTCTTAACCTACCACA	1818	Gateway	gDNA
FGE30	CACCGAAAGGACTGAGGATGGAATGG	ACACAGATGAGGTCCTTAGC	993	Gateway	gDNA
FGE31	CACCTGCAAGCCATAAATACTTAAATGGT	TGTGAATTTCTAGTTCCAGTACAAC	223	Gateway	gDNA
FGE32	CACCTAGAGGGTTGACTTTGGT	ATATATGCTCAAGGCCGGC	919	Gateway	gDNA
F16 Enhancer	CACCGTGAATCATGAGAGAGCGTG	CGAATCTGACCTCAAGTGA	903	Gateway	gDNA
rs12987787	CACCGGATCAAAGTTTGGGGAATGACA	TCTTAGAGACCCAGTAGTAAAAAC	278	Gateway	gDNA
<i>SCN1A</i> (qRT-PCR)	CGTTCATTTTCGATTGCTCGCA	GACGATGATGGCCAAGACGA	129	---	cDNA
<i>ACTB</i> (qRT-PCR)	AGAGTACGAGCTGCCTGAC	AGCACTGTGTTGGCGTACAG	184	---	cDNA

APPENDIX B: Supporting data for Chapter 3

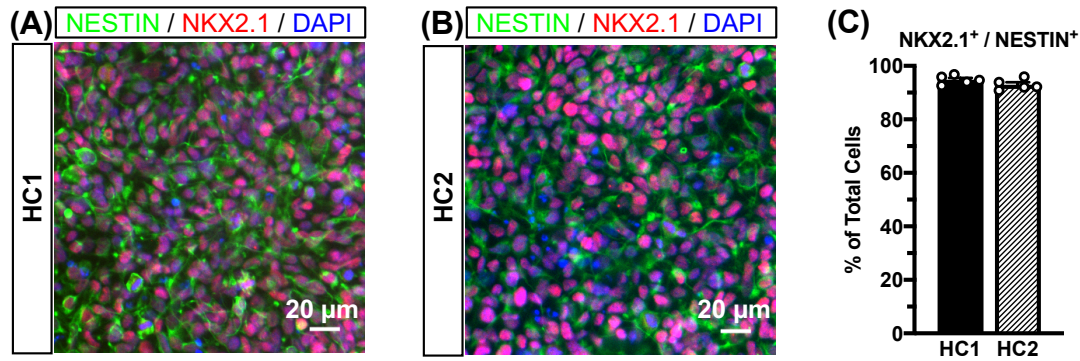


Figure B1. Neural progenitor cells (NPCs) emerge after 22 days of differentiation. (A-B) Representative immunostaining images of (A) HC1- and (B) HC2-derived cells at 22 days post-differentiation (D22, scale bars: 20 μm). (C) >90% of cells from both the HC1 and HC2 lines express the neural progenitor markers, NESTIN and NKX2.1, by D22 (n=5). Mean + SEM.

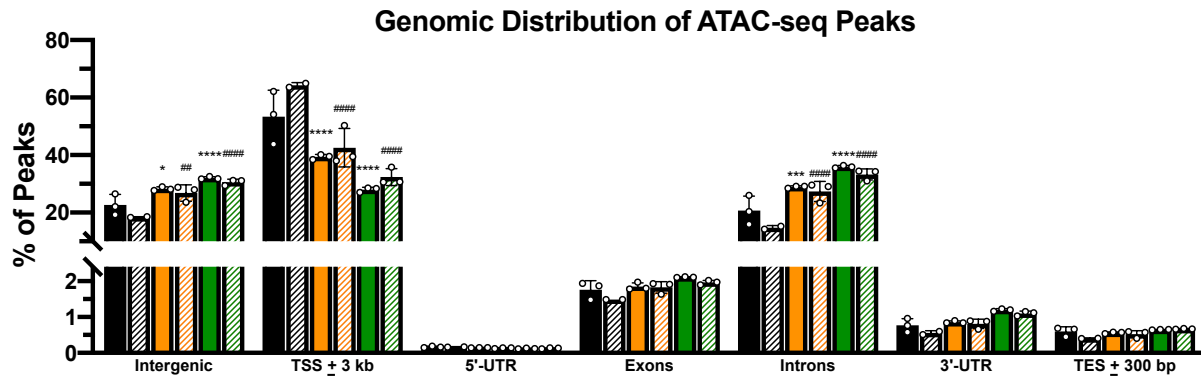


Figure B2. The genomic distribution of ATAC-seq peaks is comparable between the HC1 and HC2 lines at each stage of GABAergic interneuron (GIN) differentiation. The majority of peaks fall within 3 kb of the transcription start site (TSS ± 3kb), introns, or intergenic regions, although there is a significant shift in peak distribution from D22 to D78. There is no significant change in distribution of peaks within the 5'- or 3'-untranslated regions (UTRs), exons, or transcription end sites (TESs). Asterisks (*) denote statistical comparisons to D22 in HC1, while pound signs (#) denote statistical comparisons to D22 in HC2. Mean ± SD. * $p < 0.05$, ## $p < 0.01$, *** $p < 0.001$, ****/##### $p < 0.0001$.

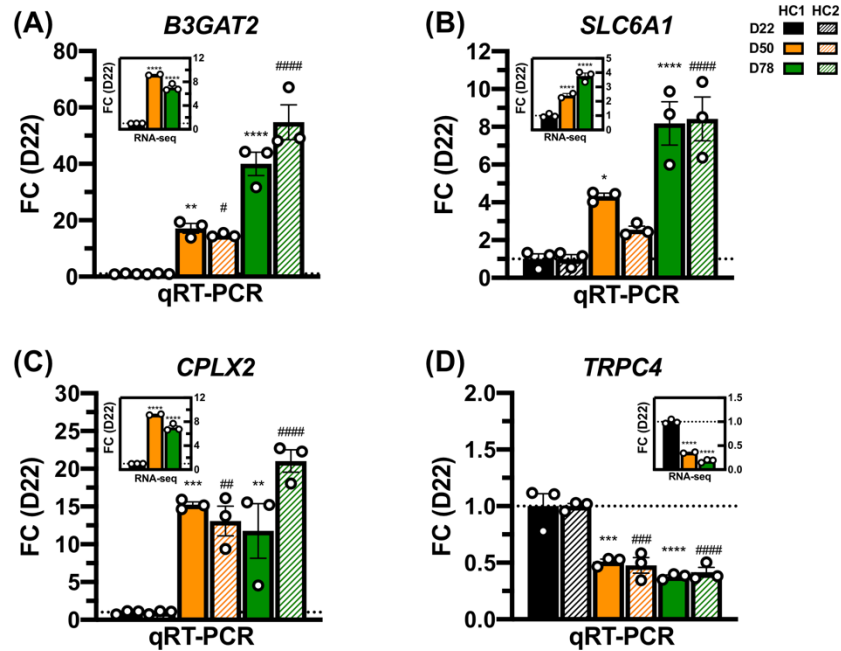


Figure B3. Differentially expressed genes (DEGs) exhibit consistent expression patterns between HC1 and HC2 cell lines. Related to Figures 3.5 & 3.8. Additional validation of DEGs identified by RNA-seq reveals comparable trends in expression between HC1 and HC2 cells across GIN differentiation. qRT-PCR results are normalized to *ACTB*, and expression is presented as fold change (FC) relative to D22 (n=3). DESeq2-normalized RNA-seq results are presented in the corner of each panel, relative to D22 (n=2-3). Asterisks (*) denote statistical comparisons to D22 in HC1, while pound signs (#) denote statistical comparisons to D22 in HC2. Mean \pm SEM. */# $p < 0.05$, **/# $p < 0.01$, ***/### $p < 0.001$, ****/#### $p < 0.0001$.

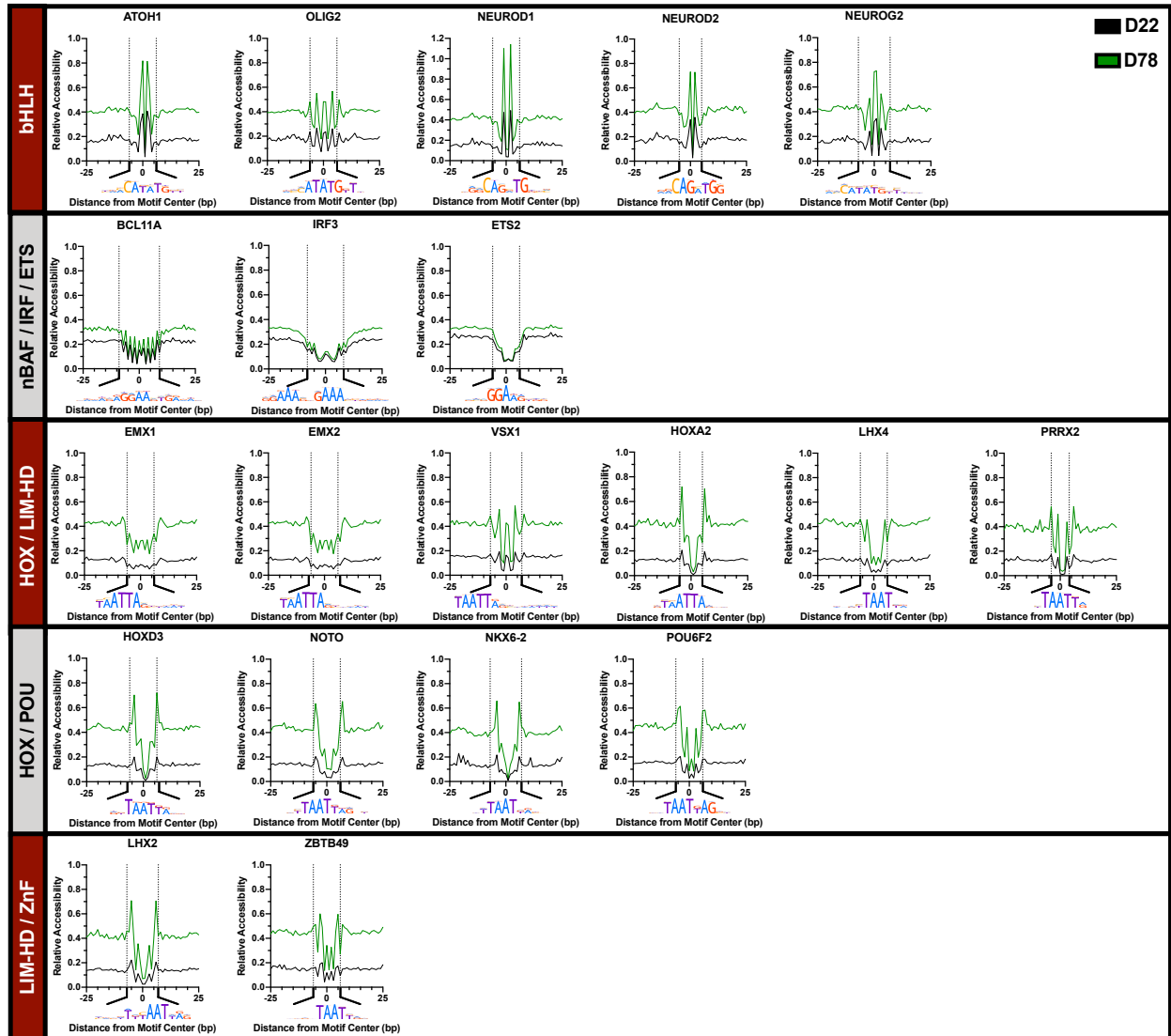


Figure B4. Transcription factor motifs enriched in +A DARs with increased accessibility over GIN differentiation exhibit discernable footprints. Related to Figure 3.6. Sequence logos derived from the HOCOMOCO TF binding model database (213). Row titles denote relevant TF families.

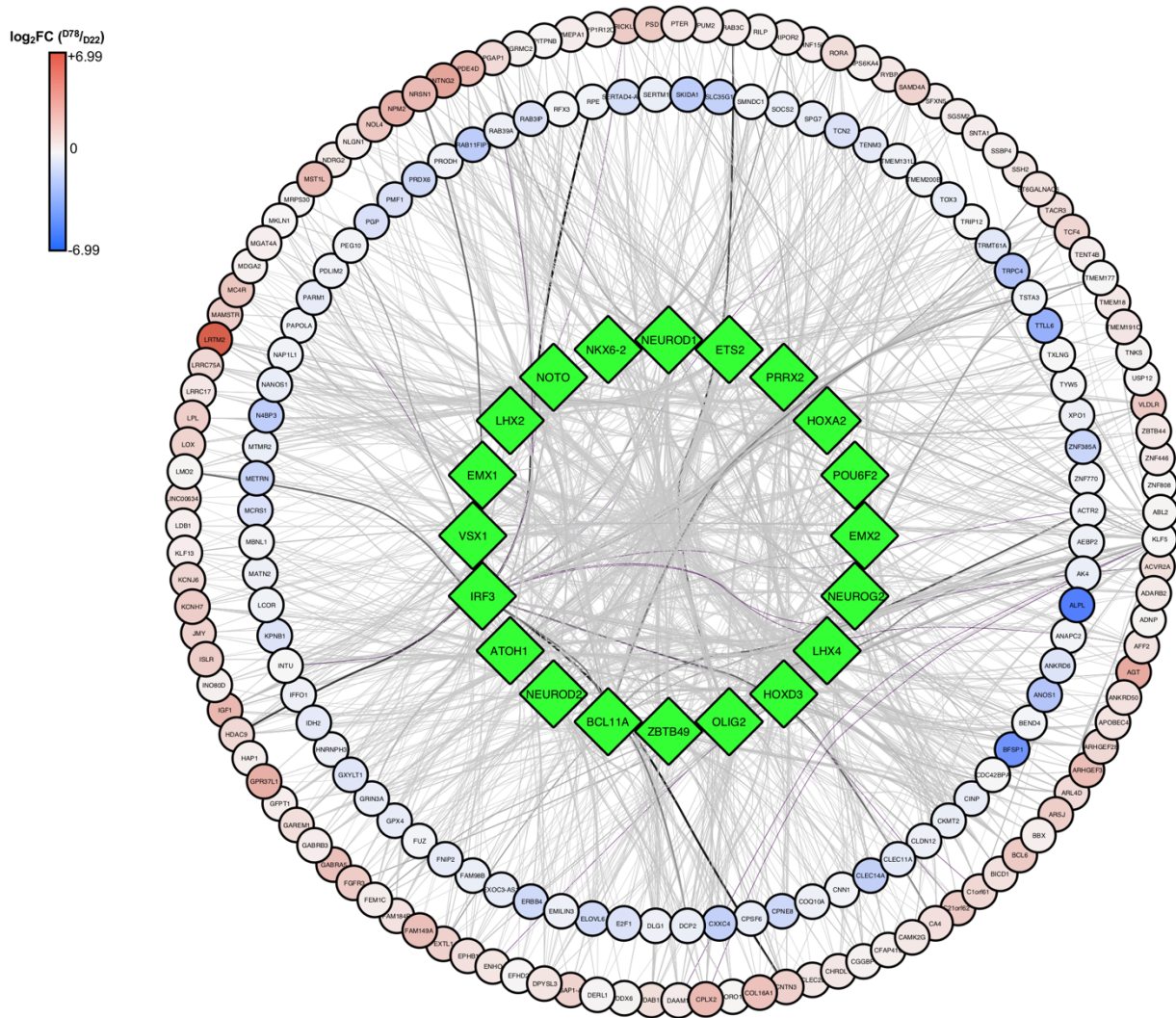
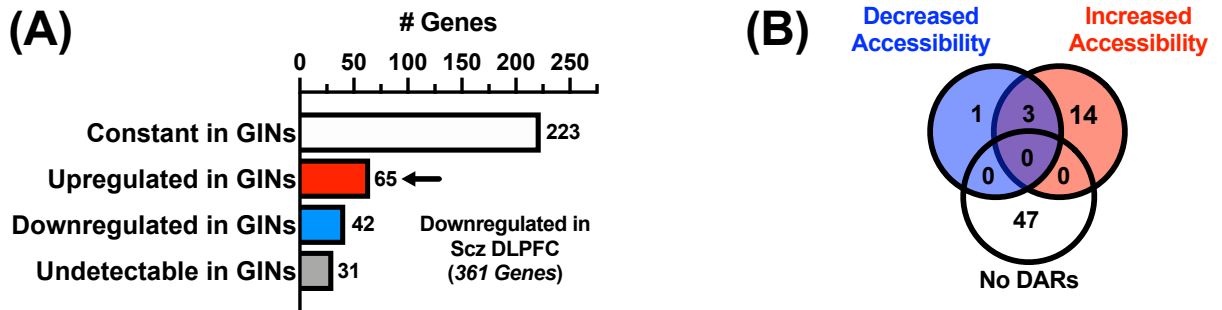


Figure B6. Transcription factors enriched in +A DARs are predicted to interact with 198 genes that are differentially expressed in the dorsolateral prefrontal cortex of schizophrenia patients. Transcription factors are denoted by green diamonds, while predicted target genes are denoted by circles (218). Circle colors denote the log₂ fold change (FC) in gene expression between D78 and D22 from RNA-seq in HC1 cells (blue: downregulated, red: upregulated).

Downregulated in Scz DLPFC, Upregulated in GINs



Upregulated in Scz DLPFC, Downregulated in GINs

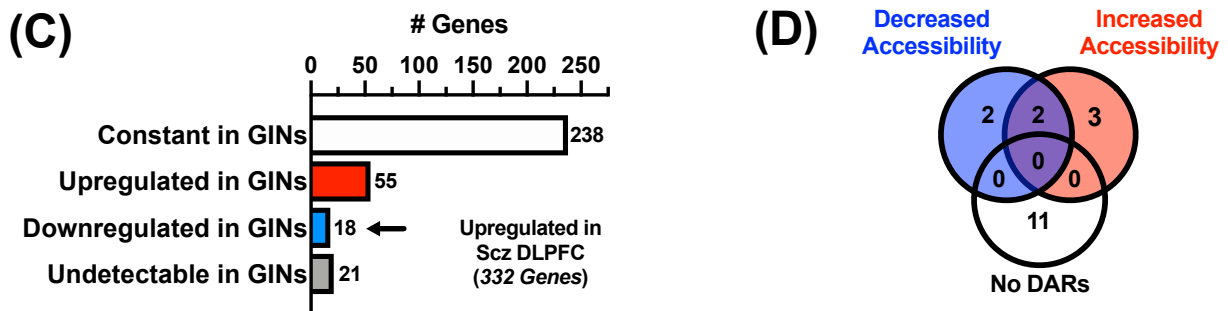


Figure B7. Overview of comparisons between DEGs associated with GIN differentiation and the schizophrenia dorsolateral prefrontal cortex. Related to Figure 3.8. **(A)** Summary of comparisons between differentially expressed genes identified in the dorsolateral prefrontal cortex of schizophrenia patients (Scz DLPFC) by Fromer et al. and the 4,840 DEGs between D78 and D22 identified in this study (218). Arrows denote the subsets of genes within each group used for further analysis. **(B-C)** Venn diagram comparisons of whether the DEGs denoted in **(A)** exhibit DARs.

Table B1. List of primer sequences for quantitative real-time PCR (qRT-PCR) analyses. Related to Figures 3.2 and B3. "Annealing Temperature" denotes the optimal annealing temperature to achieve 90-100% amplification efficiency for a given primer pair. Primers for *SCN1A* were initially generated by Frasier et al (338).

Gene-Primer	Direction	Sequence (5'-3')	Annealing Temperature (°C)
<i>SCN1A*</i>	Forward	ATGGCCATGGAGCACTATCC	58
	Reverse	CTACCAGGCTAAGCGTCACA	
<i>ACTB</i>	Forward	AGAGCTACGAGCTGCCTGAC	58
	Reverse	AGCACTGTGTTGGCGTACAG	
<i>SLC6A1</i>	Forward	CACTACCAACATGACCAGCG	60
	Reverse	GTAGACCACCTTTCCAGTCCA	
<i>NEUROD1</i>	Forward	CACTCAAGCAGGACTCCTCG	60
	Reverse	GGTCGTGGTGAAGGTGCATA	
<i>DLX3</i>	Forward	ACGCAGACACAGGTGAAAATC	58
	Reverse	AGTGGAGTGGGAAGAGGTGT	
<i>CHL1</i>	Forward	TCCCCAGTTGACAATCATCCA	58
	Reverse	TGTACCCAACCACTGTAGCG	
<i>CPLX2</i>	Forward	GCAGATCCGAGATAAGTATGGGC	58
	Reverse	CTTGAACATGTCCTGCAGCG	
<i>B3GAT2</i>	Forward	TTCCAGGAGATGCGAACCAC	58
	Reverse	CTGGGATCCACGACGCTTAA	
<i>TRPC4</i>	Forward	AACAATAGGGAGGCGAGCTG	58
	Reverse	ATCCCAGGACTTCAAAGCGG	

Table B2. List of the 10 most significant biological process gene ontology (GO) pathways identified by gene set enrichment analysis (GSEA). Related to Figure 3.3. “Size” denotes the number of genes within each gene set (NES: normalized enrichment score; FDR: false discovery rate, relative to D22).

ID	Description	Size	D50: NES	D50: FDR	D78: NES	D78: FDR
GO:0099504	synaptic vesicle cycle	189	1.5756013	<0.0001	1.5959315	0.001415
GO:0099003	vesicle-mediated transport in synapse	197	1.5349153	0.002390	1.5796325	0.003023
GO:0050808	synapse organization	370	1.5101421	0.006931	1.5545511	0.009122
GO:0017156	calcium-ion regulated exocytosis	145	1.5600656	0.000421	1.5560323	0.009335
GO:0051648	vesicle localization	298	1.5365695	0.003698	1.5354764	0.017118
GO:0061025	membrane fusion	127	1.4818105	0.023036	1.5280914	0.018965
GO:0007214	GABA signaling pathway	24	1.4254581	0.006650	1.39878299	0.029075
GO:0051932	GABAergic synaptic transmission	45	1.4731138	0.000750	1.4236231	0.038050
GO:0050890	cognition	263	1.5298067	0.002420	1.6382539	<0.0001
GO:0099177	regulation of trans-synaptic signaling	398	1.5351434	0.002773	1.696722	<0.0001

APPENDIX C: Supporting data for Chapter 4

C.1 Supporting materials and methods

C.1.1 Open field test and novel object recognition

The open field test was performed on Day 1 of the novel object recognition paradigm. Mice were individually placed in the corner of an opaque 61 x 61 x 61 cm³ Plexiglas box and given 10 min to explore. The time spent in the center of the apparatus, distance travelled, and speed were recorded. On Days 2-3, two identical objects (either transparent cubes or brown cylinders) were placed in the center of the box. Objects were alternated, such that half of the mice received cubes and half received cylinders. On Day 4, one object was replaced with its counterpart; a cylinder for a cube or vice versa. To account for position bias, the location of this “novel” object on the left or right side of the chamber was also alternated. The amount of time spent interacting with the “novel” vs. “familiar” object was recorded. Novel object preference was calculated as the percentage of time spent interacting with the “novel” object, out of the total time spent interacting with either the “novel” or “familiar” objects. Mice that spent less than a total of 10 s interacting with the objects were excluded from analysis.

C.1.2 Three-chamber social interaction

Mice were individually placed in the center of an opaque Plexiglas box, which was equally divided into three 20 x 40 x 22 cm³ accessible chambers. The left and right chambers of the box contained two identical wire cages. Mice were observed during three 10-min trials on the same day. In Trial 1, both wire cages were empty, and the test mouse was allowed to explore the entire apparatus. In Trial 2, an age-matched C57BL/6J male was placed into one of the two wire cages.

Time interacting with this “stranger” mouse vs. the empty cage was recorded as a metric of sociability. In Trial 3, a new, age-matched “stranger” C57BL/6J male was placed into the other wire cage. Time interacting with either the first (now “familiar”) mouse from Trial 2, or the new “stranger” mouse introduced in Trial 3 was recorded, as a metric of social novelty. The placement of the “familiar” or “stranger” mice in the left/right wire cage was alternated between experimental mice, but not between trials. Mice that did not enter both the left/right chambers or spent less than a total of 10 s interacting were excluded from analysis.

C.1.3 Reciprocal social interaction

Pairs of heterozygous mutant mice from separate home cages were placed into a novel clean cage and given 10 min to interact. Total time spent by either mouse performing social behaviors (sniffing, grooming, etc.) was recorded. This task was repeated with pairs of WT littermates, again from separate home cages.

C.2 Supporting figures and tables

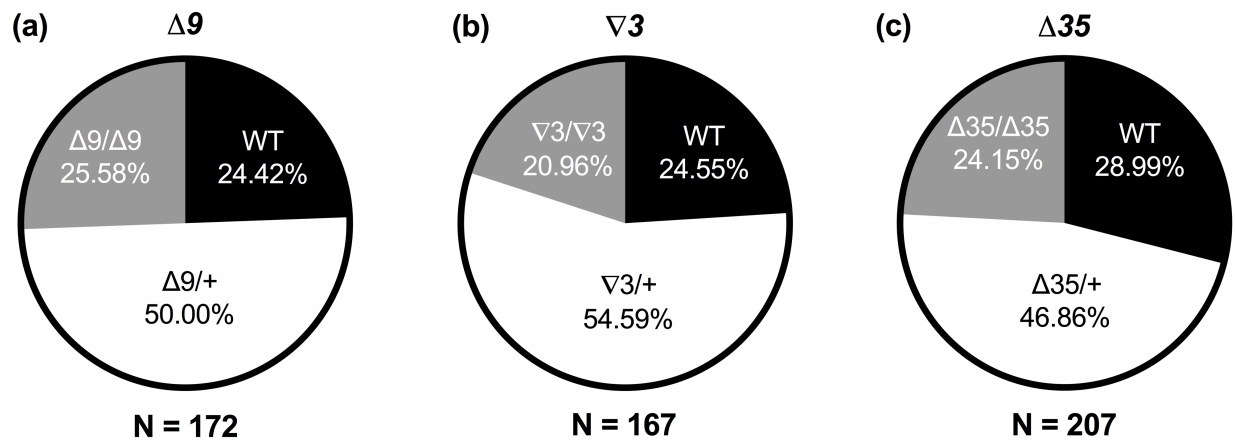


Figure C1. *Scn8a* ^{$\Delta 9/\Delta 9$} , *Scn8a* ^{$\nabla 3/\nabla 3$} , and *Scn8a* ^{$\Delta 35/\Delta 35$} homozygous mutants are born in the predicted Mendelian ratio.

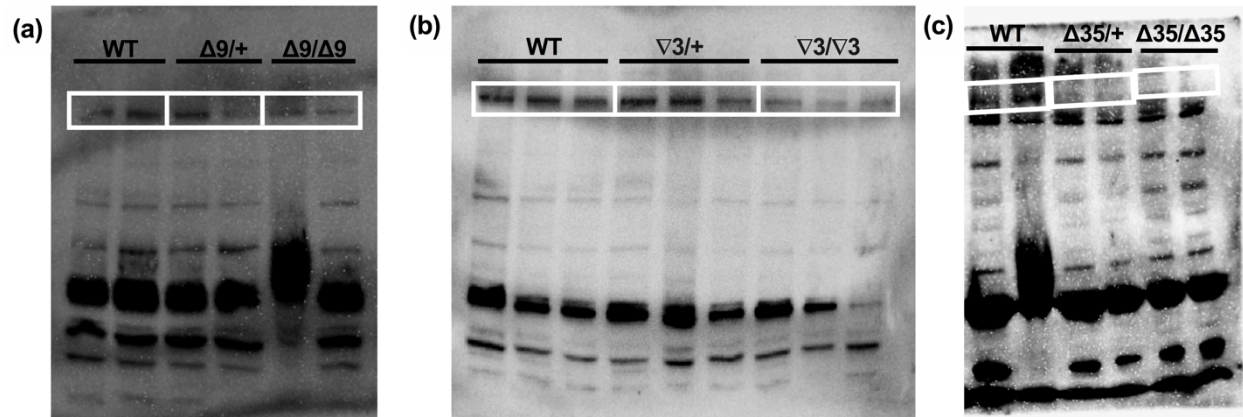


Figure C2. Representative anti- $\text{Na}_v1.6$ immunoblots. The 260 kDa $\text{Na}_v1.6$ band is outlined on each blot.

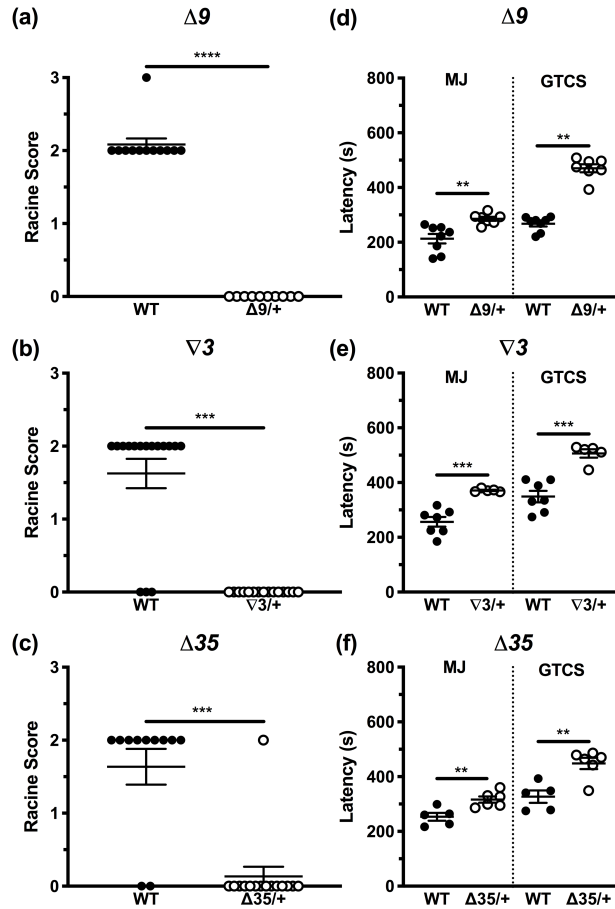


Figure C3. Female *Scn8a*^{Δ9/+}, *Scn8a*^{∇3/+}, and *Scn8a*^{Δ35/+} heterozygous mutants are resistant to induced seizures. (A-C) Female *Scn8a*^{Δ9/+}, *Scn8a*^{∇3/+}, and *Scn8a*^{Δ35/+} mutants are more resistant to 6 Hz seizures at a current of 27 mA compared to WT littermates. Sample sizes per line, where *m* denotes a mutant allele: Δ9 (WT: *n* = 8, *m*/+ : *n* = 7, from seven litters), ∇3 (WT: *n* = 7, *m*/+ : *n* = 5, from six litters), Δ35 (WT: *n* = 5, *m*/+ : *n* = 6, from seven litters). **(D-F)** Female *Scn8a*^{Δ9/+}, *Scn8a*^{∇3/+}, and *Scn8a*^{Δ35/+} mutants demonstrate increased latencies to the flurothyl-induced myoclonic jerk (MJ) and first generalized tonic-clonic seizure (GTCS) relative to WT littermates. Sample sizes per line: Δ9 (WT: *n* = 12, *m*/+ : *n* = 10, from five litters), ∇3 (WT: *n* = 16, *m*/+ : *n* = 15, from four litters), Δ35 (WT: *n* = 11, *m*/+ : *n* = 15, from seven litters). Mean ± SEM. ***P* < .01, ****P* < .001, *****P* < .0001

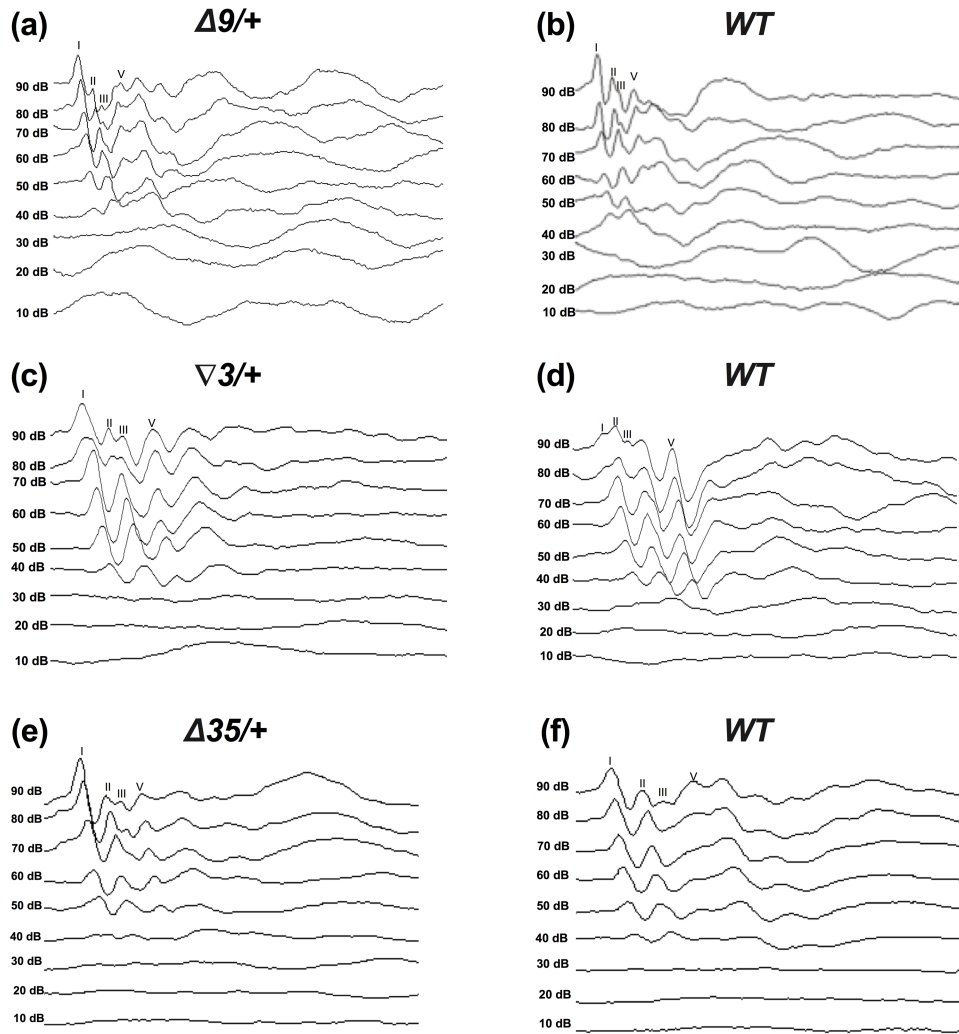


Figure C4. Representative click-test-evoked ABR waves. Heterozygous mutant mice and WT littermates from each line demonstrate comparable ABR thresholds, as indicated by the loss of ABR waveforms at similar stimulus intensities. Waves are presented in order of decreasing auditory stimulus intensity (90-10 dB) in the ABR click test for **(A-B)** *Scn8a*^{Δ9/+} mutants and WT littermates, **(C-D)** *Scn8a*^{∇3/+} mutants and WT littermates and, **(E-F)** *Scn8a*^{Δ35/+} mutants and WT littermates. Roman numerals denote ABR waves I, II, III and V.

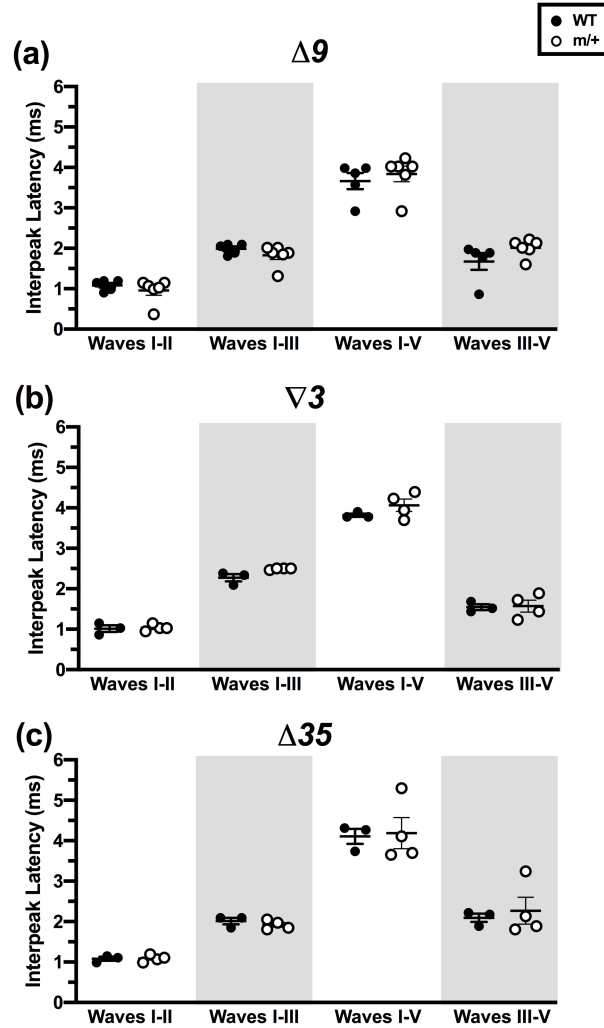


Figure C5. *Scn8a* ^{$\Delta 9/+$} , *Scn8a* ^{$\nabla 3/+$} , and *Scn8a* ^{$\Delta 35/+$} heterozygous mutants exhibit normal ABR interpeak latencies. The interpeak latency, or the time between ABR wave peaks, is comparable between *Scn8a* ^{$\Delta 9/+$} , *Scn8a* ^{$\nabla 3/+$} , and *Scn8a* ^{$\Delta 35/+$} mutants and their respective WT littermates. Sample sizes per line, where *m* denotes a mutant allele: $\Delta 9$ (WT: *n* = 5, *m/+*: *n* = 6, from three litters), $\nabla 3$ (WT: *n* = 3, *m/+*: *n* = 4, from two litters), $\Delta 35$ (WT: *n* = 3, *m/+*: *n* = 4, from three litters). Mean \pm SEM.

Behavior	Assay	Metric	Genotype	n	Mean	SEM	P	Significance
Anxiety/ Activity	Open Field Test	Time in Center (s)	WT	13	31.46	4.676	0.7110	ns
			$\Delta 9/+$	12	28.84	5.213		
		Distance Travelled (m)	WT	13	42.66	2.95	0.1371	ns
			$\Delta 9/+$	12	36.17	3.003		
		Speed (m/s)	WT	13	0.07115	0.06025	0.1348	ns
			$\Delta 9/+$	12	0.004931	0.005008		
Learning/ Memory	Novel Object Recognition	Novel Object Preference (% Time with Novel Object)	WT	11	64.46	5.456	0.0243	*
			$\Delta 9/+$	7	68.82	4.859	0.0082	**
Social Interaction	Three- Chamber Social Interaction	Sociability (% Time with Familiar Mouse in Trial 2)	WT	7	78.20	3.660	0.0003	***
			$\Delta 9/+$	14	64.82	3.701	0.0015	**
		Social Novelty (% Time with Stranger Mouse in Trial 3)	WT	7	54.52	3.904	0.2912	ns
			$\Delta 9/+$	14	58.63	2.999	0.0130	*
	Reciprocal Social Interaction	Total Interaction Time (s)	WT	6	21.35	4.660	0.0287	*
			$\Delta 9/+$	10	45.23	6.979		
		Latency to Interaction (s)	WT	6	102.8	38.29	0.0784	ns
			$\Delta 9/+$	10	41.43	11.02		

Table C1. *Scn8a* ^{$\Delta 9/+$} heterozygous mutants do not exhibit deficits in several behavioral paradigms. Male *Scn8a* ^{$\Delta 9/+$} and WT littermates at the N4 generation aged 3-5 months were tested in each assay. Sample sizes (from six to eight litters) and mean \pm SEM listed. ns $P > .05$, * $P < .05$, ** $P < .01$, *** $P < .001$

Behavior	Assay	Metric	Genotype	n	Mean	SEM	P	Significance
Anxiety/ Activity	Open Field Test	Time in Center (s)	WT	8	53.38	7.855	0.2439	ns
			∇3/+	12	42.30	5.398		
		Distance Travelled (m)	WT	8	110.1	25.29	0.2654	ns
			∇3/+	12	81.66	11.32		
		Speed (m/s)	WT	8	0.1836	0.04211	0.2629	ns
			∇3/+	12	0.1361	0.01885		
Learning/ Memory	Novel Object Recognition	Novel Object Preference (% Time with Novel Object)	WT	5	62.62	2.607	0.0084	**
			∇3/+	9	61.00	4.601	0.0437	*
Social Interaction	Reciprocal Social Interaction	Total Interaction Time (s)	WT	5	16.46	4.444	0.0497	*
			∇3/+	5	61.08	18.80		
		Latency to Interaction (s)	WT	5	66.98	38.56	0.2124	ns
			∇3/+	5	14.54	3.268		

Table C2. *Scn8a*^{∇3/+} heterozygous mutants do not exhibit deficits in several behavioral paradigms. Male *Scn8a*^{∇3/+} and WT littermates at the N4 generation aged 3-5 months were tested in each assay. Sample sizes (from four litters) and mean ± SEM listed. ns $P > .05$, * $P < 0.05$, ** $P < .01$

	$\Delta 9/+$	$\nabla 3/+$	$\Delta 35/+$	$\Delta 9/\Delta 9$	$\nabla 3/\nabla 3$	$\Delta 35/\Delta 35$
% survival to P90	100%	85-90%	100%	15-20%	0%	0%
Reciprocal social interaction	↑	↑	---	---	---	---
Rotarod performance	↓	↓	ns	---	---	---
Grip strength	ns	↓	ns	---	---	---
Acoustic startle response	↓	↓	ns	---	---	---
Auditory brainstem response	ns	ns	ns	---	---	---
Nerve conduction velocity	ns	ns	ns	↓	↓	ns

Table C3. *Scn8a* $\Delta 9$, $\nabla 3$, and $\Delta 35$ heterozygous and homozygous mutant mice exhibit several phenotypic differences from WT littermates. Arrows denote a significant increase (↑) or decrease (↓) in the parameter listed, relative to WT littermates. “ns” denotes no significant difference from WT littermates, while dashes (---) indicate phenotypes that were not assessed in the genotype listed.